Edited by
Inna Shalevska

MODERN TRENDS IN CONSTRUCTION MATERIALS TECHNOLOGIES

Collective monograph

Technology Center

2025

UDC 338.47
C88

Published in 2025
by TECHNOLOGY CENTER PC®
Kharkiv, Ukraine

C88

Authors:
Edited by Inna Shalevska
Maksym Kovzel, Oleksandr Babachenko, Daria Togobitska, Oleh Kuzmin, Oktyabrina Chemakina, Anton Kuzmin, Oleksandr Zaporozhets, Igor Dudarev, Larysa Bal-Prylypko, Oleksandr Shcheretskyi, Anatolii Verkhovliuk, Ruslan Sergiienko, Dmytro Kanibolotsky, Volodymyr Shcheretskyi, Ievgenij Dzevin, Oleg Shinsky, Inna Shalevska, Iuliia Kvasnytska, Pavlo Kaliuzhnyi, Oleksandr Neima, Anatolii Shalevskyi
Modern trends in construction materials technologies: monograph / I. Shalevska and others. — Kharkiv: TECHNOLOGY CENTER PC, 2025. — 171 p.

The monograph is devoted to the actual scientific and practical problems of materials science, foundry production and engineering and architectural solutions, which are of great importance for the industrial development and post-war reconstruction of Ukraine. The book comprehensively combines research in the field of creation of new metal materials with increased operational properties and development of inclusive and sustainable engineering approaches in construction and environmental design.
The book is addressed to scientists, practicing engineers, foundry specialists, architects and designers, as well as scientific and pedagogical workers and higher education students in the specialties of materials science, metallurgy and civil engineering.
Figures 87, Tables 18, References 151 items.

DOI: 10.15587/978-617-8360-17-7
ISBN 978-617-8360-17-7 (on-line)

Cite as: Shalevska, I. (Ed.) (2025). Modern trends in construction materials technologies: monograph. Kharkiv: TECHNOLOGY CENTER PC, 171. doi: http://doi.org/10.15587/978-617-8360-17-7

AUTHORS

CHAPTER 1

MAKSYM KOVZEL
PhD, Associate Professor, Forensic Expert
Dnipropetrovsk Scientific Research Forensic Center of the MIA of Ukraine
ORCID: https://orcid.org/0000-0001-5720-1186

OLEKSANDR BABACHENKO
Doctor of Technical Science, Senior Scientist, Corresponding Member of NAS of Ukraine, Head of the Institute
Iron and Steel Institute of Z. I. Nekrasov of National Academy of Sciences of Ukraine
ORCID: https://orcid.org/0000-0001-7501-4173

DARIA TOGOBITSKA
Doctor of Technical Sciences, Professor, Head of the Department
Department of Physico-Chemical Problems of Metallurgical Processes
Iron and Steel Institute of Z. I. Nekrasov of National Academy of Sciences of Ukraine
ORCID: https://orcid.org/0000-0001-6413-4823

CHAPTER 2

OLEH KUZMIN
Doctor of Technical Sciences, Professor
Department of Technology of Restaurant and Ayurvedic Products
National University of Food Technologies
ORCID: https://orcid.org/0000-0001-9321-6684

OKTYABRINA CHEMAKINA
PhD, Associate Professor
Faculty of Architecture, Construction and Design
State University "Kyiv Aviation Institute"
ORCID: https://orcid.org/0000-0003-2934-2752

ANTON KUZMIN
PhD student
Institute of Food Resources of NAAS of Ukraine
ORCID: https://orcid.org/0009-0008-2790-1657

OLEKSANDR ZAPOROZHETS
PhD Student
Department of Mechatronics and Packaging Technology
National University of Food Technologies
ORCID: https://orcid.org/0009-0007-5644-2819

IGOR DUDAREV
Doctor of Technical Sciences, Professor
Department of Food Technology and Chemistry
Lutsk National Technical University
ORCID: https://orcid.org/0000-0002-2016-5342

LARYSA BAL–PRYLYPKO
Doctor of Technical Sciences, Professor
Department of Meat, Fish and Seafood Technology
National University of Life and Environmental Sciences of Ukraine
ORCID: https://orcid.org/0000-0002-9489-8610

CHAPTER 3

OLEKSANDR SHCHERETSKYI
Doctor of Technical Sciences, Leading Researcher
Department of Physical Chemistry of Alloys
Physico-Technological Institute of Metals and Alloys of National Academy of Sciences of Ukraine
ORCID: https://orcid.org/0000-0001-9030-876X

ANATOLII VERKHOVLIUK
Doctor of Technical Sciences, Professor, Head of Department
Department of Physical Chemistry of Alloys
Physico-Technological Institute of Metals and Alloys of National Academy of Sciences of Ukraine
ORCID: https://orcid.org/0000-0002-2670-4052

RUSLAN SERGIIENKO
PhD, Senior Researcher
Department of Physical Chemistry of Alloys
Physico-Technological Institute of Metals and Alloys of National Academy of Sciences of Ukraine
ORCID: https://orcid.org/0000-0003-3613-9330

DMYTRO KANIBOLOTSKY
PhD, Senior Researcher
Department of Physical Chemistry of Alloys
Physico-Technological Institute of Metals and Alloys of National Academy of Sciences of Ukraine
ORCID: https://orcid.org/0009-0001-2489-9167

VOLODYMYR SHCHERETSKYI
PhD, Senior Researcher
Department of Physical Chemistry of Alloys
Physico-Technological Institute of Metals and Alloys of National Academy of Sciences of Ukraine
ORCID: https://orcid.org/0000-0002-8561-4444

IEVGENIJ DZEVIN
PhD, Senior Researcher
Department of Physics of Dispersed Systems
G. V. Kurdyumov Institute for Metal Physics of the National Academy of Sciences of Ukraine
ORCID: https://orcid.org/0000-0001-7420-7504

CHAPTER 4

OLEG SHINSKY
Doctor of Technical Sciences, Professor, Head of Department
Department of Physics and Chemistry of Foundry Processes
Physico-Technological Institute of Metals and Alloys of National Academy of Sciences of Ukraine
ORCID: https://orcid.org/0000-0001-6200-0709

INNA SHALEVSKA
Doctor of Technical Sciences, Associate Professor, Leading Researcher
Department of Physics and Chemistry of Foundry Processes
Physico-Technological Institute of Metals and Alloys of National Academy of Sciences of Ukraine
ORCID: https://orcid.org/0000-0002-8410-7045

IULIIA KVASNYTSKA
Doctor of Technical Sciences, Senior Researcher, Head of Department
Department of Special Steels and Alloys
Physico-Technological Institute of Metals and Alloys of National Academy of Sciences of Ukraine
ORCID: https://orcid.org/0000-0003-3790-2035

PAVLO KALIUZHNYI
PhD, Senior Researcher
Department of Physics and Chemistry of Foundry Processes
Physico-Technological Institute of Metals and Alloys of National Academy of Sciences of Ukraine
ORCID: https://orcid.org/0000-0002-1111-4826

OLEKSANDR NEIMA
Researcher
Department of Physics and Chemistry of Foundry Processes
Physico-Technological Institute of Metals and Alloys of National Academy of Sciences of Ukraine
ORCID: https://orcid.org/0000-0001-5438-7253

ANATOLII SHALEVSKYI
Chief Technologist
Department of Physics and Chemistry of Foundry Processes
Physico-Technological Institute of Metals and Alloys of National Academy of Sciences of Ukraine
ORCID ID: https://orcid.org/0009-0002-8534-4728

ABSTRACT

The monograph is devoted to the actual scientific and practical problems of materials science, foundry production and engineering and architectural solutions, which are of great importance for the industrial development and post-war reconstruction of Ukraine. The book comprehensively combines research in the field of creation of new metal materials with increased operational properties and development of inclusive and sustainable engineering approaches in construction and environmental design.

The first chapter substantiates the rational compositions of chromium-manganese alloys and investigates the regularities of formation of their structure, phase composition and properties in the cast state. The possibilities of reducing the energy intensity of casting processes and increasing the wear resistance of products compared to traditional alloys-analogues are shown. The prospects of using the developed materials to increase the operational stability of piercing mandrels of pipe rolling mills are determined, provided that the heat treatment regimens are optimized and metastable self-strengthening structures are formed.

The second chapter is devoted to the integration of the principles of inclusive engineering and artisanal technologies in the design of public catering establishments in the conditions of post-war reconstruction of Ukraine. The choice of environmentally friendly building materials and architectural solutions that ensure accessibility, safety, energy efficiency and compliance with sanitary and hygienic requirements (HACCP) is justified. The proposed approach contributes to the sustainable development of communities, reducing the environmental load and preserving local cultural identity.

The third chapter considers promising high-entropy alloys based on the FeNiCrCuAl and FeNiCrCuMn systems as heat-resistant casting materials of a new generation. Based on thermodynamic calculations, structural-phase analysis and research of thermophysical, mechanical and casting properties, their high structural stability and feasibility of use in conditions of elevated temperatures are confirmed.

The fourth chapter highlights the scientific and technological prerequisites for obtaining steel hollow castings with composite and reinforced non-metallic fillers by the casting method using gasified models. A mathematical description of gas-hydrodynamic processes has been developed, computer modeling and experimental verification of technological solutions that are important for the manufacture of special and protective casting products have been carried out.

The book is addressed to scientists, practicing engineers, foundry specialists, architects and designers, as well as scientific and pedagogical workers and higher education students in the specialties of materials science, metallurgy and civil engineering.

CONTENTS

LIST OF TABLES

LIST OF FIGURES

CIRCLE OF READERS AND SCOPE OF APPLICATION

The materials of the monograph will be useful for a wide range of specialists and organizations. The results of research in the field of chromium-manganese and high-entropy alloys are focused on enterprises of the metallurgical and foundry industries, in particular, manufacturers of heat- and wear-resistant parts for pipe rolling mills, energy equipment, mechanical engineering, defense and special equipment. The proposed materials and technological solutions can be used when designing new products, modernizing casting processes and reducing material and energy consumption in industrial production.

The chapters devoted to steel hollow castings with composite and reinforced non-metallic fillers are of practical interest to developers and manufacturers of foundry products for special and protective purposes, as well as for enterprises of the defense-industrial complex, where a combination of high strength, reliability and reduced mass of structures is important.

Engineering and architectural research aimed at integrating the principles of inclusive design and artisanal technologies will be relevant for architects, civil engineers, design organizations, local governments and public initiatives involved in the post-war reconstruction processes of Ukraine. The proposed approaches can be used in the creation of public catering establishments, social infrastructure and public spaces focused on the needs of veterans, people with disabilities and internally displaced persons.

The publication is of particular value for scientists and scientific and pedagogical workers, postgraduates and students of higher education institutions in the specialties "Metallurgy", "Materials Science", "Foundry", "Mechanical Engineering", "Construction and Architecture", since the results presented can be used in the educational process, during the performance of qualification work and further scientific research.

INTRODUCTION

The current stage of development of science and technology is characterized by increasing requirements for materials, their manufacturing technologies and engineering solutions used in industry, construction and social infrastructure. In the context of global challenges caused by resource depletion, increased energy intensity of production, environmental restrictions and the consequences of the full-scale war in Ukraine, the development of innovative materials and technologies that can combine high performance characteristics, economic feasibility and social orientation is of particular relevance.

Metallurgy and foundry production remain basic industries that ensure the functioning of mechanical engineering, energy, transport and defense sectors. In this context, an important scientific task is the creation of new alloys with increased wear and heat resistance, improvement of their chemical composition, structure and phase state, as well as optimization of technological processes of casting and heat treatment in order to reduce energy consumption and increase the reliability of finished products. Along with this, the development of engineering approaches to the formation of a safe, accessible and environmentally responsible environment that meets modern social challenges is relevant.

The first chapter of the monograph examines the scientific foundations of the creation of chromium-manganese alloys with rational alloying. The optimal ranges of chemical composition are substantiated, the features of the formation of the structure and phase composition in the cast state are investigated, and the thermodynamic and technological characteristics of the melting and crystallization processes are analyzed. The results of comparative tests for friction and abrasive wear are presented, which confirm the increased wear resistance of the developed alloys compared to traditional analogue materials. The directions for further increasing the operational stability of products by optimizing heat treatment modes and forming metastable structures are outlined.

The second chapter is devoted to the issues of integrating the principles of inclusive engineering and craft technologies into the design of public catering establishments in the conditions of post-war reconstruction of Ukraine. The chapter analyzes the environmental, thermophysical and operational characteristics of natural and low-carbon building materials, as well as architectural and planning solutions aimed at ensuring accessibility, safety, hygiene and energy efficiency. A methodological approach to the creation of socially oriented, culturally authentic and sustainable public infrastructure facilities is proposed.

The third chapter presents the results of research into promising high-entropy alloys based on the FeNiCrCuAl and FeNiCrCuMn systems, designed for operation at elevated temperatures. The features of their production in vacuum induction furnaces are considered, thermodynamic prediction of the phase composition and experimental confirmation of the structural state are carried out. The thermophysical, mechanical and casting properties of the alloys are studied, and their heat resistance is also assessed, which allows us to consider these materials as a promising alternative to traditional steels and cast irons.

The fourth chapter presents the scientific and technological principles of obtaining hollow steel castings with composite and reinforced non-metallic fillers by the method of casting according to

gasified models. A mathematical description of gas-hydrodynamic and thermal processes is proposed, computer modeling and experimental verification of the influence of fillers on the quality of castings are carried out. The prospects of using the developed technological solutions for the manufacture of special and protective casting products, in particular for the needs of the defense sector, are shown. Thus, the monograph comprehensively covers modern approaches to the creation of new materials, the improvement of casting technologies and the implementation of inclusive engineering solutions. The results obtained have both scientific novelty and practical value and can be used in industry, design activities, scientific research and the educational process.

DOI: 10.15587/978-617-8360-17-7.CH1

Maksym Kovzel, Oleksandr Babachenko, Daria Togobitska

1 CHROMIUM–MANGANESE ALLOYS ON OCHOBI IRON WITH INCREASED TRIBOLOGICAL PROPERTIES

ABSTRACT

The current publication reports on the magnetic field influence on the microstructure of Cz-Si doped with Al, Mg, Cu, Fe, Zr, Hf. The point is that these dopants have different effects on the interaction energy of silicon atoms in its crystal lattice and differently behave under magnetic field treatment. In this context, the problem of silicon processing is first time addressed.

It is established that the dopants (Al, Mg, Cu, Fe), which decrease the energy of atom interaction within the crystal lattice of silicon, lead to the increase in the defects of the silicon structural units after 240 hours of magnetic field treatment while 720 hours produce the decrease in the quantity of such defects.

Cz-Si doped with Zr, Hf (these dopants increase the interaction energy of the silicon crystal lattice) experiences the decrease in the quantity of defects in the structural units starting from 240 of exposing to the magnetic field.

By means of X-ray diffraction technique, the occurrence of new peaks on the scattering angles of 90–92 degrees has been detected, that is due to Si_{FCC} lattice distortion and the formation of Si orthorhomic alongside with it. This indicates phase transformations in the samples of semiconductor silicon during magnetic treatment at room temperature.

KEYWORDS

Semiconductor silicon, complex doping, interaction energy, phase transformations, dislocation density, twins, magnetic field treatment, microhardness, specific electrical resistivity, charge minority-carrier lifetime.

Commonly, power engineering for energy production has always been posed as the principle industry of any developed country. To provide energy independence is one of the strategic tasks to address in modern Ukraine's economy development. The promising way how this task can be solved is in maximizing the strategic balance by enhancing the energy share from the own energy resources. The urgency of this problem in Ukraine determines the need for the development of the alternative energy forms based on renewable sources alongside with the energy saving.

Back in 1990, the world's developed countries initiated transition stage to the new energy sources. The environmentally-friendly attitude is among the features of this stage, i.e. it strives to reduce environmental pollution and to minimize carbon dioxide and sulfur dioxide emissions. Expected that during the next two or three decades, the mankind is to introduce ecologically-friendly renewable energy sources into everyday life, primarily wind power and solar power. Ignoring these tendencies threats with ecological disasters of the future and is able make the entire life on earth endangered.

Moreover, pursuing the target of achieving European Integration, Ukraine sets the strategic goal of rapid implementation for the energy produced from the renewable energy sources. Thus, solar power is the most promising direction of such kind in Ukraine, where there is a high potential due to the country's geographical position in the terrestrial latitudes with good solar radiation intensity. The latter implies that the photovoltaic equipment can be used throughout the year. Further, the high-performance operating time in the northern areas makes up 5 months (May to September), while in the southern areas it is 7 months (April to October). However, the solar power economic features require careful further study. According to experts, the operating cost of the electrical power generated by the solar modules will reduce by 5 times during the next 10 or 15 years.

Taking into account the above stated necessity of solar engineering development, silicon, as a constituent of solar cells, draws the close attention of the scientists. In particular, thermal stability of silicon crystal properties is one of the basic parameters of semiconductor quality and at the same time it is the very factor that determines the resistance of microelectronic devices to degradation at elevated temperatures and expands the area of their operation. Furthermore, thermal stability of silicon crystals is essential for manufacturing microelectronic devices, since crystals are exposed to high temperatures in many technological processes that often irretrievably deteriorate properties of primary crystals.

The topical character of the study is determined by the need to reveal the degradation regularities in silicon physical properties and the means of their further control, as well as by the necessity to develop semiconductor devices based on silicon with stable parameters.

The manufacturing processes and operation of semiconductor devices are known to be followed by thermal and radiation effects that cause the changes in the physical properties of both in semiconductors and the devices based on them. However, there are rigorous specifications to the manufactured semiconductor devices concerning stability of their parameters under various radiation and thermal operating conditions. The potentially productive ways of control over silicon physical parameter degradation are in its thermal treatment, doping and processing within a magnetic field.

Today there is a growing demand for monocrystalline silicon for photo-emissive converters from both foreign and domestic companies. The circle of scientific interests of the global research community continues to be focused on solar cell manufacturing techniques from cheap silicon that can be represented by polycrystalline silicon of low-purity ("dirty"), thin films of amorphous silicon of polycrystalline type and other semiconductors.

Considering the full-scale opportunities for the silicon and the dedicated equipment, the need for the sufficiently high level of readiness should be provided, which enables the rapid and efficient growth of modern solar power in Ukraine.

The first section of the current publication contains the literature review on the regularities in semiconductor silicon structure formation and properties, as well as the modern views and opinions on phase transformations and martensitic transformation mechanisms that occur in semiconductor silicon. The contemporary publications targeting the problem of the magnetic field effect on the semiconductor silicon structure and properties have been reviewed. This analysis enables outlining the character of the further studies and the stages of the topical scientific and technical task to be solved for the current research: for the present publication we set the task to develop the complex resource-saving technology and energy saving solution for production of semiconductor silicon with enhanced physical and mechanical properties by influencing its liquid and solid forms physically and chemically with the objective to expand the areas of its application.

The second section provides the data on the material and the research techniques. The object of the research is monocrystalline semiconductor silicon samples (Cz-Si) grown by Czochralski method, both in undoped version and doped with single elements of B, Sn, Ge, Hf, Zr, and with the complexes of B-Sn and B-Mo, ranging from $2 \cdot 10^{-4}$ to $8.7 \cdot 10^{-2}$ at % in the initial state, after they have been exposed to the complete heating-cooling cycle, the thermal treatment regimes and the weak direct current magnetic field effect.

In the third section the structure peculiarities formed under the magnetic field effect for both the undoped Cz-Si samples and the Cz-Si doped with Al, Mg, Cu, Fe, Zr, and Hf have been analysed, with the focus on the difference in the dopant effects on the silicon atom interaction energy within silicon crystal lattice. During the magnetic treatment at room temperature, the phase transformations have been detected in semiconductor silicon samples via X-ray diffraction technique.

In the fourth section we report on the magnetic treatment effect on the microhardness values of doped Cz-Si structural units.

The fifth section reveals physical parameters and mechanical properties of the doped and undoped silicon samples before and after magnetic field treatment with the induction of 66 mT.

1.1 EARLIER RESEARCH FINDINGS AND RELEVANT LITERATURE REVIEW

1.1.1 CRYSTALLOCHEMICAL PECULIARITIES OF SEMICONDUCTOR SILICON

Silicon is an element of IVB subgroup of the periodic system, the atomic number of 14, an electron configuration of $1S^2 2S^2 P^6 3S^2 P^2$. Silicon atoms possess four valence electrons and form a diamond-type or a zinc blende type of the crystal lattice with covalent bonds and coordination number of 4 at room temperature, when silicon behaves as a typical semiconductor.

Silicon has high specific melting point and its density increases when transformed from a solid state to a liquid one [1].

Under atmospheric pressure silicon is a covalent substance with strong semiconductor properties. Interatomic bonds are defined by means of tetrahedral symmetry and have sp^3 hybrid composition. All 4 silicon atom bonds are equivalent and equally saturated.

In [1–3], it is shown that silicon undergoes the semiconductor-metal transition during melting, while at high pressure (~12 hPa) [2] there has been detected the transition from purely covalent structure ($K=4$) of a diamond to bcc tetragonal covalent metal structure within silicon (as the white tin type) and then (~16 hPa) the transition to the typical body-centered cubic metallic structure ($K=8$).

The publications [1–4] suggest that the transition to metallic state (when melting the elements belonging to IVB group (germanium and silicon) as well as compounds of AIIIBV and AIIBIV types etc.) is related to the disruption in homopolar bond space system and to the separation of many free electrons; the latter form a new configuration with electron density of higher symmetry [3].

Silicon melting causes the sharp increase in its conductivity which value becomes equal to the liquid metal conductivity value. It should be noted, that conductivity alteration is connected to the rearrangement from the "diamond structure" of a solid state to denser packing peculiar to the "metallic state" that occurs when melting these substances of short range ordering; this process is confirmed by the density increase factor that to some extent reflects the structural changes. According to the X-ray investigation data, it has been proved that the structure change occurs in many semiconductors with diamond structure (including silicon) when in a liquid state. During melting silicon coordination number increases from 4 to 6.

1.1.2 PHASE TRANSFORMATIONS IN SEMICONDUCTOR SILICON

It is peculiar of silicon to have high specific fusion heat as well as density increase during transition from a solid state to a liquid state [5, 6]. Fusion entropy of silicon is considerably higher than that of pure metals that is why its value is greatly affected by the process related to the electron delocalization at the solid-liquid transition. The electron component is connected to the chemical bond type change (mainly from covalent bonds to metallic ones) during melting that is followed by the marked increase of free electron concentration [6].

For the substances that become highly metallized at melting, solid-liquid transition is followed by disruption in the sp^3-hybrid homopolar bond space system, by detachment of four valence electrons and their transition to the free state and by major changes of the short range ordering and atom vibrational spectrum [7–9].

A distinguishing feature of the first-order phase transitions in silicon (by that we mean melting and crystallization) is the change of the free electron number and the important role of the electron component is in this transition. Apparently, at the temperature and the pressure change, allotropic transformation can be followed by the free electron number alteration.

The data on phase transitions in the solid polymorphic type of silicon are given in the publications [6–8]. Polymorphic closely-packed metallized modifications of silicon are formed at high pressure [7]. At the pressure of 12 hPa and the temperature of 20°C, the phase transition SiI→SiII has been detected by means of resistometric investigation and X-ray analysis [8]. A notable dependence has been revealed for the SiI→SiII phase transition on the shift components of load, pressure and the holding-pressure time of the sample. Due to this, the transition continues at 2–3 hPa. SiII phase is reported as one having metallic conductivity. The inverse transition SiII→SiI has not been detected.

After subjecting SiII samples to certain pressure, there have been revealed 2 modifications of Si (SiIII and SiIV) by X-ray analysis under atmospheric conditions. Heating SiIII within 200—600°C causes its lattice rearrangement and, consequently, there occurs SiIV modification with the hexagonal wurtzite-type structure. Under additional pressures, SiIV behaves as a metastable phase. Two assumptions have been suggested concerning SiIII: it either can be a stable phase under 12 hPa at 20°C with a body-centered cubic lattice, or it is a transition phase from SiII of tetragonal structure when pressure is removed. Under the pressure of 12 hPa, SiII phase transforms into superconductive state if $T = 6.7$ K [11].

In [9—11], the temperature dependence of some semiconductor silicon properties has been described, particularly, thermal expansion coefficient, hardness, lattice parameter, electrical properties at atmospheric pressure in the range from $T = 20$°C to $T < T_{melting}$. During phase transitions, semiconductor silicon undergoes discontinuous change of thermal, volumetric, mechanical and electrical properties due to the transition from one crystalline state into another. Establishing the property-temperature and property-pressure dependences allows revealing phase transition.

Normally, phase transition develops with a high rate, however, this behaviour is true only for certain regions. Being conditioned by the size and the number of a new phase regions that are formed per unit time, the volume rate of transformation is low in many cases, though the region formation rate is very high.

The volume rate of the transformation is taken into account in [9] for the studies on temperature dependence in silicon properties when heated at the rate of ≤5°C/min. These studies on semiconductor silicon properties reveal the monotonic dependence.

The abnormal character of the temperature dependence of the sample linear dimensions shows that there are different silicon phases at certain temperatures due to formation of which the registered changes occur.

In [10], the following phase transitions in silicon at heating are described. The general conclusion based on the ultrapure silicon research data is that these phase transitions can be observed in the local crystal volumes during heating with the rate of less than 5°C/min:

(I) within 250—350°C $Si_{FCC} \rightarrow Si_{ORTHORHOMBIC}$;

(II) within 680—700°C $Si_{ORTHORHOMBIC} \rightarrow Si_{BCC}$;

(III) within 1150—1200°C $Si_{BCC} \rightarrow Si_{HCP}$;

(IV) within 1420°C $Si_{HCP} \rightarrow P$.

Low-temperature transformations (I and II) have low DH values and can be referred as phase transitions that cause lattice atom shears at small distances. In this case we observe shear transformations that are based on the ordered lattice rearrangement. The lattices of both modifications are combined or adjacent while the shear transition starts heterogeneously. The nuclei appear in the areas with the dedicated dislocation nodes (the order growth rate is 10^3 m/sec). Polymorphic transformation rate is especially high in defect-free crystals. Phase transition III is accompanied by high thermal effect, so hyperthermal transformation in silicon is a first-order phase transition and it occurs due to the total rearrangement of the lattice. The specific feature of a first-order phase transition is the presence of interfaces that is why the transitions of this type lead to the fundamental crystal structure rearrangement.

The calorimetric analysis of the ultrapure semiconductor silicon [11] reveals that the phase transition is blurred and this phenomenon can be explained by as below:

– formation of polymorphic modifications with closely adjacent lattices;
– irregular distribution of impurity atoms within the crystals, namely O_2, H_2, C;
– irregular distribution of defects.

Considering the above stated, it can be suggested that when heating semiconductor silicon, its crystal lattice is proved to become denser before $T_{melting}$, conditioned by the degree of bond directions and followed by the transition to the metallic state. The transition of covalent crystals to the metallic state can be obtained regardless of the lattice disruption type and the techniques to influence the crystals.

The transition mechanism of the covalent crystals to the metallic state at various ways of the lattice excitement is the same: there occurs electron subcrystalline structure alteration, particularly, the sp^3-hybrid bond disruption is followed by the band gap narrowing and the corresponding increase in the number of charge carriers [11, 12].

The transition from the covalent bonding to the metallic one is carried out due to electron motion from the "coupled" state in the valance band to the "antibonding" conduction band, that leads to the decrease in the shear resistance of diamond lattice [12].

The experiment shows that at heating semiconductors, the transition from the semiconductor to the metal begins at the temperature considerably lower than $T_{smelting}$. It is interesting to note, that this temperature is not the same for the crystals obtained by different techniques [13]. The transition occurs due to the sequential lattice rearrangement from less dense to denser by the shear or shear-diffusion mechanism and is followed by the change in the correlation between the covalent component and the metal component of the chemical bond. In other words, in silicon there occurs direct and reverse martensitic transformation on its exposure to the different factors.

The most important feature of the diffusionless transformations is the concerted migration of large atomic groups during the new phase crystal growth. According to Kurdyumov, "Martensitic transformation is a regular lattice rearrangement in which the adjacent atoms do not interchange their places but only shear relative to each other at a distance which does not exceed the interatomic one" [14].

All the martensitic transformations without any exception have certain features conditioned by the following:

1) the cooperative character of atom migration during the crystal growth;

2) transformations in anisotropic elastic medium.

The crystals of the martensitic phase appear and reach their finite sizes at small-time intervals. The increase in the amounts of new phases takes place mainly due to the formation of new crystals, however, in some alloys there can be observed discontinuous growth of previously formed plates. The martensite crystals usually have a shape of a double convex lens and are twinned formations with a twining plane that coincides with the lens symmetry plane. Similar to twinning, such martensite crystal shape is explained by the elastic strain effect that occurs in the surrounding matrix during the growth of the new phase crystals. Theoretically, the analogy between twinning and diffusionless transformations is so due, that many authors regard twinning as a special case of diffusionless transformation during which the substance structure remains unchanged [15, 16]. Twinning can occur both with the change of the shape and without it (for instance, quartz). By analogy, diffusionless phase transformations can be subdivided into two groups:

1) diffusionless phase transformations that change the shape;

2) diffusionless phase transformations that do not lead to the change of the shape.

The transformation accompanied by the shape change is the one, during which there occurs primary macroscopic deformation; the transformation without such a change in the shape is the one, at which there is only "secondary" deformation. Thus, martensitic transformations are the diffusionless transformations accompanied by shape change. The diffusionless transformations with no shape change are more common for the crystals with complex structure, chiefly, for molecular crystals. These transformations, in case of preserving the atom migration cooperative character, can be deprived of many peculiar to martensitic transformations features related to the shape change.

In combination with the elastic medium effect on the growing crystal, the macroscopic shear, that follows martensitic transformations, causes the "elastic" martensite crystal formation. This phenomenon is analogous to elastic twinning. The martensite crystal growth takes place due to regular atom migration to new dislocations, so that the adjacent atoms of the initial lattice remain adjacent in the new lattice as well. On the separation interface of the two phases, there is one lattice which continuously transforms into the other, i.e. there is a coherent bonding between the lattices of the initial phase and the new one. With the crystal size increase, the elastic strains on the interface surface of the two phases also increase; eventually, these strains lead to plastic deformation and, consequently, to coherence violation between the two lattices and the crystal growth character alteration.

When covalent crystals are heated to the critical values at certain temperature due to the increase in the antiphase oscillation amplitude, there occurs covalent bond breakdown and the localized pairs of electrons in them become collective, that, in its turn, predetermines transition to the metallic state.

The transition of covalent crystals to the metallic state can be achieved irrespectively to the lattice excitement and the techniques of influence to which the crystal is exposed to: heating, high laser irradiation, radiation and magnetic exposure, high pressure, explosive treatment, etc.

Moreover, the mechanism of the covalent crystal transition to the metallic state is the same whatever the techniques of the lattice excitement: electron subcrystalline structure changes, namely the sp^3-hybrid bond disruption is followed by the band gap narrowing and, consequently, by the increase in the charge carriers quantity [17, 18]. The concentration of the charge carriers in InSb solid phase even at the temperature of ~420°C reaches $0.3 \cdot 10^{21}$ cm^{-3} while in InSb liquid phase at $T_{melting}$ it is $N_t = 5 \cdot 10^{21}$ cm^{-3} [18]. The same results have been obtained in [17] for semiconductor silicon: $N_t = 1.0 \cdot 10^{25}$ $cm—^{3}$ at the temperature of ~727°C, that corresponds to metallic state.

The transition from the covalent bonding to the metallic one takes place due to transferring of electrons from the "coupled state" in "antibonding" conductive area, that leads to the decrease in the shear resistance of the diamond lattice [19].

The problem of heating which initiates the transition of semiconductor into metal starting at the temperature much lower than the melting temperature (different for different crystals) [13] is relevant to [17, 18] and finds its further explanation as given below. The gradual rearrangement of the lattice into the denser one by the shear or shear-diffusion mechanism is followed by the correlation change between the covalent and metal chemical bond components. For instance, in Si, Ge, and InSb crystals there occurs direct

transformation or reverse martensitic transformation depending on the influence produced. According to the general regularities of semiconductor property changes within the range of 0.16–0.20 $T_{melting}$, the atoms in the crystal lattice interact via the covalent bond pattern while within 0.2–0.8 $T_{melting}$, heterodesmic covalent metal bonding occurs and eventually at the temperature higher than 0.8 $T_{melting}$ the metallic bonding is predominantly observed. The revealed regularity correlates with the idea of alteration of covalent crystal heat capacity at heating [20].

The classical theories tell that at the absolute zero of temperature, all atoms in the crystal are motionless and the potential energy of their interaction is minimal. At quite low temperatures atoms are supposed to have small oscillation, at that, the kinetic energy value of the atom oscillation should be small as compared to their interaction energy. With the temperature and oscillation amplitude increase, the atom interaction energy increases as well. At the temperature increase by 1 degree, the value of the oscillation energy absorbed determines the so called oscillating temperature, and, at first approximation, heat capacity (harmonious oscillator). However, when heated under conditions of constant pressure, the thermal expansion of a solid occurs during which the phenomenon grows into a more complicated character. The oscillation of the atom and its shift from the initial state of equilibrium generate the forces that affect the oscillation of the adjacent atoms. A small difference in a phase that can occur at any certain period of time leads to the fact that the atoms do not possess rigidly fixed middle positions to be independent of the adjacent atoms. Moreover, since all the interacting atoms of a solid body take part in the oscillating process, this process cannot have a single frequency. The general energy of the crystal does not change at a constant temperature, but the energy of each atom changes chaotically in the course of time. Thus, when explaining the temperature drive of the heat capacity phenomenon at the elevated temperatures, one should take into account the higher (anharmonic) expansion terms of the potential energy decomposition by shearing.

1.1.3 MARTENSITIC TRANSFORMATION MECHANISMS IN SILICON

The first instance of martensitic transformation in Si was observed under influence of the compressive loads in the temperature range of 400–700°C within the region of indentation trace left by the diamond indenter [21]. It was assumed that there are the possible mechanisms of martensitic transformations in silicon, particularly the formation of hexagonal diamond phase with cubic twinning. The martensitic transformation occurs because a structure becomes thermodynamically unstable [14]. It is usually followed by the change of the shape that is manifested through the emergence of narrow plates within the compressed matrix. Due to this, and also as a result of cooperative diffusionless reaction, the martensitic transformation sufficiently adds to the strain energy. Thus, in order to initiate the transformation of this kind, it is necessary to apply sufficient affecting forces. Such forces of the martensitic transformation provide the absence of diffusion processes and can be induced in two ways, namely by accelerated cooling and by high degree of strain. Considerable supercooling leads to the emergence of quite strong affecting forces.

The crystallography of martensitic transformation has macroscopic nature as it describes the crystallography before and after the transformation but not the further process of the latter.

Crossing of twins is the most characteristic model of martensitic transformation in Si. Each twin is formed based on the differences in the mobility of partial dislocations within Si. This phenomenon is conditioned by the difference in glissile activation energy for both head dislocations and partial dislocations of the split screw dislocation and it increases at higher temperature. According to this model, twinning in Si requires three factors as following:

— the presence of an axial segment of a screw dislocation,

— the effect of shear stress on a dislocation segment in a primary plane and a crossed plane,

— medium temperatures.

In monocrystal of Si, the martensitic transformation takes place within the temperature range of 250—700°C. Direct and reverse martensitic transformation occur in Si and they depend on the nature of its properties when being exposed to heating and cooling, due to which there can be observed some kind of hysteresis of martensitic transformation temperature interval.

By the origin, five types of twins can be distinguished:

a) concretion at random collision;

b) parallel lamination of molecules on a twin nucleus;

c) deposit of molecules on a large crystal formed in a twinning position;

d) transition from one modification to the other;

e) due to mechanical action.

The more symmetric the crystal structure is, the less likely is the twin formation. In crystals with low symmetry, different types of twinning can occur. Apparently, the formation of various types of twins is due to the lattice symmetry decrease during $Si_{FCC} \rightarrow Si_{ORTHORHOMBIC}$ phase transformation within Si samples that have been exposed to thermal treatment in the temperature range of 250—550°C. Twinning is hardly observed during thermal treatment in the region of coexistence of $Si_{FCC} \rightarrow Si_{BCC}$ (750°C).

Only shear stresses can affect twinning. Twin boundary energy during twin formation is of secondary importance. As the crystal form preserves while twinning, small distortions can be observed in the transition section. This section has a structure similarity to that of the high-temperature modification, while the twin boundary movement resembles the movement of a phase boundary at polymorphic transformation. During the closed loop of polymorphic transformations in single crystals of pure substances, a regular crystallographic direction of high-temperature grain modification is preserved; the latter is formed respectively to the primary single crystal. Moreover, in the microstructure, the changes occur connected with the new grain growth that is the result of phase transformations [15, 22]. The grains have almost similar crystal-lattice orientation, and when exposed to X-ray diffraction technique, such aggregation reveals itself as a single crystal; the same process is observed when growing monocrystalline silicon [22].

Thus, the development of two-dimensional crystal boundaries in monocrystalline silicon and the presence of two-dimensional conductivity are related to the formation of the shear phase transitions and twin boundaries.

The martensitic crystal formation not only leads to the crystal lattice type change, but also to plastic deformation of both the new phase and the matrix. The plastic deformation develops due to the slip of twinning. Such redundant or accommodative deformation is an integral part of martensitic transformation

and provides minimum energy of elastic distortion on the invariant surface of phase interfaces. The elastic resizing of the crystal can be observed under compressive stresses or tensile stresses. Similar to twinning, the formation of martensitic crystals may be caused by the parent phase strains. The strain helps to carry out transformation by 100%.

1.1.4 GENERAL PROBLEMS ON MAGNETIC FIELD EFFECT ON "NONMAGNETIC" SUBSTANCES

During the last 30 years there have been published over 200 studies on the effect of magnetic field with induction of 0.1–30 T and exposure time in the range of 10^{-6}–10^{6} sec on various properties of "nonmagnetic" substances (polymers, dielectric materials), semiconductors and metals [23–26]. In some cases, the magnetic field effect on some properties is more or less pronounced. For instance, in ionic crystals magnetic field affects the spin-dependent reactions between paramagnetic defects [23–27]. However, there are many examples described when the external phenomenological effects of placing the samples in the magnetic field are very similar to those presented in [23–27]. Nevertheless, the required conditions of spin-dependent reaction occurrence are often neglected. For example, magnetic field affects the properties of metals: the microhardness values of aluminium, bronze, bismuth, etc. but during the short time of a spin reaction totally excludes the magnetic field effect on spin-dependent reactions; the influence of the properties of polymers is observed if they do not contain spin particles. Moreover, in the scientific papers it is discussed that the magnetic field has certain effects on the "aged" crystals where there are neither processes, nor reactions, therefore the magnetic field has nothing to affect. Hard to imagine that those "unpredictable" spin-dependent reactions which require meeting of a number of experimental conditions and have the chance of about a few per cent to produce the effects in chemistry [27], could occur without providing special conditions and take place in all types of the substances wherein they are reported to act as a main technique to explain the magnetic effects. Irrespectively of the fact that a lot of scientists a priori attribute a "spin-dependent" origin to the mentioned effects, they often find it difficult to identify the type of the particles with a spin. All these make perform the further studies aimed at revealing general (rather than spin-dependent) reasons why the thermodynamically weak magnetic field has an effect on the state and properties of solids. The carried out generalizing analysis on the experimental data delivered by the various scientists and addressing the physical properties of a wide range of substances regardless of their response (i.e. the physical property of a substance that has been studied in the publications) allow determining the phase of a gradual physical property change in a magnetic field and the phase of subsequent relaxation of this property after removing of the magnetic field (**Fig. 1.1**).

The duration of these phases (t_1 and t_2 respectively) is a universal quantitative characteristic for a number of magnetic effects. Another invariant value which can be analysed regardless of both the measurement technique and the type of physical properties sensitive to the magnetic field is the relative value change of this property in saturation — D*I*/*I* (**Fig. 1.1**). By *I* we mean all the values described scientifically, whose changes under the magnetic field effect have been reported by the scientists (microhardness, dislocation pathlength, luminescence spectrum intensity, photoelectronic spectrum intensity, initial dislocation stress, electric conductivity, yield value, internal friction amplitude, etc.).

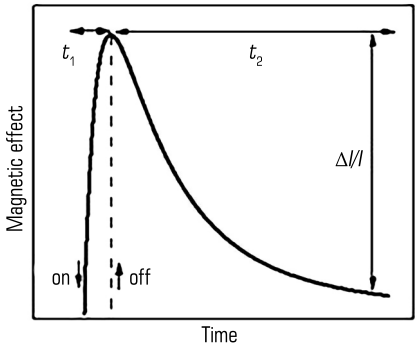

Fig. 1.1 Dependence diagram between a gradual change in the crystal physical properties within a magnetic field (with a time constant t_1) and a relaxation after the magnetic field removal (with a time constant t_2): a relative change in a physical value of DI/I is marked with a vertical arrow
Source: [27]

The dependence of time (t_1) on the magnetic strength in given in **Fig. 1.2**. It is obvious that regardless of the substance type and the research technique, t_1 value is subjected to a certain dependence: it reduces with the magnetic field (H) increase, i.e. magnetic induction process speeds up as the magnetic field increases. This is expected for one type of substance, but the demonstrable regularity in **Fig. 1.2** (that allows to discuss the universal dependence of $t_1(H)$ for various substances) suggests the assumption about the integral character of magnetic field physical effects on the substance properties.

It would be natural to assume that in the magnetic field, there occur forces that affect the crystal lattice while the development of stresses changes the other properties of substances. In this case, the spread of $t_1(H)$ dependence could be explained by the difference in magnetic sensibility χ_m of solids under study. There are certain attempts to build $t_1(\chi_m H^2/2)$ dependence, where $\chi_m H^2/2$ is the magnetic field energy of the unit volume, which does not permit eliminating the spread. This indicates that the macroscopic magnetization of the substances under analysis is irrelevant for the observed effects, and the main impact on them is apparently produced by the structure defects. In **Fig. 1.2**, the approximation of $t_1(H)$ is marked with a continuous line in double logarithmic coordinates with a linear function of $y = A + B \cdot x$, where $y = \lg t_1$, $x = \lg H$. From the approximation results, the function of $t_1 = t_0/H^2$ with the parameters of $t_0 = 2$ min, $B = -3.9 \pm 0.3$ T can be drawn. Thus, the universal function is written as $t_1 = t_0/H^4$. The paired measures, including the 4th-order ones, often occur in spin chemistry where the processes are governed by Δg spin contamination technique in a magnetic field [27].

Time (t_2) does not depend on the magnetic field. In thermodynamics, $t_1 = t_2$ equation is applied to inverse processes. Further, if a magnetic field excites solids and transfers its energy to them, time (t_1 and t_2) are to be in a linear relation. The relaxation of an excited state should occur with the same invariable of time as the transition to excited state within the magnetic field. This is true for various processes, such as

magnetization and demagnetization, chemical change in the potential with its postreduction, etc. The analysis reveals that there is no connection between t_1 and t_2 that means that the process is with the time invariable of t_2 that is often called relaxation and is in fact of a different origin. This process is represented by further transformations of the solid body defects subsystems that take place in the process with a time invariable of t_1. The attempts to obtain $t_2(H)$ dependence have been unsuccessful as well. Such dependence does not exist since the following processes that have once been initiated by the magnetic field become insensitive to the further magnetic field action and its values. The dependence between a relative change of physical properties in saturation per the time of $\Delta l/l$ is shown in **Fig. 1.3**. It turns out that the effects under study can be classified into three groups 1 (**Fig. 1.3, *a***), provided that the value of $\Delta l/l$ is built up as a magnetic energy function of a crystal lattice unit volume ($\chi_m H^2/2$). Group 1 is different from the other two groups by $\Delta l/l$ value being almost independent of the magnetic field value. Moreover, group 1 mostly includes semiconductors and metals, while in groups 2 and 3, which are highly sensitive to $\chi_m H^2/2$ value, ionic crystals and other dielectric materials prevail (**Fig. 1.3, *a***).

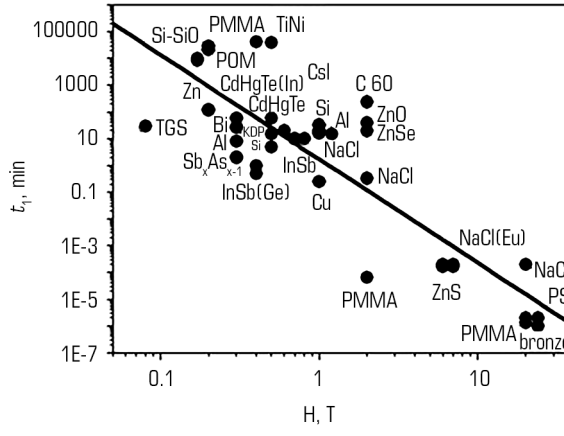

Fig. 1.2 Dependence between time t_1 and magnetic strength (H) for some substances. The approximation described in this publication is marked with a continuous line
Source: [27]

By this characteristic, group 2 and group 3 can be united into a single group that includes dielectric materials, which magnetic effect value depends heavily on the magnetic energy ($\chi_m H^2/2$) or (as it has been stated above) on the magnetic field. In **Fig. 1.3**, the continuous lines point to the approximation of 1, 2 and 3 types of $\Delta l/l$ dependences on ($\chi_m H^2/2$): $y = A + B \cdot x$, $y = \Delta l/l$, $x = (\chi_m H^2/2)$.

For all the three groups of substances, the magnetic effect is in a linear relation with magnetic energy $\chi_m H^2/2$. When small values of the magnetic energy of $\chi_m H^2/2$ or the weak magnetic fields, the effect is

almost the same (practically identical *A* coefficients) and close to 5% for each dependence of 1, 2 and 3. In large magnetic fields, *B* coefficient creates a large difference between 1, 2 and 3 groups.

One should mention that in spin chemistry [27], most effects are achieved by saturation in relatively low values (~0.1 T) of the magnetic fields while at values of the magnetic fields shown in **Fig. 1.3**, there is no dependence detected on the magnetic field. Thus, the established classification of the substances into groups can indicate the fact that the magnetic effects influencing semiconductors are really conditioned by spin-dependent reactions between the structure defects, while the strong magnetic fields can activate some other magnetic field mechanisms of action in dielectric material that have not been previously discussed.

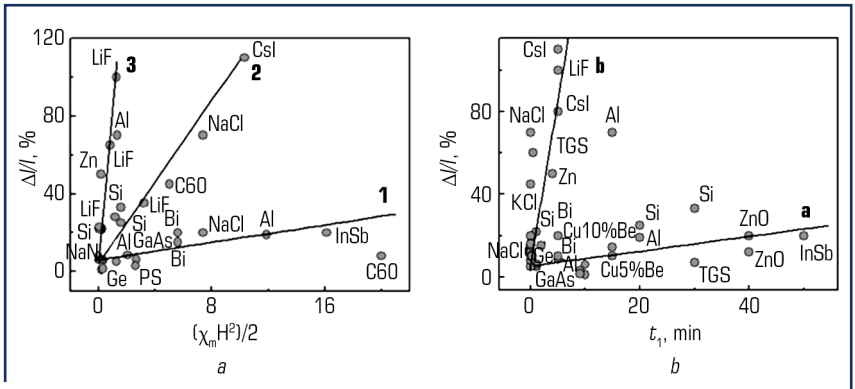

Fig. 1.3 The dependence between the relative value of property changes in solid bodies (D*l*/*l*): *a* – the magnetic energy per unit volume ($\chi_m H^2/2$); *b* – time t_1 for some substances. The approximation described in this publication is marked with a continuous line
Source: [27]

From the above mentioned it can be obviously deduced that the magnetic effect value (D*l*/*l*) is assumed to be related to the time (t_1) as it reflects time when waiting for the phenomenon to occur in a magnetic field and characterizes the kinetics of the change accumulation (that are induced by a magnetic field) in the crystal. **Fig. 1.3, *b*** shows D*l*/*l*(t_1) dependence that is also subdivided into *a* and *b* groups. Group *a* mostly includes semiconductors and metals while group *b* consists of dielectric materials. This fact emphases that there is a considerable difference in the mechanisms of the magnetic field effect on the physical properties of semiconductors and dielectric materials. **Fig. 1.3, *b*** shows the approximation of dependences D*l*/*l*(t_1) (marked with continuous lines) of *a* and *b* types per straight lines: $y = A + B \cdot x$, $y = Dl/l$, $x = t_1$ with the following parameters:

– for *a* line: $A = 5.3 \pm 3.7$; $B = 0.4 \pm 0.2$;

– for *b* line: $A = 6.4 \pm 3.5$; $B = 15.9 \pm 1.6$.

Group *b* embraces those substances, wherein the magnetic effect is in a linear relation with the time (t_1). Group *a* contains the substances with magnetic effect being independent of the time (t_1) that is expressed by

a small value of *B* coefficient. The magnetic effect value (**D***I*//*I*) with short time (t_1) is almost the same (identical *A* coefficients) and close to 5% for both *a* and *b* types of dependences.

The growing number in the publications to address the problem of a magnetic field effect on the properties of solids within the last few years allows revealing the number of general regularities for the solids:

1. Magnetic field induces the nonreversible transition to a new state after which the secondary processes occur causing sometimes the virtual crystal recovery and are perceived as "relaxation" after being excited by a magnetic field. In fact, they are the consequences of the primary processes and are insensitive to further magnetic field effects and their values.

2. On average, for a wide range of substances (dielectric materials, metals and semiconductors), the time invariable to describe the time period of the transition into a new state decreases in its value with the magnetic field (*H*) increase according to the law of $t_1 = t_0/H^4$.

3. The relative change in the physical properties of solids under $\Delta I/I$ magnetic field effect in weak fields (~0.1–1 T) is the same for a wide range of substances and makes ~5%. The influence of strong magnetic fields (3–30 T) is able to classify solids into two large groups in terms of their behaviour. Thus, the first group includes metals and semiconductors and there is $\Delta I/I$ dependence revealed on the magnetic field energy in such substance, while the second group mainly consists of dielectric materials in which $\Delta I/I$ shows strong dependence on the energy of a magnetic field per unit volume of a substance.

1.1.5 THE NATURE OF NERNST–ETTINGSHAUSEN EFFECT

Nernst-Ettingshausen effect or transverse effect is a thermomagnetic effect observed when a semiconductor with a temperature gradient is exposed to a magnetic field. This effect was discovered by Nernst and Ettingshausen in 1886, and in 1948 it was theoretically grounded by Sondheimer [28].

The nature of this effect is in the occurrence of the electric field (*E*) in a semiconductor and its direction is perpendicular to the temperature gradient vector (∇) and the magnetic induction vector (*B*), i.e. it is in the direction of the vector ($[\nabla T, B]$). If the temperature gradient and the magnetic induction are directed along *X* axis, then the electric field is parallel to *Y* axis. Therefore, there occurs the electric potential difference (*u*) between the points of *a* and *b*.

Both Nernst-Ettingshausen effect and Hall effect occur due to the flow divergence of charged particles caused by Lorentz force. However, there is the difference between them: Hall effect is responsible for the directed flow of particles resulted from the drift in the electric field, while in the case of Nernst-Ettingshausen effect, the same phenomenon is caused by diffusion.

The considerable difference between them is that unlike Hall constant, the sign of $q_{\wedge}$ is independent of the charge carrier sign. Actually, during the drift in the electric field, the charge permutation causes the drift direction alteration, that changes the sign of Hall field.

In this case, the diffusion flow is directed from the heated end of the sample towards the cold one irrespectively to the particle charge sign. Therefore, the direction of the Lorentz force for positive and negative particles is mutually antithetic, but the direction of the electric charge flows in both cases is identical.

Longitudinal Nernst-Ettingshausen Effect.

The longitudinal Nernst-Ettingshausen effect is in the change of thermal electromotive force in metals and semiconductors under the magnetic field influence.

When the magnetic field is absent, the thermal electromotive force in electron semiconductor is defined by the difference between fast electron velocity components (drifting from the hot side) and slow electrons (drifting from the cold side) along the temperature gradient.

At the presence of the magnetic field, there is the change observed in the longitudinal components (along the temperature gradient) and transverse components (transverse to the temperature gradient) of the electron velocity, this change is dependent on the rotation angle of electron velocity in the magnetic field; the angle is defined by the time of free run of the electrons τ in metals or semiconductors.

If the time of the free run for slow electrons or electron holes (in a semiconductor) is greater than that for the fast electrons, then:

$$u_{1x}(H)/u_{2x}(0) > u_{1x}(H)/u_{2x}(0),$$

where $u_{1x}(H)$, $u_{2x}(H)$ – longitudinal components of velocities for slow electrons and fast electrons under magnetic field; $u_{1x}(0)$, $u_{2x}(0)$ – longitudinal components of velocities for slow and fast electrons when the magnetic field is absent.

The value of thermal electromotive force in a magnetic field (that is proportional to the difference of $u_{2x}(H) - u_{1x}(H)$ is higher than that when the magnetic field is absent at the difference of $u_{2x}(0) - u_{1x}(0)$; vice versa, if the time of free run for slow electrons is lower than that for the fast electrons, then the magnetic field presence decreases the thermal electromotive force.

In electron semiconductors, the thermal electromotive force increases within the magnetic field provided that there is the decrease in the time of free run τ under the increase in the electron energy (scattering at the acoustic phonons). Within the same substances of electron semiconductors, the thermal electromotive force decreases under the magnetic field, if the time of free run τ increases with the increase in the electron energy (during the ionized impurity scattering) [29].

1.1.6 MAGNETOPLASTIC EFFECT IN DIAMAGNETIC CRYSTALS

In [30], was described the found and investigated decay of the particles from $CdCl_2$ impurity phase in monocrystalline matrix of NaCl (alkali-halide crystal) caused by magnetic field induction effect. Further, the structural changes started to appear in a few hours after the magnetic field induction treatment (the latency time) and lasted for several weeks. It has been revealed that the duration of the latency time and further structural changes are closely related to the "background" of the primary crystals. However, no physical model to explain these effects has been discussed in [30] and it is only stated that the magnetic field induction can affect the paramagnetic impurities which stabilise the quasi-equilibrium structure in primary crystals but cannot be controlled.

The direct magnetic field with the induction (0.5 T) causes the dislocation motion in NaCl and LiF crystals if no mechanical loads, thus changing the plastic properties of the sample. The established regularities of the magnetoplastic effect can be summarised as follows:

– the direction of the dislocation motion does not change during the magnetic field sign reversal (paired effect);

– the velocity of the dislocation motion is proportional to the square of the field induction and inversely proportional to the square root of paramagnetic center concentration within a crystal;

– dislocation pathlength tends to a constant value (saturation) depending upon the induction value of the magnetic field and the holding time for the crystals to spend within the magnetic field.

The paired nature of the magnetoplastic effect and its quadratic dependence on the induction value of a magnetic field imply the magnetostriction character of the phenomenon. To verify this assumption, the dedicated calibration measurement has been carried out to define the creep of NaCl samples at room temperature. At the load of ~30 kPa, the average dislocation pathlength during 5 minutes is similar to that of the magnetic field with 0.4 T induction holding (when without the load) during the same time. The revealed correlation should correspond to the magnetostriction constant of $m \sim \sigma / G \cdot B^2 \sim 4 \cdot 10^{-5}\ \mathrm{T}^{-2}$, where G is a shear modulus. However, the obtained value turns out to be several orders greater than the value of $m \leq 1.5 \cdot 10^{-9}\ \mathrm{T}^{-2}$ obtained for these rystals independently.

The observed magnetoplastic effect can alternatively be explained as followings: the dislocation motion in the magnetic field occurs under the far-reaching internal stress field effects, while the magnetic field effect is narrowed to disconnecting of the dislocations from the local barriers (stoppers) through the spin-dependent electronic transitions in the magnetic field within the dislocation-impurity system.

The magnetoplastic effect, that has been evidenced by the chemical technique of double etching, necessitates the search for the similar effects in a wider range of experimental conditions, for instance: in a mode of active macrodeformation and creep, during microhardness measurement and electric dipole moment generated by the charged dislocations. These vast experiments have been carried out on the crystals of ZnS, Al, Bi, Si and InSb and C_{60} fullerite monocrystals and allow the following:

– to determine activation energy, reinforcement factor, yield point, creep rate and other magnetoplastic effect parameters as well as their dependence upon the effect produced by magnetic fields on the samples;

– to find out that the magnetic field affects these point defects of low-sensitivity which have less effective radii of interaction with the dislocations as compared to the point defects that are insensitive to the magnetic field effect;

– to reveal the magnetoplastic effect in a wide range of relative deformations ranging from ~10^{-7} to ~1 and to study this effect at different stages of macroplastic deformation;

– to establish the role of internal stresses within dislocation shears in magnetic fields when no external stresses.

The magnetic treatment of the dislocation-free crystals and the further detection of the motion in as-introduced dislocations in them reveal that within the subsystem of point defects there is the following phenomenon: the magnetically stimulated residual changes reduce the free pathlength of the dislocation

under the magnetic field and increase them under conditions of mechanical load and the magnetic field absence. This difference as it has been noted earlier is conditioned in the crystals by the presence of the stoppers insensitive to the magnetic field along with magnetosensitive obstacles.

The first physical models of the magnetoplastic effect were based on the idea of the spin nature of the interaction between the dislocations and the paramagnetic point defects. Further, with the reference to this idea it was theoretically grounded, that the coeffect of the direct magnetic field and the pulsed magnetic field can cause resonance weakening of the crystals if the impulse frequency (ν) satisfies the condition of paramagnetic resonance, expressed by as given: $h\nu = g\mu_B B_0$ (h – Planck constant, g – factor of spectroscopic splitting, μ_B – Bohr magneton, B_0 – direct magnetic field induction).

Fig. 1.4 presents the dependence between the average edge dislocation pathlength and the magnetic field induction for various exposure modes. This dependence illustrates that at simultaneous exposure of NaCl:Ca (0.001%) crystals to the magnetic fields, acting perpendicular each other, namely the direct current magnetic field and the ultrahigh-frequency magnetic field, there can be observed the maximum increase in the dislocation pathlength (L) at several discrete values of (B_0). Further, the "resonance" values of the induction correspond to $B_0 = h\nu/g\mu$, and the applied frequency of ultrahigh-frequency field is $\nu = 9.5$ GHz. Under these conditions, the resonance transitions occur between the splits from spin sublevels of electrons within the direct magnetic field and the effective factors of spectroscopic splitting $g_1 \approx 2$, $g_2 \approx 4$ and $g_3 \approx 6$, respectively.

For crystals with Eu impurities the dependence is even more complex (**Fig. 1.5**). Being obtained with the standard electron paramagnetic resonance spectrometer, the electromagnetic wave absorbance spectrum for NaCl crystals heavily doped with Eu shows the extrema.

By analysing the experimental data on the obtained magnetoplastic effects in diamagnetic crystals, there have been suggested the scheme of the probable mechanism how magnetic field effects on the evolution of metastable defect complexes. It is shown in **Fig. 1.5**.

The local minimum characterizes the profile of the elastic interaction between the constituents of the complex found in the metastable state. The solid line and the dotted lines that unite the complex constituents designate the covalent bonding in the equilibrium state and in the excited state: kT – thermally stimulated process, j – exchange integral, ΔE – exchange energy differences in S- and T-states of the complex, ν_i – frequency of transitions between absorption states that practically coincide with those in the weakening spectra, this indicates the fact that impurity ions are within the magnetosensitive complexes of defects.

According to the scheme (**Fig. 1.5**), the thermal fluctuations with the frequency (ν_1) excite the complex by covalent bonding stretching (or by changing configuration coordinates (r), such as bond angles) from the primary singlet S-state to the excited S-state. When the magnetic field does not act, the complex, being exposed to the elastic forces from the crystal lattice, reverts to the original S-state due to prohibition for the complete spin that means that the complex is in dynamic equilibrium between S- and S-states.

When there is a magnetic field, the prohibition is partially lifted, and the complex with $\nu_2 = \mu_B B\Delta g/h$ frequency that has changed its multiplicity (Δg-mechanism of mixing states is the most probable under such conditions) evolves into a new electron T-state. Further, under influence of the elastic forces from the crystal lattice there occurs reverse motion of nuclei. At that, the equilibrium R_T-state between them appears to be higher than that in the singlet RS-state, since the negative J value of exchange

integrals causes the mutual repulsion of the complex constituents. Thus, with ν_3 frequency there occurs a relatively continuous triplet of *T*-state, in which the total energy of the complex constituent bonds is $\Delta E = 0.1–1$ eV, less than that in the *S*-state. The "dispersed" by this way complexes are less stable as compared to the initial ones, and the random motion of nuclei can cause either their decay with ν_4 frequency that is followed by the system escape from the local energy minimum and its further relaxation, or the restoration to the initial *S*-state with ν_5 frequency. Normally, the decay of the point defect complexes leads to the formation of weaker stoppers for the dislocations; that agrees with the experimental data on the weakening effect for the ionic crystals after they have been subjected to the magnetic fields.

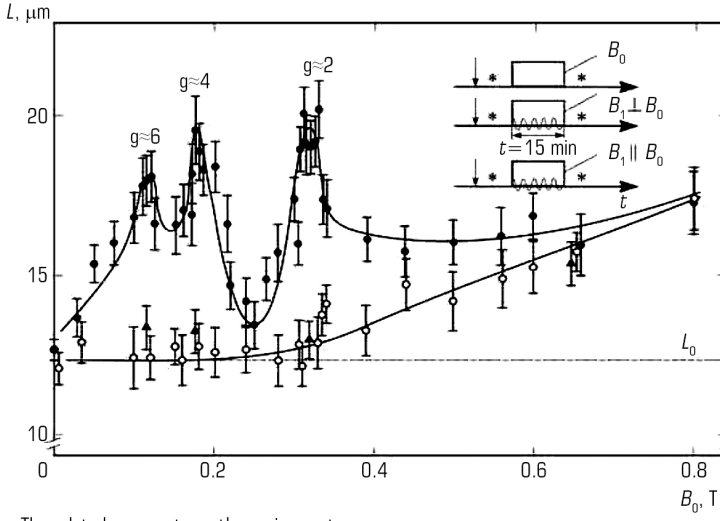

The related comments on the assignments:
○ – the absence of high-frequency current field (ν=9.5 GHz);
● – when exposed to the simultaneous action of high-frequency magnetic field and direct magnetic field in the configuration of $B_1 \perp B_0$, where B_1 – induction of the high-frequency magnetic field;
▲ – under simultaneous action of the high-frequency magnetic field and the direct magnetic field in the configuration $B_1 \parallel B_0$.

The dislocation pathlength (L_0), stipulated by the etching medium action, is shown with a shaded line for cases without external magnetic field.

The sequence of the procedures:
arrow – the inclusion of dislocations;
asterix – etching;
rectangle – exposing crystals to the magnetic field

Fig. 1.4 Dependence between the average edge dislocation pathlength (*L*) in NaCl:Ca crystals upon the direct magnetic field induction (B_0): exposure time of 15 min
Source: [30]

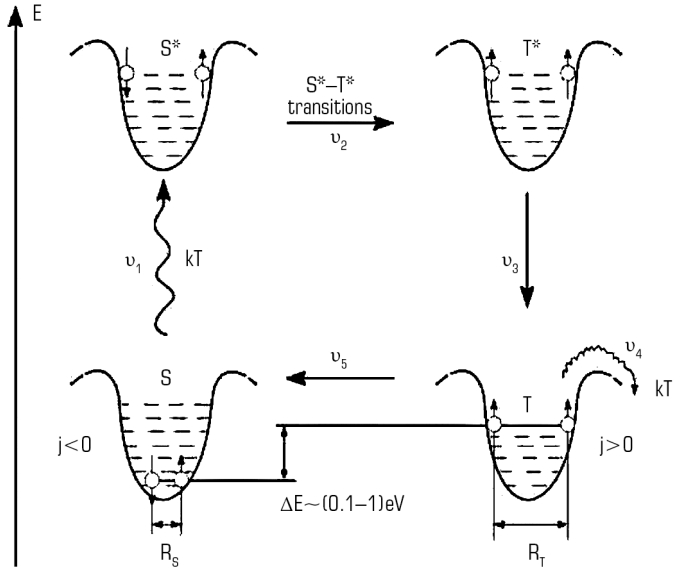

The related comments on the assignments:
S – continuous metastable singlet state of the complex;
S* – intermediate one excited by thermal fluctuations;
T* – intermediate excited triplet state, transition that is only possible in the presence of the magnetic field;
T – continuous metastable triplet state

Fig. 1.5 Schematic illustration of the process sequence in the complexes of point defects within the magnetic field: on the energy scale of *E* complex
Source: [30]

In other words it can be expressed as here: in the subsystem of the paramagnetic structural defects of the ionic crystals, spin-dependent magnetosensitive reactions are thought to considerably affect their plastic properties, while the kinetics of these reactions, according to the numerous tests, can be regulated by the weak constant fields and (what is even more efficient) by the pulsed magnetic fields.

1.2 MATERIALS AND METHODS OF THE STUDY

1.2.1 STUDY MATERIALS

In the current paper, there have been studied the samples of monocrystalline semiconductor silicon grown by Czochralski method (Cz-Si), both undoped version and doped with B, Sn, Ge, Hf, Zr, and the

complexes of B-Sn and B-Mo ranging from $2 \cdot 10^{-4}$ to $8.7 \cdot 10^{-2}$ at % in initial state, after their exposure to the full heating-cooling cycle, various thermal treatment conditions and the weak direct magnetic field effect (refer to **Table 1.1**).

Table 1.1 Properties of the studied silicon crystals

No.	Sample characteristics (technique of preparing)	Oxygen content, atm/cm^3	Carbon content, atm/cm^3	Electric resistance at room temperature, ohm	Temperature ranges of variation lg(s), lg(h), lg(m) = f(1/T) from straight-line correlation							
					1		2		3		4	
					T_{start}	T_{end}	T_{end}	T_{end}	T_{start}	T_{end}	T_{start}	T_{end}
1	Float zone melting	$4\ 10^{14}$	$3\ 10^{15}$	1200	250	400	520	770	960	1005	1040	1150
2	Czochralski method, dislocation growth	10^{17}	10^{16}	25—50	260	380	770	860	960	1130	1170	1215
3	Czochralski method, dislocation-free growth	10^{17}	10^{16}	80—100	260	460	725	770	920	970	1090	1185
4	Cast polycrystalline	$2 \cdot 10^{17}$	$1.5\ 10^{18}$	0.3—3	220	320	432	555	730	918	1065	1180
5	"Raw" silicon trichlorosilane	—	—	1—20	210	350	650	750	920	960	1040	1190
6	"Raw" silicon monosilane	—	—	1—20	150	452	635	772	924	954	—	—

Source: [31]

1.2.2 METHODS OF THE STUDY

The chemical composition of the samples under analysis was determined by the spectroscopy performed at ARL-2400 testing facility.

The microstructure of the alloys was studied on the "Neophot-21" optical microscope. For revealing the general structure of semiconductor doped silicon, the samples were exposed to etching in $HF:H_2O:Cr_2O_3$ solution at the ratio of 3:3:1 with subsequent wash in the flowing water.

The temperature dependence of the thermal expansion coefficient of a semiconductor silicon was studied using the AD-80 dilatometer in the argon flow medium at the heating and cooling rate of 5°C/min. The thermal expansion coefficient rate accuracy was 0.1%.

The change in the solubility of doping elements (dopants) and their distribution between the structural constituents was studied by means of X-ray diffraction technique while the microhardness change was studied by means of the local X-ray spectrum analysis with MS — 46 microprobes and Camebax. XRD patterns of the alloys were recorded with DRON-3M diffractometer in k_α copper radiation. Aluminium of A999 grade and chemically pure silicon were used as reference standards. In order to determine

the lattice parameters, the profiles of the diffraction extremum graphs (422) Si and (511) Si were recorded by means of the gravity center coordinate determination.

The microhardness of the modified silicon structural units was measured at PMT-3 testing facility under the load of 20 g. Each sample underwent from 36 to 76 measurements. In order to reveal the hidden regularities of silicon-based solid solution formation, the interval data imitating the distribution function [32] were used. For that purpose, the variation range of the characteristic was divided into *n* equal intervals and the number of cases in each interval was counted. The applied technique allowed taking into account and demonstrating silicon microhardness changes during doping.

XRD patterns of the alloys were recorded on DRON-3M diffractometer in k_{α} copper radiation. Chemically pure silicon was used as a reference substance.

The specific electric resistivity of doped Cz-Si was measured with 4-probe technique (the error was within of 2.5%). The minority-carrier lifetime of charges was measured on the original testing facility for radiating heat kinetics measurement, the device built in V. Ye. Lashkaryov Institute of Semiconductor Physics of the National Academy of Sciences of Ukraine (Kyiv). The instrument accuracy was ±0.1%.

The thermal treatment of the doped Cz-Si was performed in the laboratory in the chamber muffle kiln furnace of SNOL 2.5, 2.5/1.5. The desired temperature was maintained as accurate as ±0.5°C by means of VRT-3 device. The temperature measurements were taken via chrome-aluminium thermocouples on R-4833 general-purpose instrument switched on according to the lattice network (the instrument accuracy of 0.05).

The magnetic treatment of the samples was carried out in the direct current magnetic field with induction of 0.066 T. The time periods of exposing for the samples were 10 and 30 days.

The measurements of the current minority-carrier lifetime after magnetic treatment were measured by the decay of the photoinduced current that occurred in the samples exposed to the GaAs light-emitting diode by means of SEMILABWT1000B device with the accuracy of ±0.1%.

1.3 MICROSTRUCTURES OF THE SAMPLES BEFORE AND AFTER THE MAGNETIC FIELD TREATMENT

Fig. 1.6 shows the microstructures of Cz-Si samples in the initial state and after 240 and 720 hours of exposure in the direct magnetic field with the induction of 66 mT. The initial silicon microstructure is quite homogeneous with a low dislocation density (**Fig. 1.6, *a***).

240 hours of exposing to direct-current magnetic field for the monocrystalline silicon samples mean the worsening of their internal structures in terms of the significant increase in the quantity of their defects, namely the dislocation densities (**Fig. 1.6, *b–d***) and creating a great number of twins (**Fig. 1.6, *b, c***). However, the most interesting results revealed after the monocrystalline silicon treatment with the direct-current magnetic field are the formation of the polycrystalline silicon that is brought by the presence of a great number of grain boundaries.

The fact that the dislocation walls intersecting the grain boundaries just slightly change their directions or do not change them at all indicates that these boundaries are of the special type. The further exposing

to the direct-current magnetic field has not influenced the sample microstructures except the grain sizes which become smaller (**Fig. 1.6, *e*, *f***).

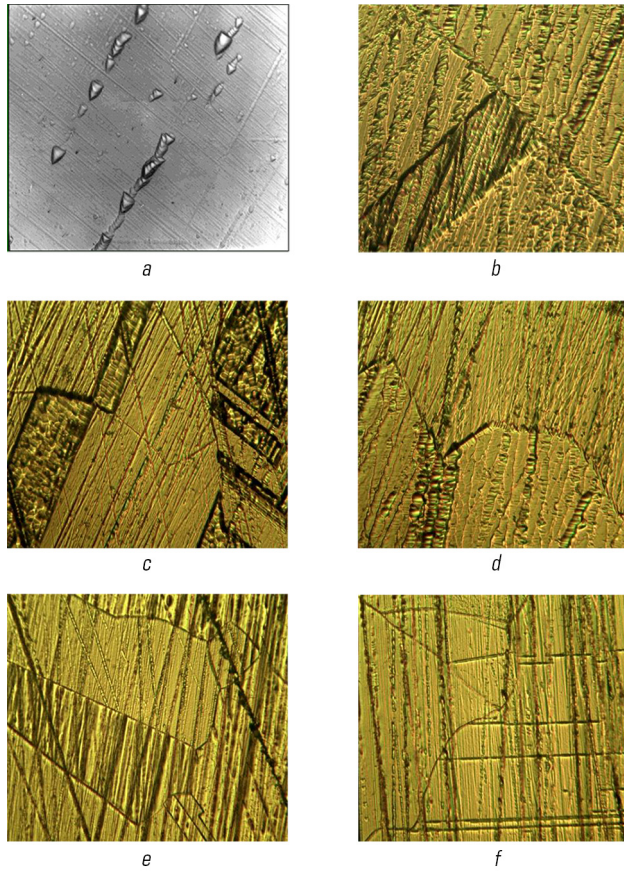

Fig. 1.6 Microstructures of Cz-Si samples: *a* – initial state, ×500; *b*, *c*, *d* – after 240 hours of exposing to direct-current magnetic field, ×400; *e*, *f* – after 720 hours of exposing to direct-current magnetic field, ×400
Source: [33–36]

The initial microstructures of the Cz-Si samples doped with aluminium (**Fig. 1.7, *a***) are characterized by rather high dislocation densities in the form of the pits after etching which form the chains. After

240 hours spent within the direct-current magnetic field (66 mT), the microstructures of the samples (**Fig. 1.7, *b–e***) show the considerable amounts of swirl-defects while the amounts of dislocations decrease to a certain degree. Etching of aluminium-doped Cz-Si samples allow to establish that 720 hours of exposing in the magnetic field result in a small quantity of single dislocations (**Fig. 1.7, *f***) and their chains in the samples but no swirl-defects have been found within such material.

The microstructures of Cz-Si samples doped with Cu are shown in **Fig. 1.8**. Initially, the samples had low densities of defects, which were mostly dislocation chains (**Fig. 1.8, *a***).

After 240 hours within the magnetic field, the sample microstructures exhibit some changes and the amount of dislocations reduces in them (**Fig. 1.8, *b, c***) while 720 hours of the mentioned treatment produce the effect of higher density of the chain-like dislocations in the microstructures of Si(Cu) samples as revealed after etching and comparing with the initial state (**Fig. 1.8, *e, f***).

In the microstructures of the Cz-Si samples doped with Zr (**Fig. 1.9**), rather high dislocation densities were found in the initial state, those dislocations were in the form of the separate pits from etching or their aggregations (**Fig. 1.9, *a***). After treating the samples with the direct-current magnetic field (B = 66 mT) during the exposing time of 240 hours, the microstructures show a considerably lower number of dislocations (**Fig. 1.9, *b***). The metallographic analysis for the samples subjected to 720 hours of exposing in the magnetic field finds neither separate pits of etching nor dislocation aggregations (**Fig. 1.9, *c, d***), only the chains of dislocations have been revealed in these samples. In general, the microstructures have improved vs those of the samples subjected to 240 hours of exposing (this is also verified by the microhardness measurements).

In **Fig. 1.10**, we demonstrate the microstructures of Cz-Si samples doped with Hf. The microstructures of the initial samples have been characterized by rather high densities of dislocations and their regular arrangement along the certain crystallographic planes (**Fig. 1.10, *a***). Etching of the samples performed after 240 hours of the magnetic field action allows to reveal considerable quantities of swirl-defects while the dislocation densities decrease in them (**Fig. 1.10, *b–d***). The notable changes are found in those sample microstructures which have undergone the magnetic field treatment during 720 hours. These changes can be described as follows: no swirl-defects and chains of dislocations like those revealed in the samples of 240-hour exposition; formation of large quantities of single dislocations like the pits from etching. Generally, the densities of the defects decrease in the samples of this type as compared against the samples with 240 hours of exposing.

In the structures of Cz-Si(Mg) samples held within the magnetic field during 240 hours (**Fig. 1.11, *b***), the considerable changes vs the initial state (**Fig. 1.11, *a***) have not been noted, however, 720 hours within the magnetic field give the rise of many single dislocations to appear in the samples, they are in the form of etching pits (**Fig. 1.11, *c, d***).

The initial structures of Cz-Si-Fe samples (**Fig. 1.12, *a***) were with rather high densities of dislocations, arranged separately or in the form of chains. 240 hours of holding the samples within the magnetic fields enable preserving the single dislocations within the structures while the structures themselves exhibit no significant changes (**Fig. 1.12, *b, c***) in general. Further, the structures of the reported samples, which have spent 720 hours within the magnetic field, resemble their initial states, however the densities of the defects decrease (**Fig. 1.12, *d–f***).

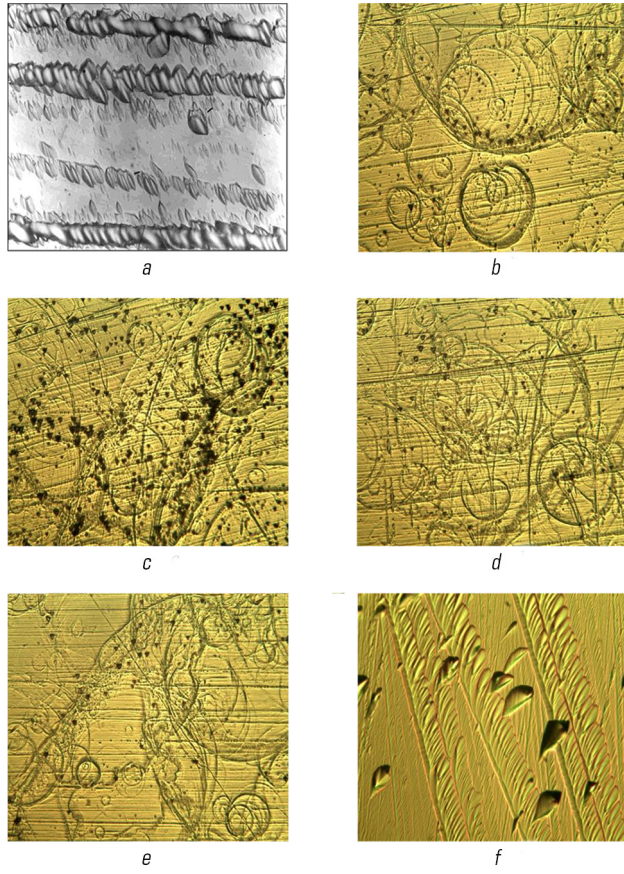

Fig. 1.7 Microstructures of Cz-Si samples doped with Al: *a* — initial state, ×500; *b*, *c*, *d*, *e* — after 240 hours of exposing to direct-current magnetic field, ×400; *f* — after 720 hours of exposing to direct-current magnetic field, ×400
Source: [33–36]

The contemporary simulations promote the idea that magnetic field causes the spin-dependent degradation of the chemical bonds in the structural nanoclusters [37], formation of vacancy and oxygen sets (V-O, $Si_XV_YO_Z$), namely *A*-defects, which are able to result into the nuclei of two-dimensional defects such as dislocations [38]. The explanations on the phase transformation and the polycrystalline silicon formation in Cz-Si under the influence of the direct current magnetic field are not available in the contemporary science.

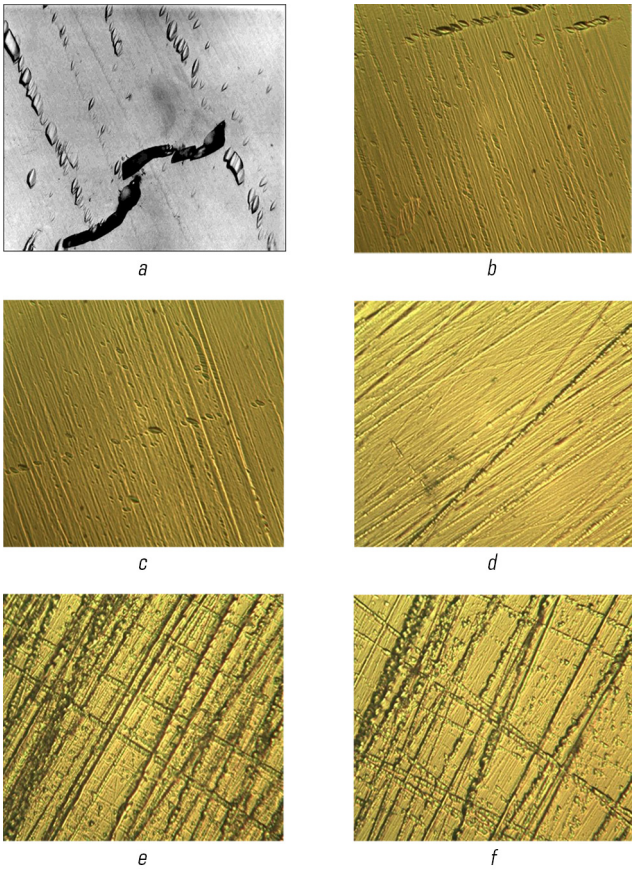

Fig. 1.8 Microstructures of Cz-Si samples doped with Cu: *a* — initial state, ×500; *b*, *c* — after 240 hours of exposing to direct-current magnetic field, ×400; *d* — after 720 hours of exposing to direct-current magnetic field (sample No. 1), ×400; *e*, *f* — after 720 hours of exposing to direct-current magnetic field (sample No. 2), ×400
Source: [33–36]

It can be assumed that the formation of polycrystalline silicon samples of undoped silicon is stipulated by those changes in the wave functions of the valency electron which have been produced by the direct-current magnetic field (this is confirmed by Larmor precession and the related Zeeman effect) and therefore the phenomenon is also promoted by the changes in the densities of the electron states in the space-and-time, that means the changes in the directions within which the covalent bindings

occur. The rearrangement of covalent binding orientations, in their turn, brings the changes in the crystal lattice type that means the phase transformation.

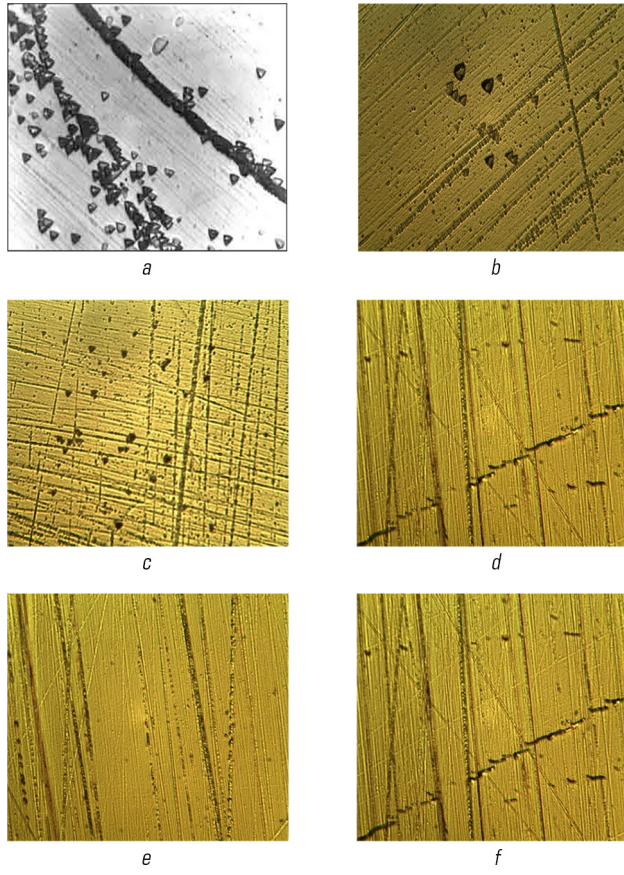

Fig. 1.9 Microstructures of Cz-Si samples doped with Zr: *a* — initial state, ×500; *b*, *c* — after 240 hours of exposing to direct-current magnetic field, ×500; *d*, *e*, *f* — after 720 hours of exposing to direct-current magnetic field, ×400
Source: [33–36]

The large number of twins formed within the structure might be assigned to the formation of silicon orthorhombic phase and silicon BCC_{III} phase with the shear pattern within the certain masses of the

sample [1–4, 6]. In undoped silicon, the shear transformation of $Si_{FCC} \leftrightarrow Si_{ORTHORHOMBIC}$ occurs at the temperatures higher than 350°C [39–43], in cases of the treatment in the magnetic field at the room temperature, this phenomenon is provoked only by the magnetic field influence.

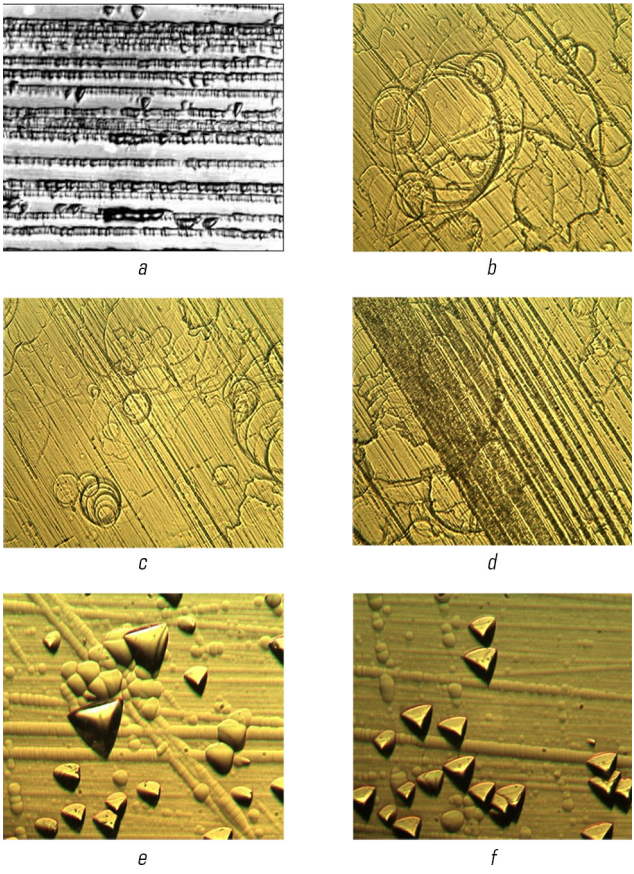

Fig. 1.10 Microstructures of Cz-Si samples doped with Hf: *a* – initial state, ×500; *b*, *c*, *d* – after 240 hours of exposing to direct-current magnetic field, ×400; *e*, *f* – after 720 hours of exposing to direct-current magnetic field, ×400
Source: [33–36]

After 720 hours of exposing, there are no significant changes found in the sample structure. At this the measurements have shown the increase in the parameters of microhardness and specific electric resistance

vs the samples which have been treated during 240 hours. This indicates the further proceeding of the phase transformation and the structure stabilization under the magnetic field effect.

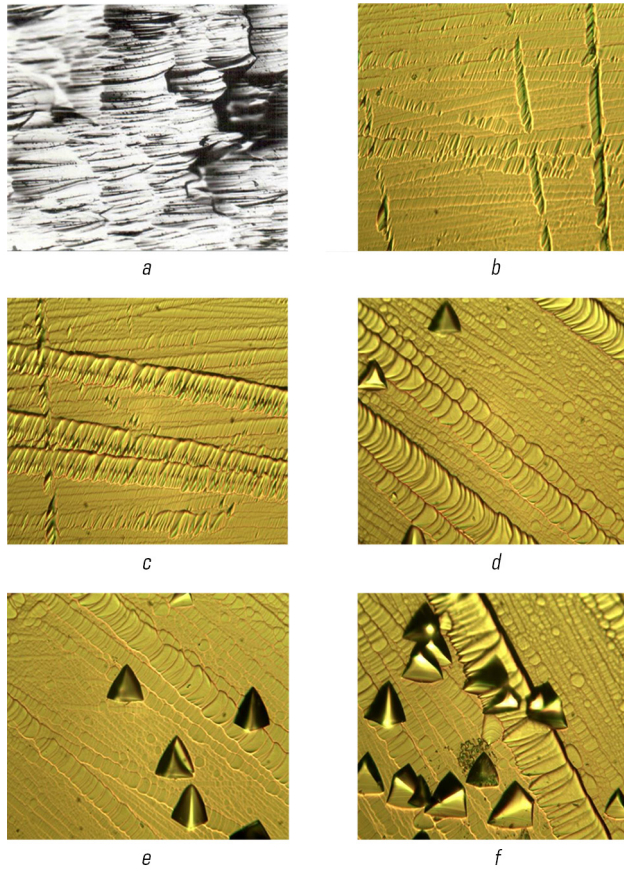

Fig. 1.11 Microstructures of Cz-Si samples doped with Mg: *a* — initial state, ×1000; *b* — after 240 hours of exposing to direct-current magnetic field, ×400; *c*, *d* — after 720 hours of exposing to direct-current magnetic field, ×400
Source: [33–36]

Note that all the above-mentioned doping elements increase the critical temperatures for $Si_{FCC} \leftrightarrow Si_{ORTHORHOMBIC}$ and $Si_{ORTHORHOMBIC} \leftrightarrow Si_{BCCIII}$ (refer to **Table 1.2**). Moreover, the doping elements increase the

thermodynamic stability of the closed packed phases of silicon to the magnetic field action (the magnetic field as well as the higher temperature add to the energy to the system). Furthermore, it might be assumed that the doping elements stabilise the high temperature phase of Si_{BCCIII}, thus eliminating low temperature shear-diffusion phase transformations as well as the formation of twins within the structure.

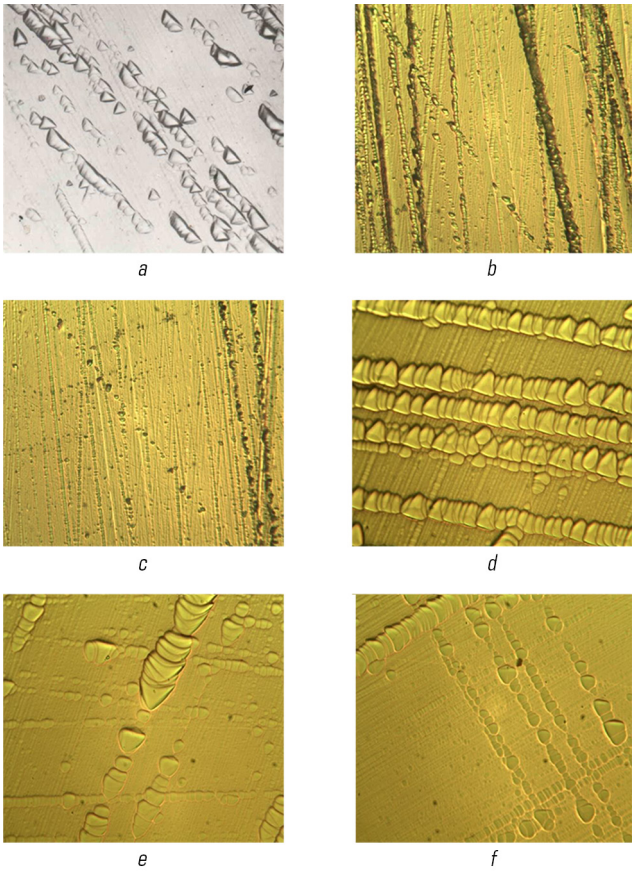

Fig. 1.12 Microstructures of Cz-Si samples doped with Fe: *a* — initial state, ×500; *b*, *c* — after 240 hours of exposing to direct-current magnetic field, ×400; *d*, *e*, *f* — after 720 hours of exposing to direct-current magnetic field, ×400
Source: [33–36]

● **Table 1.2** Temperatures of phase transformation for doped silicon and the dedicated thermal expansion coefficient values

Cz-Si/doping elements	Temperature/coefficient of thermal expansion °C/a·10^{-6}·°C^{-1}		
	I $Si_{FCC} \leftrightarrow Si_{ORTHORHOMBIC}$	II $Si_{ORTHORHOMBIC} \leftrightarrow Si_{BCC\ III}$	III $Si_{BCCIII} \leftrightarrow$ Sihcp
Cz-Si	350/4.3	700/4.4	900/5.3
Cz-Si+Al	450/5.0	750/4.5	900/6.0
Cz-Si+Zr	500/4.5	–	850/4.7
Cz-Si+Hf	380/4.5	–	850/4.7

Source: [33–36]

Considering the influence of both the magnetic field and the doping elements on the energy of silicon interatomic bonds, it is difficult to make any assumptions since the most similar changes in the structures have been observed in the samples of Cz-Si(Al) and Cz-Si(Hf) after 240 hours and 720 hours of exposing to the magnetic field (refer to **Fig. 1.7, 1.10** respectively), despite the fact that aluminium drastically decreases the energy of silicon atom interaction while hafnium increases it greatly.

Further, the similar changes have been detected within the structures of Cz-Si(Cu) and Cz-Si(Fe) (**Fig. 1.8, 1.9**). At this, copper reduces the interaction energy of silicon atoms while iron does not bear influences on it.

In the samples of doped silicon, which has undergone magnetic field exposing during 240 hours, the increase in the defects of the inner structure can be explained via the changes in the wave functions of the electrons. Quite local is the change in the wave functions of electrons and the crystal lattice rearrangement is to provoke the breakage in covalent binding of those adjacent atoms, which wave functions will not have changed enough to meet the orientation changes of covalent binding (the density of the electron states in the space-time). This local breakage of the atom binding is to cause the appearance of complete dislocations or partial ones together with the defects of atom packing.

The gradual decrease in both the density of the defects and the microhardness values of the structures in the samples of Si-Al, Si-Cu and Si-Zr after 720 hours spent in the magnetic field can be regarded as relevant to the structure stabilization during the time of quite long holding within the magnetic field as well as related to the decrease in the thermal capacity (enthalpy) of the system by means of annihilation of the certain portion of the structure defects. The same changes are observed in the samples during their annealing in the furnace [2].

Due to the commonly known property of aluminium to strongly decrease the energy of atom interaction in silicon, the easier shear-diffusion phase transformations within silicon occurs while hafnium influence is on the contrarily and drastically increases this energy that means slowing down the phase transformations and stabilizing the silicon structure of Si_{FCC} [31]. In order to identify the phases in the samples, which have been under the magnetic field treatment, the method of X-ray analysis have been applied. **Fig. 1.13** shows the diffractogram of Cz-Si sample in the initial state.

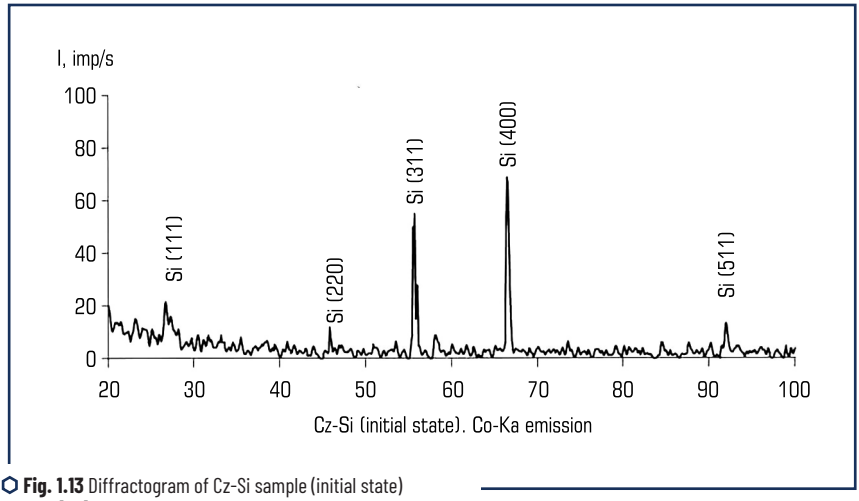

Fig. 1.13 Diffractogram of Cz-Si sample (initial state)
Source: [44]

In the initial state, Cz-Si in the diffractograms shows the reflections of FCC lattice, and line (400) possesses the maximal intensity at the scattering angles of less than 65 degrees (**Fig. 1.13**).

After treating the silicon samples with direct-current magnetic field of 0.4 T inductions, there have appeared the reflections at the scattering angles of 30–40 degrees (**Fig. 1.14**), which are interpreted as orthorhombic phase of silicon [45].

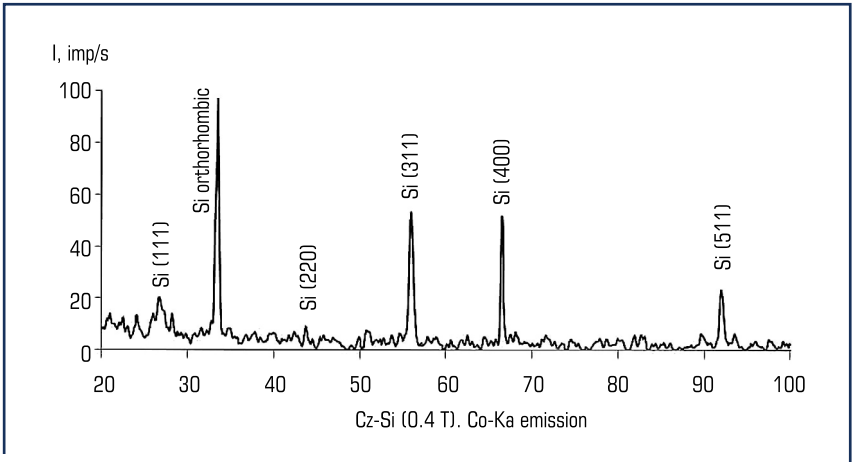

Fig. 1.14 Diffractogram of Cz-Si sample ($B = 0.4$ T)
Source: [44]

The reflection intensityies for silicon with cubic close-packed lattice at angle of 65–70 degrees decrease after the magnetic field influence. It can be explained by phase transformation initiated in silicon, namely $Si_{FCC} \leftrightarrow Si_{ORTHORHOMBIC}$ [34] under the action of the direct current magnetic field with 0.4 T of induction.

Fig. 1.15 depicts that after treating the samples with the aggressive direct current magnetic field (B = 1.2 T), there is the reduction in intensities of reflections in all the silicon phases and appears a considerable number of reflections from silicon oxide. This verifies the assumption of silicon surface activation with the direct-current magnetic field and enhancing its absorbing properties [46].

Furthermore, with the behaviour of this kind we confirm the assumption that the silicon phase structure stabilises under the action of direct magnetic field [33]. However, more detailed investigation on the line profile (511) evidences that additional phases are formed within the crystal array, and they possess the different type of the lattice.

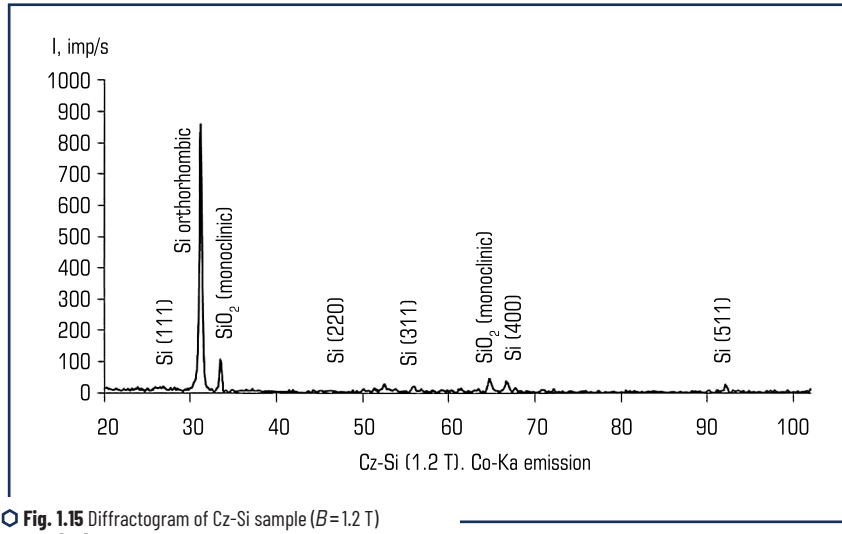

Fig. 1.15 Diffractogram of Cz-Si sample (B = 1.2 T)
Source: [44]

In **Fig. 1.16**, the curves are presented to show the differential extrema (511) for the samples in the initial state and after treating with the magnetic field: B = 0.4 T (*b*), 1.2 T (*c*). They have been obtained at the scattering angles of 90–92 degrees, which is the feature of silicon phase of cubic close-packed lattice [46].

The splits of the diffraction lines detect the presence of the distortions in the crystal lattices of Cz-Si samples. At this the split of the extremum (511) is to be assigned to overlapping of certain interferences of orthorhombic phase of silicon [41, 44, 45]. Further, the line splitting (511) increases with the increase in the induction of external magnetic field.

The splits of the differential extrema at the scattering angles of 90–92 degrees at higher values of external magnetic field induction evidence the presence of two phases in the silicon and are relevant to the formation of $Si_{ORTHORHOMBIC}$ phase within this material array. The same is observed on the differential extremum split (511) at the scattering angles of 90–92 degrees after the silicon semiconductor heat treating at the temperature range of 280–450°C, and it is assigned to the crystal lattice distortion of Si_{FCC} and formation of the certain quantity of $Si_{ORTHORHOMBIC}$ [47–48].

Eventually, the heat treatment of the silicon semiconductor gives greater splitting of the interference extremum (511) at increasing the annealing temperature from the range of 280–320°C up to the range of 400–450°C [48]. In the currently reported research, the significant splitting is observed at the increase of the external magnetic field induction from 0.4 T to 1.2 T. This evidences that the magnetic field and the heat treatment initiate the phase transformations of silicon.

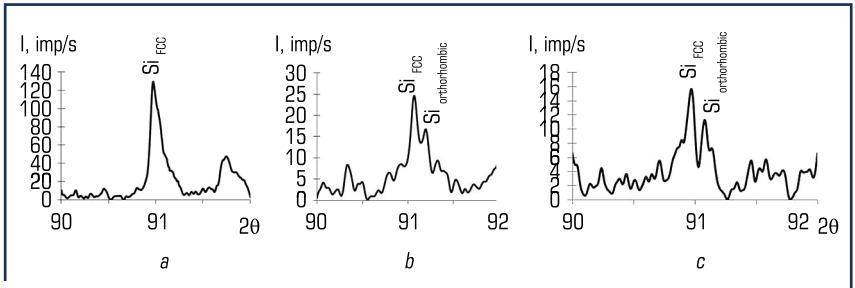

Fig. 1.16 Line profile (511) before the magnetic field action and after it:
a – initial state; *b* – 0.4 T; *c* – 1.2 T
Source: [44]

1.4 THE SAMPLE MICROHARDNESS VALUES BEFORE AND AFTER TREATING WITH THE MAGNETIC FIELD

Magnetic field acting on Si sample has certain influence on the sample microhardness values. For the sake of the reader's swift reference we consider it is reasonable to summarise the revealed data on the microhardness change in similar patterns of representation as below.

In **Fig. 1.17**, the graphs present the microhardness values of the aluminium-doped silicon samples after 240 hours (**Fig. 1.17, *a***) and 720 hours (**Fig. 1.17, *b***) of exposing to direct-current magnetic field with the induction of 66 mT.

The analysis performed for the graphs has revealed that the average microhardness of the sample matrices after 240 hours of exposition is 11000 MPa (the values vary within the range of 9000–14000 MPa), the dislocations areas demonstrate 12500 MPa (the variation range makes 11500–12500 MPa), the swirl-defect allow 10000 MPa of the value (within the range of 9000–16000 MPa).

The average microhardness per the structural units of the samples after 720 hours spent within the magnetic field becomes lower by 2500 and 950 MPa; for the matrix such change is within the range of

8500—10500 MPa while that of the dislocation areas is within the range of 9500—14000 MPa (swirl-defects have not been detected). These bring the conclusion that the ranges of the structural units' microhardness values undergo the considerable changes of decrease.

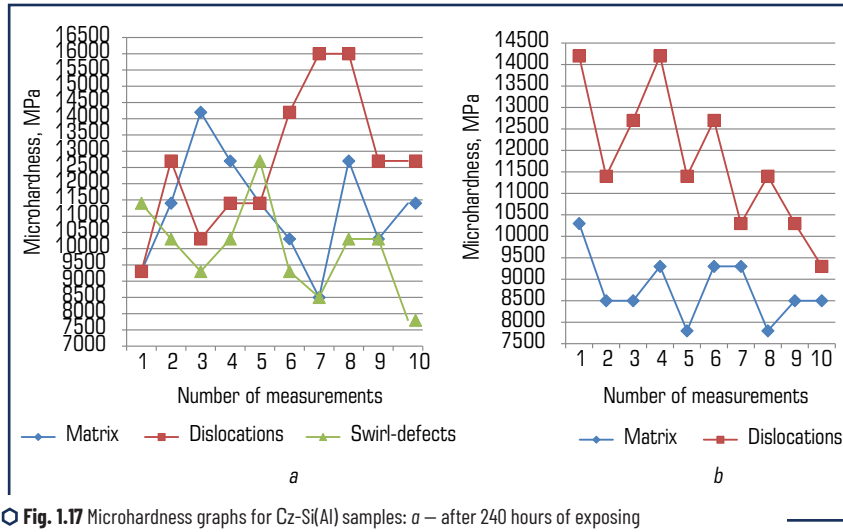

Fig. 1.17 Microhardness graphs for Cz-Si(Al) samples: *a* — after 240 hours of exposing to direct-current magnetic field; *b* — after 720 hours of exposing to direct-current magnetic field

Fig. 1.18 shows the average microhardness values per the structural units for Cz-Si(Al) samples both in the initial state and after 240- and 720-hour exposition to direct-current magnetic field. As it can be deduced from the given bar graph, the sample microhardness values notably increase after 240 hours of exposing within the magnetic field vs the initial state of the samples. The further treating of the samples (720 hours) causes the gradual decrease in the microhardness values that is connected with the decrease in the defects of the silicon samples.

In **Fig. 1.19**, we demonstrate the microhardness graphs for Cz-Si(Hf) samples after they spent 240 and 720 hours within the magnetic field for the treatment. The average microhardness values of the structural units, which Cz-Si(Hf) samples possess after 240 hours and 720 hours of the mentioned holding, are as follows: 9000 MPa (variation range is 8500—10500 MPa) and 10400 MPa (with the variations within the range of 89500—12500 MPa) for the matrices, respectively; 12400 MPa (12500—14500 MPa) and 12700 MPa (12500—16500 MPa) for the dislocation areas.

Therefore, it follows that the increase in the holding time within the magnetic field results in higher range of the microhardness value variations that is probably connected with the increase in the defects. The microhardness parameter for swirl-defects has been revealed as much as 11000 MPa in the samples after 240-hour exposing while the etched samples of 720-hour exposing have not exhibited swirl-defects.

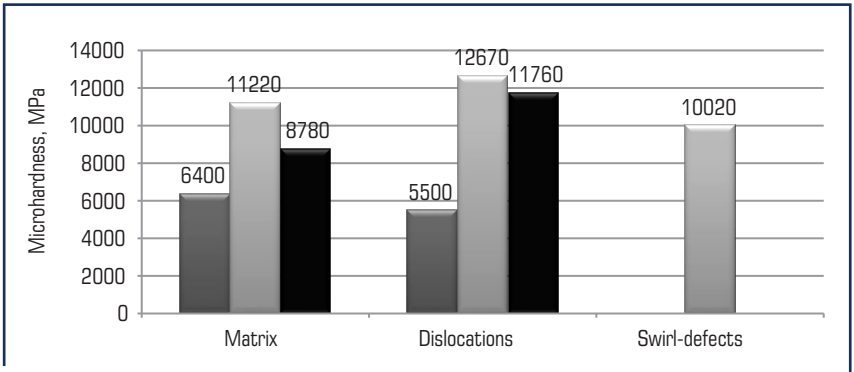

Fig. 1.18 Microhardness per the structural units for Cz-Si(Al) samples (in the initial state, after 240- and 720-hour exposition to direct-current magnetic field)

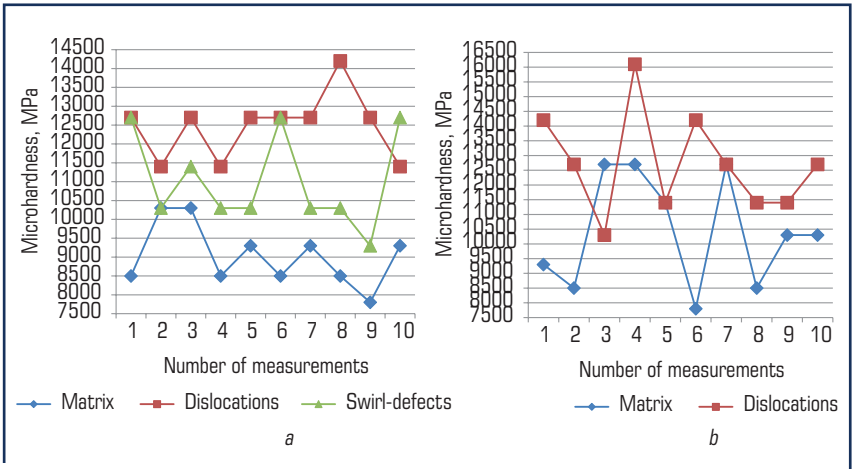

Fig. 1.19 Microhardness graphs for Cz-Si(Hf) samples: *a* – after 240 hours of exposing to direct-current magnetic field; *b* – after 720 hours of exposing to direct-current magnetic field

The microhardness average values per the structural units of Cz-Si(Hf) samples before and after the magnetic treatment are given in **Fig. 1.20**. These bar graphs show that the microhardness values gradually increase (but with slowing intensity) during further exposing to direct-current magnetic field.

In **Fig. 1.21**, we show the microhardness graphs for Cz-Si(Cu) after the action of the direct-current magnetic field. After 240 hours of magnetic field influence, the microhardness values for the matrix vary

from 7100 MPa to 9500 MPa while those for the dislocation areas are within the range of 7700—11500 MPa. After 720 hours of holding, the microhardness values show the variations from 5600 MPa to 9500 MPa for the matrix and from 6100 to 12700 MPa for the dislocation areas.

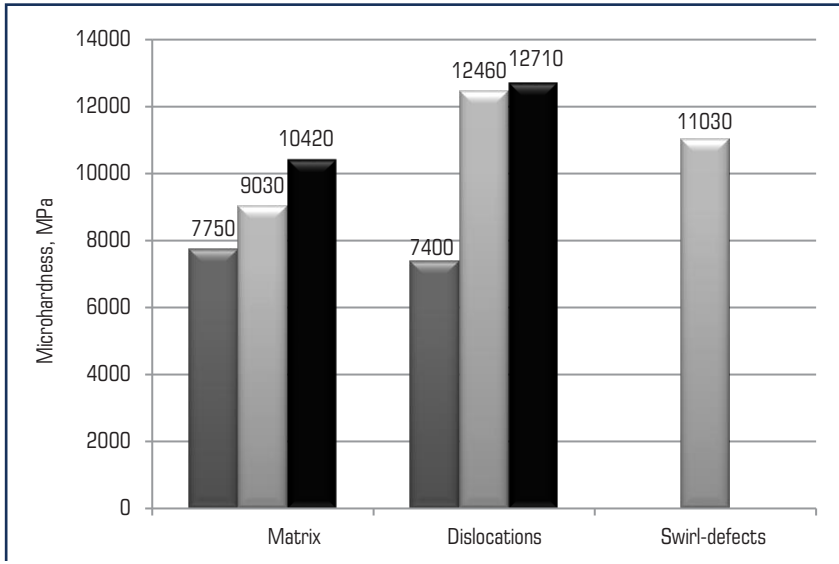

Fig. 1.20 Microhardness values per the structural units of Cz-Si(Hf) samples (in the initial state, after 240 and 720 hours of exposing to direct-current magnetic field)

The average microhardness values per the structural units of Cz-Si(Cu) samples before and after the magnetic field treatment are shown in **Fig. 1.22**. Comparing with the initial state, the microhardness parameter increases by approximately 1400 MPa in the matrix and by approximately 3500 MPa for dislocations after 240 hours of the treatment. After 720 hours spent within the magnetic field, the microhardness values increase by 100 MPa more for the matrix, but the hardness of the dislocation zone decreases by 700 MPa.

In **Fig. 1.23**, the microhardness graphs of Cz-Si(Mg) samples are presented after their exposing for 240 and 720 hours within the magnetic field. The analysis of the graphs detects that after 240-hour treatment by the magnetic field, the microhardness values of the sample matrices vary from 7700 MPa up to 10300 MPa while those of the dislocation areas are within 10300—12700 MPa. After 720 hours of the magnetic field action, the microhardness values for the matrices vary 7700—11400 MPa, while for the dislocations they are 10300—12700 MPa.

Fig. 1.24 presents the average values of microhardness per the structural units of Cz-Si(Mg) samples before and after treating with the direct-current magnetic field. This bar graph demonstrates that the microhardness values of the structural units increase during the time of exposing samples within the magnetic field. After 240 hours of holding the samples, the values for the matrix microhardness increase on

average as much as by 1800 MPa while in the dislocation zones such an increase is by 5000 MPa. The further treatment of the samples within the magnetic field leads to the greater microhardness values for the matrix by 500 MPa while the zone of the dislocations exhibits the increase by 800 MPa in this parameter.

Fig. 1.25 reports on the microhardness graphs for Cz-Si(Fe) samples after 240 and 720 hours of their exposing within the magnetic field. The dedicated measurements on microhardness per the structural units have given the following results. After 240 hours of exposing, the matrix microhardness varies within the range of 7100–9300 MPa while the microhardness of the dislocations areas varies from 8500 to 12700 MPa. After 720 hours of exposing, the hardness for matrix is within 7100–8500 MPa and for the dislocations it is within 9300–14200 MPa.

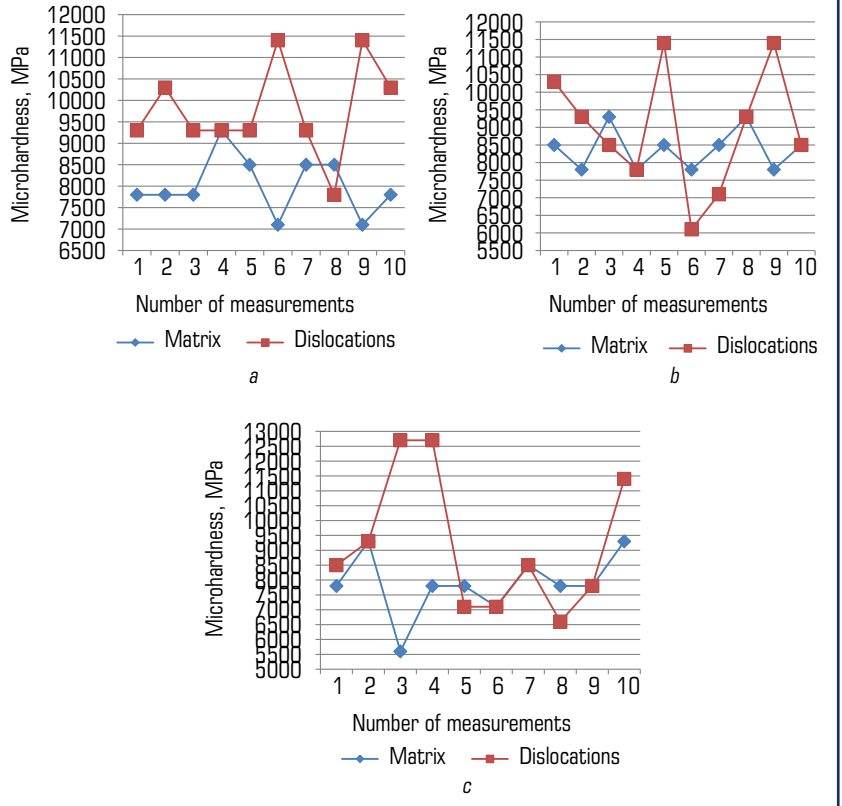

Fig. 1.21 Microhardness graphs for Cz-Si(Cu) samples: *a* – after 240 hours of exposing to direct-current magnetic field; *b*, *c* – after 720 hours of exposing to direct-current magnetic field

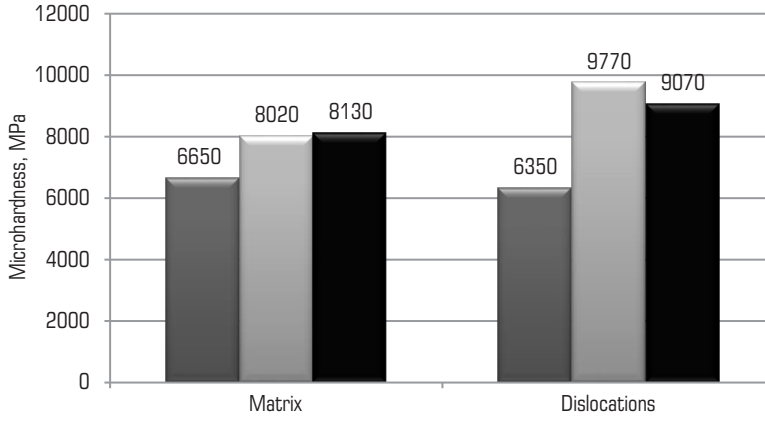

Fig. 1.22 Microhardness per the structural units of Cz-Si(Cu) samples (in the initial state, after 240- and 720-hour exposition to direct-current magnetic field)

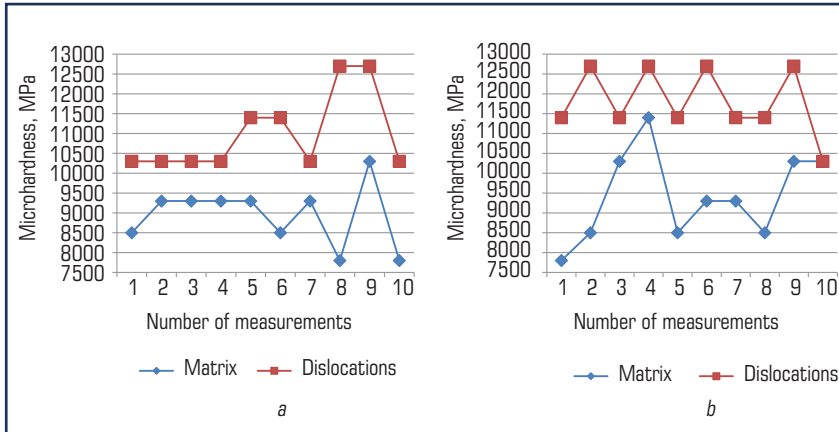

Fig. 1.23 Microhardness graphs for Cz-Si(Mg) samples: *a* – after 240 hours of exposing to direct-current magnetic field; *b* – after 720 hours of exposing to direct-current magnetic field

For the average values of microhardness per the structural units of Cz-Si(Fe) samples before and after their treatment refer to **Fig. 1.26**. After 240 hours of exposing within the magnetic field, the microhardness of the matrix values grows by 1000 MPa and that of the dislocations by 4360 MPa. The further treatment causes the decrease in the matrix microhardness by 80 MPa but increase in the microhardness values of the dislocations areas by 1300 MPa.

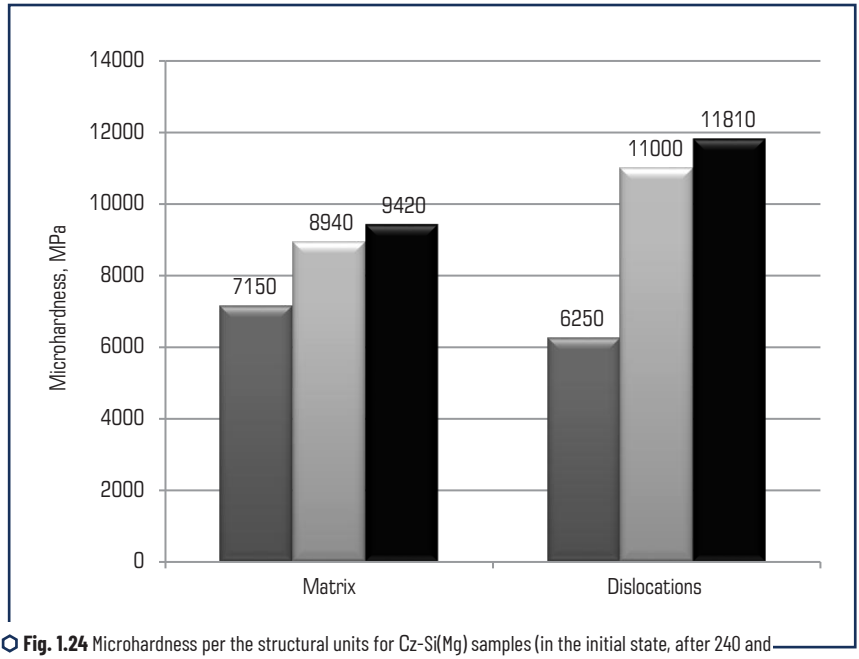

Fig. 1.24 Microhardness per the structural units for Cz-Si(Mg) samples (in the initial state, after 240 and 720 hours of exposing to direct-current magnetic field)

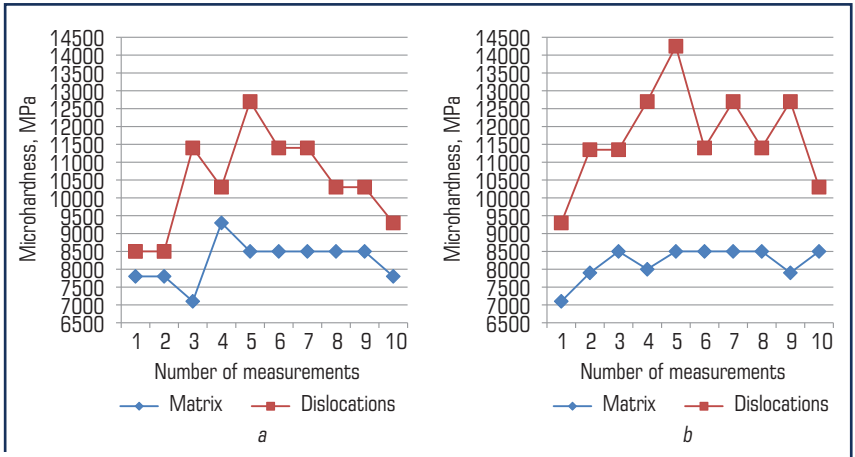

Fig. 1.25 Microhardness graphs Cz-Si(Fe) samples: *a* – after 240 hours of exposing to direct-current magnetic field; *b* – after 720 hours of exposing to direct-current magnetic field

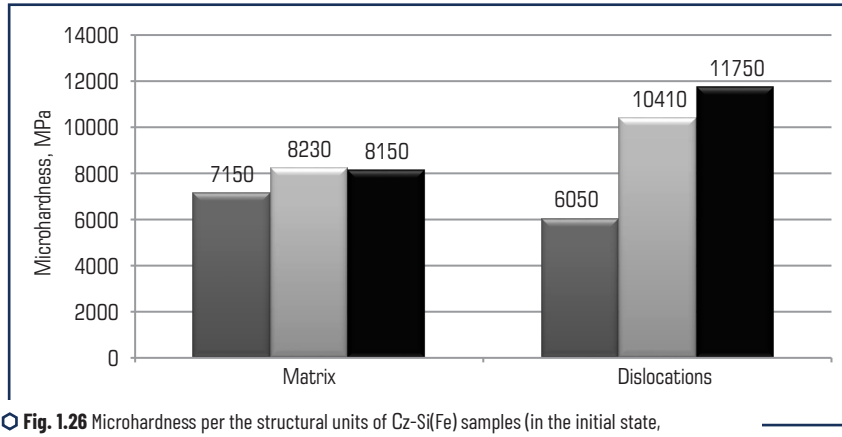

Fig. 1.26 Microhardness per the structural units of Cz-Si(Fe) samples (in the initial state, after 240 and 720 hours of exposing to direct-current magnetic field)

In **Fig. 1.27**, the microhardness average values are described graphically for the samples of Cz-Si(Zr) after 240 and 720 hours of their holding within the magnetic field. The analysis on the graphs shows that after 240 hours spent within the direct-current magnetic field, the matrix microhardness values vary within the range of 7100—14200 MPa while the dislocation areas have the range of 10300—16000 MPa for this parameter. After holding the samples during 720 hours for exposing, the matrix microhardness is 7100—11400 MPa but for the dislocation areas, it ranges within 8500—12700 MPa.

In **Fig. 1.28**, we report on microhardness values per the structural units of Cz-Si(Zr) samples before and after exposing to direct-current magnetic field. It is obvious from the bar graphs demonstrated that the microhardness values of the sample structural units increase after 240 hours of exposing within the magnetic field. The measurements after 720 hours of the treatment reveal that the microhardness values are smaller as compared with the values registered after 10 days of magnetic field treatment.

Fig. 1.29 represents the results of the microhardness measurements of the undoped silicon samples after their holding within the magnetic field during the period of 240 hours and 720 hours. The microhardness values of the sample matrices after 240 hours of treatment are 7400—12700 MPa, those of the dislocation areas are within the range of 7400—11400 MPa, the twin areas are 8500—16000 MPa. The microhardness values per the structural units after 720 hours of treating with the direct-current magnetic field are as follows: 8500—12700 MPa for matrix, 10300—14200 MPa for dislocation areas, 7000—14200 MPa for twins.

The microhardness values per the structural units of undoped silicon samples before and after their treating with the magnetic field are reported in **Fig. 1.30**. After 240 hours spent within the magnetic field, the matrix microhardness values grow stronger by 3000 MPa, the dislocation area microhardness shows the increase by 3900 MPa, a large quantity of twins appears and their average microhardness is 12000 MPa. After 720 hours of holding within the magnetic field, the microhardness values go up for the certain structural units as given: within matrix — by 200 MPa, within the dislocation zones — by 2000 MPa; however the microhardness values of twins decrease by 1500 MPa.

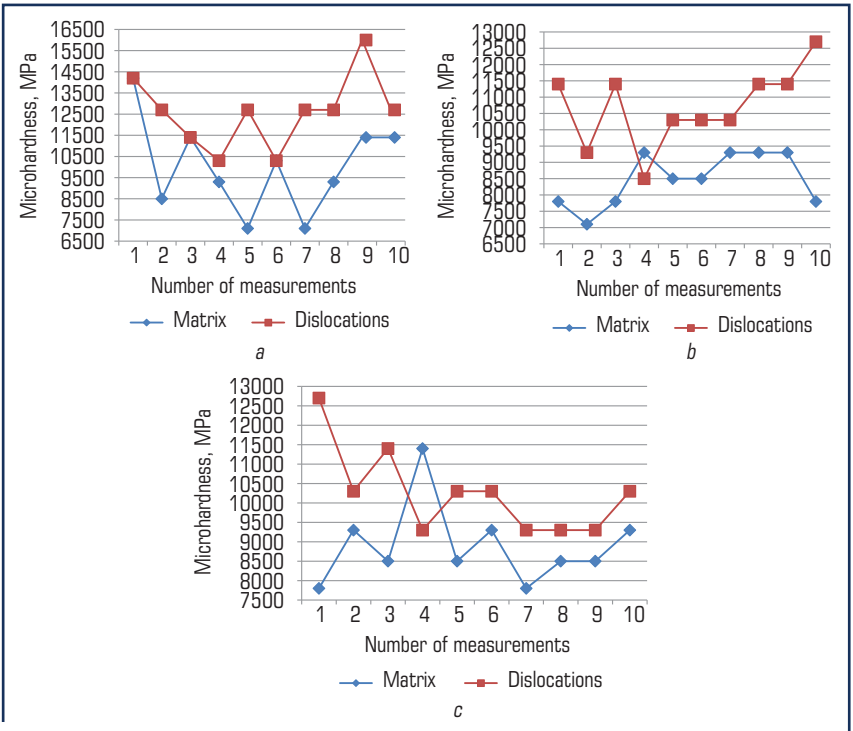

Fig. 1.27 Microhardness graphs of Cz-Si(Zr) samples: *a* – after 240 hours of exposing to direct-current magnetic field; *b*, *c* – after 720 hours of exposing to direct-current magnetic field

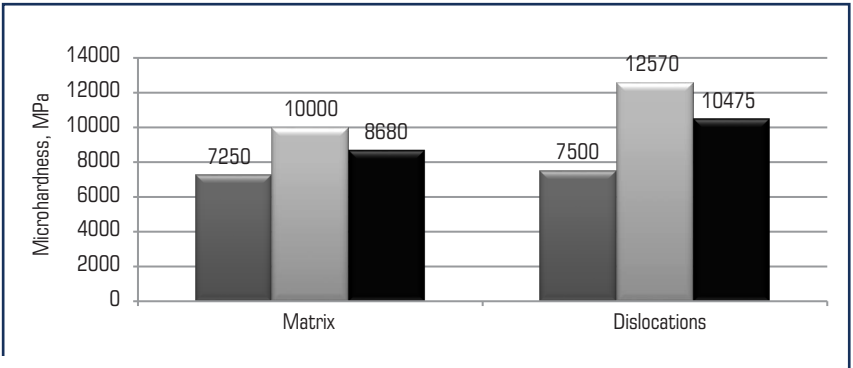

Fig. 1.28 Microhardness per the structural units of Cz-Si(Zr) samples (in the initial state, after 240 hours and 720 hours of exposing to direct-current magnetic field)

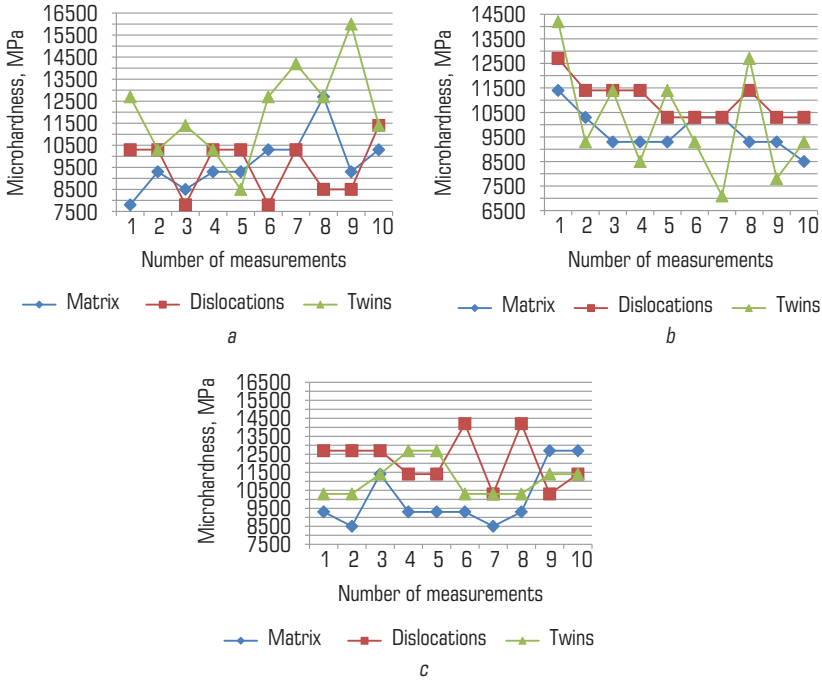

Fig. 1.29 Microhardness graphs of Cz-Si samples: *a* – after 240 hours of exposing to direct-current magnetic field; *b*, *c* – after 720 hours of exposing to direct-current magnetic field

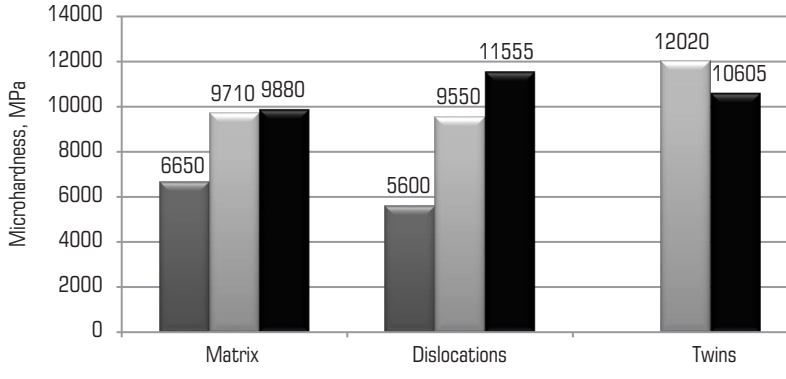

Fig. 1.30 Microhardness per the structural units of undoped silicon in the initial state, after 240 and 720 hours of exposing to direct-current magnetic field

1.5 THE PHYSICAL PARAMETERS OF THE SAMPLES BEFORE AND AFTER TREATING WITH THE MAGNETIC FIELD

Table 1.3 reports on the values of the physical parameters and the mechanical properties of the samples of both undoped and doped silicon before and after treating with the magnetic field induction of 66 mT.

In the initial state, the highest values of the specific electric resistance are possessed by Si-Zr sample, the lowest ones are the characteristics of the undoped silicon. The longest lifetime for the current minority-carriers is observed with the samples of the undoped silicon.

● **Table 1.3** Physical parameters and mechanical properties of the doped silicon samples before and after exposing to direct-current magnetic field

Sample	Properties	Initial State	240 hours of exposing	720 hours of exposing
Cz-Si	*r*, Ohm·cm	80–100	46–49	83–92
	t, μs	574	0.65	0.63
	Conduction type	P	p	P
	Hμ, MPa	6500	9500	9600
Cz-Si-Al	*r*, Ohm·cm	200–210	55–65	60–65
	t, μs	12.1–12.5	0.40	0.32
	Conduction type	P	p	P
	Hμ, MPa	6800	10750	10320
Cz-Si-Hf	*r*, Ohm·cm	180–192	12.8–14.3	13.5–14.0
	t, μs	148	23.08	28.11
	Conduction type	P	p	P
	Hμ, MPa	7750	10500	10900
Cz-Si-Cu	*r*, Ohm·cm	170–190	44.8–46.2	43.7–50.0
	t, μs	134–138	16.32	14.55
	Conduction type	P	p	P
	Hμ, MPa	6900	10450	10700
Cz-Si-Zr	*r*, Ohm·cm	308–324	13.0–23.5	22.5–25.6
	t, μs	228	93.3	69.57
	Conduction type	N	n	N
	Hμ, MPa	7900	11200	10300

Source: [33]

The date presented in the table evidence that there is a significant decrease observed in the values of the specific electric resistance and the life time for the current minority-carriers after the treating the samples of

doped silicon within direct-current magnetic field. For the samples of undoped silicon, the decrease in the life time for the current minority-carriers is as great as several orders. All the samples exhibit the drastic drop of the electric resistance after 240 hours of exposing to direct-current magnetic field, however some increase is observed in the values of this parameter with the further treatment by holding the samples in the magnetic field (Si-Cu behaved as an exception to this regularity). The sharp drops of the life times of the current minority-carriers are registered with all the samples after 240 hours of holding within the magnetic field, and they are followed by the further decrease if the holding time of 720 hours (however Si-Hf has been an exception).

In **Fig. 1.31**, we show the dependences between the life times of the current minority-carriers and the average microhardness for the undoped and the doped silicon samples before and after treating the samples with the direct-current magnetic field.

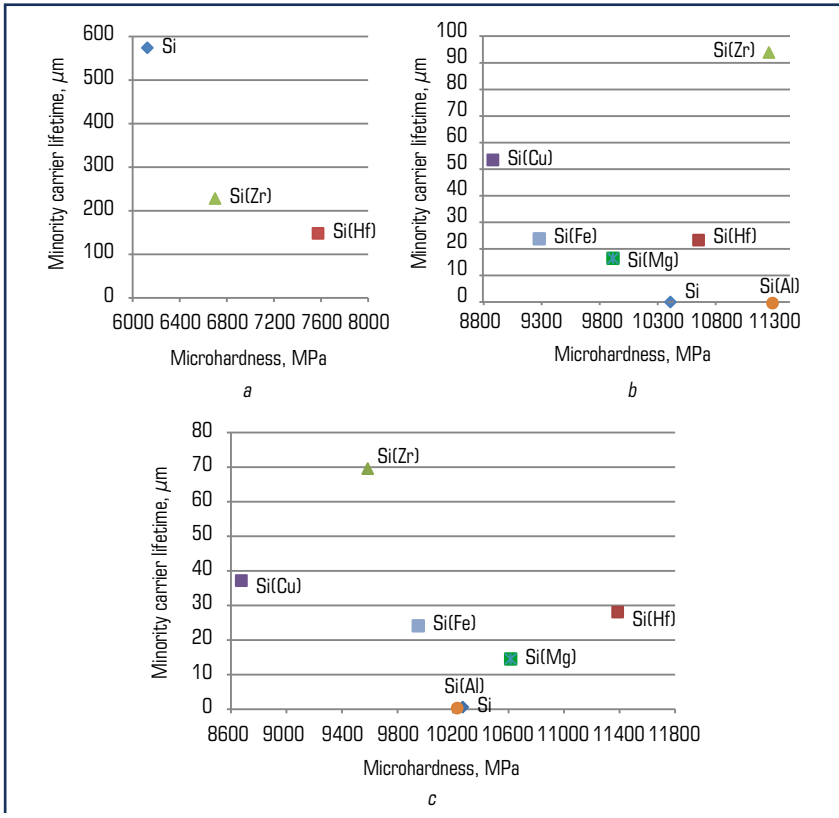

Fig. 1.31 Dependence between the time span of the current minority-carriers and the average microhardness of the samples: *a* — initial state; *b* — after 240 hours of exposing to direct-current magnetic field; *c* — after 240 hours of exposing to direct-current magnetic field

For the samples in their initial state, the dependence is discernible between the microhardness value and the life time of the current minority-carriers. After treating them with the magnetic field, this dependence considerably weakens and the notable irregularities in it are found if we study the Si samples doped with Zr, Hf (**Fig. 1.31, *b, c***) and Mg (**Fig. 1.31, *c***).

Shortening the life time for the current minority-carriers can be explained as the relevance with that oxygen which the silicon surficial layers contain. As the publication reports [34], during the time when silicon is treated within the magnetic field, the oxygen content increases drastically in its surficial layers, the same is true for the ions of the alkaline metal (K^+, Na^+), hydroxyl groups and other radicals. This is related to the surface activation and enhancing its absorption ability under the influence of weak magnetic field.

Apart from the oxygen in the principle state or the triplet state, the radical groups absorbed on the silicon surface also possess the ability of capturing the current carriers [33] and drastically decrease their lives in the free state.

Doping silicon with the elements of a greater affinity for oxygen (Zr, Hf, Al) permits the decrease in the influence of oxygen on the charge carrier life time by its binding. This is an assumable explanation for the reason why the samples doped with the mentioned elements have quite high values for the auxiliary charge carrier life time if the microhardness values are also high. The exception to this regularity is Si(Al).

CONCLUSIONS

1. The microstructure of the initial Cz-Si sample which is formed under the influence by the treatment within the magnetic field has been not studied before the research conducted for the current publication. The research reveals as follows:

— during 240 hours of exposing to the magnetic field, there is the significant increase in the number of the internal structure defects and the density of the dislocations as well as the formation of twins;

— during 720 hours of treating within the magnetic field, the polycrystalline silicon is formed with a large quantity of grain boundaries.

2. This research is the first time when it has been addressed to the problem of the magnetic field influences on the microstructure of Cz-Si doped with the elements which influence differently the energy of interaction between the silicon atoms within the crystal lattice, namely — Al, Mg, Cu, Fe, Zr, Hf.

With this publication, we show what influence produces the treatment within the magnetic field on Cz-Si doped with those elements which are able to decrease the interaction energy of silicon atoms (Al, Mg, Cu, Fe).

The data revealed can be summarized as follows:

— there is an increase in the quantity of the sample structural defects at exposing during 240 hours but their notable decrease is observed during 720 hours;

— Cz-Si doped with Zr and Hf, which increase the energy of interaction between the silicon atoms within the lattice, goes down significantly in the quantity of structural defects starting from at the point of 240 hours spent within the magnetic field.

3. By means of X-ray analysis conducted for the samples, which have been subjected to the magnetic field, it is registered that there are splits in the diffraction lines as well as the appearance of the new peaks at the scattering angles of 90—92 degrees. These phenomena are caused by the distortions of Si_{FCC} crystal lattice and forming $Si_{ORTHORHOMBIC}$ along with it. This evidences about the phase transformations in the samples of the semiconductive silicon when the magnetic treatment at the room temperature.

4. The study performed to address the problem of magnetic field influence on the microhardness of the doped Cz-Si has revealed as follows:

— the microhardness of Cz-Si doped with Al, Mg, Cu, Fe grows by 1.8—2.0 times at exposing both during 240 hours and 720 hours;

— the microhardness of Cz-Si doped with Zr, Hf grows by 1.5—1.8 times after exposing to the magnetic field during 240 hours while such values are higher by 1.2—1.5 times after 720 hours of exposition.

5. In this publication, the problem of the magnetic field treatment is first studied in terms of its influence on the physical properties of the doped Cz-Si, namely, its specific electric resistance (**r**, Ohm·cm), life time (**t**, μs). It has been revealed as follows:

— 240 hours spent within the magnetic field decrease the specific electric resistance (**r**, Ohm·cm) of Cz-Si by 1.7—2.0 times while 720 hours of exposing decrease this parameter by 1.08;

— specific electric resistance (**r**, Ohm·cm) of Cz-Si Al, Cu decreases by 3.4 times at exposing within the magnetic field during the time period from 240 to 720 hours;

— for Cz-Si doped with Zr we observe the decrease in specific electric resistance values (**r**, Ohm·cm) by 18 times after 240 hours of the mentioned exposing and by 13.5 times at 720 hours of exposition;

— for Cz-Si doped with Hf, the specific electric resistance decreases by 13.5 times after 240 and 720 hours of exposing;

— the life time for minority-carriers of the charge (**t**, μs) decreases 900 times within Cz-Si under conditions of both 240 and 720 hours of the magnetic field treatment;

— for Cz-Si doped with aluminium, the life time for minority-carriers of the charge decreases by 30 times when 240 hours of treatment while the decrease in 38 times is detected after 720 hours of exposing;

— for Cz-Si doped with copper, the life time for its minority-carriers of the charge decreases by 8—9 times both under 240 hours and 720 hours within the magnetic field;

— for Cz-Si doped with hafnium, the life time for its minority-carriers of the charge (**t**, μs) decreases by 6 times at 240 hours and by 5 times at 720 hours of exposing;

— doping with zirconium enables sustaining the longest life times for its minority-carriers of the charge (**t**, μs) vs those of the initial state: the life time for its minority-carriers of the charge experiences the shortening just by 2.4—3.2 after exposing within the magnetic field during 240 and 720 hours and they correspond to the values of 93.3 μs and 69.57 μs, respectively, compared against 0.63—0.65 of Cz-Si.

6. In this publication, we report on the development of the new complex production technology for silicon semiconductor. The technology includes the stages of silicon doping with the transition metals and rare earth metals, heat treatment at the temperatures of phase transformations and treating within the magnetic field at room temperature. These stages provide the enhanced set of the mechanical and the physical properties for Cz-Si products intended for devices.

REFERENCES

1. Glazov, V. M., Timoshina, G. G., Mikhailova, M. S. (1996). Printcipy legirovaniia kremniia dlia povysheniia ego termostabilnosti. Doklady Akademii Nauk, 347 (3), 352—355.
2. Taran, Yu. N., Glazov, V. M., Regel, A. R., Kutsova, V. Z., Koltsov, V. B., Timoshina, G. G. et al. (1991). Strukturnye prevrashcheniia pri nagreve monokristallov kremniia Fizika i tekhnika poluprovodnikov, 4 (25), 588—595.
3. Kol'tsov, V. B., Zubkov, A. M., Timoshina, M. I. (2002). Metodika issledovaniy elektrofizicheskikh svoystv monokristallov kremniya v shirokom intervale temperatur. Fizika poluprovodnikov i polumetallov. Saint-Petersburg.
4. Kozhitov, L. V., Botavin, V. V., Shepel, P. N., Timoshina, G. G., Timoshina, M. I. (2002). Issledovanie kinetiki raspada kremniia, legirovannogo perekhodnymi i redkozemelnymi elementami. Kremniy-2002. Novosibirsk, 129.
5. Novokhatskiy, I. A., Kisun'ko, V. Z., Ladyanov, V. I. (1985). Osobennosti proiavlenii razlichnykh tipov strukturnykh prevrashchenii v metallicheskikh rasplavakh. Izvestiya vuzov. Chernaya metallurgiya, 5, 1—9.
6. Kutsova, V. Z., Nosko, O. A., Timoshina, M. I. (2006). Alloying effect on structure and properties of semiconductor silicon. Proceeding of the International Conference Silicon 2006, 450—459.
7. Tonkov, E. Yu. (1988). Fazovye prevrashcheniia soedinenii pri vysokom davlenii. Vol. 1, 2. Moscow: Metallurgiya, 463, 356.
8. Kutsova, V. Z., Nosko, O. A., Timoshina, M. I. (2007). Vliianie legiruiushchikh elementov na strukturu, fazovyi sostav i svoistva poluprovodnikovogo kremniia. Kremniy-2007. Moscow: Gosudarstvennyy tekhnologicheskiy universitet "Moskovskiy institut stali i splavov", 109.
9. Glazov, V. M., Zemskov, B. S. (1967). Fiziko-khimicheskie osnovy legirovaniia poluprovodnikov. Moscow: Nauka, 372.
10. Klevan, O. S., Engh, T. A. (1995). Dissolved impurities and inclusions in FeSi and Si, development of a filter sampler. INFACON 7. Trondheim, 441—451.
11. Prikhodko, E. V. (1983). Metallokhimiia kompleksnogo legirovaniia. Moscow: Metallurgiya, 184.
12. Nesterenko, A. M., Uzlov, K. I., Kutsova, V. Z., Nyshchenko, A. N. (1988). Vliianie skorosti okhlazhdeniia na obrazovanie tverdykh rastvorov v sisteme Al-Si. Izvestiya AN SSSR, Metally, 2, 192.
13. Savitskiy, E. M., Burkhanov, S. S. (1967). Metallovedenie tugoplavkikh metallov i splavov. Moscow: Nauka, 324.
14. Liubov, B. Ia. (1969). Kineticheskaia teoriia fazovykh prevrashchenii. Moscow: Metallurgiia, 264.
15. Taran, Yu. N., Kutsova, V. Z., Uzlov, K. I., Falkevich, E. S. (1992). Shearing phase transformations in semiconductors. Proceeding of the International Conference 'Silicon 92', 88—95.
16. Milvidskiy, M. G., Osvenskiy, V. B. (1984). Strukturnye defekty v monokristallakh poluprovodnikov. Moscow: Metallurgiya, 256.
17. Glazov, V. M., Koltsov, V. B., Kutsova, V. Z., Taran, Yu. N., Timoshina, G. G., Uzlov, K. I., Falkevich, E. S. (1990). Issledovanie elektro-fizicheskikh svoystv kremniya v shirokom intervale temperatur. Elektronnaya tekhnika, 11.

18. Glazov, V. M., Kurbatov, V. A., Koltsov, V. B. (1985). Issledovanie effekta Kholla antimonidov Ga i In v tverdom i zhidkom sostoyanii. Fizika i tekhnika poluprovodnikov, 19 (4), 662—667.
19. Kopaev, Iu. V., Meniailenko, V. V., Molotkov, S. N. (1985). Neravnovesnye fazovye perekhody v kovalentnykh poluprovodnikakh pod vozdeistviem lazernogo izlucheniia. Fizika tverdogo tela, 27 (11), 3288—3294.
20. Landau, L. D., Lifshits, E. M. (1964). Statisticheskaia fizika. Moscow: Nauka, 568.
21. Tairov, Yu. M., Tsvetkov, V. F. (1980). Rost kristallov i politipizm karbida kremniya. Rost kristallov, 13, 104—111.
22. Taran, Yu. N., Kutsova, V. Z., Chervonyy, I. F., Shvets, E. Ya., Falkevich, E. S. (2004). Poluprovodnikovyy kremniy: teoriya i tekhnologiya proizvodstva. Zaporozhe: Zaporozhskaya gosudarstvennaya inzhenernaya akademiya, 344.
23. Alshits, V. I., Darinskaya, E. V., Koldaeva, M. V., Petrzhik, E. A.; Hirth, J. P. (Ed.) (2008). Magnetoplastic Effect in Nonmagnetic Crystals. Dislocations in solids. Amsterdam: Elsevier, 14 (86), 333—437. https://doi.org/10.1016/s1572-4859(07)00006-x
24. Alshits, V. I., Darinskaya, E. V., Koldaeva, M. V., Petrzhik, E. A. (2003). Magnetoplastic effect: Basic properties and physical mechanisms. Crystallography Reports, 48 (5), 768—795. https://doi.org/10.1134/1.1612598
25. Golovin, Yu. I. (2004). Magnitoplastichnost tverdykh tel (Obzor). Fizika Tverdogo Tela, 46, 769.
26. Morgunov, R. B. (2004). Spinovaia mikromekhanika v fizike plastichnosti. Uspekhi fizicheskikh nauk, 174, 131—153.
27. Buchachenko, A. L. (2013). Mass-Independent Isotope Effects. The Journal of Physical Chemistry B, 117 (8), 2231—2238. https://doi.org/10.1021/jp308727w
28. Zinenko, V. N., Sorokin, B. P., Turchin, P. P. (1983). Osnovy fiziki tverdogo tela. Moscow: Vysshaia shkola, 330.
29. Milnes, A. G., Feuch, D. L. (1972). Heterojunctions and Metall-Semiconductor Junctions. New York; London: Academic Press, 418. https://doi.org/10.1016/b978-0-12-498050-1.x5001-6
30. Zhitinskaya, M. K., Nemov, S. A., Svechnikova, T. E. (1997). Vliyanie neodnorodnostey kristallov Bi_2Te_3 na poperechnyy effekt Nernsta — Ettingsgauzena. Fizika i tekhnika poluprovodnikov, 31 (4), 441—443.
31. Chervonyi, I. F., Kutsova, V. Z., Pozhuiev, V. I., Shvets, Ye. Ya., Nosko, O. A., Yehorov, S. H., Voliar, R. M. (2009). Napivprovidnikovyi kremnii: teoriia i tekhnolohiia vyrobnytstva. Zaporizhzhia, 350.
32. Vapnik, V. N. (Ed.) (1984). Algoritmy i programma vosstanovleniya zavisimostey. Moscow: Nauka, 816.
33. Kutsova, V. Z., Nosko, O. A., Tutyk, V. A., Sulay, A. M. (2015). Struktura, mekhanichni ta elektrofizychni vlastyvosti monokrystalichnoho kremniiu pid diieiu postiinoho mahnitnoho polia. Metallurgicheskaya i gornorudnaya promyshlennost, 1, 73—79.
34. Kutsova, V. Z., Nosko, O. A., Sulay, A. M. (2014). Vliianie legirovaniia i termicheskoi obrabotki na strukturu i svoistva poluprovodnikovogo kremniia. Metallurgicheskaya i gornorudnaya promyshlennost, 6, 65—72.
35. Kutsova, V. Z., Nosko, O. A., Sulay, A. M. (2015). The structure, mechanical and electrophysical properties of monocrystalline silicon under influence of constant magnetic field. Ukrainian journal of mechanical engineering and materials science, 1 (1), 91—98.

36. Kutsova, V. Z., Nosko, O. A., Sulai, A. M. (2017). The influence of constant magnetic field on the structure and properties of monocrystalline silicon. Metaloznavstvo ta termichna obrobka metaliv, 2, 32—40.
37. Bonch-Bruevich, V. P., Kalashnikov, S. G. (1990). Fizika poluprovodnikov. Moscow: Nauka, 685.
38. Moss, T. S., Burrell, G. J., Ellis, B. (1973). Semiconductor opto-electronics. Butterworth-Heinemann, 441. https://doi.org/10.1016/c2013-0-04197-7
39. Kutsova, V. Z., Uzlov, K. Y., Khronenko, V. M. (1999). Temperaturnaya zavisimost' otnositel'nogo udlineniya sverkhchistogo kremniya. Metallurgicheskaya i gornorudnaya promyshlennost, 4, 72—74.
40. Taran, Iu. N., Kutcova, V. Z., Kovalchuk, M. G., Uzlov, K. I. (1988). Neodnorodnost beta-tverdogo rastvora v siluminakh. Metallovedenie i termicheskaia obrabotka metallov, 9, 33—37
41. Taran, Yu. N., Kutsova, V. Z. (2002). Fazovye prevrashcheniya i svoystva poluprovodnikovogo kremniya. Vysokochistye metallicheskie i poluprovodnikovye materialy. Kharkovskaya nauchnaya assambleya ISPM-8, 68—73.
42. Taran, Yu. M., Kutsova, V. Z., Nosko, O. A. (2002). Fazovi peretvorennia ta vlastyvosti napivprovidnykovoho kremniiu. Metaloznavstvo ta obrobka metaliv, 1—2, 59—65.
43. Taran, Yu. M., Kutsova, V. Z., Nosko, O. A. (2004). Semiconductor—Metal Phase Transitions. Uspehi Fiziki Metallov, 5 (1), 87—166. https://doi.org/10.15407/ufm.05.01.087
44. Kutsova, V. Z., Stetsenko, A. P., Mazochuk, V. F. (2017). Phase transformations in semiconductor silicon by the influence of magnetic field. Systemni tekhnolohii. Rehionalnyi mizhvuzivskyi zbirnyk naukovykh prats, 5 (112), 103—107.
45. Oranska, O. I., Gornikov, Yu. I., Gun'ko, V. M., Brichka, A. V. (2022). On the use of model diffraction profiles in the microstructure analysis of nanocrystalline metal oxides based on powder x-ray diffraction data. SURFACE, 14 (29), 148—158. https://doi.org/10.15407/surface.2022.14.148
46. Makara, V. A., Vasiliev, M. O., Steblenko, L. P., Koplak, O. V., Kuryliuk, A. M., Kobzar, Yu. L., Naumenko, S. M. (2009). Influence of Magnetic Treatment on the Microhardness and Surface Layers Structure of Silicon Crystals. Physics and Chemistry of Solid State, 10 (1), 193—198.
47. Nosko, O. A. (2006). Osobennosti struktury, fazovye prevrashcheniya legirovannogo kremniya i modifitsirovannykh zaevtekticheskikh siluminov i razrabotka sposobov povysheniya ikh svoystv [PhD dissertation]. Dnepropetrovsk, Ukraine.
48. Kutsova, V. Z. (1993). Teoriya i praktika upravleniya strukturoy i svoystvami liteynykh splavov na osnove alyuminiya i titana [Doctor's thesis]. Dnepropetrovsk, Ukraine.

DOI: 10.15587/978-617-8360-17-7.CH2

Oleh Kuzmin, Oktyabrina Chemakina, Anton Kuzmin,
Oleksandr Zaporozhets, Igor Dudarev, Larysa Bal-Prylypko

2 INTEGRATION OF INCLUSIVE ENGINEERING PRINCIPLES AND CRAFT TECHNOLOGIES IN THE DESIGN OF FOOD SERVICE FACILITIES IN THE CONTEXT OF POST-WAR RECONSTRUCTION OF UKRAINE: BUILDING MATERIALS, ARCHITECTURAL SOLUTIONS, QUALITY, SAFETY

ABSTRACT

The study is devoted to the integration of inclusive engineering principles and craft technologies in the design of food service facilities within the context of Ukraine's post-war reconstruction. The primary focus is on the environmentally responsible selection of building materials (wood, clay, straw, hemp fiber, arbolite concrete) and architectural solutions that address the needs of vulnerable population groups, including veterans, persons with disabilities, and internally displaced persons. Emphasis is placed on ensuring quality standards, safety (notably HACCP), and hygiene, which are critically important in the food service sector.

In the context of the war in Ukraine, which has caused extensive infrastructure destruction, there is a need to create a new architectural and construction culture oriented toward sustainable development, social inclusivity, and the preservation of local identity. The proposed approach combines circular economy principles (material reuse), craft technologies (hand labor, local resources), and inclusive design (barrier-free access, adaptive furniture, sensory comfort). This contributes to the economic recovery of communities, reduces environmental impact, and creates culturally significant spaces.

The objective is to develop a methodology for integrating inclusive engineering and craft technologies to create accessible, safe, and authentic food service facilities.

The study includes an analysis of the thermophysical characteristics of building materials such as density, heat capacity, thermal conductivity, and vapor permeability, along with a comparison of their technological complexity, environmental friendliness, and economic feasibility. Results demonstrate the advantages of materials with high heat capacity (reed panels, arbolite) for energy efficiency and low thermal conductivity (cellulose insulation, foam glass) for thermal insulation. Architectural solutions encompass ramps, wide corridors, zoning, anti-slip surfaces, and hygienic materials compliant with HACCP standards.

This approach ensures the creation of sustainable, safe, and socially inclusive spaces that support the local economy, reduce ecological footprint, and contribute to the preservation of Ukrainian identity. It is recommended to adapt regulatory frameworks and educational programs to promote these principles.

KEYWORDS

Inclusive engineering, craft technologies, design, architectural solutions, building materials, sustainable development, post-war reconstruction of Ukraine, food service facilities, quality, safety, HACCP.

The war in Ukraine has caused extensive destruction [1] to the housing stock and social infrastructure facilities, demolishing millions of square meters of residential buildings, schools, hospitals, public structures, and cultural heritage sites. In the face of such losses, the task arises not only of physical reconstruction but also of forming a new architectural and construction culture focused on the principles of sustainable development, environmental responsibility, and social sensitivity. Considering resource limitations, rising costs of building materials, and the urgent need for fast and efficient solutions, the reuse of building materials obtained from the demolition of destroyed structures becomes especially important [2–4].

In this context, the restoration of social infrastructure requires the implementation of new approaches to the design of public facilities — primarily food service establishments — that take into account the needs of vulnerable population groups, as well as quality requirements [5–7] and the safety of the food environment [7, 8]. This approach should be based on four strategic directions:

— social inclusivity, which implies the creation of a barrier-free environment accessible to all population categories, including persons with disabilities, elderly people, veterans, and internally displaced persons [9–12];

— environmental responsibility, realized through the use of renewable natural resources, reuse of building materials [2–4], and minimization of the carbon footprint at all stages of construction;

— local identity, expressed in the preservation of cultural characteristics, architectural traditions, and the material heritage [13] of a specific community;

— sanitary and hygienic safety [7, 8, 14], ensured through the implementation of quality management systems [6, 7, 15] and HACCP [7, 8, 15], which regulate spatial, engineering-technological, and operational solutions in food service establishments in accordance with food safety principles and hygiene standards.

2.1 NEW CONSTRUCTION GUIDELINES IN THE PROCESS OF UKRAINE'S RECONSTRUCTION

In the post-war period [16], when resources are limited and the need for prompt, effective, and economically viable solutions is critical, approaches based on the circular economy gain special importance. The reuse of building materials recovered from demolished structures allows not only to reduce the demand for new resources and lower transportation and disposal costs but also significantly decreases environmental impact [2, 3, 17–19]. This becomes particularly relevant in designing social infrastructure facilities, especially food service establishments, which require fast, high-quality, and accessible reconstruction [10–12].

At the same time, physical reconstruction must be accompanied by a paradigm shift: from "technocratic restoration" [2, 4, 13] to "human-centered reconstruction", which takes into account social sensitivity and the needs of vulnerable groups — including persons with limited mobility, veterans, elderly people, children, and internally displaced persons [11, 12, 14, 20, 21]. In this context, inclusive engineering design is regarded as a necessary prerequisite for creating environments that are not only accessible but also adapted to diverse physical, sensory, and cognitive needs [9–12, 14, 20, 21].

Craft technologies [14], based on manual labor, local knowledge, and the use of natural materials, play a special role in this approach. Their advantage lies in high adaptability to local contexts: from small

communities and rural areas to temporary facilities, including field kitchens, mobile canteens, and modular cafés. Combined with inclusive engineering, they enable the creation of spatial solutions that are environmentally balanced, technically simple to implement, and socially acceptable. Moreover, this approach encourages community involvement in reconstruction processes, fostering economic recovery at the local level [11, 12, 14].

Another critically important aspect is the preservation and restoration of local identity, which for decades has suffered destruction and homogenization. Local identity includes architectural styles, materials, color schemes, decorative motifs, landscape features, linguistic and cultural codes, and social rituals that form the unique character of each territory, creating a distinct "national style" [22]. In the design of food service establishments, this is expressed, for example, through the use of traditional forms (such as clay facades, wooden elements, ceramic inserts), the introduction of ethnodesign elements in interiors, and the use of local products in menus.

Combined with inclusive and ecological approaches, local identity creates the foundation for culturally significant, socially cohesive, and sustainable gastronomic spaces that reflect the uniqueness of the community while meeting modern technical, ergonomic, and sanitary-hygienic standards. This allows avoiding the stereotypical "standardized design" characteristic of "soviet architecture" and instead promotes a conscious transformation of space through the lens of authenticity, safety, and quality. It imparts a unique character to the community, supports its historical memory, roots social bonds, and contributes to sustainable development.

2.1.1 THE ROLE OF CRAFT APPROACHES IN THE CONTEXT OF THE CIRCULAR ECONOMY

In the process of Ukraine's post-war reconstruction, craft approaches [14] are gradually gaining status as one of the key vectors for implementing the principles of the circular economy [4, 23, 24], especially in the context of architectural and engineering design of social facilities — particularly food service establishments. These approaches imply a shift away from the linear model of "production — consumption — disposal" toward a cyclical model, where materials receive a second life and architectural solutions focus on restoration, reuse, recycling, and prolonged service life [23].

Craft technologies involve the manual or semi-manual production of building materials with maximal use of local resources — natural, renewable, and low-toxicity. This not only reduces dependence on industrial supply chains but also allows flexible adaptation of designs to local conditions and community needs. In the design of food service facilities, this approach offers several advantages:

— enables the creation of aesthetically expressive, individualized interiors featuring elements of regional style (clay, wood, straw, ceramics, linen textiles);

— allows for the reuse of materials (e.g., bricks, wood, stone) for facades, bar areas, furniture, or decorative elements;

— contributes to reducing the carbon footprint and the volume of construction waste, aligning with the ecological goals of reconstruction [4, 23].

At the same time, the material life cycle — from the original source to reintegration into a new structure — becomes a central category in engineering design [9]. Within this approach, not only the primary

parameters of the material (strength, thermal insulation, moisture resistance) are planned, but also its potential for further utilization, reclamation, or reassembly.

The application of craft technologies is particularly effective when combined with modular constructions and adaptive architecture, enabling the creation of both permanent and temporary food service facilities — mobile canteens, summer kitchens, social cafés — that account for seasonality, population migration, or fluctuating demand.

Engaging the community — local artisans, small entrepreneurs, and craftsmen — in this process not only supports the local economy but also fosters social responsibility in projects, enhances their cultural rootedness, and stimulates the development of craft food productions closely linked to the food service establishment.

Thus, craft technologies in the architecture of food service facilities in post-war Ukraine represent not only aesthetics and tradition but also a strategic resource for sustainable reconstruction, integrated into the principles of ecological feasibility, economic efficiency, and social inclusion.

2.1.2 THE ROLE OF INCLUSIVITY IN DESIGN

Inclusive engineering in Ukraine's post-war reconstruction acquires particular importance as an interdisciplinary approach that combines technical, architectural, social, and humanitarian dimensions in the design, construction, and operation of the physical environment [9, 11, 12]. Its key goal is to create spaces that are physically, sensorially, and psychologically accessible, functional, safe, and comfortable for all user categories — regardless of age, gender, physical or cognitive characteristics [10, 14, 25].

Inclusivity becomes especially relevant in the design of food service establishments [5, 11, 14], which perform not only service functions but also social, rehabilitative, and integrative roles. In the context of the return to peaceful life of a significant number of veterans [26], persons with disabilities, and internally displaced persons, food service facilities become spaces for meeting, socializing, employment, and support, requiring a particularly sensitive architectural approach.

This approach goes beyond mere formal compliance with technical accessibility standards and includes a profound rethinking of architectural-spatial models [27], engineering systems [9, 27], and technological processes, taking into account the real-life experiences of users. The principle "the environment must adapt to the person, not vice versa" demands the involvement of specialists in ergonomics, psychology, interior design, and medical rehabilitation.

In establishments that combine food service functions with craft production (such as bakeries, mini-workshops, or family cafés), inclusivity acquires an additional dimension — production accessibility. This concerns not only the physical adaptation of work areas (surface heights, safe equipment placement, presence of tactile or visual markers) but also an inclusive work culture that supports the participation of people with functional limitations in production and service processes. This promotes not only economic integration but also reduces labor market discrimination, increases autonomy, and fosters local entrepreneurship.

Thus, inclusive engineering in the design of food service establishments is not only a tool for spatial accessibility [14, 28] but also a powerful mechanism for creating a just, "humane", and sustainable

environment where technical solutions meet real user needs and architecture becomes an instrument of social cohesion and dignity.

2.1.3 RELEVANCE OF THE RESEARCH DIRECTION

The full-scale war in Ukraine has caused a profound transformation of the social, engineering, and architectural environment, posing new demands on the spatial design, construction, and operation of public facilities. Today, the task is not only the physical reconstruction of damaged housing and social infrastructure but also the rethinking of approaches to architectural and structural modeling, taking into account the principles of sustainable development, environmental responsibility, social justice, and cultural rootedness.

In conditions of resource scarcity, rapid urbanization, and the need for quick solutions, inclusive engineering practices oriented toward the needs of a wide range of users — especially persons with disabilities, combat veterans, elderly people, children, and internally displaced persons — gain special relevance. The growing share of the population with functional limitations requires fundamentally new approaches to shaping the physical environment, where accessibility, comfort, safety, and adaptability are considered the basic characteristics of spatial quality.

At the same time, the role of craft technologies is increasing — as an alternative to mass industrial construction — that ensures the use of local resources, consideration of the local context, community involvement in reconstruction, and the restoration of local identity. The combination of manual production methods, artisanal practices, and modern materials science approaches creates conditions for forming a more flexible, ecological, and socially sensitive architectural environment.

At the intersection of inclusive engineering and craft technologies, a promising research direction is emerging that allows the design of food service establishments not only as functional objects but also as centers of social integration, cultural renewal, and spatial justice. These facilities must meet criteria of environmental sustainability, technological adaptability, economic feasibility, and regulatory safety, taking into account quality standards and HACCP principles.

In this context, the aim of the research is the integration of inclusive engineering principles and craft technologies into the design process of food service establishments with an emphasis on the selection of building materials, architectural solutions, and spatial organization in the context of Ukraine's post-war reconstruction. Special attention is paid to safety, quality, social sensitivity, environmental responsibility, and cultural appropriateness.

Research objectives:

— to analyze current challenges and trends in the field of inclusive engineering, particularly considering the needs of persons with disabilities, veterans, and internally displaced persons;

— to investigate the potential of craft technologies for implementing circular economy principles and preserving local identity in construction;

— to develop methodological approaches for combining inclusive engineering and craft practices in the production of building materials and the implementation of architectural solutions involving local resources;

– to assess the impact of the proposed approach on the level of social integration, environmental sustainability, and economic efficiency within food service projects;

– to formulate recommendations for adapting regulatory frameworks and educational programs to disseminate principles of inclusive and craft approaches in architectural design and construction practice.

2.2 MATERIALS AND METHODS

2.2.1 MATERIALS

The study analyzed building materials that comply with the principles of the circular economy, inclusive engineering, and craft technologies, taking into account the requirements of DSTU 9191:2022 [29]. Building products were characterized by origin (organic and inorganic) and type (concretes, arbolites, fibrous, bituminous, etc.), as well as suitability for designing food service establishments in the context of Ukraine's post-war reconstruction. The thermophysical properties of the building materials were evaluated:

– density (ρ_0) – from 35 to 1000 kg/m^3;

– specific heat capacity (C) – from 0.84 to 2.3 kJ/(kg·K);

– declared thermal conductivity (λ_0) – from 0.039 to 0.16 W/(m·K);

– calculated moisture content by mass (w), for operating condition A – from 0.1 to 16%; for operating condition B – from 0.2 to 24%;

– calculated thermal conductivity (λ_d) for operating condition A – from 0.045 to 0.24 W/(m·K); for operating condition B – from 0.048 to 0.3 W/(m·K);

– calculated heat absorption coefficient (s) for operating condition A – from 0.41 to 6.75 W/(m^2·K); for operating condition B – from 0.45 to 7.7 W/(m^2·K);

– calculated vapor permeability (δ) for operating conditions A and B – from 0.002 to 0.49 mg/(m·h·Pa).

The selection of materials was based on their environmental friendliness (low carbon footprint, biodegradability), local availability, hygienic compliance (adherence to HACCP principles), as well as suitability for craft production, which promotes community involvement.

2.2.2 METHODS

The research methodology involved a comprehensive approach to assessing materials and architectural solutions for the creation of inclusive, environmentally sustainable, and safe food service establishments. A comparative analysis of the thermophysical characteristics of materials according to DSTU 9191:2022 [29] was applied to determine their effectiveness in energy-efficient structures.

The evaluation criteria included:

1) technological accessibility (ease of production, use of local resources);

2) environmental sustainability (possibility of reuse, low environmental impact);

3) social inclusivity (adaptability to the needs of vulnerable groups, including persons with disabilities and veterans);

4) economic feasibility (optimization of construction costs).

Additionally, the compliance of materials and solutions with safety and hygiene standards (HACCP) was analyzed, as well as their potential to implement local identity through ethno-design. Both quantitative methods (analysis of thermophysical parameters) and qualitative methods (comparison of architectural solutions such as zoning, barrier-free access, non-slip coatings) were used for evaluation.

2.3 RESULTS

2.3.1 PRINCIPLES OF INCLUSIVE ENGINEERING IN THE FIELD OF BUILDING MATERIALS

In the modern competitive environment, craft productions, like food service establishments, face the need to increase business efficiency to maintain their viability and adapt to social changes. Considering factors such as employee health, motivation, inclusivity, and professional skill development becomes not only socially necessary but also economically viable.

Inclusive engineering in the field of building materials involves a systematic integration that combines technical, social, and economic aspects [20] aimed at ensuring a barrier-free environment and improving the quality of working conditions.

Technical aspects of implementing inclusive solutions in food establishments include architectural and planning measures (ramps with a slope of up to 8%, handrails, non-slip coverings, designated parking spaces), engineering and technical solutions (standardized ventilation and air conditioning systems, energy-efficient heating, alternative energy sources), ergonomic equipment (adjustable furniture, lifts), information tools (Braille, sound systems), and specialized premises (accessible lobbies, restrooms, cloakrooms) [20] (**Fig. 2.1**).

Social aspects include rehabilitation practices, staff motivation, ensuring inclusivity, and developing employee competencies, which together form a comprehensive model of sustainable production [20, 30–32].

Rehabilitation — one of the key aspects of the engineering approach to work organization — involves not only adapting work areas for people with disabilities but also creating conditions for the social reintegration of groups such as war veterans [32]. This includes the accessibility of the architectural environment, specialized equipment, compliance with microclimate parameters [14], and staff training to work in an inclusive environment.

Employee motivation in craft productions is closely related to corporate culture, which takes into account the social significance of work, its contribution to the community, and the personal value of the employee. This is implemented through clearly defined goals, training programs, and opportunities for professional growth [33].

Inclusivity as a strategy covers not only physical accessibility but also the creation of cultural diversity. This requires staff training in cultural and gender sensitivity, which is the basis for forming a safe and supportive environment [33]. Employee competence — another key element of the engineering approach — concerns not only technical skills but also the development of communication, organizational, and adaptive abilities necessary for work in the modern production environment [31, 33].

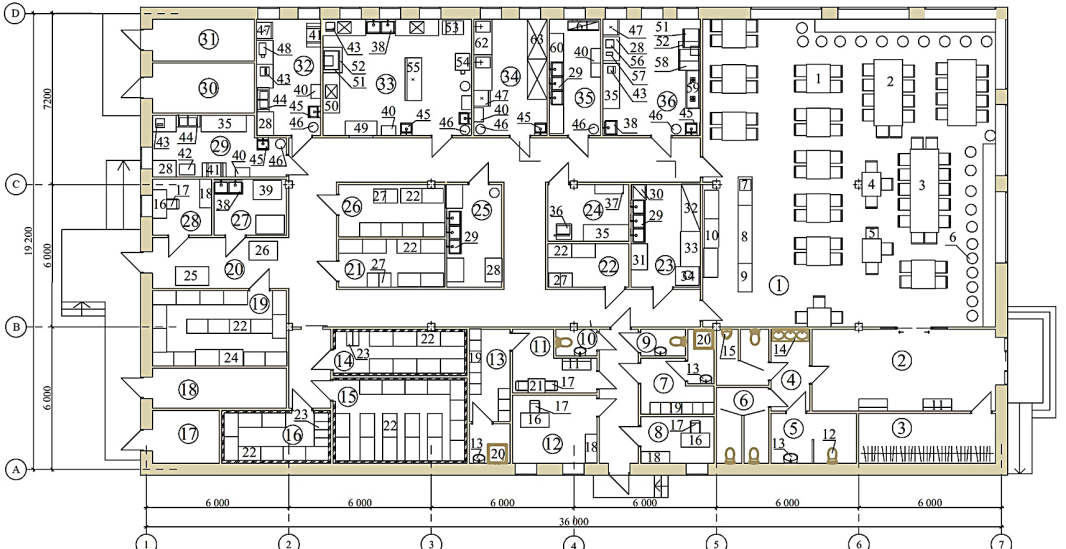

1 – restaurant hall; 2 – vestibule; 3 – cloakroom; 4 – restroom; 5 – restroom for persons with reduced mobility; 6 – guest restrooms; 7 – male staff cloakroom; 8 – office; 9 – male staff restrooms; 10 – female staff restrooms; 11 – staff room; 12 – director's office; 13 – female staff cloakroom; 14 – refrigerated room for meat and fish; 15 – refrigerated room for vegetables, fruits, and greens; 16 – refrigerated room for dairy, gastronomy, and eggs; 17 – exhaust ventilation room; 18 – heat station; 19 – dry goods storeroom; 20 – loading area; 21 – vegetable and root vegetable storeroom; 22 – janitorial inventory and equipment room; 23 – dishwashing area; 24 – bread slicing room; 25 – egg processing room; 26 – dry products storeroom; 27 – ware and inventory washing and storage area; 28 – storekeeper's office; 29 – vegetable processing room; 30 – electrical room; 31 – supply ventilation room; 32 – meat and fish processing room; 33 – pastry room; 34 – cold kitchen; 35 – kitchenware washing area; 36 – hot kitchen

Fig. 2.1 Floor plan at elevation 0.000 of a foodservice enterprise
Source: [20]

Finally, ensuring team stability, reducing staff turnover, and improving brand image require the implementation of long-term strategies that combine social responsibility and economic efficiency [30, 33].

The economic aspects of inclusive solutions in food service establishments involve reducing staff turnover and lowering recruitment and training costs by creating a comfortable working environment. The requirement to provide at least 5% of seats in dining areas for wheelchair users expands the customer base and increases profitability, while the possibility of receiving state support encourages the implementation of accessible solutions [20].

Thus, the principles of inclusive engineering in the field of building materials are not limited to technical aspects but also cover social, psychological, cultural, and economic parameters that form the foundation of a sustainable, safe, and "human-centered" production environment.

2.3.2 PRINCIPLES OF CRAFT TECHNOLOGIES IN THE FIELD OF BUILDING MATERIALS

In the post-war period of Ukraine's reconstruction, there is an increasing interest in the use of local natural building materials — wood, straw, clay, hemp fiber, and others. Importantly, these materials harmoniously combine environmental friendliness, locality, and the possibility of manual production — key characteristics of the craft approach that align with the ideas of the circular economy. Traditional Ukrainian structures, such as adobe and rammed clay blocks, demonstrate high adaptability and durability. Their potential for reuse, recycling, or complete biodegradation makes them ideal for sustainable construction, especially in socially oriented and rehabilitation projects of post-war recovery.

Modern scientific research highlights the relevance of bio-based composites, in particular hempcrete, which is characterized by a low carbon footprint, high thermal insulation, hygroscopicity, and biodegradability [34].

Another promising direction is wood-concrete (arbolite) — lightweight concrete based on wood chips and plant fibers with gypsum binder [35], which provides excellent thermal insulation properties. Local production based on wood waste makes this technology accessible to small communities and enterprises.

Rammed clay and adobe technologies, deeply rooted in Ukrainian architecture, are being revived today as environmentally friendly and affordable construction methods [36]. Modern developments combine traditional methods with innovative solutions, such as the use of straw blocks, "super-adobe" technology, and other natural materials. There are already modern eco-houses in Ukraine made of adobe, confirming the viability of these approaches.

A distinctive feature of using these materials is their craft nature — local raw materials, small production volumes, involvement of local communities, and the possibility of rapid implementation of innovations [35]. This not only supports the development of crafts and the local economy but also aligns with the principles of inclusive engineering. In particular, the simplicity and accessibility of producing clay or arbolite blocks make it possible to involve different social groups in construction, including people with disabilities.

In the context of post-war reconstruction, this integration of craft technologies and the principles of inclusive design is especially relevant for creating food service establishments that should be not only

energy-efficient and environmentally friendly but also maximally accessible. The use of natural materials contributes to a healthy microclimate, reduces the impact of chemicals and temperature fluctuations, which is important for vulnerable population groups.

Fig. 2.2–2.10 present the calculated thermophysical characteristics of building materials — products made from natural organic and inorganic raw materials in accordance with the requirements of DSTU 9191:2022 [29]. The comparative characteristics of the thermal insulation material take into account its density (ρ); heat capacity (C); thermal conductivity (λ); moisture content by mass (w); heat absorption coefficient (s); and vapor permeability (δ) under operating conditions (A, B). According to DBN V.2.6-31:2021 [37], operating conditions A are applied to internal walls and enclosing structures in dry rooms, while B — to external walls and structures operating in normal, humid, or wet environments.

According to thermophysical properties, building products can be classified into three categories:

1) high heat capacity ($C \geq 2.0$ kJ/(kg·K));

2) medium heat capacity ($C \approx 1.0$—2.0 kJ/(kg·K));

3) low heat capacity ($C \leq 1.0$ kJ/(kg·K)).

Products with high heat capacity ($C \geq 2.0$ kJ/(kg·K)):

— reed thermal insulation boards — 2.3 kJ/(kg·K), characterized by high heat capacity, which ensures high heat retention ability. They are used as natural thermal insulation materials in walls, floors, and roofs, especially in environmentally oriented construction. Due to their natural composition, they have good vapor permeability, help regulate indoor humidity, and create comfortable microclimatic conditions. In addition to thermal insulation, these boards provide environmental friendliness and biodegradability, although they may require additional protection against moisture and pests. The use of reed boards is advisable in projects focused on sustainable development and natural materials;

— fiberboard and particleboard — 2.3 kJ/(kg·K), characterized by high heat capacity, suitable for interiors and internal partitions where temperature regulation without sharp fluctuations is needed. These materials have high vapor permeability, which helps maintain optimal humidity levels. Thanks to their natural composition, the boards are environmentally friendly, have good sound insulation properties, but require protection from moisture and pests. Ideal for projects emphasizing a healthy environment and energy efficiency;

— wood concrete (arbolite) products on Portland cement — 2.3 kJ/(kg·K), used for load-bearing and self-supporting walls of low-rise buildings; enclosing structures where a combination of thermal insulation and strength is important; ecological facilities (housing, public buildings, inclusive spaces) — due to natural fillers and vapor permeability; structures where smooth leveling of temperature fluctuations is needed — arbolite accumulates heat during the day and releases it at night. Arbolite works well in external walls, especially in regions with sharp daily temperature fluctuations, and in passive heating systems.

Products with high heat capacity (C ≥ 2.0 kJ/(kg·K)) effectively accumulate and release heat, ensuring a stable microclimate and comfort indoors even under significant daily temperature fluctuations, making them optimal for energy-efficient and environmentally friendly constructions.

Materials with high heat capacity are especially effective in passive heating systems and in regions with a continental climate.

Fig. 2.2 Comparison of the heat capacity of products made from natural organic and inorganic raw materials (C, kJ/(kg•K)) depending on the density of materials (ρ_0, kg/m^3) in the dry state

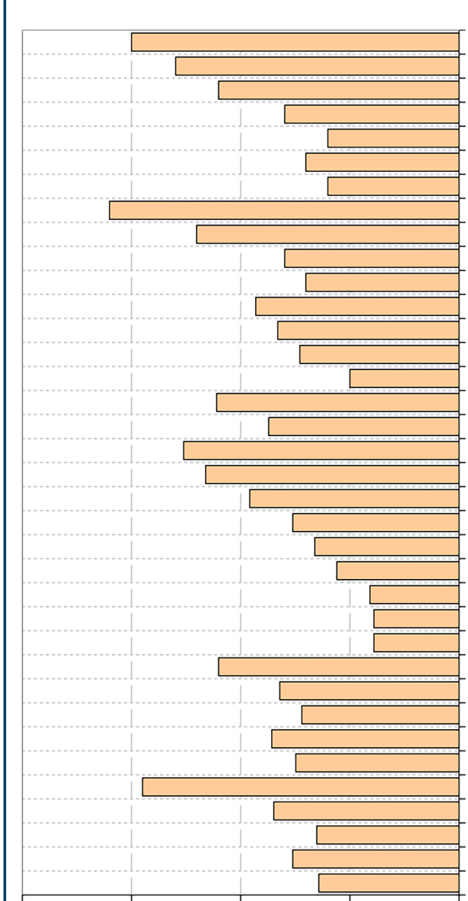

1 – perlite-phosphogel products (200)*; 2 – perlite-phosphogel products (300); 3 – wall polystyrene concrete blocks (200); 4 – wall polystyrene concrete blocks (300); 5 – wall polystyrene concrete blocks (600); 6 – perlite-cement and perlite-gypsum thermal insulation products (300); 7 – perlite-cement and perlite-gypsum thermal insulation products (450); 8 – perlite-bentonite thermal insulation products (250); 9 – perlite-bentonite thermal insulation products (300); 10 – perlite-bentonite thermal insulation products (400); 11 – cellulose insulation (35); 12 – cellulose insulation (50); 13 – cellulose insulation (65); 14 – cellulose insulation (100); 15 – cement-polystyrene products (250); 16 – cement-polystyrene products (300); 17 – cement-polystyrene products (400); 18 – cement-polystyrene products (500); 19 – cement-polystyrene products (550); 20 – perlite-bitumen thermal insulation products (300); 21 – perlite-bitumen thermal insulation products (400); 22 – foam glass products (120); 23 – silicate-cement blocks (300); 24 – silicate-cement blocks (400); 25 – silicate-cement blocks (500); 26 – wood concrete (arbolite) products on Portland cement (300); 27 – wood concrete (arbolite) products on Portland cement (400); 28 – wood concrete (arbolite) products on Portland cement (600); 29 – wood concrete (arbolite) products on Portland cement (800); 30 – reed thermal insulation boards (200); 31 – reed thermal insulation boards (300); 32 – fiberboard and particleboard (200); 33 – fiberboard and particleboard (400); 34 – fiberboard and particleboard (600); 35 – fiberboard and particleboard (800); 36 – fiberboard and particleboard (1000)

**(material density, ρ_0, kg/m^3)*

Fig. 2.3 Comparison of the declared thermal conductivity of products made from natural organic and inorganic raw materials (λ_0, W/(m•K)) depending on the density of materials (ρ_0, kg/m^3) in the dry state

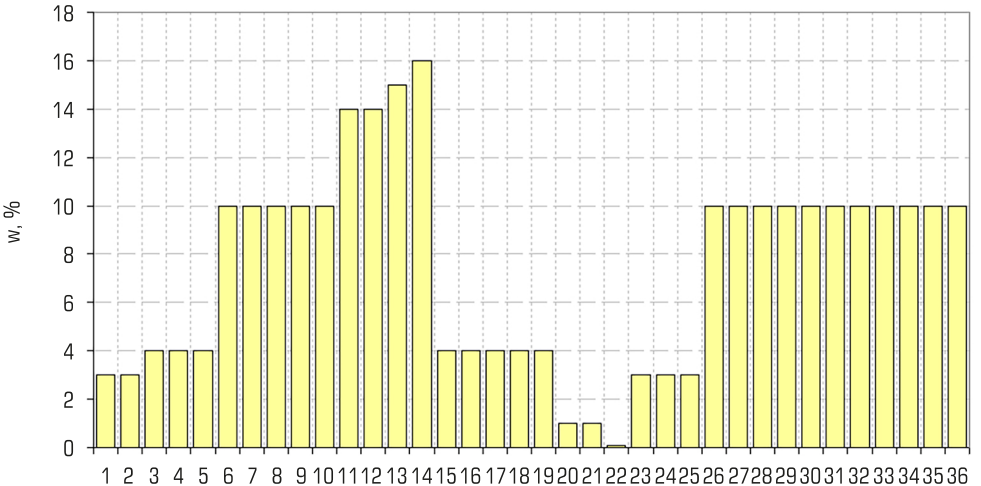

1 – perlite-phosphogel products (200)*; 2 – perlite-phosphogel products (300); 3 – wall polystyrene concrete blocks (200); 4 – wall polystyrene concrete blocks (300); 5 – wall polystyrene concrete blocks (600); 6 – perlite-cement and perlite-gypsum thermal insulation products (300); 7 – perlite-cement and perlite-gypsum thermal insulation products (450); 8 – perlite-bentonite thermal insulation products (250); 9 – perlite-bentonite thermal insulation products (300); 10 – perlite-bentonite thermal insulation products (400); 11 – cellulose insulation (35); 12 – cellulose insulation (50); 13 – cellulose insulation (65); 14 – cellulose insulation (100); 15 – cement-polystyrene products (250); 16 – cement-polystyrene products (300); 17 – cement-polystyrene products (400); 18 – cement-polystyrene products (500); 19 – cement-polystyrene products (550); 20 – perlite-bitumen thermal insulation products (300); 21 – perlite-bitumen thermal insulation products (400); 22 – foam glass products (120); 23 – silicate-cement blocks (300); 24 – silicate-cement blocks (400); 25 – silicate-cement blocks (500); 26 – wood concrete (arbolite) products on Portland cement (300); 27 – wood concrete (arbolite) products on Portland cement (400); 28 – wood concrete (arbolite) products on Portland cement (600); 29 – wood concrete (arbolite) products on Portland cement (800); 30 – reed thermal insulation boards (200); 31 – reed thermal insulation boards (300); 32 – fiberboard and particleboard (200); 33 – fiberboard and particleboard (400); 34 – fiberboard and particleboard (600); 35 – fiberboard and particleboard (800); 36 – fiberboard and particleboard (1000)

**(material density, ρ_0, kg/m^3)*

Fig. 2.4 Comparison of the calculated mass moisture content of products made from natural organic and inorganic raw materials (w, %) under service conditions (A), depending on the density of materials (ρ_0, kg/m^3)

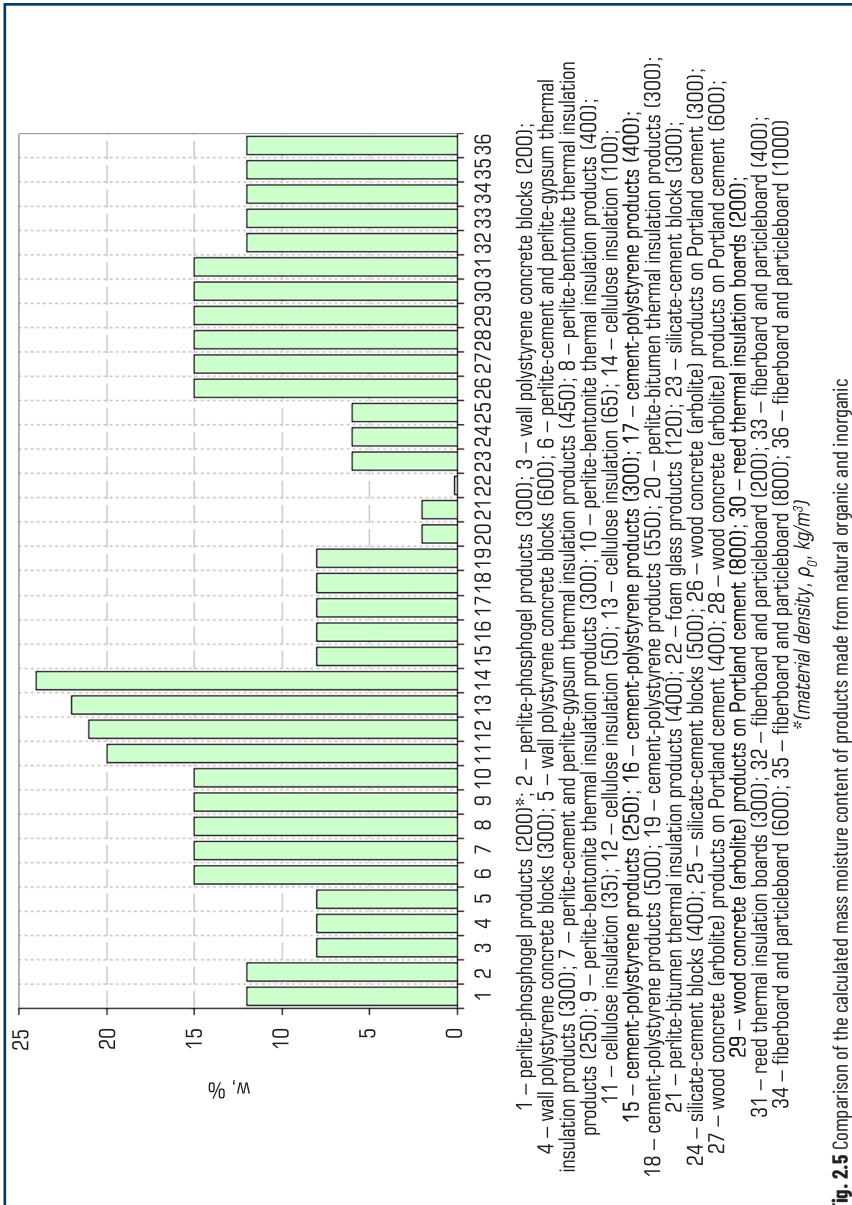

Fig. 2.5 Comparison of the calculated mass moisture content of products made from natural organic and inorganic raw materials (w, %) under service conditions (B), depending on the density of materials (ρ_0, kg/m^3)

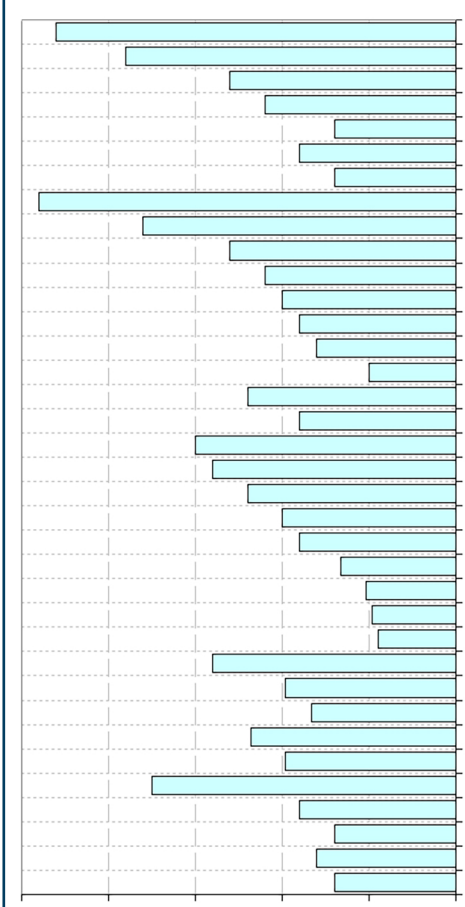

Fig. 2.6 Comparison of the calculated thermal conductivity characteristics of products made from natural organic and inorganic raw materials (λ_d, W/(m•K)) under service conditions (A), depending on the density of materials (ρ_0, kg/m³)

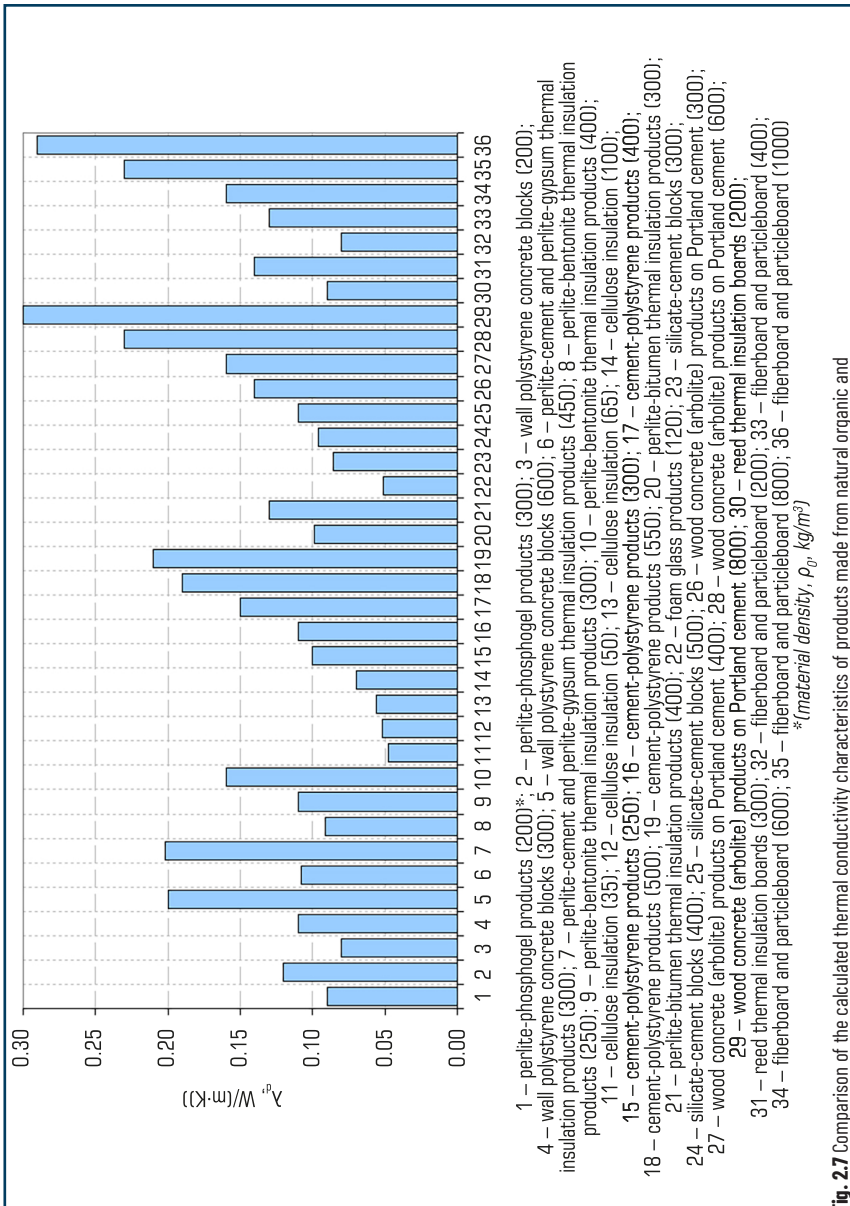

Fig. 2.7 Comparison of the calculated thermal conductivity characteristics of products made from natural organic and inorganic raw materials (λ_d, W/(m•K)) under service conditions (*B*), depending on the density of materials (ρ_0, kg/m^3)

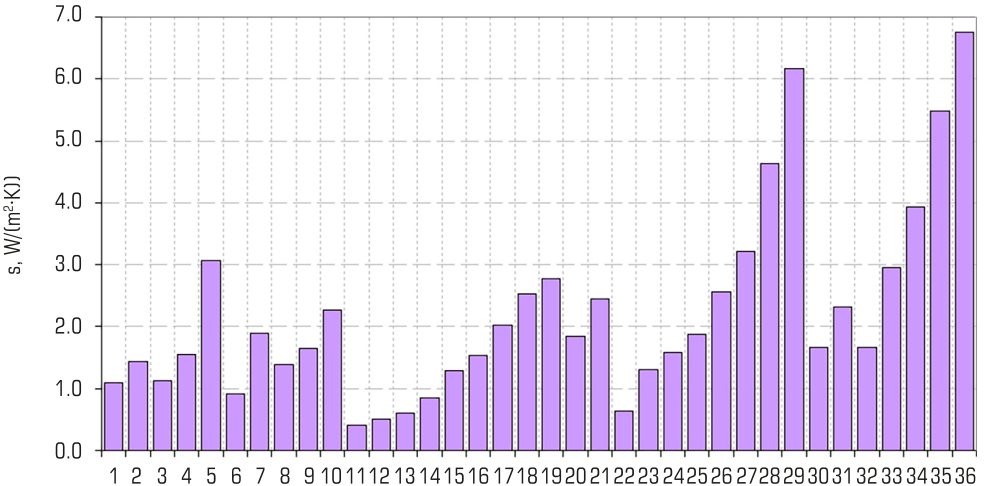

1 – perlite-phosphogel products (200)*; 2 – perlite-phosphogel products (300); 3 – wall polystyrene concrete blocks (200); 4 – wall polystyrene concrete blocks (300); 5 – wall polystyrene concrete blocks (600); 6 – perlite-cement and perlite-gypsum thermal insulation products (300); 7 – perlite-cement and perlite-gypsum thermal insulation products (450); 8 – perlite-bentonite thermal insulation products (250); 9 – perlite-bentonite thermal insulation products (300); 10 – perlite-bentonite thermal insulation products (400); 11 – cellulose insulation (35); 12 – cellulose insulation (50); 13 – cellulose insulation (65); 14 – cellulose insulation (100); 15 – cement-polystyrene products (250); 16 – cement-polystyrene products (300); 17 – cement-polystyrene products (400); 18 – cement-polystyrene products (500); 19 – cement-polystyrene products (550); 20 – perlite-bitumen thermal insulation products (300); 21 – perlite-bitumen thermal insulation products (400); 22 – foam glass products (120); 23 – silicate-cement blocks (300); 24 – silicate-cement blocks (400); 25 – silicate-cement blocks (500); 26 – wood concrete (arbolite) products on Portland cement (300); 27 – wood concrete (arbolite) products on Portland cement (400); 28 – wood concrete (arbolite) products on Portland cement (600); 29 – wood concrete (arbolite) products on Portland cement (800); 30 – reed thermal insulation boards (200); 31 – reed thermal insulation boards (300); 32 – fiberboard and particleboard (200); 33 – fiberboard and particleboard (400); 34 – fiberboard and particleboard (600); 35 – fiberboard and particleboard (800); 36 – fiberboard and particleboard (1000)

**(material density, ρ_0, kg/m³)*

Fig. 2.8 Comparison of the calculated heat absorption coefficient characteristics of products made from natural organic and inorganic raw materials (*s*, W/(m²•K)) under service conditions (*A*), depending on the density of materials (ρ_0, kg/m³)

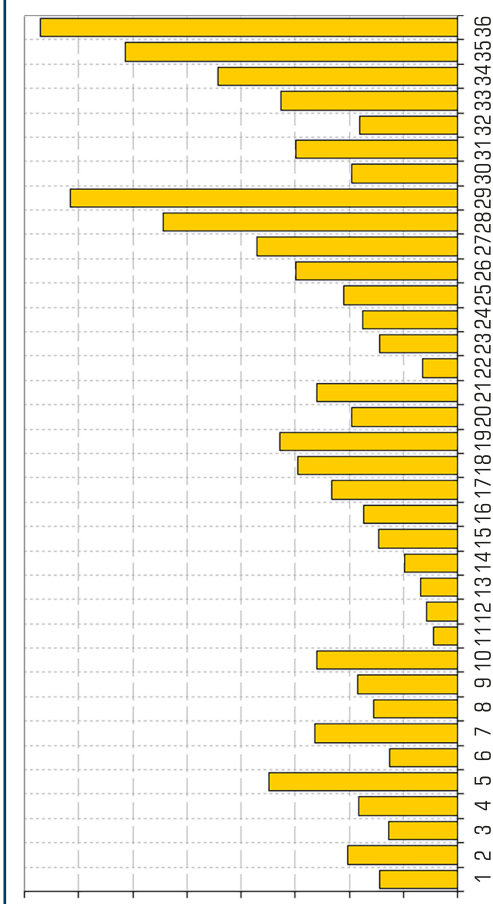

Fig. 2.9 Comparison of the calculated heat absorption coefficient characteristics of products made from natural organic and inorganic raw materials (s, W/(m²·K)) under service conditions (*B*), depending on the density of materials (ρ_0, kg/m³)

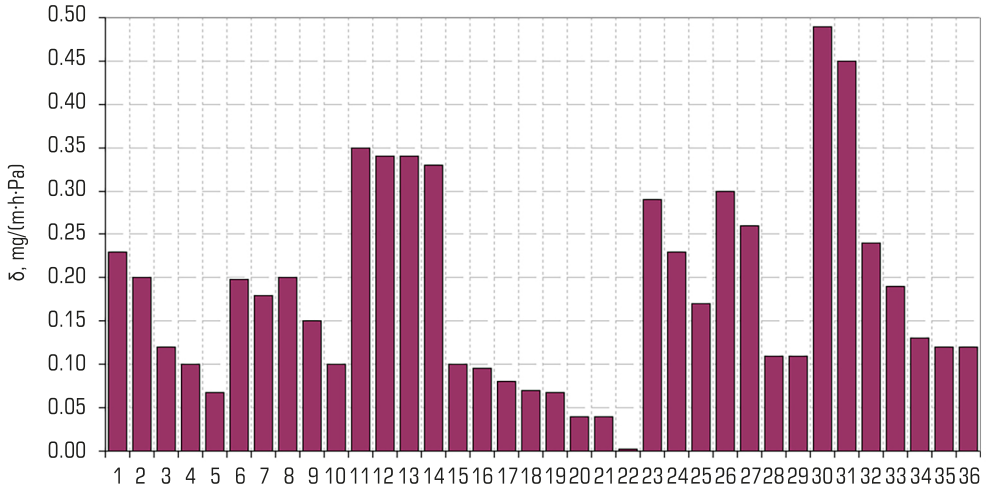

1 – perlite-phosphogel products (200)*; 2 – perlite-phosphogel products (300); 3 – wall polystyrene concrete blocks (200); 4 – wall polystyrene concrete blocks (300); 5 – wall polystyrene concrete blocks (600); 6 – perlite-cement and perlite-gypsum thermal insulation products (300); 7 – perlite-cement and perlite-gypsum thermal insulation products (450); 8 – perlite-bentonite thermal insulation products (250); 9 – perlite-bentonite thermal insulation products (300); 10 – perlite-bentonite thermal insulation products (400); 11 – cellulose insulation (35); 12 – cellulose insulation (50); 13 – cellulose insulation (65); 14 – cellulose insulation (100); 15 – cement-polystyrene products (250); 16 – cement-polystyrene products (300); 17 – cement-polystyrene products (400); 18 – cement-polystyrene products (500); 19 – cement-polystyrene products (550); 20 – perlite-bitumen thermal insulation products (300); 21 – perlite-bitumen thermal insulation products (400); 22 – foam glass products (120); 23 – silicate-cement blocks (300); 24 – silicate-cement blocks (400); 25 – silicate-cement blocks (500); 26 – wood concrete (arbolite) products on Portland cement (300); 27 – wood concrete (arbolite) products on Portland cement (400); 28 – wood concrete (arbolite) products on Portland cement (600); 29 – wood concrete (arbolite) products on Portland cement (800); 30 – reed thermal insulation boards (200); 31 – reed thermal insulation boards (300); 32 – fiberboard and particleboard (200); 33 – fiberboard and particleboard (400); 34 – fiberboard and particleboard (600); 35 – fiberboard and particleboard (800); 36 – fiberboard and particleboard (1000)

**(material density, ρ_0, kg/m^3)*

Fig. 2.10 Comparison of the calculated vapor permeability characteristics of products made from natural organic and inorganic raw materials (δ, mg/(m•h•Pa)) under service conditions (*A*, *B*), depending on the density of materials (ρ_0, kg/m^3)

Products with medium heat capacity ($C \approx 1.0–2.0$ kJ/(kg·K)):

— perlite-bitumen insulation products — 1.68 kJ/(kg·K), characterized by medium thermal inertia. They are used as lightweight insulation layers in roofs, floors, and walls; in constructions where minimal weight with sufficient insulation is required; in systems that do not demand significant heat accumulation, such as for rapid heating and cooling of rooms; and in combination with more massive materials to balance insulation and inertia. They are moisture-resistant and biologically durable, but due to bitumen content, they are less eco-friendly and vapor-impermeable, which limits their use in inclusive spaces with higher microclimate demands;

— polystyrene concrete wall blocks — 1.06 kJ/(kg·K), have moderate heat accumulation ability. Thanks to this combined with low density and thermal conductivity, they effectively reduce heat loss but respond quickly to temperature changes. Such blocks are applied in quick-assembly and lightweight wall constructions, especially in post-war recovery conditions, combined with materials of higher thermal inertia to ensure stable indoor microclimate;

— perlite-phosphogel products — 1.05 kJ/(kg·K), possess moderate heat storage capacity. This, combined with low density and thermal conductivity, makes them effective insulation materials that significantly reduce heat loss in enclosing structures. They are typically used for insulating walls, roofs, and floors, particularly in buildings where structural lightness and good energy-saving properties are important.

Products with medium heat capacity ($C \approx 1.0–2.0$ kJ/(kg·K)) provide a balance between insulation properties and rapid response to temperature changes, making them suitable for lightweight and fast-assembly constructions, but requiring combination with more massive layers for stable microclimate.

Products with low heat capacity ($C \leq 1.0$ kJ/(kg·K)):

— perlite-cement and perlite-gypsum insulation products (0.84 kJ/(kg·K)) — have low heat capacity, indicating a limited ability to accumulate heat. They are used as effective lightweight thermal insulation materials in walls, floors, and roofs of buildings. They combine well with other more massive structural elements, reducing heat loss. They are characterized by vapor permeability, which contributes to humidity regulation and maintaining microclimatic conditions indoors. They are more environmentally friendly due to their natural components;

— perlite-bentonite thermal insulation products (0.84 kJ/(kg·K)) — characterized by low heat capacity and increased strength due to the inclusion of bentonite. They are used as lightweight thermal insulation layers in wall and roof structures where thermal insulation and shape stability are important. They provide adequate vapor permeability and moisture resistance. They contribute to creating a comfortable microclimate by regulating humidity;

— cellulose insulation (0.84 kJ/(kg·K)) — an eco-friendly insulation material made from recycled cellulose with low heat capacity, providing minimal heat accumulation and rapid temperature changes. They are widely used for insulating walls, roofs, and floors. They have high vapor permeability and "breathability", making it optimal for inclusive and ecological projects and requires additional treatment for moisture and pest protection;

— cement-polystyrene products (0.84 kJ/(kg·K)) — lightweight thermal insulation materials combining the insulating properties of expanded polystyrene with the strength of cement binder. Low heat capacity causes rapid temperature changes in the material, suitable for constructions with minimal thermal inertia.

They are used in external walls, floors, and facades. They have relatively low vapor permeability, which may require additional measures to maintain microclimate;

— foam glass products (0.84 kJ/(kg·K)) — thermal insulation materials based on foamed glass with low heat capacity, providing lightness and low thermal inertia. They are used in roofs, foundation insulation, and external walls and characterized by high moisture resistance and chemical inertness, making them durable. Relatively high cost and brittleness limit their widespread use;

— silica-cement blocks (0.84 kJ/(kg·K)) — building materials with reduced heat capacity, providing low thermal inertia. They are used in load-bearing and self-supporting wall structures with additional insulation. They maintain shape well and resist moisture exposure. Vapor permeability is moderate, allowing use in various climatic conditions.

Materials with heat capacity ≤ 1.0 kJ/(kg·K) are typically characterized by low thermal storage capacity, making them effective lightweight thermal insulators for rapid temperature regulation of indoor spaces. They are widely used in external enclosing structures, roofs, and floors, providing reduction of heat losses. At the same time, they vary in vapor permeability, strength, and environmental properties, which influences the choice of material depending on the specific project requirements, especially in the context of inclusive and sustainable construction.

Craft technologies allow the production of materials from natural, local components, ensuring not only ecological compatibility but also optimal thermophysical properties. Materials with high heat capacity, produced using craft methods, are used in heavy external structures for heat accumulation and stabilization of indoor microclimate. Medium heat capacity products serve as intermediate layers where a balance between heat storage and rapid heat release is required, contributing to a comfortable temperature regime. Lightweight materials with low heat capacity, made from natural components by craft technologies, are used in internal insulation layers for quick response to temperature changes, providing dynamic thermal regulation.

Thus, the integration of craft production principles with consideration of materials' heat capacity enables the creation of adaptive, ecological, and energy-efficient building structures that meet the requirements of inclusivity and sustainable development in the post-war reconstruction of Ukraine.

The lowest declared thermal conductivity values (λ_0) are observed for: cellulose insulation (ρ_0 35–100 kg/m^3) – λ_0 = 0.039–0.056 W/(m·K); foam glass products (ρ_0 120 kg/m^3) – λ_0 = 0.05 W/(m·K); reed insulation boards (ρ_0 200 kg/m^3) and wood fiber and wood chip boards (ρ_0 200 kg/m^3) – λ_0 = 0.060 W/(m·K). These materials best retain heat, making them effective thermal insulators at relatively small thicknesses.

The highest vapor permeability is found in reed insulation boards (ρ_0 200 kg/m^3) – δ = 0.49 mg/(m·h·Pa). In contrast, foam glass products (ρ_0 120 kg/m^3) have extremely low vapor permeability (δ = 0.002 mg/(m·h·Pa)), acting as a vapor barrier. Materials with a low heat absorption coefficient, such as cellulose insulation (ρ_0 35–100 kg/m^3) – s = 0.41–0.97 W/(m^2·K) – are suitable for interior partitions. A high heat absorption coefficient is characteristic of wood fiber and wood chip boards (ρ_0 1000 kg/m^3) – s = 7.7 W/(m^2·K) (under service condition B) – used for external or massive structures.

Craft thermal insulation materials based on arbolite, reed, cellulose, and wood are suitable for ecological construction and have: low thermal conductivity, good vapor permeability, moderate density, and comply with sustainable building principles:

— provide natural thermoregulation, reducing the need for heating and air conditioning;

— possess hygienic properties if properly treated (vacuum impregnation, natural antiseptics based on essential oils);

— have a low carbon footprint and promote biodegradation after the end of their life cycle;

— allow significant construction cost reduction due to local availability and ease of use.

The Ukrainian experience closely aligns with international trends in sustainable construction and is widely applied in Europe and North America in accordance with ecological standards and other decarbonization programs [34]. Although Ukrainian developments are still at early stages of commercialization, they have high potential and can significantly influence the formation of a new building culture that combines ecology, social justice, and local identity.

2.3.3 COMPREHENSIVE ASSESSMENT OF BUILDING MATERIALS QUALITY

The comprehensive assessment of building materials quality (K_0, points) was determined according to four key criteria (**Table 2.1**):

— thermal protection — based on the calculated thermal conductivity of materials λ_d (W/m·K);

— inclusiveness — evaluated through the vapor permeability of materials δ (mg/m·h·Pa);

— environmental performance — assessed by the natural origin, biodegradability, and chemical safety of materials;

— local availability — defined by the possibility of producing the material locally without the need for import.

Thermal protection of materials was assessed using a five-point scale according to the following values of thermal conductivity λ_d (W/m·K):

5 points — λ_d < 0.08, very good (excellent) thermal protection;

4 points — λ_d 0.08—0.15, good thermal protection;

3 points — λ_d 0.15—0.20, moderate thermal protection;

2 points — λ_d 0.20—0.25, poor thermal protection;

1 point — λ_d > 0.25, very poor thermal protection.

Thermal protection of materials makes it possible to evaluate their ability to retain heat and reduce energy consumption for building heating.

Inclusiveness of materials was assessed using a five-point scale according to the following values of vapor permeability δ (mg/m·h·Pa):

5 points — $\delta \geq 0.20$, very good (excellent) inclusiveness;

4 points — δ 0.15—0.20, good inclusiveness;

3 points — δ 0.10—0.15, moderate inclusiveness;

2 points — δ 0.05—0.10, poor inclusiveness;

1 point — $\delta < 0.05$, very poor inclusiveness.

The inclusiveness of materials directly influences indoor comfort and safety by regulating the microclimate and preventing condensation.

Table 2.1 Comprehensive assessment of the quality of building materials based on the criteria of thermal protection, inclusivity, environmental sustainability, and local availability

No.	Material name	Thermal protection, points	Inclusivity, points	Environmental sustainability, points	Local availability, points	Comprehensive quality assessment of building materials, points	Comprehensive ranking
1	2	3	4	5	6	7	8
1	Perlite — phosphogel products (200)	5	5	3	3	4.00	12
2	Perlite — phosphogel products (300)	4	4	3	3	3.50	18
3	Polystyrene concrete wall blocks (200)	5	3	2	2	3.00	25
4	Polystyrene concrete wall blocks (300)	4	3	2	2	2.75	27
5	Polystyrene concrete wall blocks (600)	3	2	2	2	2.25	36
6	Perlite — cement and perlite — gypsum thermal insulation products (300)	4	4	3	3	3.50	19
7	Perlite — cement and perlite — gypsum thermal insulation products (450)	4	4	3	3	3.50	20
8	Perlite — bentonite thermal insulation products (250)	4	4	3	3	3.50	21
9	Perlite — bentonite thermal insulation products (300)	4	3	3	3	3.25	24
10	Perlite-bentonite thermal insulation products (400)	4	2	3	3	3.00	26
11	Cellulose insulation (35)	5	5	5	5	5.00	1
12	Cellulose insulation (50)	5	5	5	5	5.00	2
13	Cellulose insulation (65)	5	5	5	5	5.00	3
14	Cellulose insulation (100)	5	5	5	5	5.00	4
15	Cement — polystyrene products (250)	4	2	2	2	2.50	32
16	Cement — polystyrene products (300)	4	3	2	2	2.75	28
17	Cement — polystyrene products (400)	4	2	2	2	2.50	33
18	Cement — polystyrene products (500)	4	2	2	2	2.50	34
19	Cement — polystyrene products (550)	4	2	2	2	2.50	35
20	Perlite — bitumen thermal insulation products (300)	4	1	3	3	2.75	29
21	Perlite — bitumen thermal insulation products (400)	4	1	3	3	2.75	30

Continuation of Table 1

1	2	3	4	5	6	7	8
22	Foam glass products (120)	5	1	3	2	2.75	31
23	Silicate — cement blocks (300)	4	5	3	3	3.75	14
24	Silicate — cement blocks (400)	4	5	3	3	3.75	15
25	Silicate — cement blocks (500)	4	4	3	3	3.50	22
26	Wood concrete (arbolite) products on Portland cement (300)	4	5	4	5	4.50	8
27	Wood concrete (arbolite) products on Portland cement (400)	4	5	4	5	4.50	9
28	Wood concrete (arbolite) products on Portland cement (600)	3	3	4	5	3.75	16
29	Wood concrete (arbolite) products on Portland cement (800)	2	3	4	5	3.50	23
30	Reed thermal insulation boards (200)	5	5	5	5	5.00	5
31	Reed thermal insulation boards (300)	4	5	5	5	4.75	7
32	Wood fiber and particle boards (200)	5	5	5	5	5.00	6
33	Wood fiber and particle boards (400)	4	4	5	5	4.50	10
34	Wood fiber and particle boards (600)	4	3	5	5	4.25	11
35	Wood fiber and particle boards (800)	3	3	5	5	4.00	13
36	Wood fiber and particle boards (1000)	2	3	5	5	3.75	17

Environmental friendliness of materials was assessed using a five-point scale according to the following criteria:

5 points — natural, biodegradable materials (wood, reed, cellulose);

4 points — natural materials with cement additives or minimally processed (arbolite);

3 points — mineral, conditionally ecological materials (perlite, mineral boards, foam glass);

2 points — synthetic materials with limited recyclability (polystyrene concrete, cement — polystyrene composites);

1 point — chemically treated materials.

Local availability of materials was assessed using a five-point scale according to the following criteria:

5 points — easily manufactured in a craft-based manner from local raw materials;

4 points — local raw materials but requiring factory production;

3 points — requiring industrial-scale production;

2 points — demanding specialized industry;

1 point — imported materials.

For each material, the arithmetic mean score across all four criteria was calculated, providing a comprehensive rating of the material's suitability for use in inclusive and energy-efficient building structures.

The summarized results of the comprehensive material quality assessment (**Fig. 2.11**) demonstrated that the highest scores across all criteria were achieved by cellulose insulation, reed-based thermal insulation boards, and wood-fiber materials. Their overall scores (5.00 and 4.75—5.00) indicate excellent thermal insulation properties, high environmental friendliness and inclusivity, as well as the availability of local raw materials. Such materials exemplify a balanced approach to creating modern building structures that not only reduce energy consumption but also contribute to the formation of barrier-free environments through ecological safety and adaptability to the needs of diverse users. The high ranking of arbolite products based on Portland cement further confirms the potential of combining traditional and natural components to ensure comprehensive sustainability.

At the same time, a number of materials, such as high-density polystyrene concrete blocks, cement-polystyrene products, and foam glass, received significantly lower scores (2.25—2.75). This indicates limited inclusivity and environmental friendliness, despite satisfactory thermal insulation properties.

Perlite-bitumen and perlite-bentonite materials demonstrated average results, highlighting the need for further modernization and adaptation to contemporary requirements. Thus, the analysis confirmed that priority in designing inclusive and sustainable environments should be given to materials derived from natural and renewable resources, whereas traditional synthetic or high-tech solutions require additional improvements to meet the criteria of accessibility and ecological safety.

2.3.4 INCLUSIVE ENGINEERING AND ACCESSIBILITY ARCHITECTURE IN FOOD SERVICE SPACES

Creating accessible, safe, and inclusive environments in food service establishments must consider the diverse needs of consumers, including people with disabilities, veterans, elderly individuals, parents with young children, as well as those with sensory or cognitive differences.

Principles of inclusive engineering involve designing spaces that do not require users to adapt but rather adapt to diverse functional needs. Key solutions include:

— barrier-free access to the building: ramps with non-slip surfaces, automatic doors, sufficiently wide entrances and corridors;

— navigational orientation within the interior: use of tactile, visual, and auditory landmarks, contrasting zone markings;

— ergonomic functional zones: height-adjustable tables, adapted restrooms, accessible bar counters and reception areas;

— reduction of sensory overload: subdued lighting, natural colors, low-contrast textures, sound insulation, softened acoustic background — essential for people with post-traumatic stress disorder or hypersensitivity.

An important component of inclusive spaces is architectural zoning: avoiding "blind spots", clearly

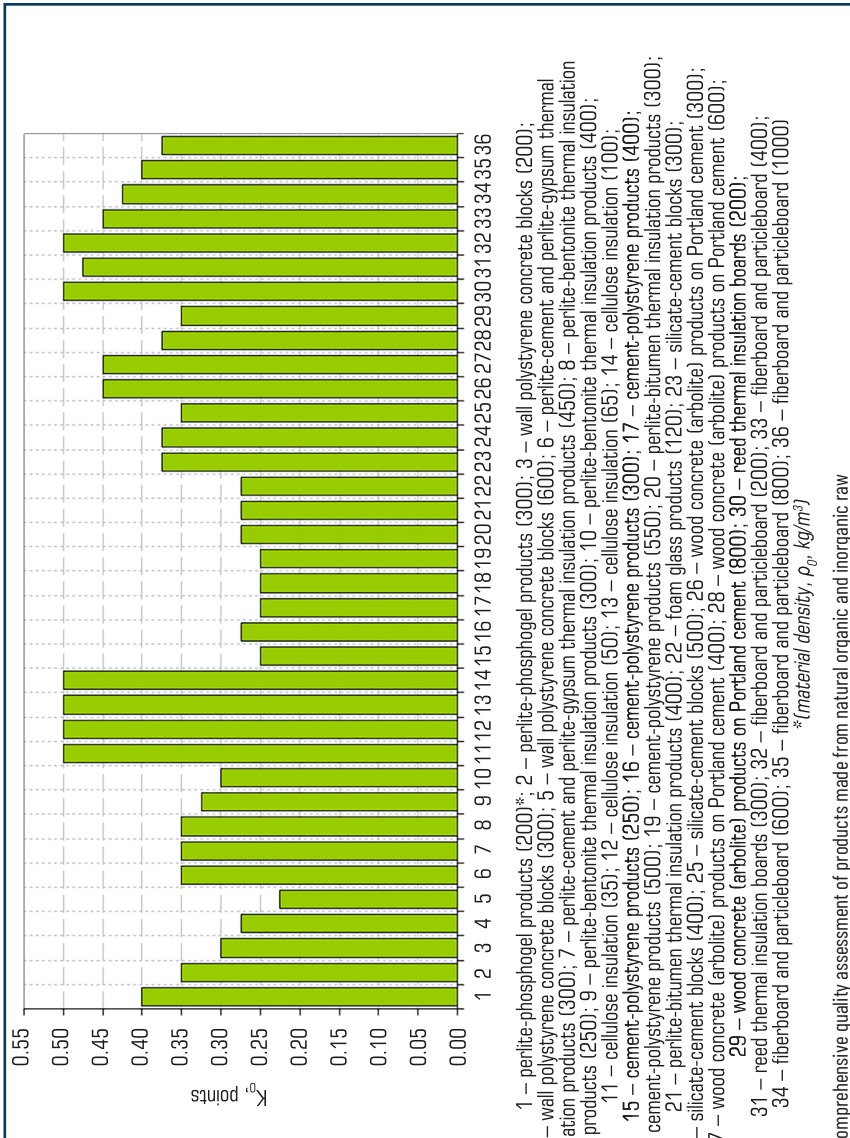

Fig. 2.11 Comprehensive quality assessment of products made from natural organic and inorganic raw materials ($K_{0'}$ points) under operating conditions (A, B) depending on material density ($\rho_{0'}$ kg/m^3)

separating staff and visitor flows, and providing quiet areas that allow for emotional comfort restoration.

Inclusivity must be integrated at all stages of design — from urban planning to interior design.

The interior can serve not only decorative but also navigational functions. Natural finishing materials — wood, textiles, ceramics — can include tactile markers or be visually contrasting to facilitate navigation. For example, embossed wooden panels or patterned clay tiles serve not only as aesthetic but also functional accessibility elements. This also emphasizes the establishment's local identity, combining inclusivity with cultural heritage.

Restrooms, kitchens, and other technical rooms must be hygienically safe and adapted to the needs of all staff and visitors. Surfaces should be non-slip, antibacterial, fire-resistant, and easy to clean. The use of non-toxic paints, varnishes, and sealants ensures compliance with food safety standards and HACCP requirements.

The inclusive approach to designing food service establishments fulfills not only a technical role but also a social integrative function. Facilities that consider the needs of people with limited mobility become spaces for rehabilitation, autonomy, and social interaction. This is especially relevant for veterans, individuals with musculoskeletal disorders, sensory impairments, or psycho-emotional traumas.

Craft technologies are gaining particular importance as a tool for integrating local knowledge, resources, and cultural practices. In the sphere of public catering establishments, they perform a dual function: on one hand — an aesthetic and identificational role (through reflecting regional style), and on the other — an ecological and functional role (thanks to the use of natural materials with a low environmental footprint).

Craft approaches allow architectural and construction solutions to be adapted to the local climate, cultural context, and the needs of specific communities. Such technologies contribute to reducing energy consumption, supporting local production, and restoring the authentic character of the environment.

Craft technologies fit within the logic of the circular economy, where key roles are played by resource renewability, material durability, and closed-loop models. Building materials produced by craft methods possess high reparability and the ability to be reused or recycled with minimal environmental impact.

The use of materials based on arbolite, reed, cellulose, and wood ensures natural regulation of humidity and temperature indoors, which is critically important in food service spaces. These solutions also promote energy saving by reducing the need for technical climate control systems. Wood, handmade clay tiles, reed panels, or textiles made of natural fibers not only serve decorative purposes but also emphasize the ethnocultural uniqueness of the region.

The practice of restoring facades and interiors of cafes and restaurants using natural materials is actively developing in Ukraine. In particular, the use of locally sourced wood species, clay (saman), and straw insulation demonstrates a successful synergy of traditions and modern engineering solutions. These approaches not only reduce construction costs but also support local employment and create opportunities for social entrepreneurship based on artisanal work.

Thus, craft technologies in the architecture of food service establishments act as a tool for socio-ecological transformation, combining sustainability, authenticity, functionality, and community involvement in the restoration process.

2.3.5 QUALITY AND SAFETY: SPATIAL AND TECHNOLOGICAL SOLUTIONS

Ensuring quality and safety are fundamental requirements for the operation of public catering establishments, especially in the context of post-war reconstruction. Increased sanitary and hygienic risks [7, 8, 14], resource shortages, and the need for rapid adaptation of the built environment demand a comprehensive approach to designing engineering and architectural solutions. In this context, the integration of HACCP principles [7, 8, 38–40], quality management systems [6, 7, 15], and inclusive engineering [9–12] forms the foundation for creating a reliable, safe, and sustainable food environment.

The quality of a facility's physical environment is determined not only by comfort and aesthetics but primarily by the conformity of functional zoning and technological processes to safety standards. The main criteria for spatial quality include:

— rational functional zoning, involving clear separation of "clean" and "dirty" zones, sequential arrangement of technological process stages: raw material reception, storage, preparation, thermal processing, serving of finished products, dishwashing, etc.;

— adherence to HACCP principles, particularly avoiding cross-flow of raw materials, finished products, waste, and personnel, reducing the risk of microbiological contamination;

— microclimate control — temperature, humidity, ventilation, and lighting levels according to hygienic norms and food safety standards;

— use of hygienic finishing materials — moisture-resistant, heat-resistant, non-toxic, smooth-textured, easy to clean and disinfect.

Thus, a quality environment in a food service facility is shaped at the intersection of spatial logic, engineering design, and sanitary-hygienic control standards.

Within an inclusive approach, it is important to adapt the food space not only to technological requirements but also to the needs of vulnerable users — persons with disabilities, veterans, elderly people, and workers with limited mobility.

Engineering adaptation not only reduces risks of injury and overload but also creates a space of social support that promotes rehabilitation and employment of vulnerable groups.

In the context of safety regarding building structures and finishes, the choice of materials plays a crucial role, directly affecting hygiene and sanitary safety of premises. Key requirements for materials include:

— biological safety — resistance to mold formation, fungi, and parasite colonization;

— chemical neutrality — absence of volatile toxic substances, formaldehydes, phthalates, hazardous dyes, and sealants;

— heat and moisture resistance — the ability to maintain physico-chemical properties under exposure to high temperatures and moisture, especially critical for kitchens and sanitary facilities;

— compliance with food safety standards set forth in normative legal documents and other industry regulations.

The use of tested, environmentally safe, and certified materials is a prerequisite for forming a sustainable, safe environment that meets HACCP requirements and quality management system principles.

CONCLUSIONS

The conducted analysis demonstrates that post-war reconstruction in Ukraine requires the creation of accessible environments for persons with disabilities, veterans, and internally displaced persons. Inclusive engineering involves adapting public catering spaces through barrier-free access (ramps, wide aisles), ergonomic furniture, contrast lighting, and reducing sensory overload for individuals with post-traumatic stress disorder or sensory impairments. These solutions promote social integration and rehabilitation of vulnerable groups.

Craft technologies based on local materials are effective tools for implementing circular economy principles. They ensure resource reuse, reduce carbon footprint, and support local communities. The use of traditional materials (such as adobe and reed panels) emphasizes local identity, fostering the creation of authentic spaces with ethnodesign elements.

A proposed integration methodology includes the use of eco-friendly materials with high heat capacity (e.g., arbolite, reed panels) for stable microclimate and low thermal conductivity materials (cellulose insulation, foam glass) for thermal insulation. Architectural solutions involve zoning, hygienic coatings, and adaptive elements that comply with HACCP standards and meet the needs of vulnerable groups.

The combination of inclusive engineering and craft technologies enhances social integration through accessible spaces, ecological sustainability by reducing resource consumption, and economic efficiency through local production. This creates a comfortable and safe environment that supports rehabilitation and social cohesion.

To promote the principles of inclusive and craft approaches, it is necessary to consider accessibility and environmental requirements and develop new academic disciplines within bachelor's, master's, and PhD educational programs that address circular economy, craft technologies, and inclusive design.

These conclusions confirm that integrating inclusive engineering and craft technologies shapes sustainable, safe, and culturally significant spaces in public catering establishments, contributing to Ukraine's recovery.

CONFLICT OF INTEREST

There is no conflict of interest. The authors declare that they have no financial, academic, personal or other conflicts of interest that could influence the content, results or interpretation of this study.

USE OF ARTIFICIAL INTELLIGENCE

The authors of this study state that AI tools were not used as a replacement for critical thinking, expertise, and human evaluation.

During the preparation of this work, the authors used Chat GPT (Chat GPT 5.1) for purely mechanical work, editorial assistance: stylistic improvement, grammar, spelling, and translation of sources/references.

The authors carried out a full check of all materials obtained with the participation of AI by: comparing each fragment with primary sources and current scientific literature; manually clarifying terms, definitions, and content in accordance with the research methodology; verifying statistical data, facts, international examples, and regulatory references; ensuring compliance with academic standards, research logic, and the requirements of the target publication. The use of AI tools did not affect the scientific results, empirical conclusions, statistical models, and research position of the authors. All key findings, conceptual models, methodological positions and recommendations of the study are formulated solely by the authors and reflect their own scientific position. After using this tool/service, the authors reviewed and edited the content of the work and bear full responsibility for the content of the published article.

REFERENCES

1. Korzh, N., Onyshchuk, N. (2023). Balanced development of the food industry in the post-war period: assessment, trends, management. Ukrainian Journal of Food Science, 11 (1), 16–28. https://doi.org/10.24263/2310-1008-2023-11-1-5
2. Ivanova, H. P., Olishevska, V. Ye., Hapieiev, S. M., Olishevska, S. O. (2024). Construction Industry in Ukraine: Transformations and Prospects in the Context of Martial Law and Postwar Reconstruction. Science and Transport Progress, 4 (108), 80–88. https://doi.org/10.15802/stp2024/317405
3. Kucher, A., Kucher, L., Rudenko, D., Synytsia, O. (2024). Development of "green" building in the context of "green" post-war recovery. Journal of Innovations and Sustainability, 8 (2), 10. https://doi.org/10.51599/is.2024.08.02.10
4. Bielohrad, A. (2024). Assessment of the opportunities of demolition waste using as a building material of the future in Ukraine. Technology Audit and Production Reserves, 3 (3 (77)), 25–29. https://doi.org/10.15587/2706-5448.2024.307317
5. Kuzmin, O., Levkun, K., Riznyk, A. (2017). Qualimetric assessment of diets. Ukrainian Food Journal, 6 (1), 46–60. https://doi.org/10.24263/2304-974x-2017-6-1-7
6. Koretska, I., Kuzmin, O., Poliovyk, V., Deinychenko, L., Berezova, G., Stukalska, N. (2021). Quality rating of desserts based on fruit and berry raw materials. Ukrainian Journal of Food Science, 9 (1), 71–87. https://doi.org/10.24263/2310-1008-2021-9-1-8
7. Pylypenko, I., Pylypenko, L., Yamborko, A., Danylova, O. (2017). Methodology for accelerated monitoring and assurance of sanitary quality and food safety. Ukrainian Food Journal, 6 (2), 211–225. https://doi.org/10.24263/2304-974x-2017-6-2-4
8. Brovenko, T., Bal-Prylypko, L., Tolok, G., Beiko, L. (2025). Methods of microbiological analysis: Monitoring and ensuring food safety. Animal Science and Food Technology, 16 (1), 74–91. https://doi.org/10.31548/animal.1.2025.74
9. Yaroshenko, O. M., Anisimova, H. V., Koliesnik, T. V., Kaplina, H. A., Babych, N. O. (2022). National Strategy for a Barrier-Free Environment: Problems, tolerance and implementation. International Social Work, 67 (1), 226–241. https://doi.org/10.1177/00208728221126002

10. Badyal, P., Moffat, T. (2025). Considerations for diverse, equitable, and inclusive school food programs in the USA and Canada. Health Promotion International, 40 (2). https://doi.org/10.1093/heapro/daaf015
11. Pasenidou, F. (2024). A co-designed by students "architecture of schooling" framework: Informing a novel architecture lens within the field of inclusive education. International Journal of Educational Research, 128, 102498. https://doi.org/10.1016/j.ijer.2024.102498
12. Petrunchak, D., Banyeva, I., Matviyenko, S. (2025). Social aspects of inclusive tourism: improving the accessibility of the hotel and restaurant sector in Ukraine. Market Infrastructure, 83, 331—337. https://doi.org/10.32782/infrastruct83-57
13. Zosim, S., Nikolaienko, V. A., Nikolaienko, V. V. (2024). Preservation of National Traditions of Ukrainian Architecture During the Reconstruction of Destroyed Cities and Villages In the Post-War Period. International Journal of Conservation Science, 15 (SI), 221—234. https://doi.org/10.36868/ijcs.2024.si.18
14. Dudariev, I. M., Kuzmin, O. V., Taraimovych, I. V., Panasiuk, S. H., Shemet, V. Ya., Chemakina, O. V., Kuzmin, A. O. (2024). Kraftovi kharchovi tekhnolohii: rozroblennia, doslidzhennia, inzhynirynh. Oldi Plus, 322.
15. Zanozovska, O. (2013). Quality management of domestic dairy enterprises based on HACCP principles. Current state and perspectives of enterprises' development in conditions of international economic activity. Banská Bystrica: Matej Bel University, 203—206.
16. Levytska, N., Kotsiubanska, O. (2023). Food industry of Ukraine during the Russian invasion: losses, experience, adaptation. Ukrainian Food Journal, 12 (2), 199—206. https://doi.org/10.24263/2304-974x-2023-12-2-4
17. Atstāja, D., Koval, V., Purviņš, M., Butkevičs, J., Mikhno, I. (2022). Construction Waste Management for Improving Resource Efficiency in The Reconstruction of War-Destroyed Objects. Economics. Ecology. Socium, 6 (2), 46—57. https://doi.org/10.31520/2616-7107/2022.6.2-5
18. Martsynyuk, Ye., Khandogina, O. (2025). Key characteristics of war-related debris and their implications for local waste management. Municipal Economy of Cities, 2 (190), 56—62. https://doi.org/10.33042/2522-1809-2025-2-190-56-62
19. Demian, P., Hassan, T. M., Kalmykov, O., Demianenko, I., Makarov, R. (2024). BIM Implementation in Post-War Reconstruction of Ukraine. Buildings, 14 (11), 3495. https://doi.org/10.3390/buildings14113495
20. Kuzmin, A., Chemakina, O., Matyiashchuk, O., Kuzmin, O. (2025). Accessibility and comfort of foodservice enterprises: Principles of inclusive engineering. Scientific progress: Theories, applications and global impact. European Open Science Space, 33—40. https://doi.org/10.70286/EOSS-14.07.2025
21. Abdelfattah, D., Nasreldin, R. (2025). Towards inclusive public open space in CBD case study of King Abdallah financial district. Journal of Urban Management. https://doi.org/10.1016/j.jum.2025.06.007
22. Novoselchuk, N. (2022). National traditions in the architecture of Ukrainian modernism of the early 20th century. Docomomo Journal, 67. https://doi.org/10.52200/docomomo.67.07
23. Kolupaieva, I., Lindahl, M. (2025). Policy recommendations for building a circular Ukraine. Journal of Cleaner Production, 492, 144835. https://doi.org/10.1016/j.jclepro.2025.144835

24. Hudym, M., Kononenko, H., Izbash, Y. (2022). Current state, issues and perspectives of construction waste recycling in Ukraine. International Science Journal of Engineering & Agriculture, 1 (5), 65–69. https://doi.org/10.46299/j.isjea.20220105.08
25. Gebeshuber, I. C., Hersh, M. (2024). Beyond Boundaries: Harnessing Unique Intellectual Abilities through Inclusive Engineering Education. IFAC-PapersOnLine, 58 (3), 129–133. https://doi.org/10.1016/j.ifacol.2024.07.138
26. Pekarchuk, O., Palianytsia, K. (2024). Specificity of the interior formation of the universal physical rehabilitation hall for military personnel. Visnik Nacionalnogo Universitetu "Lvivska Politehnika". Seria Arhitektura, 2, 133–143. https://doi.org/10.23939/sa2024.02.133
27. Gawlak, A., Matuszewska, M., Ptak, A. (2021). Inclusiveness of Urban Space and Tools for the Assessment of the Quality of Urban Life – A Critical Approach. International Journal of Environmental Research and Public Health, 18 (9), 4519. https://doi.org/10.3390/ijerph18094519
28. Abdelkarim, S., Ahmad, A. M., Zahrah, J., Makhoul, N., Al-Nuaimi, M., Naji, K. (2023). Criteria and Challenges of Inclusive Design In The Built Environment. Proceedings of the 2nd International Conference on Civil Infrastructure and Construction (CIC 2023). Qatar University Press, 49–58. https://doi.org/10.29117/cic.2023.0011
29. DSTU 9191:2022. Teploizoliatsiia budivel metod vyboru teploizoliatsiinoho materialu dlia uteplennia budivel (2023). Kyiv: UkrNDNC.
30. Dankevych, A., Stoyanova-Koval, S., Polova, O., Los, Z., Burdeina, N., Kazak, O. (2024). State of economic security and directions of restoration socio-economic development and food security in the conditions of war. Financial and Credit Activity Problems of Theory and Practice, 2 (55), 441–460. https://doi.org/10.55643/fcaptp.2.55.2024.4170
31. Adobor, H., McMullen, R. (2007). Supplier diversity and supply chain management: A strategic approach. Business Horizons, 50 (3), 219–229. https://doi.org/10.1016/j.bushor.2006.10.003
32. Lee Park, C., Fracarolli Nunes, M., Machuca, J. A. D. (2024). Reputational enablers for supplier diversity: An exploratory approach on the inclusion of war veterans and disabled people. Journal of Purchasing and Supply Management, 30 (5), 100898. https://doi.org/10.1016/j.pursup.2024.100898
33. Zvieriev, M. V., Kuzmin, A. O., Chemakina, O. V. (2024). Stratehii pidvyshchennia efektyvnosti restorannoho biznesu cherez reabilitatsiiu, motyvatsiiu, inkliuzyvnist ta rozvytok kompetentnostei. Innovatsiini tekhnolohii v hotelno-restorannomu ta turystychnomu biznesi. Kyiv, 215–216.
34. Steyn, K., de Villiers, W., Babafemi, A. J. (2025). A comprehensive review of hempcrete as a sustainable building material. Innovative Infrastructure Solutions, 10 (3), 97. https://doi.org/10.1007/s41062-025-01906-1
35. Linnik, D. S. (2021). Hempcrete on a complexly modified composite gypsum binder. [Extended abstract of PhD thesis dissertation; Odesa State Academy of Civil Engineering and Architecture].
36. Blahovestova, O. O., Pechertsev, O. O. (2019). Using traditional and modern construction technologies in design of ecological settlements. Naukovyi Visnyk Budivnytstva, 98 (4), 187–192.
37. DBN Ukrayiny V.2.6-31:2021. Teplova izolatsiya ta enerhetoefektyvnistʹ budivelʹ (2021). Derzhavne pidpryyemstvo «Derzhavnyi naukovo-doslidnyi instytut budivelʹnykh konstruktsiy».

38. Evtushenko, O., Siryc, A., Porodko, R. (2016). Development of the occupational safety in the food industry with regard for the risk-based approach. Ukrainian Food Journal, 5 (1), 174—186.
39. Pylypenko, I., Pylypenko, L., Yamborko, A., Ilyeva, O., Kotlyar, E., Babenko, D. (2017). Identification of bacillary microbial contaminants and food poisoning agents from ukrainian plant raw materials and products. Ukrainian Food Journal, 6 (1), 7—19. https://doi.org/10.24263/2304-974x-2017-6-1-3
40. Ivanov, V., Shevchenko, O., Marynin, A., Stabnikov, V., Gubenia, O., Stabnikova, O., Shevchenko, A., Gavva, O., Saliuk, A. (2021). Trends and expected benefits of the breaking edge food technologies in 2021—2030. Ukrainian Food Journal, 10 (1), 7—36. https://doi.org/10.24263/2304-974x-2021-10-1-3

DOI: 10.15587/978-617-8360-17-7.CH3

Oleksandr Shcheretskyi, Anatolii Verkhovliuk, Ruslan Sergiienko,
Dmytro Kanibolotsky, Volodymyr Shcheretskyi, Ievgenij Dzevin

3 PROSPECTIVE COMPOSITIONS OF HEAT-RESISTANT HIGH-ENTROPY ALLOYS FOR FOUNDRY PRODUCTION

ABSTRACT

The work investigates promising compositions of high-entropy alloys (HEAs) based on the FeNiCrCuAl and FeNiCrCuMn systems, which have the potential for use as heat-resistant materials in foundry production. It is shown that the use of a specially designed vacuum medium-frequency induction furnace allows obtaining high-quality ingots with active mixing of the melt and temperatures up to 1800°C. The thermodynamic parameters (entropy and enthalpy of mixing, atomic radii, electronegativities, VEC, Ω parameter) were calculated, on the basis of which the phase composition was predicted. X-ray phase analysis confirmed the formation of solid solutions with FCC and BCC lattices, an ordered B2 phase (of the NiAl type). In addition to phase analysis and structural study, the thermophysical properties (melting and crystallization heats, liquidus-solidus temperatures) of alloys, and elastic properties by the dynamic mechanical analysis (DMA) method, were investigated in a wide temperature range. The dependences of the elastic modulus and the loss factor on temperature were established. The heat resistance of alloys (at 900°C and 1000°C) was assessed, which showed high stability of the structure of high-entropy alloys in an oxidizing environment. The casting properties of the experimental alloys – fluidity and linear shrinkage – were studied using spiral and U-shaped test molds, which allowed comparing them with the indicators of cast irons and steels. The fluidity of high-entropy alloys of the FeNiCrCuMn system is lower, and that of alloys of the FeNiCrCuAl system is higher compared to standard steels (G25, GX10CrNiMn18-9-1). Thus, the results of the study confirm the feasibility of using alloys of the FeNiCrCuMn and FeNiCrCuAl systems as heat-resistant casting materials of a new generation.

KEYWORDS

High-entropy alloys, heat resistance, phase composition, elastic properties, thermophysical parameters, B2-phase, fluidity, induction melting.

In the early 2000s, a new type of materials was discovered – high-entropy alloys (HEAs) [1–3]. Traditional alloys have one or two main chemical elements, to which other elements are added in relatively low concentrations to achieve the desired properties. Whereas HEAs have at least five main elements, which are in an equiatomic or close to equiatomic composition. Due to the high concentration of components, such alloys have a high entropy of mixing, and it is entropy to a much greater extent than enthalpy that ensures the thermodynamic stability of HEAs. High-entropy alloys, due to the different diameters of the

atoms that make up their composition, have a deformed crystal lattice of the face-centered cubic (FCC) or body-centered cubic (BCC) types. Such alloys are characterized by unique properties: high values of the yield strength at room temperature, fracture toughness at low temperatures, resistance to softening at elevated temperatures, and wear resistance. High-entropy alloys with a BCC lattice are usually characterized by high hardness, while those with FCC lattice are characterized by high plasticity.

But conventional single-phase high-entropy alloys also have a number of disadvantages. Hard high-entropy alloys are brittle, while plastic ones have too low a yield strength. Conventional high-entropy alloys have poor casting properties: high volumetric and linear shrinkage and low fluidity. Also, individual components and the technology for producing high-entropy alloys are quite expensive. Usually, the method of arc remelting in a vacuum is used. These disadvantages limit the areas of practical use of high-entropy alloys.

One of the methods for improving the operational properties of HEAs is the manufacture of alloys with several high-entropy phases. This work is devoted to the development of cheap multiphase high-entropy alloys from available components with the prospects for mass casting production.

If the entropy of mixing ΔS_{mix} of the solution takes on large positive values, this leads to a significant negative contribution to the Gibbs free energy of mixing and stabilization of the corresponding solid phase. In the approximation of an ideal solution, the entropy of mixing ΔS_{mix} can be calculated as

$$\Delta S_{mix} = -R\sum_{i=1}^{N} c_i \ln(c_i), \tag{3.1}$$

where c_i – the mole fraction of component i in the melt, R – the universal gas constant.

In the case of equal molar concentrations c_i of each element, equation (3.1) takes the form

$$\Delta S_{mix} = R\ln n, \tag{3.2}$$

where n – the number of components in the alloy.

Alloys with an entropy of mixing greater than 12.5 J/mol K are considered high-entropy alloys [4].

The second thermodynamic function characterizing the stability of the phase is the alloy's enthalpy of mixing ΔH_{mix}, and its effect on the phase composition of the alloy is ambiguous. According to [5], the values of this function should be in the range –15 kJ/mol < ΔH_{mix} < 5 kJ/mol. At ΔH_{mix} > 5 kJ/mol, there is a lower degree of mixing of the components, which leads to segregation of elements in the alloy, and at high positive values of the enthalpy of mixing, stratification is possible. At high negative enthalpy of mixing ΔH_{mix} < –15 kJ/mol, the formation of intermetallics and ordered phases during melt crystallization is possible [6]. Only zero or small values of the enthalpy of mixing contribute to the random distribution of atoms in the crystal lattice sites and the formation of a disordered solid solution [7]. The enthalpy of mixing of a disordered multicomponent single-phase alloy is calculated by the equation [8, 9]

$$\Delta H_{mix} = \sum_{i=1;j\neq i}^{N} 4\Delta H_{ij}^{mix} c_i c_j, \tag{3.3}$$

where ΔH_{ij}^{mix} – enthalpy of mixing of a binary equiatomic alloy of components i and j; c_i, c_j – molar fractions of components in the corresponding multicomponent alloy.

The values ΔH_{ij}^{mix} calculated by the Miedema model for atomic pairs between elements with atomic numbers from 1 to 94 are presented in works [10–12].

The entropy of mixing is not always the dominant factor that ensures the formation of a single-phase structure and affects the microstructure. In work [13], the structures of HEAs were analyzed and three principles of the formation of solid solutions were formulated:

1) to obtain a high entropy of mixing, it is necessary that the number of main constituent elements be at least five;

2) the maximum difference in the atomic radii of the elements should not exceed 12%;

3) the enthalpy of mixing should vary in the range –40 kJ/mol < ΔH_{mix} < 10 kJ/mol.

In [5, 14], more precise parameters have been established, namely the coefficients Ω and δ_r, which can be used to predict phase formation in high-entropy alloys. The thermodynamic parameter Ω considers the influence of entropy and enthalpy of mixing, as well as the melting point on the formation of a solid solution [15]:

$$\Omega = \frac{T_m \Delta S_{mix}}{\left|\Delta H_{mix}\right|}, \tag{3.4}$$

$$T_m = \sum_{i=1}^{n} c_i \left(T_m\right)_i, \tag{3.5}$$

where T_m – the average melting point of an n-element alloy, K; $(T_m)_i$ – the melting point of the i-th element.

To describe the influence of differences in the atomic radii of the constituent elements, the empirical parameter δ_r can be expressed as follows:

$$\delta_r = \sqrt{\sum_{i=1}^{n} c_i \left(1 - \frac{r_i}{\bar{r}}\right)^2}, \tag{3.6}$$

$$\bar{r} = \sum_{i=1}^{n} c_i r_i, \tag{3.7}$$

where r_i – the atomic radius of the i-th component, $\bar{r}$ – the average atomic radius (taking into account atomic fractions).

A large difference in the atomic radii of the elements significantly affects the formation of a solid solution. Strong lattice distortions lead to an increase in the strain energy, and therefore to an increase in the free energy, which is accompanied by a decrease in the probability of solid solution formation, so the difference in the atomic radii of the elements should not exceed 6.6%.

Thus, the parameters Ω and δ_r can be a fairly reliable tool for separating between the formation of solid solutions and intermetallic phases in multicomponent systems. At a high value of the parameter Ω > 1.1 and a small value of the parameter $\delta_r \leq 4.6\%$ according to [5] or $\delta_r \leq 6.6\%$ according to [14], a solid solution based on phases with FCC or BCC lattice will form in the structure of the high-entropy alloy.

Based on the analysis of the structures of high-entropy systems, it can be stated that the formation of a solid solution is likely at the following values of the parameters mentioned above: $\Omega > 1.1$ and $\delta_r \leq 6.6\%$.

To describe the collective behavior of components in high-entropy alloys, the authors of [16, 17] proposed two additional parameters: the electronegativity difference ($\Delta\chi$) and the valence electron concentration (VEC). The value of $\Delta\chi$ is determined according to the classical Hume-Rothery rule:

$$\Delta\chi = \sqrt{\sum_{i=1}^{n} c_i \left(\chi_i - \overline{\chi}\right)^2}, \tag{3.8}$$

where χ_i – the Pauling electronegativity for the *i*-th element:

$$\overline{\chi} = \sum_{i=1}^{n} c_i \chi_i. \tag{3.9}$$

The current literature does not provide ranges of $\Delta\chi$ values that would indicate the formation of solid solutions in the HEAs structure, however, the study [18] showed that with a large value of $\Delta\chi$, the formation of intermetallic compounds or an amorphous phase is more likely. Judging from the tabular data [16, 18] and the relationship between the enthalpy of mixing and electronegativity [17], it can be concluded that for the existence of disordered solid solutions in the structure of high-entropy alloys, the difference in electronegativity ($\Delta\chi$) should not exceed 0.12 (or $\Delta\chi \leq 12\%$).

According to the Hume-Rothery rule [19], the valence electron concentration (VEC) predicts the type of crystal lattice. The valence electron concentration can also be used to predict the formation of intermetallics [20]. VEC is determined from the following equation:

$$VEC = \sum_{i=1}^{n} c_i \left(VEC\right)_i, \tag{3.10}$$

where $(VEC)_i$ – VEC for the *i*-th element.

VEC is a key physical parameter that governs the tendency for the formation of FCC and BCC solid solutions, a high VEC value (> 8), the FCC phase is formed, in the interval 6.87 < VEC < 8, a mixed BCC + FCC structure is formed, and at a lower VEC value (< 6.87) – the BCC phase [17].

In [21], a simple and practical pseudo-binary method was proposed for the design of eutectic HEA using the VEC and ΔH_{mix} parameters. Using this strategy, a series of nanostructured eutectic HEAs consisting of an ordered body-centered cubic (B2) phase and a phase with FCC lattice were successfully developed. By adding aluminum to high-entropy basic systems ($CoCrFeNi_2$, $Co_2CrFeNi$, $CoCrFe_2Ni$) with a FCC lattice, eutectic high-entropy alloys were obtained. Their eutectic structure consists of a mixture of a solid solution with FCC structure and intermetallic compounds (FCC/IMC). All developed alloys demonstrated unique mechanical properties with a tensile strength above 1000 MPa and a total elongation of more than 10%. When developing eutectic HEAs with FCC/IMC structure, the FCC solid solution is selected according to the following criteria: -5 kJ/mol $< \Delta H_{mix} < 0$ kJ/mol and VEC ≥ 8.

High-entropy alloys constitute a new class of structural materials that demonstrate a unique combination of high strength, heat resistance, corrosion resistance and wear resistance even under extreme operating conditions. Due to their stable microstructure and stability at high temperatures, HEAs are promising for use in the aerospace and energy industries (in particular, in elements of gas turbine engines and nuclear reactors), in military equipment, cryogenic systems, the chemical industry, as well as in the production of tools and bioinert implants and wear-resistant coatings [22, 23]. On their basis, unique new generation composite materials with controllable properties for critical engineering applications can be created [24, 25]. Another promising direction is the new HEAs based on lightweight elements that combine high thermal stability of the structure and resistance to local overheating during the joining processes involving high-energy sources [26].

3.1 PREPARATION OF HIGH–ENTROPY ALLOYS

To smelt high-entropy alloys in an argon atmosphere, a specialized induction vacuum furnace was developed and fabricated. It was based on a shaft-type vacuum resistance furnace, and its schematic diagram is shown in **Fig. 3.1** [27]. The tungsten heater was replaced by an inductor powered by a thyristor converter with a power of 6 kW and a frequency of 20–22 kHz. Melting was performed in an alundum crucible placed inside a graphite cup. The wall thickness of the graphite cup was optimized to minimize electromagnetic shielding of the charge, thereby ensuring active stirring of the melt during the process. The furnace manufactured in this way provided intensive mixing of the melt and overheated the alloy to a temperature up to 1800°C. The following were used as charge materials: carbonyl iron of special purity TU 6-09-3000-78 (Fe ≥ 99.99% wt.); cathode nickel (Ni ≥ 99.99% wt.); flakes of electrolytic chromium, grade ERX1 and chromium grade X99 in the form of small pieces; metallic manganese grade Mn997 (99.7 wt.%); copper grade M1 (99.9 wt.%) (the foreign equivalent Cu-ETP (99.9 wt.%)), aluminum ingot grade A85 (99.85 wt.%) (the foreign equivalent ENAW-1085 (99.85 wt.%)); electrolytic cobalt grade K0 (Co ≥ 99.98% wt.). Also, as a source of iron, nickel and chromium, stainless steel of the grade 10H18N9L (the foreign equivalents GX10CrNiMn18-9-1, EN 10213) was used. The technology for obtaining samples was as follows: after loading components into a crucible with a total mass of no more than 1500 grams, the working chamber was evacuated (P = 2.10-2 Pa), then flushed 2 times with high-grade argon (99.993%) and the furnace was filled with it to an excess pressure of 15–20 kPa. When heated to 1000°C, the heating rate did not exceed 25°C/min, so as not to crack the alundum crucible. During melting, the excess pressure of argon in the chamber rose to 30–40 kPa. After melting and dissolving all elements, the alloy was overheated to a temperature of 1550–1600°C and held in a liquid state for at least 30 min. The total duration of melting, including heating and holding the alloy in its liquid state, was at least 90 minutes. After holding the alloy in a liquid state in a high-purity argon environment, it was cooled together with the furnace to room temperature. The high-entropy alloys obtained in this way were remelted once more in an argon environment, and after the melting was completed, the furnace lid was opened, and the melt was poured into molds using traditional sand-clay casting. The chemical composition of the experimental HEA samples was determined using an X-ray fluorescence express analyzer (XRF) "EXPERT 3L".

The chemical composition of the obtained alloys is shown in **Table 3.1**.

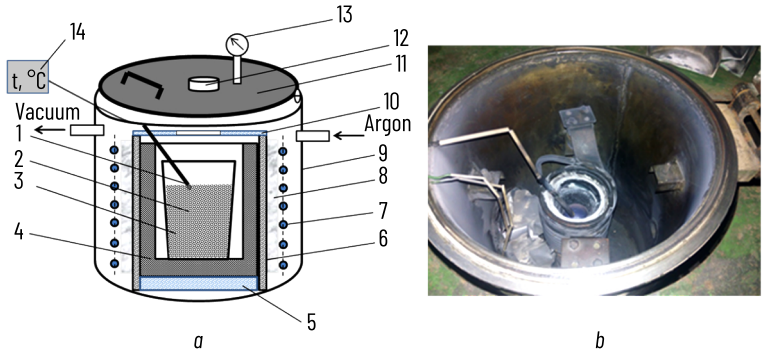

Fig. 3.1 Schematic diagram of vacuum induction furnace for smelting samples of high-entropy alloys: *a* – schematic diagram; *b* – photograph ; 1 – thermocouple; 2 – charge material; 3 – alundum crucible; 4 – graphite cup; 5 – alundum stand; 6 – alundum tube; 7 – inductor; 8 – kaolin wool; 9 – vacuum chamber; 10 – alundum cover with a viewing window; 11 – chamber cover; 12 – viewing window; 13 – vacuum gauge; 14 – temperature recording device

Table 3.1 Chemical composition of HEA samples, expressed in atomic percent

No.	Fe	Ni	Cr	Co	Mn	Cu	Al	C	Si	P+S
1	23.88	20.42	14.54	–	18.49	21.92	–	0.430	0.300	0.036
2	23.99	20.66	12.65	–	0.11	20.66	21.32	0.430	0.170	0.018
3	21.77	20.58	14.02	–	0.354	23.22	19.50	0.302	0.233	0.020
4	17.10	22.17	18.58	–	–	23.51	18.56	–	0.076	0.012
5	18.96	19.97	20.10	–	20.30	20.42	–	–	0.213	0.042
6	19.30	20.13	18.60	–	–	20.85	21.03	–	0.077	0.013
7	20.48	21.63	18.54	21.38	17.97	–	–	–	–	–
8	24.09	20.43	14.14	–	19.27	21.27	–	0.380	0.368	0.040
9	24.72	20.80	12.41	–	19.64	21.63	–	0.381	0.388	0.038
10	19.10	21.52	17.79	–	–	21.87	19.65	–	0.065	0.015

3.2 X–RAY PHASE ANALYSIS, MICROSTRUCTURE AND THERMODYNAMIC PARAMETERS OF HIGH–ENTROPY ALLOYS

X-ray phase analysis of the alloys was performed by X-ray diffraction on DRON-3, and Bruker D8 Advance diffractometer (Germany) using Mo-Kα (λ = 0.07093187 nm), Co-Kα (λ = 0.178897 nm) radiations, respectively, and with focusing of X-rays according to the Bragg-Brentano geometry. Depending on the type of radiation, measurements were carried out in the angular ranges of 10°—55° and 15°—135° with a step of 0.02° or 0.05°, respectively, with a pulse accumulation time of 2 s. For accurate determination of the lattice parameters in the region of far diffraction peaks at large angles, a step of 0.01° and an accumulation time of 12—16 s was used, depending on the type of sample. To study the microstructure and chemical phase composition of the HEA samples, a REM106I scanning electron microscope with an energy-dispersive microanalyzer (manufactured by OJSC "SELMI") was used. **Fig. 3.2** shows the diffraction patterns obtained on Samples No. 4 and No. 5 of the FeNiCrCuAl and FeNiCrCuMn systems, respectively. High-entropy alloys of the FeNiCrCuAl system demonstrate two phases with different crystal lattices, in particular BCC (the space group Pm3m) and FCC (the space group Fm3m). A solid solution based on the BCC phase has an ordered structure of type B2, which is characterized by a uniform distribution of all elements within the phase and exists in equiatomic NiAl alloys. The structure of type B2 is similar to a disordered solid solution based on a phase with a BCC structure of type A2 and differs in that the position in the center of the unit cell is occupied by one specific type of atoms, while another type occupies the corner positions. This is confirmed by the presence of a diffraction maximum (100) at $2\theta \approx 36°$ for Co-Kα radiation (**Fig. 3.2, *a***, Sample No. 4). The alloys of the FeNiCrCuMn system have a multiphase structure, but with different FCC lattices (FCC1, FCC2) with different periods and a BCC lattice (A2) (the space group Im3m) (**Fig. 3.2, *b***, Sample No. 5). The lattice periods were calculated for each reflection (*hkl*) in the X-ray diffraction pattern, and then the average value of the lattice parameters was determined. For certain X-ray diffraction patterns, Miller indices corresponding to large diffraction angles were selected to determine the lattice parameters. Specifically, the (321) peak from Sample No. 6 was observed at angles of 54.81° and 55.18°, using molybdenum radiation with wavelengths MoKα_1 = 0.7093187 Å and MoKα_2 = 0.710806 Å, respectively. The calculation of lattice parameters was also carried out on the basis of diffractograms using cobalt radiation (CoKα1 = 1.78897 Å). Lattice parameters depend on the chemical composition and for alloys of the FeNiCrCuAl system (Samples No. 3, 4, 6) the parameter of the BCC lattice varies from 2.8788 Å to 2.8900 Å, and the FCC lattice from 3.6358 Å to 3.6500 Å (**Table 3.2**). For alloys of the FeNiCrCuMn system (Samples No. 1, 5), the parameter of the FCC1 lattice changes from 3.6700 Å to 3.6800 Å, and the FCC2 lattice does not change at 3.6200 Å (**Table 3.2**). For alloys of the FeNiCrCuMn system, the diffraction pattern of one of the phases is similar to austenite or an iron-manganese alloy Fe_3Mn_7 with FCC1 lattice periods of 3.6700 Å, 3.6800 Å, respectively, and the second phase is similar to solid solutions in copper-iron alloys, but with slightly smaller parameters of the face-centered cubic FCC2 lattice (3.6200 Å). According to Vegard's law, the theoretical parameters of crystal lattices of alloys with the nominal charge composition $Fe_{20}Ni_{20}Cr_{20}Cu_{20}Al_{20}$ and $Fe_{20}Ni_{20}Cr_{20}Cu_{20}Mn_{20}$ were calculated. It turned out that they differ from the experimental ones, and the theoretical parameter of the BCC lattice has a larger value (2.9125 Å), and the parameters of the FCC lattice have smaller values (3.5039 Å, 3.6152 Å) compared to the experimental periods.

The discrepancy in the values of the experimentally determined and theoretically calculated parameters can be due to both the inaccuracy of the calculation and the change in the electronic structure, chemical composition, local order, magnetic and many other properties of solid solutions. In addition, the calculations did not take into account the influence of impurities of silicon, carbon, phosphorus and sulfur.

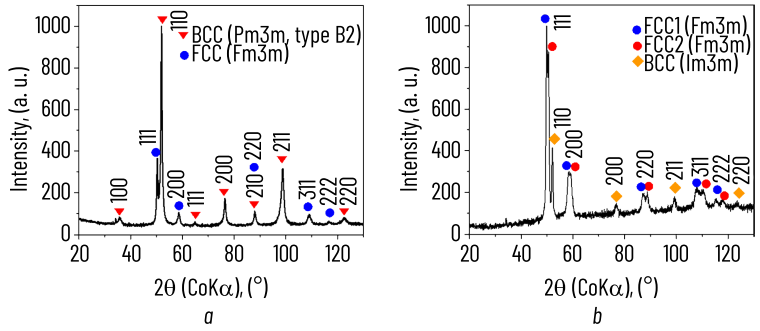

Fig. 3.2 X-ray diffraction patterns of high-entropy alloys: *a* — FeNiCrCuAl system (Sample No. 4); *b* — FeNiCrCuMn system (Sample No. 5)

Table 3.2 Results of phase analysis and lattice parameters of alloys of the FeNiCrCuAl, FeNiCrCuMn, FeCoNiCr systems

Sample	Lattice (space group)	Radiation	Lattice parameter, Å
1	**2**	**3**	**4**
Fe20Ni20Cr20Cu20Al20	BCC (Im3m) FCC (Fm3m)	calculation	2.9125 3.6152
Fe20Ni20Cr20Cu20Mn20	FCC (Fm3m)	calculation	3.5039
1	FCC 1 (Fm3m) FCC 2 (Fm3m)	CoKα	3.6800 3.6200
3	BCC (Pm3m) FCC (Fm3m)	CoKα	2.8800 3.6400
4	BCC (Pm3m) FCC (Fm3m)	CoKα	2.8900 3.6500
5	FCC 1 (Fm3m) FCC 2 (Fm3m) BCC (Im3m)	CoKα	3.6700 3.6200 2.8800

Continuation of Table 3.2

1	2	3	4
6	BCC (Im3m) BCC (Fm3m)	CoKα MoKα MoKα CoKα MoKα	2.8788±0.00460 2.8894±0.00536 2.8830* 3.6358±0.00517 3.6480±0.00510
FeNiCoCr	BCC (Fm3m)	CoKα MoKα	3.5702±0.00239 3.5768±0.0015**

*Note: The lattice parameters were calculated from peaks with Miller indices *(321), **(331) and (420).*

Typical microstructures of the cast high-entropy alloy samples of the FeNiCrCuAl and FeNiCrCuMn systems after crystallization are shown in **Fig. 3.3**. The cast samples exhibit a heterogeneous structure consisting of several phases, including dendrites, an interdendritic region, and a third phase enriched in copper. The branches of the dendrites have a rounded shape for both alloy systems. The chemical composition of the individual phases was determined using local chemical analysis (EDX analysis). In **Fig. 3.3, *a, b***, the structural components are indicated by numbers (1–7), and their corresponding chemical composition is presented in **Table 3.3**.

More refractory elements, such as iron and chromium, are concentrated in the branches of the dendrites, while the interdendritic regions are enriched in elements with lower melting points, such as copper, aluminum, manganese, and nickel. Unlike other alloy components, copper shows a tendency to segregation, forming a separate phase (**Fig. 3.3, *a***, point 4, **Fig. 3.3, *b***, point 7). This is due to its limited solubility in the FeNiCrAl-based solid solution and thermodynamic tendency to form copper-enriched regions, therefore, copper-enriched regions have a lower mixing entropy (**Table 3.3**). The calculated valence electron concentrations of individual phases indicate the potential formation of solid solutions with FCC or BCC lattices. In alloys of the FeNiCrCuAl system, the white elongated regions in the interdendritic space of alloy No. 4, enriched in copper (**Fig. 3.3, *a***, point 4), are characterized by the VEC equal to 9.566 el/at. This indicates the probable formation of a phase with FCC lattice. At the same time, the dendrites and the interdendritic space, where the VEC varies from 7 to 8 el/at (**Table 3.3**), probably contain a mixture of solid solutions with FCC and BCC lattices. This range of VEC corresponds to the transition zone between the stability of BCC and FCC phases, which indicates the possible coexistence of both types of crystal structures in the microstructure of the alloy. In alloys of the FeNiCrCuMn system, the dendrites have an elongated oval shape with uneven edges (**Fig. 3.3, *b***). The concentration of valence electrons suggests a high probability of forming two solid solutions in the interdendritic space of alloy No. 5, based on phases with a face-centered cubic lattice (**Table 3.3**, items 6 and 7). This is further supported by the results of X-ray phase analysis. The dendrites` branches of the alloy No. 5 of the FeNiCrCuMn system are enriched in chromium, therefore these regions are characterized by a lower mixing entropy compared to the interdendritic space (**Table 3.3**, point 5).

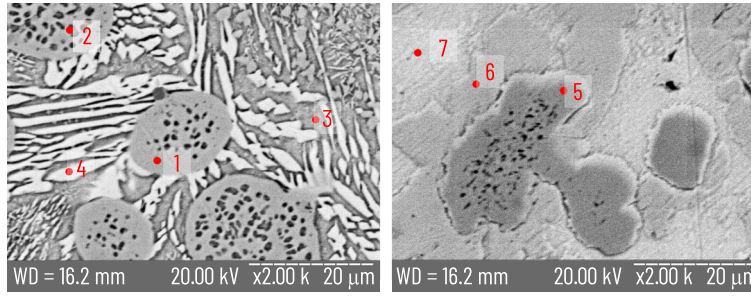

a *b*

Fig. 3.3 Microstructures of cast high-entropy alloys: a — No. 4 and b — No. 5 of the FeNiCrCuAl and FeNiCrCuMn systems. Individual phases are indicated by numbers, and their chemical composition is given in **Table 3.3**

Table 3.3 Chemical composition of individual phases in high-entropy alloys of the FeNiCrCuAl and FeNiCrCuMn systems

Alloy No.	Point	Chemical composition (at.%)						VEC (el/at)	ΔSmix (J/mol·K)	Lattice
		Fe	Ni	Cr	Cu	Al	Mn			
4	1	37.78	5.61	46.78	4.15	5.68	—	7.017	9.809	BCC FCC
	2	26.75	12.36	34.53	13.09	13.27	—	7.286	12.576	BCC FCC
	3	8.18	34.25	4.31	23.47	29.80	—	7.814	11.709	BCC FCC
	4	3.73	13.36	1.47	67.51	13.92	—	9.566	8.259	FCC
5	5	28.36	6.21	52.33	2.00	—	11.1	6.250	9.903	BCC
	6	25.31	25.39	19.99	10.01	—	19.3	8.215	13.016	FCC
	7	5.46	19.51	2.88	44.80	—	27.4	9.404	10.760	FCC

As shown in **Table 3.4**, the increased content of chromium and iron in the dendrites of alloys of both systems caused an increase in the microhardness of the dendritic branches, which turned out to be 1.1–2 times higher compared to the microhardness of the interdendritic regions. At the same time, in alloy No. 3, the opposite trend is observed — the interdendritic region demonstrates a slightly higher hardness.

Table 3.4 The microhardness of the structural constituents in FeNiCrCuAl and FeNiCrCuMn high-entropy alloy samples

Alloy No.	Microhardness, Hμ (kgf/mm²)		
	Interdendritic space	Dendrites	Shell around dendrites
1	233±39	233±32	–
2	198±20	296±58	–
3	328±51	290±52	–
4	245±24 263±57	322±41	–
5	194±25	288±41	330±44
6	343±42	375±60	–
8	172±13	192±37	–
10	195±17 252±28	381±42	–

To further evaluate phase formation and the development of solid solutions in the studied FeNiCrCuAl and FeNiCrCuMn alloys, key thermodynamic parameters were calculated, as summarized in **Table 3.5**. The concentration of valence electrons in the alloys of the FeNiCrCuMn system (Samples No. 1, 5, 8, 9) varied from 8.397 to 8.589 el/at, and for the alloys of the FeNiCrCuAl system (Samples No. 2–4, 6, 10) – from 7.601 to 7.846 el/at. These values indicate the formation of solid solutions with FCC lattice in the alloys of the FeNiCrCuMn system, and in the alloys of the FeNiCrCuAl system – a mixture of two phases with BCC and FCC lattices, which was previously confirmed by X-ray phase analysis. For the studied systems, the value of the thermodynamic parameter Ω exceeds 1.1. The alloys have relatively small negative values of the enthalpy of mixing ΔH_{mix} from –4.867 to –3.23 kJ/mol for the FeNiCrCuAl system and small positive values of ΔH_{mix} from 1.798 to 2.427 kJ/mol for the FeNiCrCuMn alloy system. All values of ΔH_{mix} are in the range –15 kJ/mol < ΔH_{mix} < 10 kJ/mol [5, 17, 28]. In addition, the configurational entropy coefficient $\Delta S_{mix}/R \geq 1.61$ also indicates the probability of solid solution formation (**Table 3.5**). A literature review of high-entropy systems shows that solid solution formation is likely when $\delta_r \leq 6.6\%$. The FeNiCrCuAl system exhibits an average atomic radius difference of ≤ 6.4%, influenced by the presence of aluminum (143 pm), while in the FeNiCrCuMn system it is about 4%. In the FeNiCrCuMn system, all elements have similar radii (from 124 to 130 pm), which contributes to a smaller δ_r and, accordingly, a higher probability of forming stable solid solutions. For reference, the atomic radii of elements in the studied systems are: Fe – 126 pm, Ni – 124 pm, Cr – 130 pm, Cu – 128 pm, Mn – 127 pm. The difference in electronegativity ($\Delta\chi$) has a minimal effect on the formation of a solid solution. Studies [16–18] show that at $\Delta\chi$ values exceeding 0.117, the formation of intermetallics is likely.

Table 3.5 Thermodynamic parameters of high-entropy alloys

Alloy No.	ΔSmix/R*	ΔSmix (J/mol·K)	ΔHmix (kJ/mol)	Ω	δr (%)	$\Delta\chi$	VEC	Lattice
1	1.635	13.597	1.992	11.50	4.091	0.147	8.56	FCC
2	1.628	13.538	–4.867	4.315	6.349	0.132	7.69	BCC+ FCC
3	1.644	13.669	–3.863	5.527	6.011	0.129	7.823	BCC+FCC
4	1.608	13.371	–3.230	6.587	5.461	0.125	7.846	BCC+FCC
5	1.624	13.504	2.427	9.549	3.256	0.143	8.397	FCC
6	1.615	13.424	–4.231	5.025	5.721	0.125	7.601	BCC+FCC
7	1.609	13.374	–4.153	5.814	3.171	0.136	8.033	FCC
8	1.636	13.601	1.799	12.74	4.046	0.148	8.540	FCC
9	1.628	13.535	1.798	12.62	4.066	0.148	8.589	FCC
10	1.612	13.404	–3.772	5.639	5.588	0.124	7.745	BCC+FCC

*Note: *R – universal gas constant (8.314463 J/mol·K).*

3.3 CASTING PROPERTIES OF HIGH-ENTROPY ALLOYS

To evaluate alloys as casting materials, their technological characteristics, which are commonly called casting properties, are studied. To date, the casting properties of high-entropy alloys remain insufficiently studied, which determines the relevance of the presented work. The main casting properties include fluidity, linear and volumetric shrinkage, crack resistance. In addition, this these characteristics include macro- and microstructure, the tendency of the alloy to gas saturation, contamination with oxide films during melting, as well as the manifestation of liquation heterogeneity of the composition. In this work, fluidity (λ) (the ability of the alloy to fill the cavity of the casting mold and accurately reproduce its configuration) and linear shrinkage (ε_l) were studied. To determine them, special test molds were developed that allow obtaining quantitative data: U-shaped cast iron test mold with a vertical channel, which is an improved modification of the Nehendzi–Samarin mold, and a sand-clay test mold with an annular channel [29]. For the manufacture of sand-clay test molds, quartz sand was used as a filler. Liquid glass (4–5% by mass), technical lignosulfonates and kaolin (2–3% by mass), as well as the special surfactant (mixture of sodium salts of alkylbenzenesulfonic acids), fuel oil (1–1.5% by mass) and technical urea were used as binders. To prevent the formation of burn-in on the surface of the castings during pouring, the inner surface of the sand-clay sample was covered with antipenetration paste, which included: marshalite (ground powdered quartz), polyvinyl butyral, technical alcohol, acetone and nitro enamel.

To ensure the feeding of the mold with liquid metal until complete solidification in the U-shaped channel, a sand-clay pouring cup (funnel) was used, which provided effective thermal insulation of the melt (**Fig. 3.4**). The dimensions of the pouring cup: external dimensions — diameter 90 mm, height 90 mm; cavity dimensions — diameter 50 mm, height 65 mm. The metal flowed from the cup into the cast-iron U-shaped sample through a transition channel 30–35 mm long and 13 mm in diameter, which ensured uniform metal flow from the funnel. This contributed to the initial stabilization of the filling rate of the cast iron mold, while the final stabilization was provided by the central downgate of the U-shaped mold itself. The temperature of the metal in the cast iron U-shaped test mold was controlled using a tungsten-rhenium thermocouple installed in the central riser near its junction with the U-shaped channel (**Fig. 3.4**, designation 3). Based on these measurements, the key thermal parameters of the experiment were determined: liquidus temperature, solidus temperature, cooling rate.

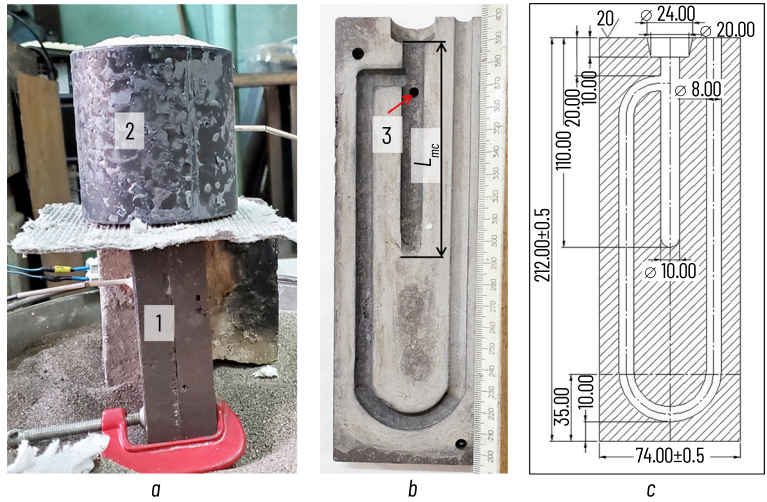

Fig. 3.4 Cast iron U-shaped test mold for determining fluidity and linear shrinkage of alloys according to the Nehendzi–Kuptsov method: *a* — photograph of the collected test mold; *b* — manufactured cast iron test mold; *c* — test mold`s drawing ; 1 — cast iron U-shaped test mold; 2 — sand-clay pouring cup (funnel); 3 — thermocouple installation location in the central downgate of the U-shaped test mold

The inner surface of the cast iron test mold was painted with a special water-based refractory paint (disthene-sillimanite — 70% by weight, perlite — 25%, bentonite — 2.5%, dextrin — 2.5%). Both halves of the mold after assembly were fixed with guide rods and a clamp. The temperature of the U-shaped mold was 16°C (room temperature). The pouring cup and the sand-clay mold with an annular channel, which was used as a test mold for fluidity, were dried at a temperature of 600°C for 3–4 hours.

After drying, the pouring cup was installed on the upper part of the U-shaped cast iron test mold, and the sand-clay test mold with an annular channel — on a special ceramic stand. One portion of molten metal weighing about 600 g was poured into the funnel of a U-shaped cast iron test mold, and the second portion of the same mass was poured into a sand-clay mold for fluidity test. The temperature of the melt before pouring was controlled in the furnace, then in the pouring cup and in both test molds (**Table 3.6**). The pouring time was 3–4 seconds.

Table 3.6 Pouring temperatures for fluidity and linear shrinkage of various alloys

Alloy	$t_{furnace}$, °C	$t_{pouring\ cup}$, °C	$t_{U\text{-}mold}$, °C	λ, mm	ε_l, %
FeNiCrCuMn	1450–1500	1400–1406	1180–1206	142–147 {65–105}	2.22–2.63
FeNiCrCuAl	1550–1600	–	–	320	2.50
G25 (AISI 1025)	1570	1514	1446	277{114}	1.95±0.15
GX10CrNiMn18-9-1 (AISI 304L)	1550	1459	1398	262{179}	2.66±0.058

*Note: In curly brackets is the length of the cost annular channel of the sand-clay mold (**Fig. 3.6**). $t_{furnace}$ — metal temperature in the crucible of the induction furnace before casting; $t_{pouring\ cup}$ — metal temperature in the pouring cup above the U-shaped test mold; $t_{U\text{-}mold}$ — metal temperature at the entrance to the U-shaped channel*

A control series of experiments were conducted to study the fluidity and linear shrinkage of high-entropy alloys of the FeNiCrCuMn and FeNiCrCuAl systems. For comparison, the casting properties of steel grades G25L (AISI 1025) and GX10CrNiMn18-9-1 (AISI 304L) were also determined.

As shown in **Fig. 3.5, 3.6** and **Table 3.6**, the fluidity of the FeNiCrCuMn high-entropy alloy is lower than that of standard steels, whereas the FeNiCrCuAl alloy exhibits higher fluidity. It is known that the fluidity of alloys is significantly affected by the chemical composition and other technological properties [30]. The increased fluidity of the FeNiCrCuAl system alloy can be explained by a shorter crystallization interval compared to the FeNiCrCuMn system alloy. In order to finally draw a conclusion about the fluidity of high-entropy alloys, it is necessary to conduct additional experiments: stabilize the metal pressure in the test mold, its geometric dimensions and configuration; control the temperature of the melt overheating above the liquidus temperature; and also control the temperature in the pouring cup.

It should also be taken into account that when using a massive metal U-shaped test mold, the influence of the thermophysical properties of the alloy under study on the result can be very significant. This influence increases with increasing heat transfer intensity from the metal to the mold. In this case, the thermophysical parameters of the alloy may become the predominant factor governing fluidity, diminishing the influence of other melt properties. No tendency to the formation of hot cracks was detected in the studied high-entropy alloys.

The linear shrinkage in this work was determined as the difference between the linear dimensions of the foundry mold cavity (L_{mc}) filled with molten metal and the dimensions of the resulting casting (L_c) after cooling, according to the formula [29]

$$\varepsilon_l = \frac{L_{mc} - L_c}{L_c} \cdot 100\%. \quad (3.11)$$

Prior to pouring the metal into the fluidity test mold, the linear dimension of the mold cavity (L_{mc}) was measured (**Fig. 3.4, *b***). After solidification, the length of the casting (L_c) formed in the central downgate of the U-shaped test mold was recorded (**Fig. 3.5**), and the linear shrinkage was subsequently calculated. The linear shrinkage of castings from high-entropy alloys of the FeNiCrCuMn and FeNiCrCuAl systems approaches the shrinkage of high-alloy steels and ranges from 2.22% to 2.63% (**Table 3.6**). The value of the linear shrinkage depends on the chemical composition of the alloy, the temperature and rate of filling the mold, as well as the cooling rate of the casting itself. It is known that the linear shrinkage of castings of gray cast iron is on average 1%, of steel — 2%, and for most other alloys — about 1.5%.

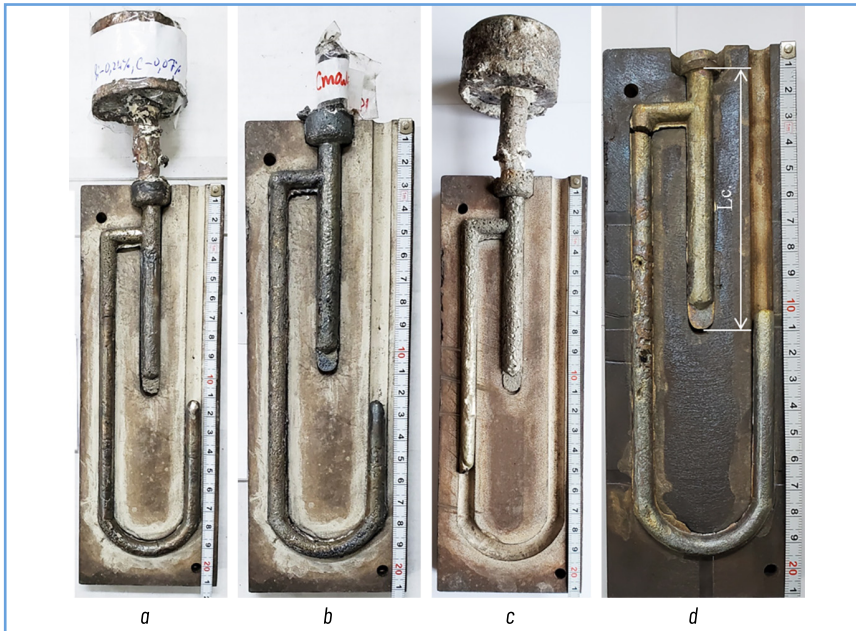

Fig. 3.5 Filled U-shaped channels in the Nehendzi–Kuptsov test mold with overfills for determining the fluidity of various alloys: *a* — casting from stainless steel GX10CrNiMn18-9-1 (λ = 262 mm); *b* — steel casting G25 (λ = 277 mm); *c* — high-entropy alloy casting of the FeNiCrCuMn system (λ = 142 mm); *d* — high-entropy alloy casting of the FeNiCrCuAl system (λ = 320 mm)

a *b*

c *d*

Fig. 3.6 Assembled complex sand-clay test mold and castings from various alloys for determining fluidity and mechanical properties: *a* — complex ring test mold; *b* — high-entropy alloy casting of the FeNiCrCuMn system (λ = 105 mm); *c* — stainless steel casting GX10CrNiMn18-9-1 (λ = 179 mm); *d* — gray cast iron (λ = 265 mm)

3.4 STUDY OF THE PHYSICAL AND MECHANICAL PROPERTIES OF HIGH-ENTROPY ALLOYS

Uniaxial tensile testing is relatively straightforward to analyze and enables the determination of several key mechanical properties of a material in a single test. These properties serve as quality indicators and are essential for engineering design calculations. Testing of samples with a diameter of 6 mm and a length of 30 mm was carried out on a tensile machine model P5.

Samples with a diameter of 3 mm and a length of 35 mm were stretched on a 1246P-2/2300 NIKIMP installation in accordance with the requirements of DSTU EN 10002-1:2006. The stretching rate was constant and was 1 mm/min, which corresponded to a deformation rate of $\dot{\varepsilon} = 10^{-3}$ s^{-1}. The load and elongation of the samples were measured using force and displacement sensors (extensometers) with adapters. During the tests, the yield strength ($\sigma_{0.2}$), the ultimate tensile strength (σ_u), relative elongation (δ), reduction of area (ψ) and the elastic modulus (E) were determined.

Brinell hardness was determined by applying a load of 750 kgf for 15 seconds using a hardened steel ball with a diameter of 5 mm pressed into the material. To determine the hardness by the Vickers method, a tetrahedral diamond pyramid with an angle at the apex of 136° was pressed into the samples. During the tests, loads of 10, 20 and 30 kgf were used; the holding time did not exceed 15 s.

The samples` hardness of alloys of the FeNiCrCuAl system (Samples No. 2–4, 6, 10) (**Table 3.7**) is more than one and a half times higher than the hardness of samples of the FeNiCrCuMn system (Samples No. 1, 5, 8, 9). The formation of a B2-ordered body-centered cubic (BCC) phase at higher aluminum contents is the main factor responsible for the hardness increase. In addition, a significant difference in the atomic radii of aluminum compared to other alloy elements causes local distortions of the crystal lattice, which additionally contributes to increasing hardness and temporary resistance to fracture. The results obtained are consistent with the data of other studies. In particular, in [31], experimental values of microhardness and reduced Young's modulus for the studied alloys in the entire range of aluminum concentrations are given. The dependence of microhardness is monotonic and reaches a maximum when the alloy consists entirely of a solid solution based on the BCC phase. Samples of the FeNiCrCuAl system with a mixed structure (with BCC and FCC lattices) in the cast state are characterized by brittle fracture in the elastic region: $\delta < 0.1\%$, $\psi < 0.1\%$, without a clearly defined conditional yield point (**Fig. 3.7**). In contrast, alloys of the FeNiCrCuMn system with FCC structure demonstrate high plasticity: $\delta = 40\%$, $\psi = 64\%$ (**Table 3.7**).

The ultimate strength or temporary fracture resistance (σ_u) was used in the formula [32]:

$$HB(HV) = k\sigma_u, \tag{3.12}$$

where the coefficient k is 2.54 for alloys of the FeNiCrCuMn system and 3.04 for alloys of the FeNiCrCuAl system were calculated.

Thus, high-entropy alloys with aluminum content are brittle, but are characterized by the highest hardness. In contrast, samples of the FeNiCrCuMn system with FCC structure have significant plasticity and relatively low hardness, while their ultimate tensile strength and yield strength are not inferior to those of high-alloy standard steels.

The tensile strength of alloys of the FeNiCrCuAl system exceeds the strength of high-strength cast iron of the EN-GJS-600-3 grade. Therefore, the mechanical properties of high-entropy alloys are determined by their crystal structure and elemental composition: alloys with a BCC lattice are characterized by high strength and low plasticity, while materials with FCC lattice, on the contrary, are characterized by lower strength but high plasticity.

Table 3.7 Hardness and mechanical properties of high-entropy alloys

Alloy No.	Hardness (kgf/mm²)		σ_u, MPa	$\sigma_{0.2}$, MPa	δ, %	ψ, %	Elastic modulus, GPa
	HB	HV					
1	156±13.5	–	603	335	40	64	122
2	309±6.4	–	997	–	–	–	–
3	228±36	246.4±10.5	735	–	–	–	136
4	304±25	–	981	–	–	–	–
5	218±18.5	–	842	–	–	–	–
6	291±8		939				
7	–	152±5.5	587	–	–	–	–
8	125±12	–	483	–	–	–	–
9	157±3.64	–	606	–	–	–	–
10	275±17.3	–	887	–	–	–	–

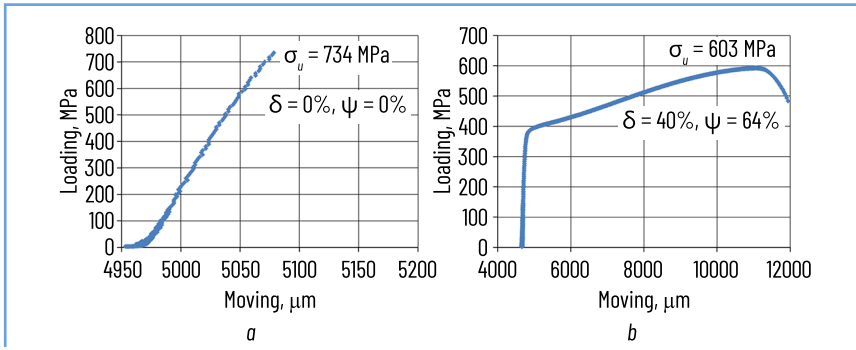

Fig. 3.7 Load-strain curves obtained during tensile testing of cast alloy samples belonging to the following systems: *a* — FeNiCrCuAl; *b* — FeNiCrCuMn

3.5 STUDY OF THE THERMOPHYSICAL CHARACTERISTICS OF THE OBTAINED ALLOYS

The thermophysical characteristics of the alloys were studied using a synchronous thermal analyzer (STA) of the STA 449F1 brand, manufactured by NETZSCH, Germany. STA is a combination of two research methods that are implemented simultaneously on one sample — thermogravimetry (TG) and differential scanning calorimetry (DSC). The main advantage of synchronous thermal analysis is that the mass change and thermal effects are measured on one sample simultaneously.

This approach provides a comparison of the results obtained by eliminating the influence of such factors as material heterogeneity, experimental conditions, sample preparation, etc. In addition, the combination of TG and DSC provides a more accurate determination of enthalpy values, since at any moment of the experiment the actual mass of the sample is known. In addition, the STA method saves time and sample material, which is especially important if the amount of the studied substance is limited, as well as when working with expensive or scarce materials.

The study of the thermophysical characteristics of the HEAs were carried out in crucibles made of alumina, in a dynamic environment of high-purity argon (20 ml/min). The heating and cooling rate was 20 K/min. The accuracy of temperature measurement was ±1°C. The sensitivity of the DSC signal registration was less than 1 μW. At the same time, the accuracy of determining enthalpy and heat capacity is ensured at the level of 3%. Thermal balances allow, during the experiment, to determine the current mass of the sample with an accuracy of 1×10^{-7} grams. The high sensitivity of the DSC allows to detect even insignificant thermal effects that arise in the material when heated or cooled, on the other hand, to record changes in the thermophysical properties of the sample under study. The ability of thermal balances to record the slightest change in the mass of the sample during the experiment allows to record the processes that occur in alloys during heating. Therefore, by the increase in the mass of the sample, it is possible to detect and control the oxidation of alloys. The loss of mass of the sample can be used to track the process of evaporation and decomposition. Therefore, synchronous thermal analysis is widely used in the study of high-entropy and amorphous alloys [33].

When studying the obtained high-entropy alloys, the melting point of the alloy (t_s — solidus temperature) was determined, and during cooling, the crystallization point (t_l — liquidus temperature) and the crystallization interval of the alloy were determined as the difference $\Delta t = t_s - t_l$. The alloy samples were heated to a temperature of 1450°C at a rate of 20 K/min, then cooled below 200°C and heated again to 1450°C (**Fig. 3.8**).

It is possible to distinguish the difference between the alloys of two different systems FeNiCuCrMn and FeNiCuCrAl during their melting (**Fig. 3.9**). The thermogram of the alloy containing manganese clearly shows two separate melting peaks from two different phases, while in alloys of the FeNiCuCrAl system containing aluminum, one broad asymmetric peak was usually recorded.

The results of the studies are given in **Table 3.8**.

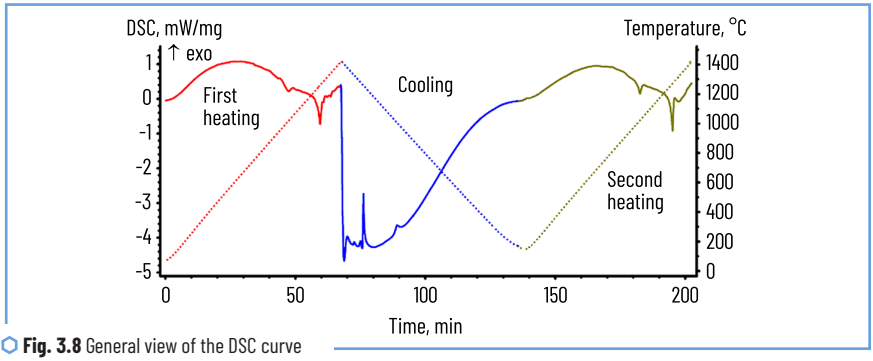

Fig. 3.8 General view of the DSC curve

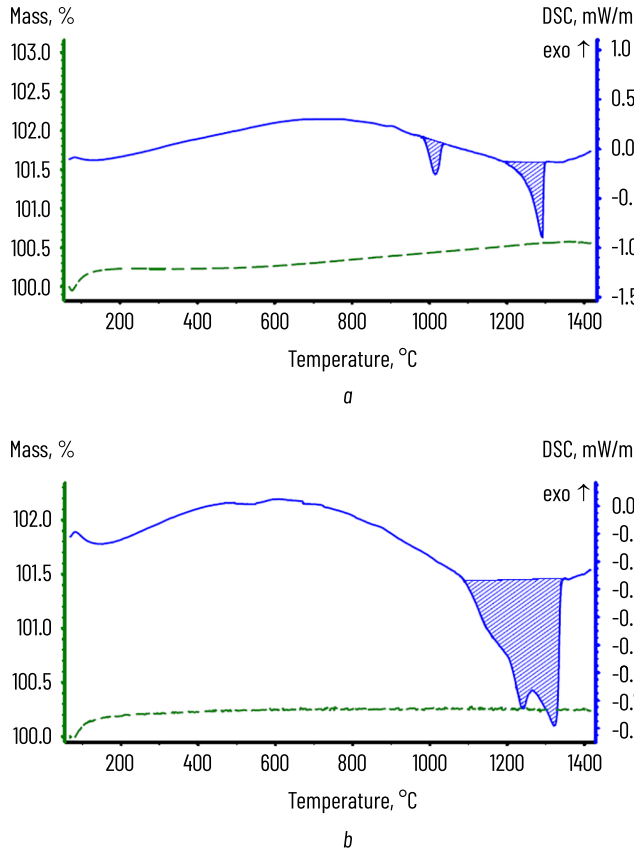

Fig. 3.9 STA curves: *a* — FeNiCrCuMn system; *b* — FeNiCrCuAl system

Table 3.8 Solidus, liquidus temperatures and crystallization intervals of high-entropy alloy samples

Sample No.	Solidus temperature, °C	Liquidus temperature, °C	Crystallization interval, °C	Melting heat, J/g	
				Solidus	Liquidus
1	2	3	4	5	6
1	988.6	1284.4	295.8	29	80
2	1200	1310.8	110.8	223*	–
3	1090	1320.8	230.8	226*	–

Continuation of Table 3.8

1	2	3	4	5	6
4	1123	1350	227	241*	–
5	996.9	1306.2	309.3	24	76
6	1098.5	1342.3	243.8	3,6	119
8	984.6	1281.2	296.6	30	131
9	990.8	1285.2	294.4	26	120
10	1100	1345.5	245.5	279*	

*Note: *Double peaks that cannot be separated.*

3.6 STUDY OF ELASTIC PROPERTIES OF HIGH–ENTROPY ALLOYS BY DMA METHOD

In this work, dynamic mechanical analysis (DMA) was first used to study the elastic properties and internal friction of high-entropy alloys depending on temperature. The basics of the DMA method were developed by K. Menard in 1998 [34]. DMA provides an opportunity to investigate the change in elastic properties of materials under the action of small periodic, usually sinusoidal dynamic loads depending on temperature, time and frequency. One of the leading companies in the world that produce DMA analyzers is the NETZSCH company (Germany). The DMA 242C analyzer of this company was used for the research.

Main technical characteristics of the DMA 242C analyzer of the NETZSCH company:

– temperature range: –170...600°C;

– frequency range: 0.01...100 Hz;

– range of adjustable loads: Max. ± 8 N static and Max. ± 8 N dynamic;

– range of deformation amplitudes: Max. ± 240 μm;

– sensitivity to the magnitude of deformation: 0.5 nm.

The appearance and schematic diagram of the DMA 242C analyzer are shown in **Fig. 3.10**.

As can be seen from the above characteristics, in this case very small loads are applied to the sample (total 1.6 kg), therefore this method is rarely used for metals and alloys. This method is widely used to study the mechanical characteristics of rubber, polymer films, polymers and fibers.

Based on the fact that the mechanical properties of alloys are structurally sensitive, that is, a change in the phase composition or structure of the material necessarily affects its mechanical characteristics, the DMA method was used not for its direct purpose – determining the absolute values of mechanical characteristics, but to study the features of structure formation in HEAs during their heat treatment and loading.

The principle of DMA operation is based on the registration of the reaction of the material (elongation, stress, phase shift, amplitude) to the action of small periodic dynamic loads depending on temperature, time and frequency. If a mechanical force (F) is applied to the sample under study, it will cause the

corresponding reaction of the material – deformation, stress, amplitude and phase shift. Registration of changes in parameters and appropriate mathematical processing make it possible to assess the influence of factors on the elastic properties of the material.

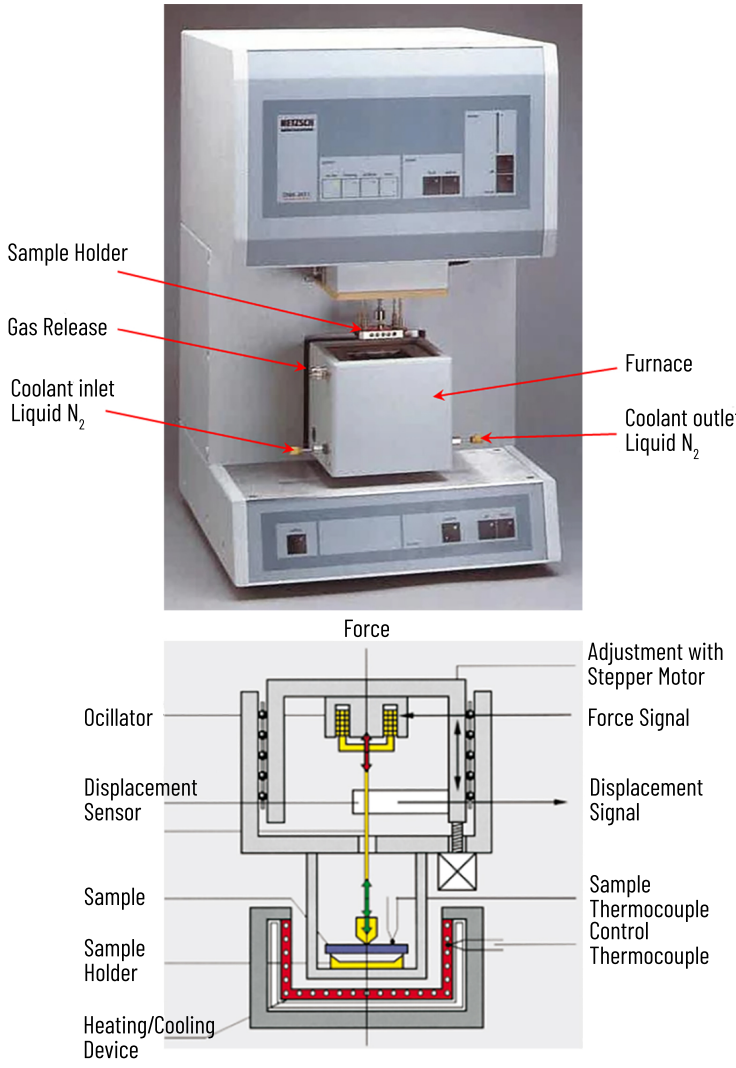

Fig. 3.10 Appearance and schematic diagram of the DMA 242C analyzer

As is known, the complex modulus of elasticity of a viscoelastic material can be written as:

$$|E| = \frac{\sigma}{\varepsilon}, \tag{3.13}$$

where E – the complex modulus, MPa; σ - the load, N; ε – the strain, μm; or

$$|E| = \sqrt{\left[E^{I}(\varepsilon)\right]^{2} + \left[E^{II}(\varepsilon)\right]^{2}}, \tag{3.14}$$

where E_I – the modulus of elasticity, characterizing the elastic properties of the material; E_{II} – the loss modulus, characterizing the conversion of mechanical energy into other types of energy, for example, into heat, and is a measure of the unreturned, lost energy of oscillations; ω – the frequency of oscillations.

Moduli of elasticity are vector quantities, the relationship between them is shown by the equations:

$$E^{I} = |E|\cos\delta, \tag{3.15}$$

$$E^{II} = |E|\sin\delta. \tag{3.16}$$

For an elastic material: $\alpha = 0$, cos 0 = 1, sin 0 = 0

$$E = E^{I}. \tag{3.17}$$

For a viscous material: $\alpha = 90^{\circ}$, $\cos 90^{\circ} = 0$, $\sin 90^{\circ} = 1$

$$E = E^{II}. \tag{3.18}$$

Often, to assess the elastic properties of materials, a quantity called the loss coefficient, or the tangent of the loss angle, or the internal friction of the viscoelastic system is used, it is defined as

$$\tan\alpha = \frac{E^{II}(\omega)}{E^{I}(\omega)}. \tag{3.19}$$

DMA analysis makes it possible to determine all the above parameters depending on time, temperature, load value and frequency. Additionally, it is possible to determine the coefficients of thermal expansion of the material.

DMA studies were carried out by the three-point bending method on samples measuring 2×1×45 mm at a static load of 8 N and a dynamic load of 7 N, a maximum amplitude of 100 μm and frequencies of 1, 5, 10 Hz.

Since there are no values of the elastic characteristics of high-entropy alloys in the literature, to assess the reliability of our results, a theoretical calculation of the elastic modulus was performed according to the additivity law:

$$E_{theor} = \sum_{i=1}^{n} c_i E_i, \tag{3.20}$$

where E_i – the Young's modulus of the i-th element; $c_i \leq 1$ – the concentration of the i-th element in atomic ratio; n – the number of elements in the alloy. The values of Young's modulus of pure metal elements are given in **Table 3.9**. The results of the studies are given in **Table 3.10** and **Fig. 3.11, 3.12**.

Table 3.9 Values of Young's modulus of pure metals

Metal	Al	Fe	Cr	Co	Ni	Mn	V	Ti	Zr	Nb	Hf	Ta
Young's modulus, GPa	70	210	250	200	200	194	135	120	97	105	137	186

Table 3.10 Elastic properties of the studied alloys

Alloy	Etheor, GPa	Eexp, GPa	Eexp/Etheor
$Ti_2ZrHfNbTa$	130.9	91	0.7
$TiZr_2HfNbTa$	134.2	119	0.88
$CrMnFeCo_2Ni_3$	210.7	194	0.92
$Al_5Cr_{15}Mn_{11}Fe_{18}Co_{17}Ni_{31}V_3$	202.9	147	0.72
$Al_{27}Cr_{16}Fe_{20}Co_{18}Ni_{19}$	174.9	131.2	0.75

Young's modulus and internal friction of the alloy are structurally sensitive parameters, therefore, using dynamic mechanical analysis, it is possible to establish those structural changes that are not recorded by DSC analysis, since they occur without thermal effects, or these effects are strongly stretched in time, therefore, DMA analysis can be used to study martensitic transformations [35, 36], relaxation in amorphous alloys [37] and other effects that are poorly recorded by other methods. The studies conducted in this way show that most of the obtained HEAs have structural transformations in the temperature range from 100 to 300°C.

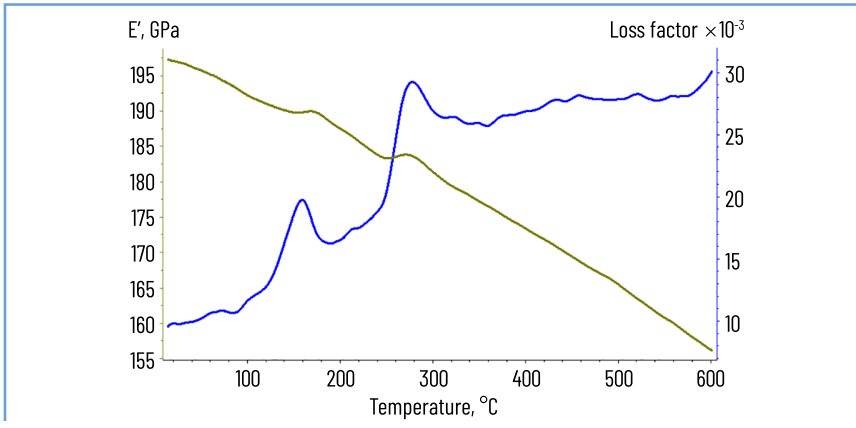

Fig. 3.11 Curves of dynamic mechanical analysis of high-entropy alloy $CrMnFeCo_2Ni_3$

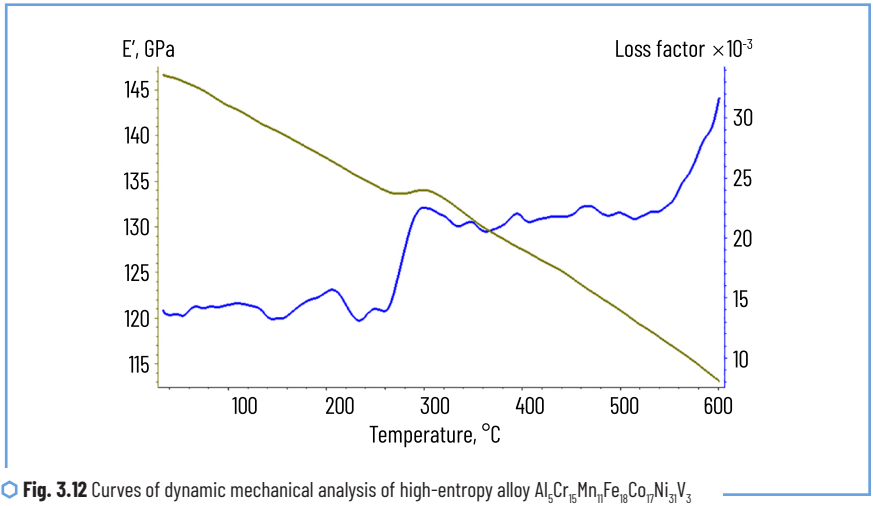

Fig. 3.12 Curves of dynamic mechanical analysis of high-entropy alloy $Al_5Cr_{15}Mn_{11}Fe_{18}Co_{17}Ni_{31}V_3$

3.7 RESEARCH ON THE HEAT RESISTANCE OF HIGH-ENTROPY ALLOYS

The heat resistance of high-entropy alloys was studied using the method of GOST 6130-71 "Methods for determining heat resistance", recording the ratio of the change in sample weight to its surface area (mg/cm^2). Using this method, the heat resistance of HEA samples that demonstrated low kinetics during heating and aging in an artificial air atmosphere at temperatures of 900°C or 1000°C was studied and the data were compared with standard alloys with different oxidation resistance.

To study the heat resistance, a STA 449 Jupiter F1 synchronous thermal analysis device was used. The study was carried out in an inert gas flow (high-purity argon 20 ml/min) and in a dynamic oxidizing environment (artificial air 20/80 O_2/N_2, 100 ml/min). The experiments were carried out on cast samples of the same size and shape. To establish the temperature and quantitative parameters of oxidation, two measurement modes were used: the study of oxidation kinetics and the study of heat resistance.

Mode 1. The samples were heated in air to 1450°C. The temperature of the onset of intensive oxidation was recorded using the thermogravimetry (TG) curve, which was determined by a sharp increase in the weight of the sample. The temperature of the onset of the exothermic effect and its enthalpy, which corresponds to the formation of an oxide film, were determined using the differential scanning calorimetry (DSC) curve. This mode allows to establish the characteristic temperatures of the onset of intensive oxidation with high accuracy (±1°C). The specific oxidation intensity was calculated as the ratio of the thermal effect to the surface area of the sample (J/g cm^2).

Mode 2. The samples were heated at the maximum possible rate of 50 K/min, subjected to isothermal holding in a stream of artificial air at 900°C and 1000°C for 4 hours with continuous control of the sample weight.

Heat resistance was estimated as the specific increase in the sample weight during the exposure time, related to its surface area (mg/cm^2.h).

Thermogravimetric diagrams of the oxidation of the samples were recorded and processed using the Netzsch Proteus software package.

There are compositions of the samples used for the studies in **Table 3.1**. In addition, Sample 7_1 was added to the study, which is close to Sample 7 but in its composition manganese was replaced by aluminum (actual composition in wt % of Al-15, Cr-17, Fe-23, Co-21, Ni-22).

For comparison of heat resistance, standard alloys G45, SM96, GX10CrNiMn18-9-1 were used. During the study, it was found that alloys G45, SM96 have low heat resistance compared to the studied samples of high-entropy alloys, therefore their values were not included in the final heat resistance comparison diagrams, these data can be found in **Table 3.11**.

Table 3.11 STA results of oxidation studies of standard alloys

No.	Alloy	Onset temperature of the intensive, oxidation °C	Oxidation intensity, J/g cm^2	Average oxidation at 900°C, mg/cm^2 h	Average oxidation at 1000°C, mg/cm^2 h
1	G45(C45)	948	2840	3.28	5.7
2	SM96	1113	358.3	0.85	2.31
3	GX10CrNiMn18-9-1	1142	1497	0.02	0.17

High-strength alloy SM96 with a special coating is used for the manufacture of blades of gas turbine engines, although it is excluded from the final comparison diagrams, it is heat-resistant, since compared to steel G45, its oxidation resistance is almost 4 times higher. Oxidation of this alloy occurs in two stages. The first stage begins at 1113°C and continues to 1318°C, in this temperature range there is moderate oxidation of the alloy, which leads to an increase in its weight by 0.63%. More intensive oxidation of this alloy begins at a temperature of 1318°C.

GX10CrNiMn18-9-1 steel showed sufficiently high heat resistance, therefore its results are shown in **Fig. 3.13** and **3.14** under number 8. Although this alloy has an temperature of intensive oxidation above 1000°C. Within prolonged exposure at 1000°C, its low oxidation intensity is initially maintained, but after 200 min exposure, the sample begins to oxidize intensively and the surface of the sample is quickly covered with a dense layer of oxide. After 30 minutes, an oxide layer forms on the surface of the sample, blocking access to the metal surface and the oxidation rate decreases, **Fig. 3.15**.

HEA Sample No. 1 when heated to 1000°C has a threshold for increasing the intensity of oxidation at a temperature close to 400°C and from this temperature gradually oxidizes (**Fig. 3.16**). Other HEA samples with manganese (Samples No. 5, 7) behave in a similar way. When exposed for 4 hours at 900°C, they continue to oxidize evenly, the intensity of oxidation decreases with exposure time, which is obviously a consequence of the oxide layer. But when heated to 1000°C, the intensity of oxidation remains approximately the same.

HEA No. 4 when heated to 1000°C practically does not oxidize during heating (**Fig. 3.17**). When exposed for 4 hours at 900°C, it oxidizes evenly with a very low intensity (average oxidation rate 0.001 mg/min). The same, low level of oxidation intensity is maintained when exposed at a temperature of 1000°C. HEA No. 6 behaves similarly, which is close in chemical composition to HEA No. 4 and contains Al at the base of its chemical composition.

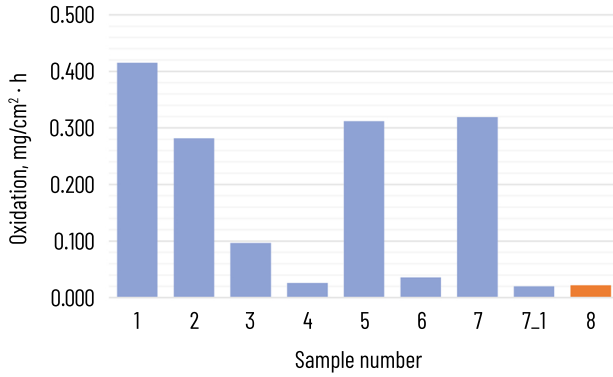

Fig. 3.13 Average oxidation of samples mg/cm²·h at 4-hour isothermal holding at 900°C

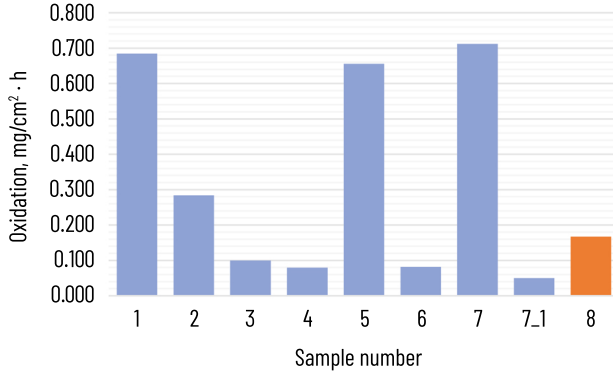

Fig. 3.14 Average oxidation of samples mg/cm²·h at 4-hour isothermal holding at 1000°C

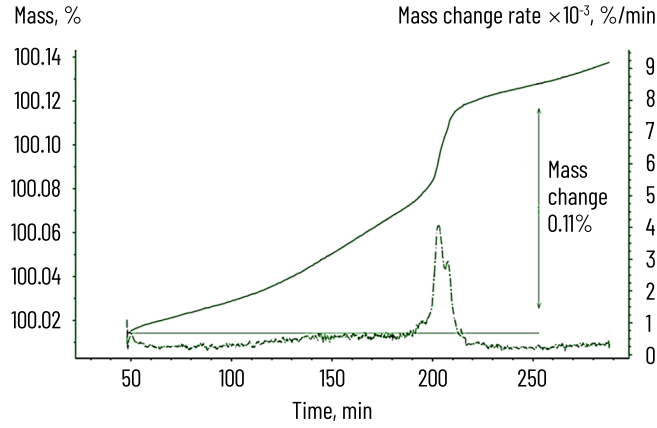

Fig. 3.15 Thermogravimetric diagram of steel GX10CrNiMn18-9-1 when exposed to artificial air at 1000°C

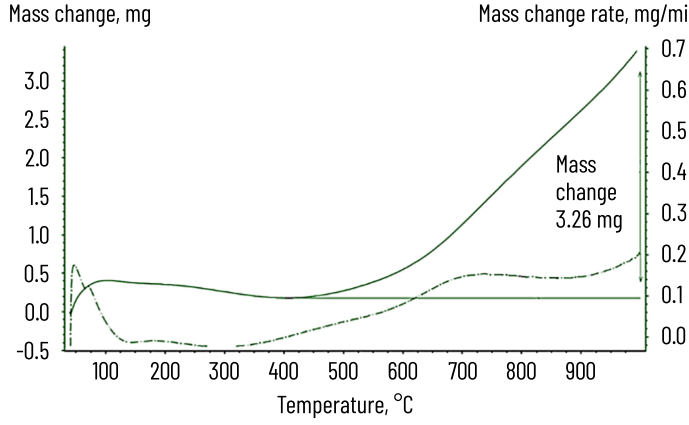

Fig. 3.16 Thermogravimetric diagram of the HEA Sample No.1 when heated to 1000°C

HEA Sample No. 3, similar in chemical composition, is oxidized more intensively, but still at a relatively low level. It demonstrates equally high heat resistance and its oxidation rate is in the range from 0.002 mg/min to 0.003 mg/min when exposed for 4 hours both at 900°C and at 1000°C.

HEA No. 2, when heated to 1000°C begins to gain weight of the oxide film at temperatures above 400°C, and already at a temperature of 516°C begins to oxidize intensively, rapidly gaining weight with an intensity of up to 0.219 mg/min (**Fig. 3.18**). The surface of the sample is quickly covered with a layer of oxide, which

blocks access to the metal surface and already at a temperature close to 800°C the oxidation rate decreases, but above 900°C the oxidation intensity begins to increase again.

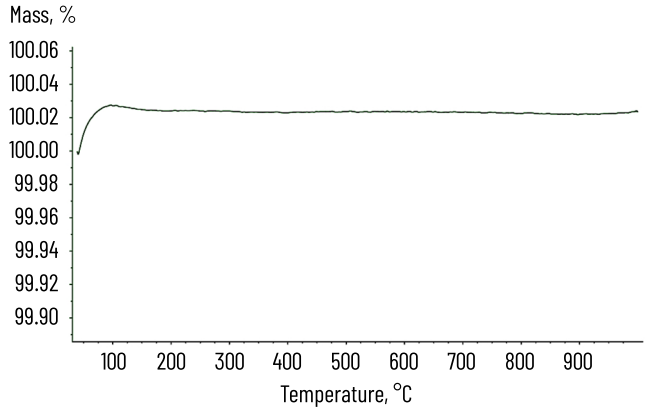

Fig. 3.17 Thermogravimetric diagram of HEA Sample No. 4 when heated to 1000°C

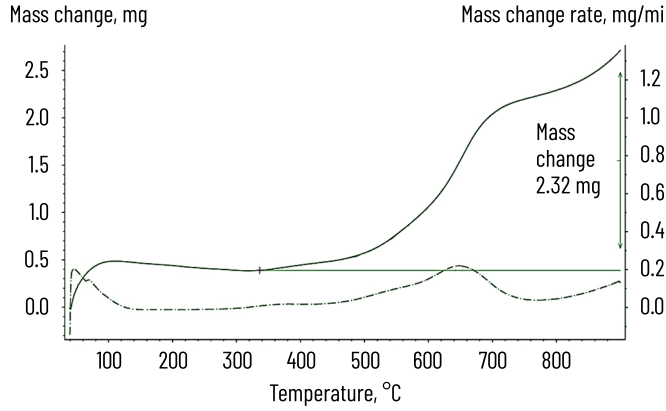

Fig. 3.18 Thermogravimetric diagram of the HEA Sample No. 2 when heated to 1000°C

After 4 hours at 900°C, the sample continues to oxidize evenly, but with a low oxidation intensity, since the oxide layer protects the surface of the sample. Approximately the same oxidation intensity is maintained after 4 hours at a temperature of 1000°C. Such a strong difference in heat resistance is probably directly related to the decrease in the chromium content in the sample.

A representative example is HEA Sample No. 7_1. Its composition is similar to that of HEA No. 7, but with manganese content replaced by aluminum. This substitution immediately altered the oxidation behavior. The heat resistance of this alloy at 900°C reaches the level of the reference alloy GX10CrNiMn18-9-1 (**Fig. 3.13**) and significantly surpasses it at 1000°C (**Fig. 3.14**). Furthermore, intensive oxidation is absent up to its melting point of approximately 1379°C.

HEA Samples No. 1, 5, 7 have average heat resistance, which significantly exceeds standard structural steels (G45) and even the heat-resistant alloy SM96. They begin to oxidize at 400—500°C, but the oxide layer at higher temperatures partially protects the materials.

HEAs samples No. 3, 4, 6, 7_1 practically do not oxidize at 900°C and 1000°C, surpassing steel GX10CrNiMn18-9-1 at temperatures above 900°C. Therefore, the oxidation behavior of the studied samples of high-entropy alloys differs depending on their composition. Thus, samples containing a combination of a significant amount of Al (6—11%) and Cr (14—18%), which contribute to the formation of protective oxide films Al203 and Cr203, have the best performance and an intensive oxidation temperature above 1000°C. Samples containing manganese and not containing aluminum have the lowest heat resistance in this alloy system. All samples with a high Mn content (~16—19%) showed the worst performance. HEA Sample No. 2 (Al ~11%, but Cr only ~13%) has worse resistance than HEA No. 3 (Al ~10%, Cr ~14%), which emphasizes the importance of the combination of these elements. The content of Copper (Cu) can worsen heat resistance, the most resistant samples are: No. 6 — has an average Cu content of ~20%, No. 7_1 does not contain copper at all (in its composition it is replaced by cobalt). HEA Sample No. 3 has the highest Cu content ~23.2%, which may also be the reason for the deterioration of heat and scale resistance indicators despite the presence of Al and Cr in sufficiently large quantities. This suggests that an excess amount of copper may be harmful and it is advisable to completely or partially replace it with cobalt to increase heat resistance.

CONCLUSIONS

A specially designed vacuum medium-frequency induction furnace provides reliable melting of high-entropy alloys (HEAs) at temperatures up to 1800°C with active mixing of the melt. This allows obtaining homogeneous ingots with precise chemical composition and minimizing the formation of non-metallic inclusions.

Thermodynamic analysis of HEAs compositions (estimation of mixing entropy, enthalpy, δ_r, $\Delta\chi$, VEC, Ω) showed that most of the studied alloys meet the criteria for the formation of solid solutions. In alloys with aluminum, the probability of the formation of ordered intermetallic phases of type B2 (NiAl) was revealed.

X-ray phase analysis confirmed the presence of FCC and BCC phases, in particular phases of type γ-Fe, B2-NiAl. In alloys with a high Mn content, two FCC phases with different lattice parameters are formed. The calculated lattice periods correlate with the theoretical VEC parameters.

Thermophysical characteristics of the alloys (liquidus/solidus temperatures, heats of fusion and crystallization) were determined experimentally based on STA studies. It was shown that the crystallization intervals for HEAs significantly affect their fluidity and dendritic morphology during casting.

The HEAs elastic properties were investigated by the method of dynamic mechanical analysis (DMA). It was found that the elastic modulus E' decreases with increasing temperature, and the loss tangent tgδ demonstrates stable viscoelastic behavior up to 600—700°C. This indicates good stability of the structure under thermomechanical loading.

The heat resistance of the alloys was tested at temperatures of 600—800°C. FeNiCrCuMn and FeNiCrCuAl alloys showed a slight change in mass, preservation of phase composition and microstructure, which indicates a high level of oxidative stability and suitability for long-term operation at high temperatures in air.

The casting properties of the HEAs (fluidity, shrinkage) were studied using spiral and U-shaped test molds. The best indicators were obtained for the the FeNiCrCuAl system alloys, which demonstrated a filling length of up to 320 mm, which exceeds the indicators of gray and special cast iron.

High-entropy alloys based on the FeNiCrCuAl system is promising heat-resistant casting material of a new generation. It combines good fluidity, high thermal stability, favorable microstructure and resistance to oxidation, which opens up wide possibilities for their practical application in critical machine components, heat exchangers, energy and chemical equipment.

FINANCING

The work was carried out within the framework of the program of Scientific and scientific-technical (experimental) works of the National Academy of Sciences of Ukraine in the priority area "Resource-saving, energy-saving and environmentally safe technologies of innovative materials for industry, medicine and defense" for 2025—2026, contract No. 5.9/25-П(1) dated 01.01.2025.

CONFLICT OF INTEREST

The authors declare that they have no conflict of interest in relation to this research, whether financial, personal, authorship or otherwise, that could affect the research and its results presented in this paper.

USE OF ARTIFICIAL INTELLIGENCE

The authors confirm that they did not use artificial intelligence technologies in creating the submitted work.

REFERENCES

1. Yeh, J.-W. (2002). U.S. Patent No. 2002/0159917 A1. High-entropy multielemental alloys. Available at: https://patents.google.com/patent/US20020159914A1/

2. Ranganathan, S. (2003) Alloyed pleasures: multimetallic cocktails. Current science, 85 (10), 1404—1406. Available at: https://www.currentscience.ac.in/Volumes/85/10/1404.pdf
3. Yeh, J.-W., Chen, S.-K., Lin, S.-J., Gan, J.-Y., Chin, T.-S., Shun, T.-T., Tsau, C.-H., & Chang, S.-Y. (2004). Nanostructured High-Entropy Alloys with Multiple Principal Elements: Novel Alloy Design Concepts and Outcomes. Advanced Engineering Materials, 6 (5), 299—303. https://doi.org/10.1002/adem.200300567
4. Miracle, D., Miller, J., Senkov, O., Woodward, C., Uchic, M., Tiley, J. (2014). Exploration and Development of High Entropy Alloys for Structural Applications. Entropy, 16 (1), 494—525. https://doi.org/10.3390/e16010494
5. Zhang, Y., Zhou, Y. J., Lin, J. P., Chen, G. L., Liaw, P. K. (2008). Solid-Solution Phase Formation Rules for Multi-component Alloys. Advanced Engineering Materials, 10 (6), 534—538. https://doi.org/10.1002/adem.200700240
6. Zhang, Y., Zuo, T. T., Tang, Z., Gao, M. C., Dahmen, K. A., Liaw, P. K., Lu, Z. P. (2014). Microstructures and properties of high-entropy alloys. Progress in Materials Science, 61, 1—93. https://doi.org/10.1016/j.pmatsci.2013.10.001
7. Zhang, Y., Lu, Z. P., Ma, S. G., Liaw, P. K., Tang, Z., Cheng, Y. Q., Gao, M. C. (2014). Guidelines in predicting phase formation of high-entropy alloys. MRS Communications, 4 (2), 57—62. https://doi.org/10.1557/mrc.2014.11
8. Miedema, A. R., de Châtel, P. F., de Boer, F. R. (1980). Cohesion in alloys — fundamentals of a semi-empirical model. Physica B+C, 100 (1), 1—28. https://doi.org/10.1016/0378-4363(80)90054-6
9. Niessen, A. K., de Boer, F. R., Boom, R., de Châtel, P. F., Mattens, W. C. M., Miedema, A. R. (1983). Model predictions for the enthalpy of formation of transition metal alloys II. Calphad, 7 (1), 51—70. https://doi.org/10.1016/0364-5916(83)90030-5
10. Takeuchi, A., Inoue, A. (2005). Classification of Bulk Metallic Glasses by Atomic Size Difference, Heat of Mixing and Period of Constituent Elements and Its Application to Characterization of the Main Alloying Element. Materials Transactions, 46 (12), 2817—2829. https://doi.org/10.2320/matertrans.46.2817
11. Boer, F. R. de, Mattens, W. C. M., Boom, R, Miedema, A. R., Niessen, A. K. (1998). Cohesion in metals. Transition metal alloys. Netherlands, 774.
12. Debski, A., Debski, R., Gasior, W. (2014). New Features of Entall Database: Comparison of Experimental and Model Formation Enthalpies. Archives of Metallurgy and Materials, 59 (4), 1337—1343. https://doi.org/10.2478/amm-2014-0228
13. Zhang, Y. (2010). Mechanical Properties and Structures of High Entropy Alloys and Bulk Metallic Glasses Composites. Materials Science Forum, 654-656, 1058—1061. https://doi.org/10.4028/www.scientific.net/msf.654-656.1058
14. Yang, X., Zhang, Y. (2012). Prediction of high-entropy stabilized solid-solution in multi-component alloys. Materials Chemistry and Physics, 132 (2-3), 233—238. https://doi.org/10.1016/j.matchemphys.2011.11.021
15. Yeh, J.-W.; Gao, M. C., Yeh, J.-W., Liaw, P. K., Zhang, Y. (Eds.) (2016). Overview of High-Entropy Alloys. High-Entropy Alloys. Springer International Publishing 1—19. https://doi.org/10.1007/978-3-319-27013-5_1
16. Guo, S., Liu, C. T. (2011). Phase stability in high entropy alloys: Formation of solid-solution phase or amorphous phase. Progress in Natural Science: Materials International, 21 (6), 433—446. https://doi.org/10.1016/s1002-0071(12)60080-x

17. Guo, S., Ng, C., Lu, J., Liu, C. T. (2011). Effect of valence electron concentration on stability of fcc or bcc phase in high entropy alloys. Journal of Applied Physics, 109 (10). https://doi.org/10.1063/1.3587228
18. Singh, A. K., Subramaniam, A. (2014). On the formation of disordered solid solutions in multi-component alloys. Journal of Alloys and Compounds, 587, 113–119. https://doi.org/10.1016/j.jallcom.2013.10.133
19. Jiang, L., Lu, Y. P., Jiang, H., Wang, T. M., Wei, B. N., Cao, Z. Q., Li, T. J. (2016). Formation rules of single phase solid solution in high entropy alloys. Materials Science and Technology, 32 (6), 588–592. https://doi.org/10.1179/1743284715y.0000000130
20. Zhu, J. H., Liaw, P. K., Liu, C. T. (1997). Effect of electron concentration on the phase stability of NbCr2-based Laves phase alloys. Materials Science and Engineering: A, 239-240, 260–264. https://doi.org/10.1016/s0921-5093(97)00590-x
21. Jin, X., Zhou, Y., Zhang, L., Du, X., Li, B. (2018). A new pseudo binary strategy to design eutectic high entropy alloys using mixing enthalpy and valence electron concentration. Materials & Design, 143, 49–55. https://doi.org/10.1016/j.matdes.2018.01.057
22. Li, H., He, W., Wang, F., Han, X., Wang, X., Wang, G. et al. (2024). Wear performance of FeCuMoTiV high entropy alloy coatings by laser cladding. Surface Topography: Metrology and Properties, 12(2), 025013. https://doi.org/10.1088/2051-672x/ad4403
23. Li, H., Shen, W., He, W., Jiao, L., Zhang, C., Song, Z. et al. (2025). Preparation of AlCoCrFeNi HEA wear-resistant coatings by laser cladding on the surface of (ZrB2+Al3Zr)/AA6016. Materials Today Communications, 48, 113575. https://doi.org/10.1016/j.mtcomm.2025.113575
24. Zhang, X., Li, H., Jiao, L., Wang, G., Wang, X., Zhang, C. et al. (2024). Effect of Rotational Speed on Microstructure and Properties of Al-Based Composite Reinforced with High-Entropy-Alloy Particles Fabricated by Friction Stir Processing. Advanced Engineering Materials, 26 (23). https://doi.org/10.1002/adem.202401417
25. Li, H., Li, C., Qiao, Y., Lu, S., Wang, F., Sun, C. et al. (2022). Preparation of in-situ ZrB2/A356 composites and high-temperature tribological studies. Materials Research Express, 9 (4), 046508. https://doi.org/10.1088/2053-1591/ac62b6
26. Korzhyk, V., Khaskin, V., Grynyuk, A., Peleshenko, S., Kvasnytskyi, V., Fialko, N. et al. (2022). Comparison of the features of the formation of joints of aluminum alloy 7075 (Al-Zn-Mg-Cu) by laser, microplasma, and laser-microplasma welding. Eastern-European Journal of Enterprise Technologies, 1 (12 (115)), 38–47. https://doi.org/10.15587/1729-4061.2022.253378
27. Shcheretskyi, O. A., Sergiienko, R. A., Verkhovliuk, A. M. (2022). Development and smelting of casting high-entropy alloys based on the Fe-Co-Ni-Mn-Cr system. Casting Processes, 148 (2), 50–59. https://doi.org/10.15407/plit2022.02.050
28. Yeh, J.-W. (2013). Alloy Design Strategies and Future Trends in High-Entropy Alloys. JOM, 65 (12), 1759–1771. https://doi.org/10.1007/s11837-013-0761-6
29. Verkhovliuk, A. M., Sergiienko, R. A., Shcheretskyi, O. A., Serhiiko, R. S., Potrukh, O. G., Kanibolotsky, D. S. et al. (2024). Casting properties of high-entropy alloys of the FeNiCrCuAl and FeNiCrCuMn systems. Casting Processes, 158 (4), 56–65. https://doi.org/10.15407/plit2024.04.056

30. Lakhnenko, V. L., Shcheretskyi, A. A., Apukhtin, V. V., Gavrilyuk, K. V. (2005). Methodological aspects of determining the fluidity of alloys with significantly different thermophysical characteristics. Casting Processes, 3, 28—34.
31. Kao, Y.-F., Chen, T.-J., Chen, S.-K., Yeh, J.-W. (2009). Microstructure and mechanical property of as-cast, -homogenized, and -deformed AlxCoCrFeNi (0≤x≤2) high-entropy alloys. Journal of Alloys and Compounds, 488 (1), 57—64. https://doi.org/10.1016/j.jallcom.2009.08.090
32. Pavlina, E. J., Van Tyne, C. J. (2008). Correlation of Yield Strength and Tensile Strength with Hardness for Steels. Journal of Materials Engineering and Performance, 17 (6), 888—893. https://doi.org/10.1007/s11665-008-9225-5
33. Shcheretskyi, O. A., Verkhovliuk, A. M., Sergiienko, R. A., Zadorozhnyy, V. Yu.; Fesenko, O., Yatsenko, L. (Eds.) (2021). Obtaining Nanostructured Materials by Heat Treatment of Amorphous Zirconium-Based Alloy. Nanooptics and Photonics, Nanochemistry and Nanobiotechnology, and Their Applications. Springer, 257—271. https://doi.org/10.1007/978-3-030-74800-5_17
34. Menard, K. P. (2008). Dynamic Mechanical Analysis: A Practical Introduction. CRC Press. https://doi.org/10.1201/9781420053135
35. Koval, Yu. M., Odnosum, V. V., Slipchenko, V. M., Filatova, V. S., Filatov, A. S., Shcheretskyi, O. A., Firstov, G. S. (2024). Influence of Grain Size on Shape Memory and Internal Friction in $Cu_{69.26}Al_{25.86}Mn_{4.88}$ Alloy. Metallofizika i Noveishie Tekhnologii, 46 (9), 933—941. https://doi.org/10.15407/mfint.46.09.0933
36. Ivanova, O., Shcheretsky, O., Podrezov, Y., Karpets, M. (2017). Young's modulus and damping capacity of Ti 3 Sn intermetallic compound with 1 at% and 3 at% of Zr and Al additions. Materials Science and Engineering: A, 683, 252—255. https://doi.org/10.1016/j.msea.2016.12.030
37. Sergiienko, R. A., Shcheretskyi, O. A., Zadorozhnyy, V. Yu., Verkhovliuk, A. M., Louzguine-Luzgin, D. V. (2019). Investigation of Zr55Cu30Al10Ni5 bulk amorphous alloy crystallization. Journal of Alloys and Compounds, 791, 477—482. https://doi.org/10.1016/j.jallcom.2019.03.270

DOI: 10.15587/978-617-8360-17-7.CH4

Oleg Shinsky, Inna Shalevska, Iuliia Kvasnytska,
Pavlo Kaliuzhnyi, Oleksandr Neima, Anatolii Shalevskyi

4 CAST STRUCTURES WITH COMPOSITE AND REINFORCED NON-METALLIC FUNCTIONAL FILLER

ABSTRACT

The chapter presents the results of research on the scientific and technological prerequisites for obtaining steel hollow castings with composite and reinforced non-metallic filler by the lost foam casting method.

A system of equations was obtained that describes the gas-hydrodynamic conditions of lost foam casting with polystyrene patterns saturated with reinforcing elements (RE), and taking into account the heat exchange between RE and the matrix melt during mold filling and casting solidification.

Modern domestic and foreign materials for cast structures for protective purposes were analyzed and the prospects for the use of low-alloy and microalloyed steels were determined. It was established that optimal performance characteristics are achieved under the conditions of the correct selection of heat treatment modes, which provides a combination of high strength with sufficient plasticity.

To determine the influence of composite and non-metallic fillers on the possibility of obtaining a high-quality casting, computer simulation methods were used and the results obtained were verified by full-scale experiments.

The research conducted by the authors at the Physico-Technological Institute of Metals and Alloys of the National Academy of Sciences of Ukraine and carried out within the framework of project No. 2023.04/0029, state registration 0124U003980, supported by a grant from the National Research Foundation of Ukraine under the program "Science for Strengthening the Defense Capability of Ukraine" is of high scientific and practical importance for the manufacture of special-purpose foundry products and will be useful for specialists-manufacturers of foundry, scientists and scientific and pedagogical workers in the specialty "Metallurgy" (Foundry).

KEYWORDS

Reinforced cast structure, reinforcing filler, matrix melt, gas-hydrodynamic conditions, heat exchange processes, computer simulation, polystyrene foam pattern, cast steel, alloying, lost foam casting, heat treatment of steel, technological process.

Modern foundry production today is focused on a significant reduction in the metal content of products, simultaneously with the complication of their geometry and functional purpose. Therefore, the creation of scientifically based new technologies for the manufacture of hollow steel structures with special

properties by the method of lost foam casting using reinforcing fillers is relevant and required additional research into the processes of heat and mass transfer and gas-hydrodynamics and the determination of optimal technological parameters.

To implement in industry a new design of cast hollow steel modules with a spherical surface and high-hardness compacted fillers and metal composites with a steel shell, the technology of lost foam casting was adapted, which made it possible to obtain a given binary design of modules of the system "steel shell – compacted filler in a bound state" and "steel shell – reinforced metal composite" in a single-cycle technological process and directly in the mold.

The new technological process for producing cast binary modules is based on the use of polystyrene foam patterns filled with the specified dispersed materials, which are installed in a mold, in which a vacuum is created and directly in the presence of the pattern, the liquid metal of the shell is poured. Under the conditions of heat exchange between the liquid metal and the polymer pattern, the latter undergoes thermal destruction, and its volume is filled with liquid metal. Under the influence of the heat flow from the metal, the filler forms a solid material in the form of a metal composite with a reinforcing steel phase, which corresponds in chemical composition to the shell metal. In this case, the liquid metal seeps into the filler due to the pressure gradient between the metal P_m and the porous filler P_f (P_m–P_f), since a vacuum is formed in the latter within (0.1...0.2) P_a (P_a – atmospheric pressure).

4.1 DETERMINATION OF THE THERMOPHYSICAL MODEL OF THE INTERACTION OF THE REINFORCING FILLER AND THE STEEL MATRIX MELT IN THE MOLD

The production of reinforced castings by lost foam casting are accompanied by complex gas-hydrodynamic and heat-mass exchange processes. When obtaining hollow castings by reinforcing them with metal and non-metallic fillers located in polystyrene foam patterns, new multi-component systems arise for the theory of casting processes: "metal – pattern – filler – mold" and "metal – reinforcing filler – mold". Therefore, the study of the regularities of heat and mass exchange in these systems in the manufacture of shell binary cast structures and their mathematical description is relevant. In this case, it is necessary to determine the influence of the presence of solid and porous polystyrene foam patterns, metal and non-metallic materials in the mold on the conditions of heat exchange in the mold. The phenomenon of liquid flow during lost foam casting is essentially a problem of unsteady flow with free boundaries. Molten metal flowing in the mold during lost foam casting destroys the polystyrene foam pattern, forming a gas gap between the molten metal and the pattern. The rate of destruction of the pattern and the pressure in this gap depend on the heat exchange in the mold, and in the presence of reinforcing elements this process is complicated. There is information on the development of a two-dimensional thermal model, which is based on the mass and energy balance in the gas gap between the polystyrene foam pattern and the molten metal. The pressure in the gap is determined by the mass and energy balance method, which directly takes into account such important process parameters as the permeability of the coating, foam characteristics, pouring temperature and metal properties, but does not take into account the presence of additional reinforcement [1].

Therefore, research devoted to the development of a thermophysical model of the interaction of the reinforcing filler, polystyrene foam pattern and liquid steel in the mold during lost foam casting was relevant.

At the same time, the development of a thermophysical model of the interaction of the reinforcing filler, liquid steel and polystyrene foam pattern in the mold during lost foam casting will make it possible to predict the conditions of the melt flow, its solidification and cooling in the mold, which makes it possible to create promising casting methods for obtaining high-quality reinforced structures, including hollow binary modules for protective structures.

The authors established the conditions of heat exchange in the mold in which the reinforcing elements are placed, under different flow regimes of the matrix alloy in the porous channels of the polystyrene foam pattern.

The process of interaction of molten metal with mono- and reinforced polystyrene foam pattern during lost foam casting was investigated.

According to previously established laws on the conditions of casting solidification, movement of matrix alloy (MA) in the mold in the presence of metal reinforcing elements (RE), their interaction with the polystyrene foam pattern and thermal destruction products in the form of liquid, gaseous and solid phases, a physical model of mass and heat transfer was developed during the formation of the structure and properties of cast reinforced structures in multicomponent systems new to the theory of casting processes: "metal – pattern – RE – mold" [2, 3].

At the same time, the boundary temperature conditions and the final temperature at the heat exchange boundary of the "MA-RE" system were established

$$T_k = \frac{T_L - T_S}{2}, \tag{4.1}$$

where T_L, T_S – liquidus and solidus temperatures for the matrix alloy, °C.

For the integrated MA-RE system, the heat exchange contact area will be $n.S_P$, $n.S_{MRE}$, respectively, where n –the number of reinforcing elements located in the mold cavity, pcs., and their mass will be

$$m = 0.785 \cdot n \cdot g_{MRP} \cdot R^2_{MRP} \cdot L_{MRP}, \text{ kg} \tag{4.2}$$

where g_{MRP} – density, kg/m^3; L_{MRP} – characteristic length of the reinforcing element, m.

It should be noted that the vertical reinforcing elements installed in the mold (in this case, it is possible to consider them in the form of rods) complicate the flow area of the liquid metal (mold) and have a certain effect on the thermophysical and hydrodynamic processes occurring in it.

When obtaining castings, the resistance of the filler metal medium to be poured depends on the temperature conditions of filling the mold, the dimensions and geometry of the reinforcing elements and their placement in the mold cavity. It should be noted that the liquid alloy with dense packing of RE flows through "capillary" thin channels, which are formed by particles of these elements or in the cavity of the mold, in which RE are located at a fixed distance from each other.

To simplify the problem, it is possible to use the conditions of heat exchange in the form of a limit in a single channel of length L, filled with rods according to the heat balance scheme presented in works [3, 4] and in **Fig. 4.1, *a***, and has the form

$$c_p \cdot \rho \cdot V_{cp} \cdot F_c \cdot \left(T_{b_1} - T_{b2}\right) = \alpha_c \cdot F_n \cdot \left(T_c - T_b\right)_c, \quad (4.3)$$

where T_{b2} – the average temperature at the channel outlet over the channel cross section, °C;

T_{b1} – the average temperature at the channel inlet over the channel cross section, °C;

C_p – the specific heat capacity, J/(kg×°C);

ρ – the MA density, kg/m^3;

F_c – the cross-sectional area of a single capillary channel, m^2;

V_c – the average flow velocity in the channel, m/s;

F_n – the total contact area of the liquid metal with the surface of the channel (filler), m^2;

T_c – the average wall temperature along the channel length, °C;

T_b – respectively, the average temperature of the liquid alloy along the channel length, °C;

α_c – the heat transfer coefficient at the boundary of the porous channel formed between the RE and the MA melt, W/m^2,°C.

It is also recommended to determine the heat transfer coefficient by formulas, the structure of which depends on the MA flow regime in the pore channels (laminar or turbulent) [4]. At the same time, for practical use and study of the kinetics of changes in the temperature of the matrix melt in the pore space, it is recommended to represent the contact surface of heat exchange in the system "matrix melt – reinforced phase" through the equivalent (integral) radius of the reinforcing element R_{ae} [2]. In this case, the heat transfer coefficient for the MA laminar flow in the channels formed by the RE is determined by the equation of the dimensionless heat transfer coefficient Nu_D [4]

$$Nu_{\overline{D}} = \frac{\alpha_c \overline{D}}{\lambda_c} = 1.86\left(\mathrm{Re}_{\overline{D}} \cdot \mathrm{Pr}\right)^{0,33} \cdot \left(\frac{\overline{D}}{L}\right)^{0,33} \cdot \left(\frac{\mu_b}{\mu_s}\right)^{0,14}, \quad (4.4)$$

where $\overline{D}$ – the given channel diameter, m;

λ_c – Nusselt criterion, which characterizes the similarity of heat transfer processes at the interface between the wall and the fluid flow;

$\mathrm{Pr} = \frac{\nu}{a}$ – Prandtl criterion;

$\mathrm{Re} = \frac{V \cdot \overline{D}}{\nu}$ – Reynolds criterion;

n – viscosity coefficient, m^2/s;

α_c – thermal diffusivity coefficient, m^2/s;

μ_b – dynamic viscosity at metal temperature T_b, H×s/m^2;

μ_c – dynamic viscosity at wall temperature T_s(T_s^3 T_L);

T_L – liquidus temperature of the matrix alloy °C.

For turbulent MA flow regime in RE porous channels, the formula for *Nu* is recommended

$$Nu_{\overline{D}} = \frac{\alpha_c \cdot \overline{D}}{\lambda_c} = 0{,}036 \cdot \mathrm{Re}_D^{0{,}8} \cdot \mathrm{Pr}^{0{,}33} \cdot \left(\frac{\overline{D}}{L}\right)^{0{,}055}, \quad (4.5)$$

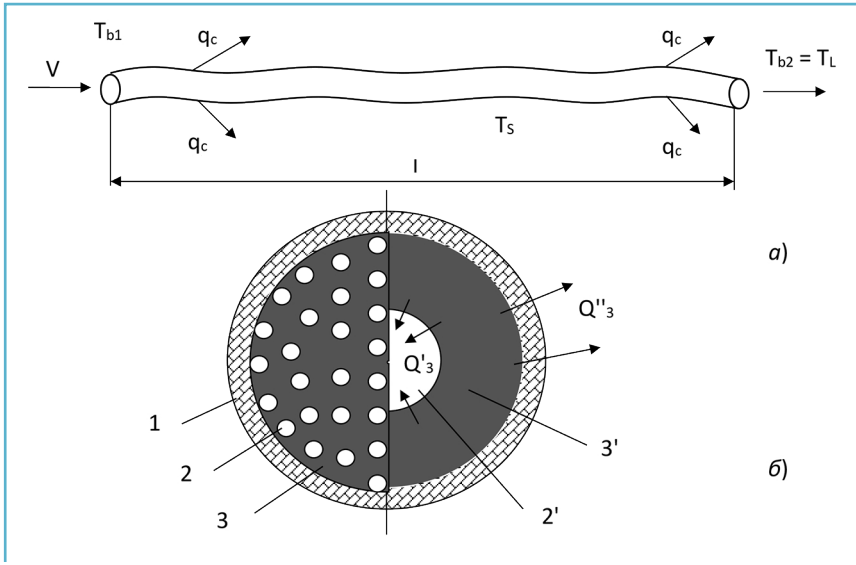

Fig. 4.1 Heat exchange scheme during melt flow in the pore space of the reinforcing phase along: a - the length; b - the cross-section of the mold with RE oriented in it: (*b*): 1 — shell (mold); 2 — reinforcing element; 3 — matrix melt; 2′ — equivalent cross-section of the reinforcing element; 3′ — equivalent cross-section of the matrix melt
Source: [3]

However, despite the achievements in the theory of MA melt flow in the RE environment located in the cavity of the mold, in the theory of lost foam casting the features of the interaction of thermal destruction products of the gasified pattern (GP) and their influence on the gasohydrodynamics of the process and the formation of the quality of cast blanks in the absence of a macroreinforcing phase were more often considered.

The RE presence directly in the polystyrene GP, and the latter is located in the cavity of the mold, allows to change the conditions of filtration and mass transfer of vapor-gas (VGP) and liquid products (LP), which are formed during the destruction of the pattern and modify the gas dynamics of the process, as well as the conditions for forming the quality of castings.

The features of VGP filtration through the known system: " VGP — coating — mold" and the new "VGP RE channel — GP — coating — mold" were considered, taking as a basis the physical model of the process of filling the mold with GP with "zero" open porosity, which is presented in the works [2, 5].

When filling the mold through the gap "metal — pattern" and channels around the reinforcing elements, the GP undergoes the VGP filtration process. During the mold pouring with liquid MA 1 (**Fig. 4.2**) at a speed W_1, the GP decomposes at a linear speed W_5, and since $W_1 < W_5$, a "meta l- pattern" gap d_1 is formed, in which a backpressure R_f is formed due to the VGP formation. At the same time, the LP covers the entire surface of the MA flow front in the form of a thin film "*D*" [6]. The heat flux from the liquid MA to the GP is transmitted by radiation and thermal conductivity through the LP film "*D*" and the gas-saturated gap "*d*". In this case, the heat exchange surface on the side of the pattern F_5 is reduced by the area of the RE F_a compared to the monopattern. In addition, part of the pattern destruction products at the time of the formation of the gap d_1 is filtered in the VGP form into the depth of the mold under the action of the P_f–P_a pressure gradient, first through the refractory coating (RC) 2 and accumulates on the grains of the molding material (MM) 4 in the form of a condensed liquid phase (CLP).

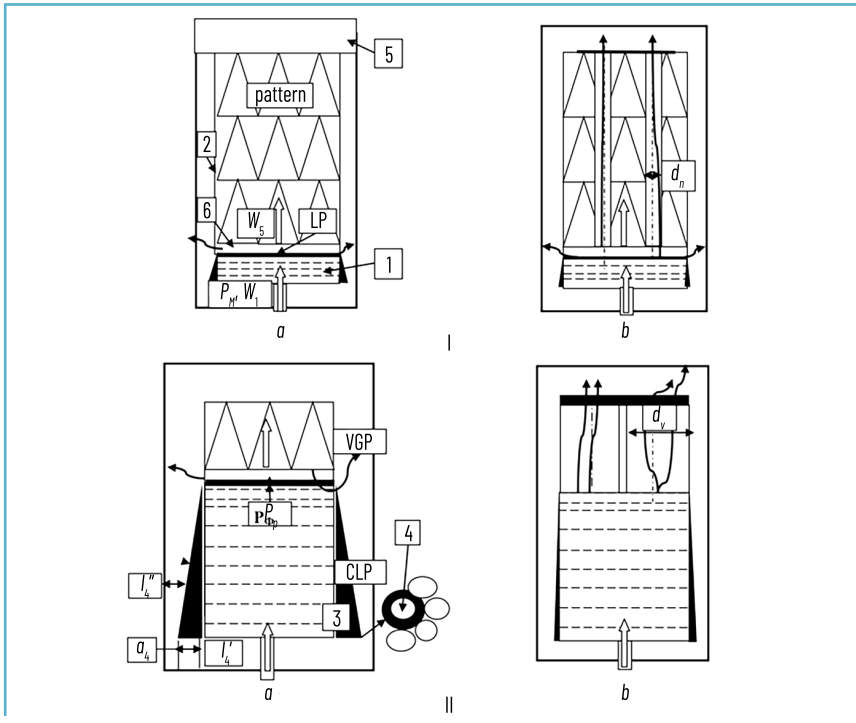

Fig. 4.2 Physical model of the interaction of a gasified pattern with metal during the period of filling the mold with: a - a mono pattern; b - reinforced pattern: 1 — metal; 2 — refractory coating on the-pattern; 3 — zone of low gas permeability (LGP); 4 — molding material (MM); 5 — mold; 6 — gap "metal — pattern"; products of thermal destruction of polystyrene: LP — liquid, VGP — vapor-gas; CLP — VGP condensate on MM grains; P_p, P_m — VGP pressure in the gap and metal, respectively; W_1, W_5 — linear velocity of destruction of the pattern and metal rise in the mold; I — initial stage of pouring, II — final stage of pouring
Source: [3]

At the same time, a zone of low gas permeability 3 (LGP) with a width of a_4 is formed at a distance of l_4 from the "metal- mold" boundary due to partial CLP overlap of the MM channels. In this case, the VGP flow passes through four zones in the mold: RC with a thickness d and gas permeability K_p, two MM layers with a thickness $l_{4'}$ and $l_{4''}$ and gas permeability $K_{4'}$ and LGP with a width of a^4 with gas permeability K_{LGP}.

In the same period, when the mold is filled with MA, VGP is also filtered through channels with a diameter d_n–d_g, which formed around the RE by GP thermal destruction due to temperature exchange between the RE and the GP. At the same time, a new heat exchange system is also formed: "GP (VGP) – RE (pore channels)", which leads to additional GP thermal destruction and an increase in the channel diameter to the value d_y [2].

In this case, the VGP is filtered through the channel with an area F_d and the RC into the mold wall with the formation of a similar LGP. Under the action of the pressure gradient (P_p–P_y), the LP formation in a mixture with VGP is carried to the end surface of the mold, and does not accumulate in the pore channel or on the surface of the metal flow front.

Based on the presented physical model of VGP filtration in the mold, the kinetics of the change in the gas regime during the lost-foam casting (LFC) process was described using the well-known system of equations (6), which is presented in works [3, 5]

$$\begin{cases} \dfrac{dy}{d\tau} = \dfrac{\left(\dfrac{\alpha\Delta T}{r\rho_5(1+N)} - \left(1-\dfrac{\delta}{\delta_c}\right) + \dfrac{\lambda\Delta T}{\delta r\rho_5(1+N)}\right)}{\left(1+\dfrac{\alpha\Delta T}{r\rho(1+N)} - \dfrac{\rho_5\tau\left(1-\delta/\delta_0\right)}{y'(1+M_G\tau)\rho_c\left[\left(\delta/\tau W_1\right)^{0.05}\right]}\right)} - W_1, \\ \dfrac{dQ}{d\tau} = W_5\rho_5 m_G V_G F_5(1-\varphi) - \delta P_5 P_f K_4 \varphi_G \left[\dfrac{c\left(l_4' - l_4''\right) + a_4}{\left(l_4' + l_4''\right)a_4}\right], \\ c = 0.0014\cdot\dfrac{r\cdot m_G\cdot\rho_5\cdot R_5}{a_4}, l_4' = (3.2-0.012T_3)\tau, \\ a_4 = 0.015T_3, \varphi = 0.32\cdot K_p^{1/3}, P_{\varphi i} = \dfrac{PQ}{F_5\delta}, \end{cases} \quad (4.6)$$

where α – heat transfer coefficient, W/(m^{2}K);

ρ_5 – pattern density;

ρ_p – liquid phase density, kg/m^3;

t – time, s;
y' – thickness of spheroids P_p, m;
ΔT – temperature difference between metal and melting pattern, K;
V_g – specific VGP volume, m^3/kg;
λ – thermal conductivity coefficient of vapor-gas phase, W/(m×K);
r – heat of fusion of pattern material, J/kg;
N – melting criterion;
δ – gap, m;
δ_0 – gap at which $W_5 < W_1$, m;
M_r – degree of destruction;
φ – accumulation of liquid GP products;
F_5 – cross-sectional area of pattern (casting), m^2;
P_5 – perimeter of pattern (casting) cross-section, m;
K_4 – gas permeability of the molding material, m^2/(N s);
K_p – gas permeability of the coating, units;
l_4', l_4'' – length of the molding material layer, m;
a_4 – LGP width, m;
φ_g – gas permeability reduction coefficient;
Q – VGP volume, m^3;
P_f – pressure in the gap, Pa;
T_3 – temperature of the alloy being poured, K;
τ_1 – time from the moment of pouring the metal into the mold, s.

Given that the GP has pore channels around the reinforcing elements with an area of ΣF_d, then the contact area of the heat flow of the metal with the GP F_k can be represented by the following equations (4.7)–(4.9)

$$F_K = F_5 - \sum_{i=1}^{i=n} F_i, m^2 \tag{4.7}$$

or

$$F_K = F_5 - \xi F_5, \quad \xi = \frac{\sum_{i-1}^{i=n} F_i}{F_5}, m^2 \tag{4.8}$$

and finally

$$F_K = (1-\xi)F_5, m^2 \tag{4.9}$$

where F_k; F_5; F_i – area of thermal contact, monopattern and pore channels around RE, respectively, m^2; ξ – porosity degree of the pattern.

As a result of the formation of a new VGP filtration system, namely: "VGP – reinforced phase – pore channels – coating –mold", the total VGP filtration area can be determined by the following mathematical dependence (4.10)

$$F_{\Sigma} = \left(\delta\Pi_5 + \xi F_5\right), m^2. \tag{4.10}$$

At the same time, the cross-sectional area of the elementary pore channel F_i is a variable value, because under the action of heating its VGP contact surface, the GP material around the RE decomposes at a speed a_5', which leads to an increase in its diameter d_i. The change in the total area of the GP channels can be described by the following expression, assuming that the channels have a cylindrical shape (4.11), (4.12) [3]:

$$\sum F_i' = \sum_{i=1}^{i=n} \frac{\pi d_\tau^{\,2}}{4}, m^2 \tag{4.11}$$

$$d_\tau = \left(1 + 2a_5' T_G\right) d_n, \tag{4.12}$$

where d_n – the initial diameter of the elementary pore channel, equal to the diameter of the reinforcing element d_a, m;

d_τ – the current diameter of the elementary pore channel around the reinforcing element, m;

a_5 – the linear melting velocity of the GP in the pore channel, m/s;

T_g – the VGP temperature, K;

τ – the current pouring time, s.

In order to use equations (4.11), (4.12) in the mathematical model (4.6), the following transformations should be performed, namely (4.13):

$$\frac{\xi_\tau}{\xi_n} = \frac{\left(d_n + 2a_5' T_G \cdot \tau\right)^2 4\pi}{4\pi d_n^{\,2}}, \tag{4.13}$$

and finally, the variable porosity (14):

$$\xi_\tau = \frac{\left(d_n + 2a_5' T_G \tau\right)^2}{d_n^{\,2}} \cdot \xi_n. \tag{4.14}$$

In this case, the system of equations of the gas dynamics of the casting process in the presence of GP with RE in the mold has the following form (4.15):

$$\begin{cases} \dfrac{dy}{d\tau} = \dfrac{\left(\dfrac{\alpha\Delta T}{r\rho_5(1+N)} - \left(1-\dfrac{\delta}{\delta_0}\right) + \dfrac{\lambda\Delta T}{\delta r\rho_5(1+N)}\right)}{\left(1+\dfrac{\alpha\Delta T}{r\rho_5(1+N)} - \dfrac{\rho_5\tau\left(1-\dfrac{\delta}{\delta_0}\right)}{y'(1+M_6\tau)\rho_{c_{-p}}\left[\left(\dfrac{\delta}{\tau W_1}\right)^{0.05}\right]}\right)} - W_1, \\ \dfrac{dQ}{d\tau} = (1-\xi_\tau)F_5W_5\rho_5M_6a_5(1-\varphi) - \\ -\left(\delta P_5 + \dfrac{\left(d_n + 2a_5'T_6\tau\right)^2}{d_n^2}\cdot F_5\right)\varphi_\Gamma\Delta\rho K_4\dfrac{L_\Sigma - c\left(l_4' - l_4''\right)}{\left(l_4' - l_4''\right)a_4}, \\ P_{\varphi i} = \dfrac{PQ}{F_5\delta}, L = (3.2-0.012T_3)\cdot\tau_3, a_4 = 0.015T_3, \varphi_\Gamma = 0.32\cdot K^{1/3}, a_5' = 1\cdot10^{-3}. \end{cases} \quad (4.15)$$

To determine the coefficient, it is possible to use the data of work [7] and construct the dependence $d = f(T_g)$, where d – the diameter of the pore channel, and T_g – the temperature of the gas passing through this channel. According to the graph (**Fig. 4.3**), this dependence is expressed by a straight line. In this case, the equation for determining the coefficient a_5' has the following form (4.16)

$$a_5' = \frac{\Delta d}{2\Delta T_6\cdot 10}, \quad (4.16)$$

where 10 is the time of gas passage through the pore channel of the GP in the experiment, C.

Then the value of the coefficient is $a_5' = 1\times10^{-3}$ mm/s °C.

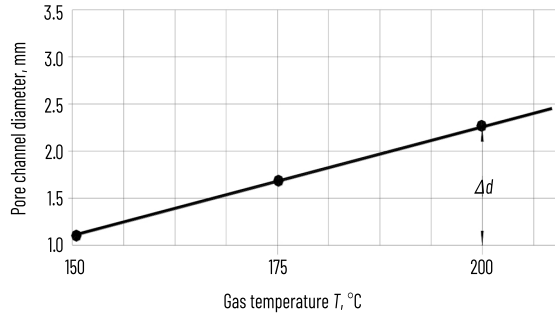

Fig. 4.3 Kinetics of change in linear dimensions of the pore channel in the polystyrene foam pattern

Now the system of equations (4.15) can be used to determine the parameters, including the back pressure of the VGP P_p, the gap "metal – pattern" δ and the rate of metal rise in the mold W_1 with a reinforced GP.

It is also important to note that the amount of LP products that accumulate on the surface of the metal flow front is also reduced by the value $(F_5 - \Sigma F_d)$. In this case, to determine the volume of LP accumulation, the time of its gasification on the contact surface for time t_g and the hardening coefficient R, it is advisable to use the system of equations (4.15) by supplementing it with the expression $\left(1-\xi_\tau\right)F_5$.

Then the system of equations describing the gas-hydrodynamic conditions of lost foam casting with polystyrene patterns saturated with RE, and taking into account the heat exchange between the RE and the MA during mold filling and matrix alloy solidification, has the final form (4.17):

$$
\begin{cases}
P_p = 0.13\varphi_G \dfrac{\eta T_p I_4}{c} a_5 t_G^{\,m-1}, \\
\xi_1 = \dfrac{1.13 b_4 \left(T_p - T_m\right) \cdot \left[1 + \dfrac{100\left(1-c_\tau\right)^3 \delta_1 3}{1.13 b_4 \left(T_p - T_m\right)}\right]}{L_1 \rho_1 \left[1 - \dfrac{c_1}{L_1}\left(T_3 - T_{kp}\right)\right]} \cdot \sqrt{t_G}, \\
C_\tau = \dfrac{\left(d_n + 2a_5^{'} \cdot T_G \cdot \tau\right)^2}{d_n^2}, \\
P_M = \rho_1 g_1 W_1 t_G, \\
t_G = \left(\dfrac{\left(1-c_\tau\right)^3 \delta_1^{\,3}}{a_5} \cdot 10^3\right)^{\frac{1}{m}}, \\
\begin{cases}
\tau = \dfrac{C_p \rho_1 V_c \sqrt{\xi} \cdot D_1}{\alpha_{-}\left(T_{-} - \left[T_1\right]\right)}, \\
\left(T_c - \left[T\right]\right)_c = \left(\dfrac{T_3 + \left[T_1\right]}{2} - \left[T_1 + KpP_5 / 25\right]\right),
\end{cases} \\
Nu_{\overline{D}} = \dfrac{\alpha_c \overline{D}}{\lambda_c} = 1.86\left(\mathrm{Re}_{\overline{D}} \cdot \mathrm{Pr}\right)^{0.33} \cdot \left(\dfrac{\overline{D}}{L}\right)^{0.33} \cdot \left(\dfrac{\mu_b}{\mu_s}\right)^{0.14}, \\
Nu_{\overline{D}} = \dfrac{\alpha_c \cdot \overline{D}}{\lambda_c} = 0.036 \cdot \mathrm{Re}_D^{\,0.8} \cdot \mathrm{Pr}^{0.33} \cdot \left(\dfrac{\overline{D}}{L}\right)^{0.055}.
\end{cases}
\tag{4.17}
$$

where η – the coefficient of VGP dynamic viscosity;

T_p – the metal temperature, K;

T_m – the mold temperature, K;

C – the permeability, Darcy;

t_G – the gasification time of the pattern;

d_p – the diameter of the pore channel (reinforcing element);

φ_g – the SRC resistance coefficient;

b_4 – the heat storage capacity of the mold, W×s$^{0.5}$/m^2×K;

l_4 – the mold wall thickness, m;

D_1 – the diameter (reduced thickness) of the casting, m;

F_1, F_p – the cross-sectional area of the casting and the pore space, respectively, m^2;

ξ – the porosity coefficient of the mold;

λ_c – the thermal conductivity coefficient, W/(m×K);

$\mathrm{Pr} = \frac{\nu}{a}$ – Prandtl criterion;

$\mathrm{Re} = \frac{V \cdot \overline{D}}{\nu}$ – Reynolds criterion;

n – the viscosity coefficient, m^2/s;

α_c – the thermal diffusivity coefficient, m^2/s;

μ_b – dynamic viscosity at metal temperature T_b, N×s/m^2;

μ_c – dynamic viscosity at wall temperature T_s (T_s ^{3} T_L), N×s/m^2;

T_L – liquidus temperature of matrix alloy °C.

Thus, hydro-gas-dynamic, thermophysical models were created that describe the features of gas dynamics and heat and mass transfer in molds with reinforcing elements, a polystyrene foam pattern saturated with RE, which allow predicting the flow conditions of the matrix alloy, its solidification, and cooling in molds, which makes it possible to create promising casting methods using gasifying patterns to obtain high-quality reinforced structures with various functional properties from iron-carbon and non-ferrous alloys.

4.2 ANALYSIS AND SELECTION OF STEEL GRADES FOR THE MANUFACTURE OF HOLLOW CAST STRUCTURES FOR MULTIFUNCTIONAL PURPOSES

High requirements for the level of physical and mechanical properties of cast alloys, as well as the technological possibility of forming hollow castings with metallic and non-metallic reinforcing phases by lost foam casting, determine the feasibility of developing new high-strength economical alloyed steels. Such steels should provide the required set of operational properties without the use of scarce and expensive alloying elements, as well as contribute to the creation of highly efficient casting technologies and optimal heat treatment modes to obtain high-quality parts of protective structures [8–11].

Modern requirements for materials, in particular, for multifunctional protective structures, provide for a combination of high strength, sufficient plasticity and resistance to dynamic loads. The choice of material is a key factor determining the reliability and durability of structures manufactured by casting methods.

In this regard, there is a need for systematic research of alloys suitable for forming thin-walled castings of complex configuration [12].

For the analysis, domestic and foreign analogues of steels and iron-based alloys used in the production of cast structures were considered [13–15]. Based on the comparative analysis, it was established that among such materials, low- and medium-carbon low-alloy, microalloyed and modified steels have the greatest prospects. The urgent need for protective structures and structural requirements for their component modules – the level of physical and mechanical properties of steels, the possibility of manufacturing structural modules with non-metallic and metallic reinforcing phases (NRP and MRP) requires the development of new high-strength economically alloyed cast steels that do not contain expensive and scarce alloying elements, highly efficient technologies for manufacturing cast elements of a cellular structure and optimal modes of their heat treatment. A review of world analogues of steels used for the manufacture of multifunctional modules of protective structures has established that the steels used for their manufacture must provide a tensile strength of 500...950 MPa; yield strength – 450...800 MPa, relative narrowing 15...30%; impact toughness 50...70 J/cm2. In addition, given the great need for protective structures, steels for cast modules should not contain scarce and expensive alloying elements – nickel, molybdenum, copper, etc. An analysis of modern technical literature has established that for cast modules of protective structures, the required level of physical and mechanical properties of steels of the C-Si-Mn system is currently provided exclusively by their complex alloying with chromium, nickel, molybdenum, vanadium and the corresponding labor-intensive heat treatment regimes. Thus, regulatory documents for foundry steels in the USA – A352...A732 and Germany – DIN1681 provide for the manufacture of cast parts used as elements of protective structures, steels of the C-Si-Mn system, which are alloyed with the above chemical elements. This makes it possible, after appropriate heat treatment regimes, to obtain metal in products with a yield strength of over 400 MPa.

Based on previous studies [13], it can be stated that the processes of high-quality and optimal additional alloying, microalloying with carbide and nitride-forming elements and modification with nitrogen can achieve the required physical and mechanical properties (tensile strength at rupture 550...900 MPa, yield strength at rupture 450...750 MPa, relative elongation 15...30%, impact toughness 55...75 J/cm^2).

The physical and mechanical properties were determined and the microstructure of the experimental steels was considered using modern testing equipment and analytical methods. Special attention was paid to the influence of heat treatment modes on the operational characteristics of the metal, since energy consumption and stability of the properties of cast parts during mass production depend on this.

The blanks for samples for various purposes were manufactured in dry, heated sand-clay molds. To determine the mechanical properties, samples were made from blanks with a diameter of 12 mm and a length of 70 mm, to determine the impact toughness of steels, blanks with dimensions of 12 mm×12 mm×60 mm were cast, from which standard samples were made.

To compare the physical and mechanical properties and the results of metallographic studies, samples from blanks made using the tooling developed by us and cut from a tertiary blank in accordance with the requirements [14] were used.

To determine the impact toughness of the studied steels, blanks with dimensions of 12 mm×12 mm×60 mm were cast, from which standard samples were made.

To study other properties of steels (for example, choosing the optimal heat treatment regime for steels, studying the structure, etc.), cylindrical blanks with a diameter of 20 mm and a length of 90 mm and the lower part of the riser of the sprue system were used.

In order to determine the correctness of the choice of the tooling developed by us, a comparative assessment of the quality of the metal in the blanks made using the proposed tooling and made using a tertiary blank (DSTU 8781:2018, option 2) or a square (**Fig. 4.4, *a***). The metal has almost the same properties, but a complex test is more effective and much cheaper for the manufacture of samples from experimental steels (**Fig. 4.4, *b***). Obtaining high-quality metal in the samples using this technology is ensured by a massive boss under the riser.

a *b*

Fig. 4.4 Pattern tooling for the production of cast blanks: *a* — square, riser and tertiary blank; *b* — complex tooling (without riser)

The analysis of a large amount of material presented in the works of scientists of the Physico-Technological Institute of Metals and Alloys of the National Academy of Sciences of Ukraine on the use of alloying, microalloying and modification processes of C-Si-Mn alloys has identified specific areas for improving these processes for lost foam casting: approximate temperatures of base melts before performing the processes of additional alloying, microalloying and modification of base steels and pouring them into molds and specific individual chemical elements and complexes of elements to minimize their quantity with the maximum increase in the properties of experimental steels [15].

The studies have established that the optimal content of the main chemical elements in medium-carbon steels to achieve high strength and ductility should be as follows, wt.%: C = 0.30…0.55; Mn = 0.40…1.20; Si = 0.30…0.60.

In order to achieve the required indicators of physical and mechanical properties for alloying, microalloying and modification of base steels, it is advisable to use the following chemical elements: for alloying and microalloying — titanium, niobium, chromium and vanadium, for modification — nitrogen and rare earth metals on a cerium basis.

Taking into account the interaction of chemical elements in the C-Si-Mn system, to determine the optimal chemical composition of steels that can provide the required level of physical and mechanical properties of the metal of cast modules and their corrosion resistance in various aggressive environments, the effect of changing the content of the main chemical elements within the following limits was studied: carbon – from 0.25% to 0.60%, silicon – from 0.30% to 0.90%, manganese – from 0.50% to 2.0%. The content of phosphorus and sulfur did not exceed 0.045% of each element. The nitrogen and vanadium content was calculated for each steel grade taking into account that the equilibrium temperature of dissolution (separation) of the vanadium nitride phase in a solid solution does not exceed 1030°C [16].

Previous studies conducted at the Physico-Technological Institute of Metals and Alloys of the NAS of Ukraine on the influence of microalloying and modification processes with vanadium and nitrogen on the properties of structural steels of the C-Si-Mn-Cr system of ferritic-pearlitic and pearlitic classes have established that the separation of dispersed particles of VN and AIN in a solid solution provides a comprehensive increase in the strength and plasticity characteristics of steels to the level of properties of steels alloyed with molybdenum, nickel, niobium, vanadium, etc.

In this case, the process of dispersion strengthening of steel is implemented during the tempering of the product after normalization or quenching, which should occur at temperatures 100...150°C lower than the equilibrium temperature of dissolution (formation) of the vanadium nitride (VN) phase.

According to the results of previous studies, 35KhGAFL steel was selected, which has the highest indicators of casting and physical and mechanical properties for casting the above-mentioned protective modules [17–21].

Based on thermodynamic calculations of the equilibrium temperature of formation of the nitride disodium phase in a solid solution, it was established that the optimal range of austenitizing heating of 35KhGAFL steel during normalization and quenching is 920–940°C with holding for 1 hour.

After normalization, the samples were cooled in air, and during quenching – in water. Tempering was carried out at temperatures of 510–600°C with holding for 1 hour and subsequent cooling in air. Physical and mechanical properties were determined after normalization, quenching and tempering (**Table 4.1**).

After normalization (austenization), a fine-grained structure is observed in 35KhGAFL steel samples: 6–7 points and 7–8 points, respectively. The choice of heat treatment modes allows to provide the necessary set of steel properties depending on the operating conditions of protective structures.

To reduce the cost of casting and energy consumption, it is recommended to carry out normalization at 930°C with air cooling. The properties obtained under this mode fully comply with the technical requirements, and the grain size of the steel is 7–8 points, which indicates an optimal fine-grained structure [20].

The microstructures of steels after normalization and tempering are shown in **Fig. 4.5.** The microstructure of 35KhGAFL steel after normalization at a temperature of 930°C is pearlitic-ferritic: pearlite is thin-lamellar, ferrite is located outside the austenite grains in the form of broken meshes. Tempering of steel after normalization contributes to an increase in hardness due to the dispersion segregation of the vanadium nitride phase inside the grains.

Table 4.1 Heat treatment modes and physical and mechanical properties of 35KhGAFL steel

Heat treatment modes		Physical and mechanical properties of steel				
normalization, quenching °C, cooling medium	$\sigma_т$, MPa tempering °C	$\sigma_в$, MPa	ψ, %	KCU, J/cm^2	Hardness, HRC	
	no less than					
normalization at a temperature of 930°C, air	without tempering	600.0	850.0	22.0	72.0	20.0
	510	600.0	850.0	24.0	82.0	22.5
	550	600.0	890.0	24.0	82.0	22.0
	600	605.0	915.0	23.0	67.0	25.0
quenching from a temperature of 930°C, water	510	1010.0	1150.0	20.0	75.0	31.0
	550	795.0	980.0	27.0	84.0	26.0
	600	850.0	1010.0	24.0	75.0	26.0
Requirements according to the technical specifications	450…750		550…900	15…30	55…75	≥15

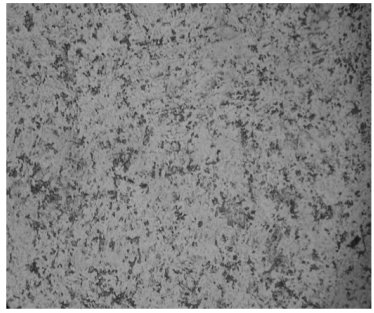

a

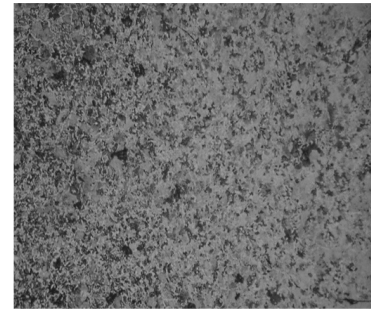

b

Fig. 4.5 Microstructures of the experimental 35KhGAFL steel after normalization at a temperature: *a* — of 930°C; *b* — normalization at a temperature of 930°C + tempering at a temperature of 510°C; ×200

Another urgent task during the production of castings using the lost foam casting process is to determine the level of non-metallic inclusions of medium and large sizes in the metal of the products. It is important to know not only the level of contamination of the metal with non-metallic inclusions, but also their morphology, size, shape and reasons contributing to their formation. In this case, it will be possible to use certain technological measures that will reduce their number or change their shape, for example, convert non-metallic inclusions from an acute-angled shape to a globular one, which will significantly increase the physical and mechanical properties of the metal.

The metal contamination index by non-metallic inclusions was determined by the linear method according to the requirements [21, 22] on unetched sections made from steel blanks. The results of the numerical values of each type of non-metallic inclusions and the total metal contamination index are given in **Table 4.2.**

Table 4.2 Metal contamination index of multifunctional modules by non-metallic inclusions of different morphology and the total contamination index

No.	Type of non-metallic inclusions	Contamination index of 35KhGAFL steel
1	Nitrides	0
2	Oxides	0.001127
3	Silicates	0.000407
4	Sulfides	0.008800
5	Total steel contamination index	0.002414

Analysis of the obtained results of the study of non-metallic inclusions in the recommended 35KhGAFL steel allowed to establish that the general index of contamination of the cast metal of samples cut from real modules made using polystyrene foam patterns is at the level of indicators for the metal of carbon steel products obtained using traditional casting technologies in one-time volumetric sand-clay molds [23].

Relatively large non-metallic inclusions of an oxide nature are observed in 35KhGAFL steel. Their appearance may be due to the presence of slag particles, since the samples were cut from the upper part of the cast module, or as a result of secondary oxidation of the melt during pouring the molds.

The heat treatment modes of the recommended steel do not significantly affect the morphology and number of non-metallic inclusions, with the exception of the normalization process. Prolonged cooling of the metal in air contributes to a partial redistribution of morphological types of inclusions – in particular, the proportion of sulfides increases, which is explained by a decrease in the solubility of sulfur in iron with a decrease in the temperature of the metal.

Based on the conducted studies, the optimal heat treatment regime is one that involves quenching from a temperature of 930°C in water with subsequent tempering at 510°C.

After such treatment, the steel is characterized by the following properties:

– tensile strength σ_v – not less than 1150 MPa;

– yield strength σ_t – not less than 1010 MPa;

– relative elongation δ – 16%;

– relative narrowing ψ – 20%;

– impact toughness KCU – 70 J/cm^2;

– hardness – 31 HRC.

The results obtained confirm that 35KhGAFL steel provides increased strength and ductility combined with good castability, which is crucial for the manufacture of thin-walled hollow elements of complex geometry [24].

4.3 DETERMINATION OF THE REINFORCEMENT INFLUENCE ON THE HYDRODYNAMICS OF MOLD FILLING AND THERMAL PROCESSES IN THE FUNCTIONAL FILLER

The influence of reinforcing steel elements and reinforcement directly from the liquid alloy of the shell on the hydrodynamics of mold filling and thermal processes in the functional filler was determined using computer simulation. Successful computer simulation can help reduce the number of tests and reduce the time for developing new castings due to a better understanding of the complex mechanisms and interaction of various technological parameters in the mold filling process, especially in the gasified pattern casting process [25, 26]. In accordance with the tasks of implementing technologies for obtaining lightweight high-strength steel hollow structures with non-metallic and metallic functional filler, the following types of them were proposed:

1 – steel shell filled with non-metallic functional material;

2 – steel shell with non-metallic functional material, which is reinforced with metal elements that simultaneously combine the shell and functional material;

3 – steel shell with non-metallic functional material, which is reinforced by solidification in its channels of liquid alloy of the shell, which at the same time combines the shell and functional material.

Computer simulation of the processes of pouring and solidification of the lost foam casting was performed using the Procast software. 3D drawings of the cell model of one element of the module (**Fig. 4.6**), gating system, reinforcement, core (functional filler) built in the CAD system were saved in IGES format and loaded into the simulation program. The element size when applying the mesh to the model, core and reinforcement was set to 2 mm. The total number of calculated elements was 739 thousand. The following materials were set from the database: Steel AISI 1040 – for the alloy, Sand LFC – for the mold, Foam 30 kg/m^3 – for the model, Resin bonded sand permeable – for the core, Chill Carbon steel – for the reinforcement. The pouring temperature of the steel was set at 1580°C, the initial temperature of the mold, core, model and reinforcement, and the environment was 20°C. The heat transfer coefficients were set as follows: between liquid metal and foam – FOAMHTC 840, FOAMHTCMAX 10460, between liquid metal and mold/core – 500, between metal and reinforcement – 3000, between mold and core – 400. The boundary conditions were: inlet pressure on the upper surface of the riser 1.05 atm, temperature 1580°C, pressure around the mold 1 atm [9].

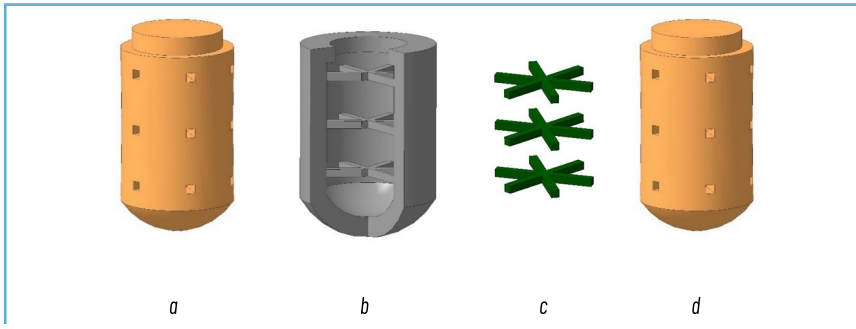

Fig. 4.6 General view of 3D models: *a* – cell; *b* – cell with membranes; *c* – reinforcement, *d* – core with channels

Fig. 4.7 shows the process of pouring an experimental cell with a functional filler without reinforcement. Under these conditions, the metal front moves from top to bottom with gradual spreading to the sides and the closing of two flows in the part opposite the supply point. In the case of the presence of polystyrene foam elements between the walls of the cell as a functional material, the nature of pouring is similar (**Fig. 4.8**). The presence of processes of filling thin channels of membranes (4x4 mm) is distinctive. Since the metal fills the cylindrical part of the cell, the metal enters each "beam" of the membrane from the main wall and moves to the point of their intersection.

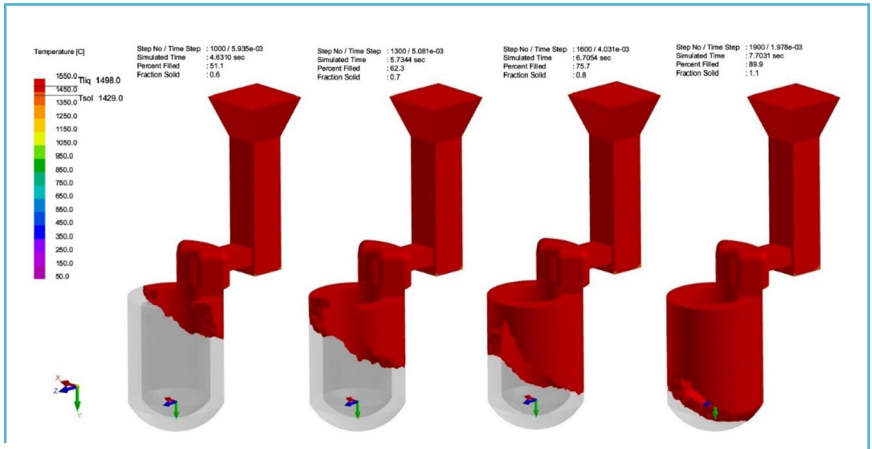

Fig. 4.7 The process of pouring an experimental cell (without reinforcement)

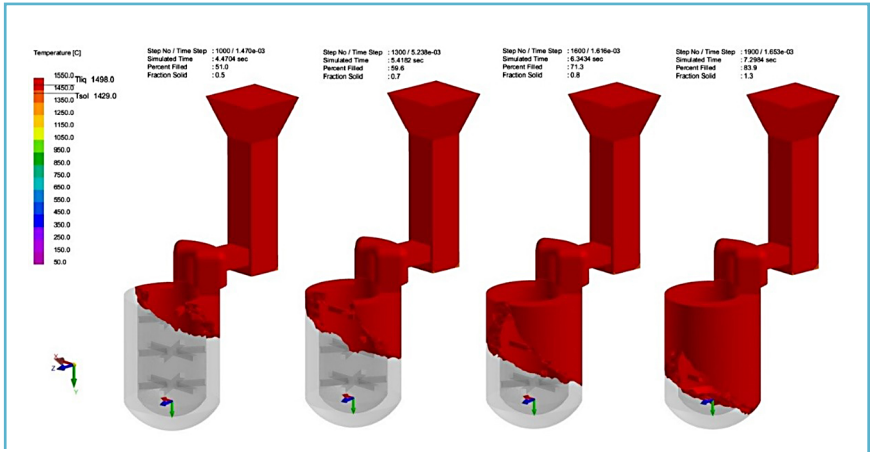

Fig. 4.8 The process of pouring an experimental cell with thin channels for reinforcement

The flow rate of liquid metal in the channels for reinforcement is shown in **Fig. 4.9.** At the beginning of filling the upper channel, the flow rate is about 2 cm/s. Then the speed increases to 4 cm/s. At the end of filling the channel, the speed briefly rises to 8 cm/s.

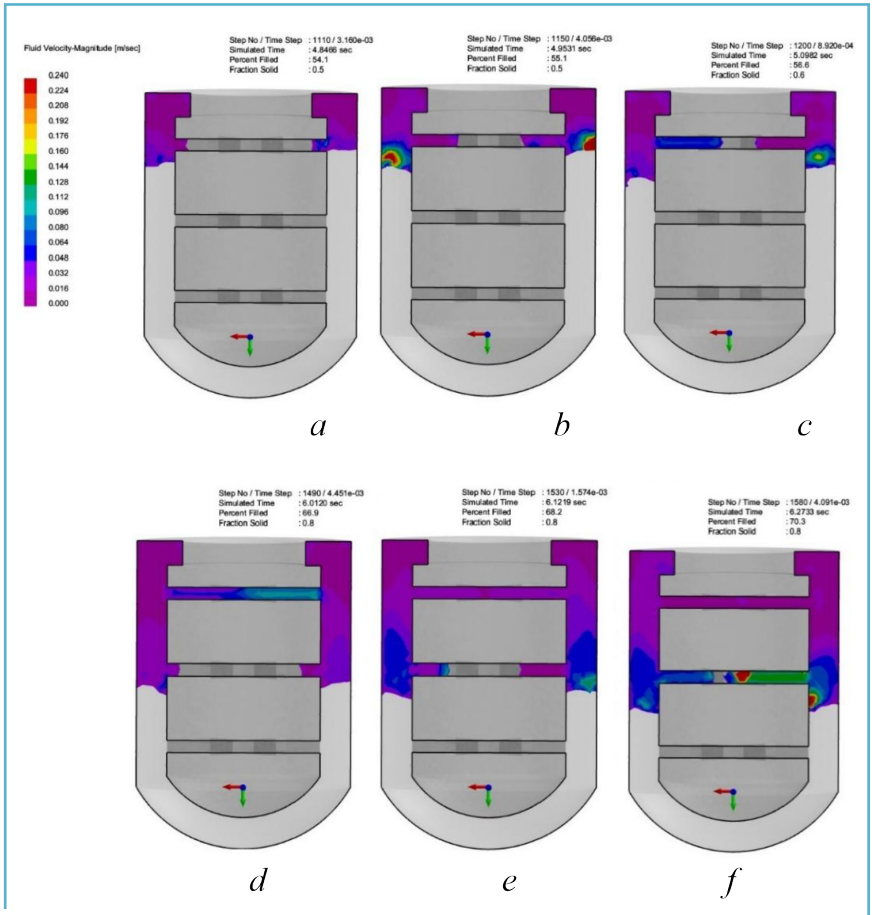

Fig. 4.9 The flow rate of liquid metal in the channels of the functional filler: *a* – 4.8 s, *b* – 5.0 s, *c* – 5.1 s, *d* – 6.0 s, *e* – 6.1 s, *f* – 6.3 s

A similar picture occurs when filling the middle and lower partitions. At the beginning of filling the channels, the speed is 2–3 cm/s. Then the speed increases to 6 cm/s, and briefly rises to 10–12 cm/s. It is believed that the optimal speed is 3–4 cm/s. When the metal moves through thin channels, a high speed contributes to their filling, since at a low speed the flow may stop due to its cooling.

Fig. 4.10, *a* shows the temperature fields of the longitudinal section of a casting with a functional filler, a casting with a functional filler and reinforcement (**Fig. 4.10, *b***), a casting with membranes and a functional filler (**Fig. 4.10, *c***).

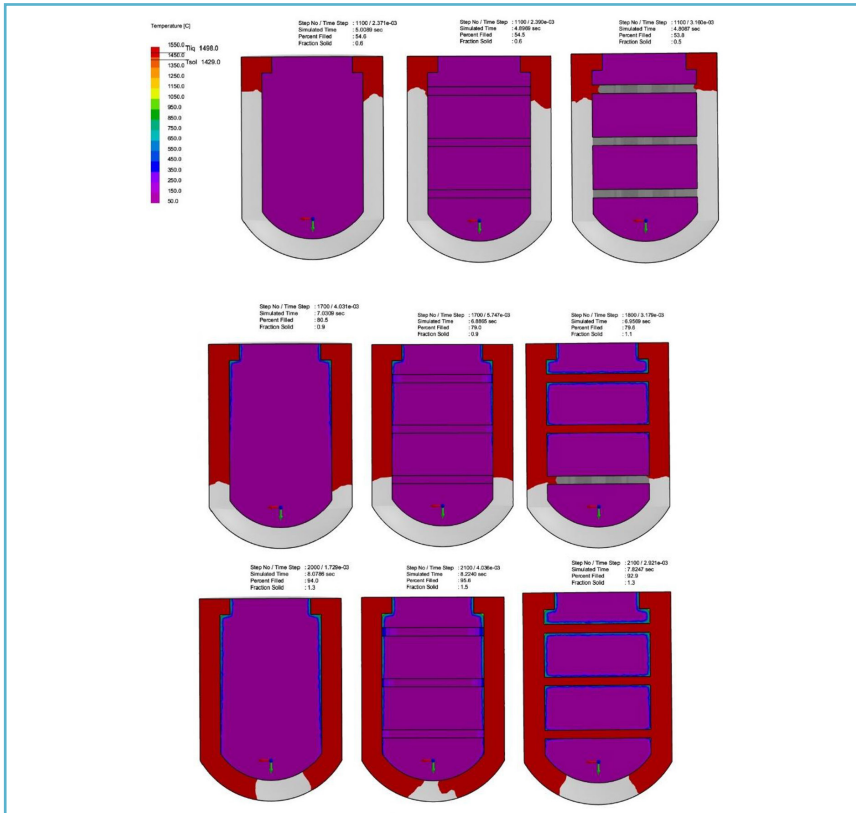

Fig. 4.10 Temperature fields (cell cross-section) during pouring: *a* – casting with functional material; *b* – casting with reinforced filler; *c* – casting with functional filler reinforced from the liquid phase of the shell metal

The nature of filling the casting cavity for the first two cases is the same. In the third variant, the nature of filling is somewhat different, which is associated with the presence of partitions. During pouring, the functional material is heated only in the contact zone to approximately 400°C. At the end of pouring, the upper part of the functional filler is heated to a depth of up to 2 mm to a temperature of 700°C.

Fig. 4.11 shows the temperature fields of the longitudinal section of the casting during solidification and cooling of the metal. **Fig. 4.12** shows the solidification time of the section of the castings. 30 seconds after filling the casting, the functional filler is heated to a depth of up to 7 mm. Complete heating of the

functional filler in the first variant occurs in 180 s, in the variant with reinforcement — in 130 s, in the variant with reinforcement from the liquid phase of the shell metal — in 100 s.

The highest temperature to which the functional filler is fully heated in the first case is 850°C, in the case of using reinforcement — 1050°C, in the case of casting with membranes — 1150°C. Thus, the best conditions for sintering the functional filler are created in the second two variants.

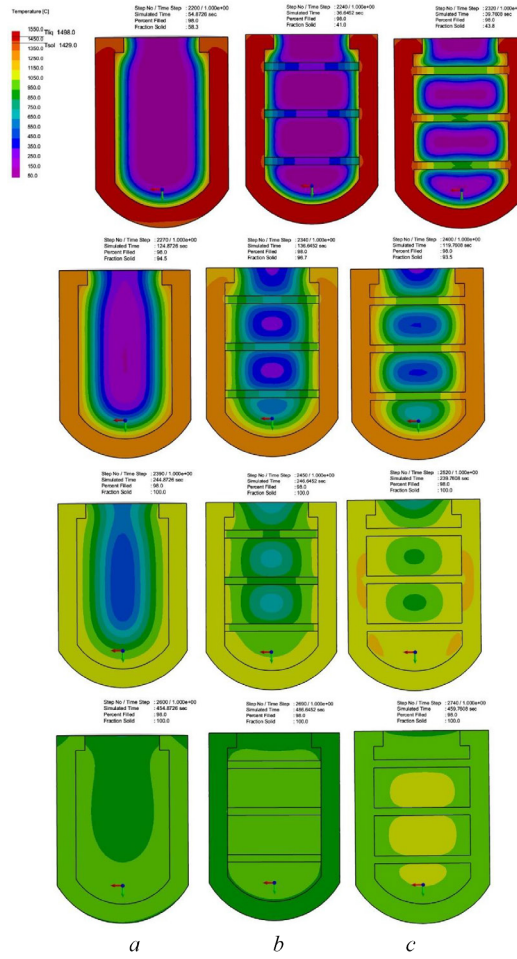

Fig. 4.11 Temperature fields (cell cross-section) during solidification and cooling: *a* — casting with functional material; *b* — casting with reinforced functional material; *c* — casting with functional filler, which is reinforced from the liquid phase of the shell metal

The presence of reinforcement or membranes affects the solidification processes (**Fig. 4.12**). The reinforcement acts as a refrigerator and reduces the solidification time of the casting by 11 s. The membranes harden quite quickly (12 s) and partially cool the casting, but reduce the solidification time of the casting by only 6 s.

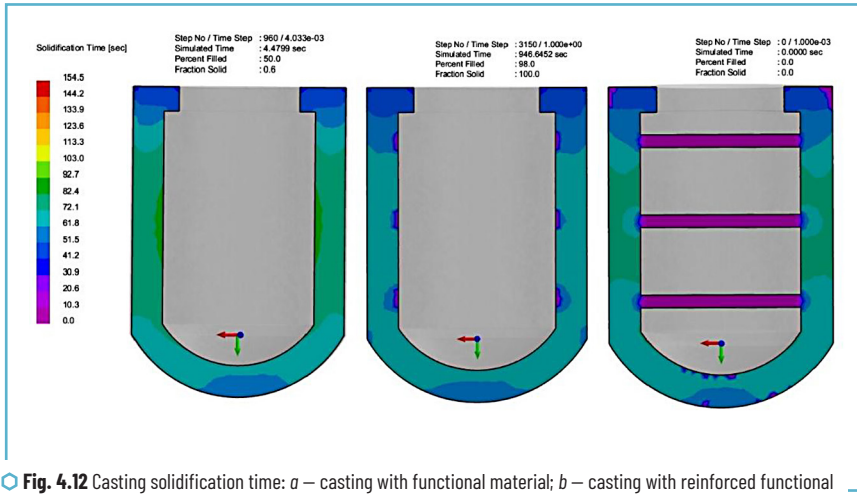

Fig. 4.12 Casting solidification time: *a* — casting with functional material; *b* — casting with reinforced functional material; *c* — casting with functional filler, which is reinforced from the liquid phase of the shell metal

The nature of filling the cell without membranes, determined on the basis of simulation, is typical for the upper feed for lost foam casting due to the presence of a polystyrene foam pattern, which exerts thermomechanical resistance. In the presence of membranes, significant changes in the nature of filling the main wall of the cell do not occur, due to the fact that the volume of the membranes is 3.5% of the total volume of the cell. However, the metal flow rate in the membranes is 3–4 times higher than the metal flow in the cavity of the main wall of the casting, which is due to hydrodynamic pressure.

The results of the study of the temperature fields of the casting and the functional filler during pouring, solidification and cooling of the metal showed that when using reinforcement and the presence of metal membranes, better conditions are created for sintering the functional filler due to the heat of the matrix metal.

The increase in the heating rate of the functional filler in the presence of steel reinforcement is associated with the higher thermal conductivity of the steel, which is heated by the heat of the casting. In the case of a casting with membranes, they increase the area of the contact surface for heat exchange of the metal with the functional filler. In addition, the casting with membranes has a larger mass, respectively, the amount of heat transferred by the matrix metal to the functional filler increases.

Reducing the hardening time, i.e. increasing the hardening rate, creates conditions for increasing the mechanical properties of the casting.

In addition to the hardening rate, the level of mechanical properties of steel is affected by the presence of casting defects, so the work analyzed the shrinkage that is formed in the cell casting. The shrinkage fields of the first and third types of shells are presented in **Fig. 4.13.** The simulation results showed that in a casting without partitions, shrinkage is concentrated in the pouring part. At the same time, in a casting with a filler, which is reinforced from the liquid phase of the shell metal, shrinkage cavities are also present in the center of the partitions. This is explained by the formed "thermal node", which occurs when six "beams" are connected, which solidifies without being fed with liquid metal from the main walls of the shell or pouring.

To prevent shrinkage in the center of the partitions, another design was proposed, in which the central part has the shape of a ring. The simulation results of the solidification of this version of the casting **(Fig. 4.14)** showed that there is a certain porosity in the partitions (reinforcement formed from the liquid phase of the shell metal). However, the size of the shrinkage defects has significantly decreased compared to the previous version.

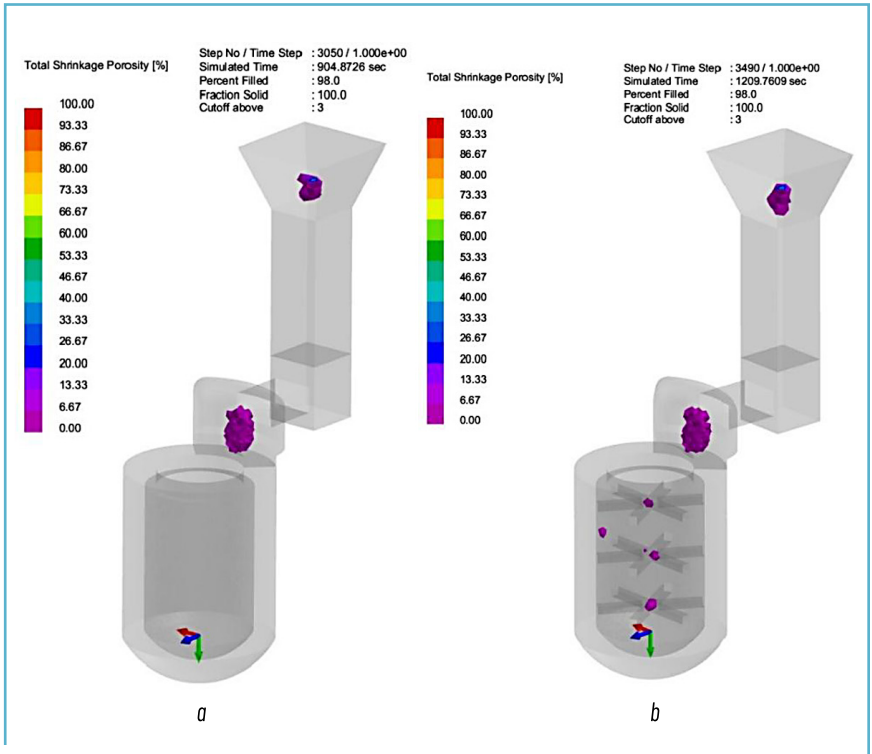

Fig. 4.13 Shrinkage fields: *a* — casting with functional filler; *b* — casting with functional filler reinforced from the liquid phase of the shell metal

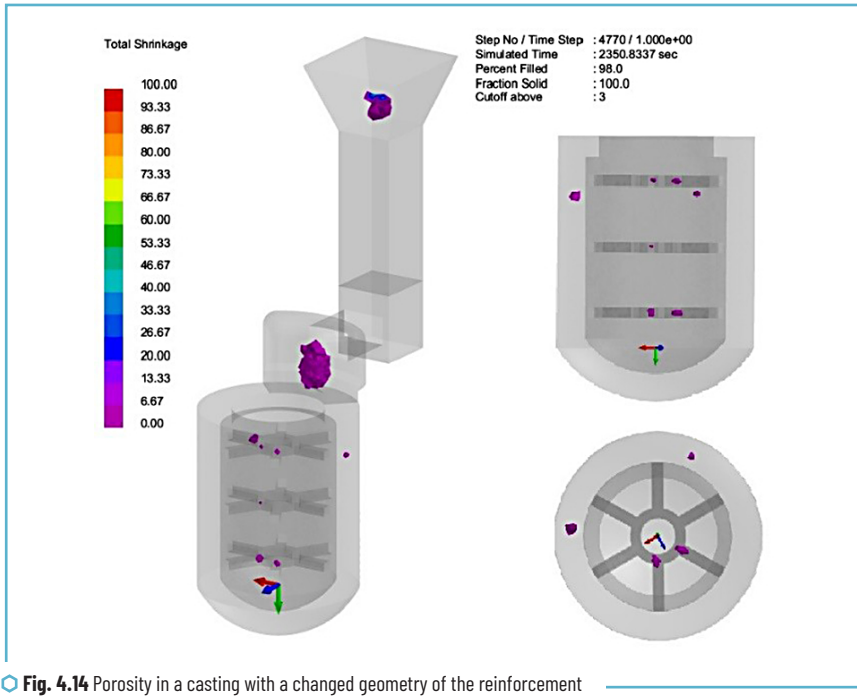

Fig. 4.14 Porosity in a casting with a changed geometry of the reinforcement

Thus, the conducted studies have shown the feasibility of using solid reinforcement and reinforcement from liquid metal to increase the mechanical adhesion of the shell metal with the functional filler and create better conditions for its sintering for the purpose of strengthening.

4.3.2 STUDIES ON THE SELECTION OF A FUNCTIONAL FILLER

The functional filler of the metal shell must satisfy several parameters – availability, low mass, refractoriness, etc. At the same time, the filler must have sufficient hardness to resist the penetration of objects (fragments, bullets, etc.) into them, and have a low density so as not to significantly increase the total mass of the protective module.

The properties of some common materials (**Table 4.3**) that can be used as fillers are analyzed. The most accessible and cheap is quartz sand, which has a sufficiently high refractoriness and hardness, is characterized by a small bulk mass. Electrocorundum and silicon carbide are more refractory and hard, but they are more expensive and have a higher density. An accessible material that has a low bulk density is expanded vermiculite, but is characterized by low refractoriness and low hardness.

Table 4.3 Characteristics of non-metallic fillers

No.	Name	Chemical formula	Density, kg/m^3	Bulk weight, kg/m^3	Melting temperature (fire resistance), °C	Mohs hardness
1	Crystalline quartz (quartz sand)	SiO_2	2650	1400–1700	1713 (1650)	5.5–7.0
2	Electrocorundum	Al_2O_3	3990	2400	2050	9.0
3	Expanded vermiculite	$(Mg, Fe^{2+}, Fe^{3+})_3 [(OH)_2 (Al, Si)_4 4H_2O$	380	200	~1300	1.0–1.5
4	Silicon carbide	SiC	3210	1900	2730	9.5

For practical testing of the behavior of functional fillers in combination with the shells of protective structures, cylindrical samples were filled with different fillers. Polystyrene cylinders were made – outer diameter 66 mm, inner 40 mm, height 50 mm. As fillers, quartz sand of fraction 0.16–0.2 mm, fraction 0.8–1.0 mm, expanded vermiculite of fraction 1.0 mm, normal electrocorundum of fraction 0.8 mm (F24) were used. Liquid glass was used as a binder, which was added in an amount of 7% by weight of the core mixture.

8 samples of models with different fillers were made (**Fig. 4.15**):

1 – quartz sand of fraction 0.16–0.2 mm;

2 – a mixture of vermiculite and quartz sand of fraction 0.16–0.2 mm;

3 – quartz sand of fraction 0.16–0.2 mm mixed with aluminum shavings;

4 – quartz sand of fraction 0.8–1.0 mm;

5 – quartz sand of fraction 0.8–1.0 mm mixed with polystyrene granules;

6 – quartz sand of fraction 0.8–1.0 mm with polystyrene foam membranes;

7 – vermiculite;

8 – normal electrocorundum.

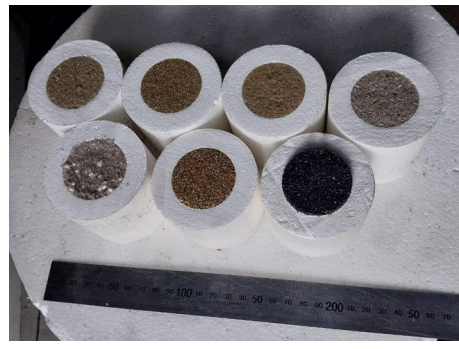

Fig. 4.15 Cylindrical samples with different fillers

The core mixtures were obtained by mixing the components until the refractory particles were completely "wetted" with liquid glass. Then the mixture was "stuffed" into the cylinder hole and left for 24 hours in a warm room to cure and dry the mixture. After that, the elements of the gating system were glued and a refractory coating was applied (**Fig. 4.16, *a*).** After the coating dried, the pattern blocks were molded in dry quartz sand using the traditional LFC technology. The molds were poured with liquid steel 45L. After the castings cooled, they were knocked out of the mold (**Fig. 4.16, *b***) and separated from the sprues (**Fig. 4.17**).

a *b*

Fig. 4.16 Samples: *a* — pattern blocks; *b* — casting bushes

Fig. 4.17 Cast samples with different fillers

To study the interaction of fillers with the shell metal, a longitudinal section of the cylinders was performed (**Fig. 4.18–4.20**). Samples with quartz sand were characterized by metal penetration to a depth of 1 mm, and samples with a mixture of vermiculite and quartz sand — to a depth of 2—3 mm. Aluminum chips, which were added to the sand to "bind" the sand grains, melted only in a 5 mm thick layer adjacent to the shell metal.

Coarse sand had larger porosity between the sand grains, which should contribute to better metal penetration. However, no significant increase in the penetration depth was observed, only within 1–2 mm. In the filler with the addition of polystyrene foam granules, the thickness of the penetration layer increased to 3 mm, but the cavities formed after the polystyrene foam granules burned out did not fill with metal. Moreover, the formed cavities reduced the filler's resistance to spalling. When using polystyrene foam membranes, the shell metal penetration layer into the filler increased to 3–4 mm.

Samples with expanded vermiculite had shells and were characterized by significant defects. This is explained by the low fire resistance of this filler. Because of this, the mixture with vermiculite also had high spalling.

In samples with electrocorundum filler, the penetration layer was 1–2 mm. These samples were also characterized by average spalling. The reason for this is that the material used consists of particles of the same fraction. For example, quartz sand by its nature consists of particles of different sizes. In this case, the binder creates more bonds, since small grains are located between large ones. Therefore, to increase the strength of corundum fillers, it is necessary to mix several fractions to get more bonds in the mixture. Also, samples with corundum had a greater mass than samples with quartz sand.

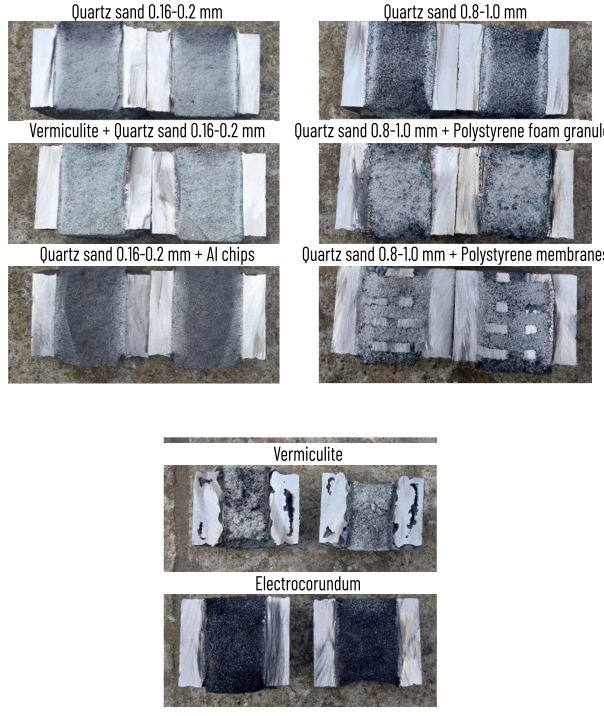

Fig. 4.18 Sections of cast samples with fillers

Fig. 4.19 Sections of cast samples with different fillers

Fig. 4.20 Section of samples with quartz sand filler and membranes obtained by liquid-phase reinforcement

The conducted studies have shown that a mixture of quartz sand with liquid glass is the most suitable functional filler for shell modules. Adding vermiculite to quartz sand may also be promising in order to reduce the mass of the cast module. The use of reinforcement of the filler from the liquid phase of the shell contributed to an increase in the metal penetration layer and the formation of a metal composite.

4.3.3 DEVELOPMENT OF TECHNOLOGY FOR MANUFACTURING MODULE CASTING

Taking into account previous experience in obtaining similar castings, a gating-feeding system was developed, the general view of which is shown in **Fig. 4.21,** for a 500x500 mm module casting. The lower metal supply was selected to ensure uniform filling and uniform gasification of the pattern. To compensate for shrinkage, a riser was placed above the casting.

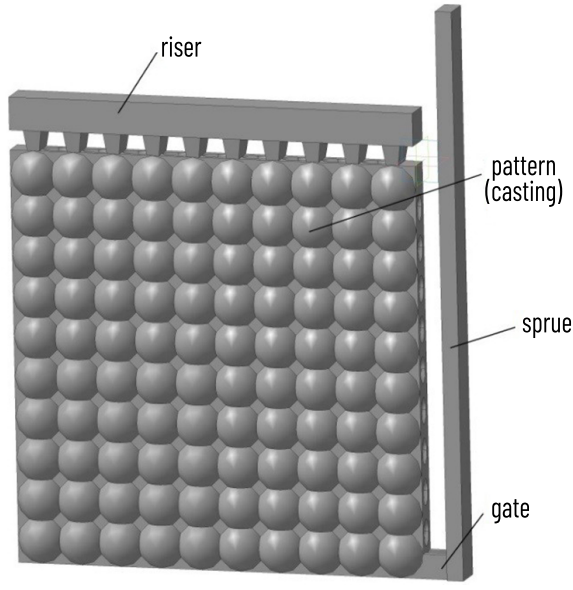

Fig. 4.21 General view of the gating system

Simulation of the pouring and solidification processes of the module casting by lost foam casting was performed using the Procast software.

The parameters necessary for simulation — the properties of 45L steel, polystyrene foam and quartz sand — were selected from the database. The pouring temperature of the steel was set to 1580°C, the initial temperature of the mold — 20°C.

The results of the simulation of pouring a casting of a module 500x500 are shown in **Fig. 4.22**. The total pouring time is 45 s. Filling occurs from one side of the gates. The metal front moves from right to left and from bottom to top simultaneously. This nature of pouring is due to the thermomechanical resistance of the polystyrene foam pattern.

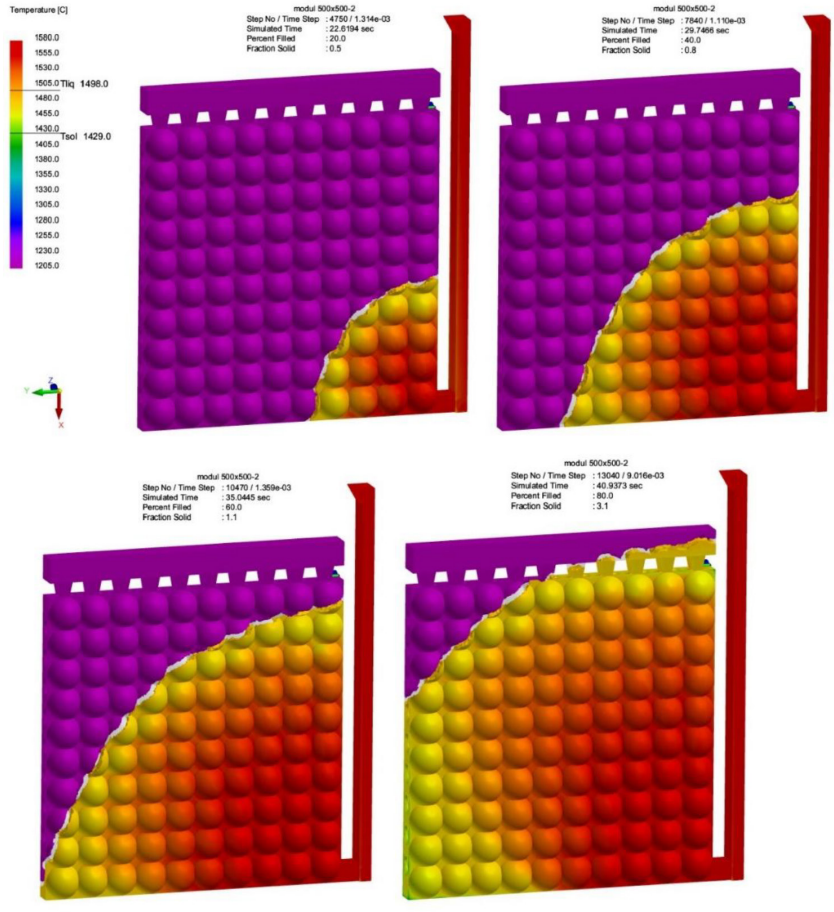

Fig. 4.22 Hydrodynamics of pouring a casting of a module 500x500

An important parameter of the pouring process that affects the formation of casting defects is the melt velocity in the mold. Therefore, the melt flow velocity when filling the casting cavity was investigated.

As the simulation results show (**Fig. 4.23**), the melt front velocity is within 3–5 cm/s throughout the entire pouring time. In the gate and the cell near it, the flow velocity reaches a value of 15 cm/s, which is due to the hydrodynamic pressure created by the metal in the sprue.

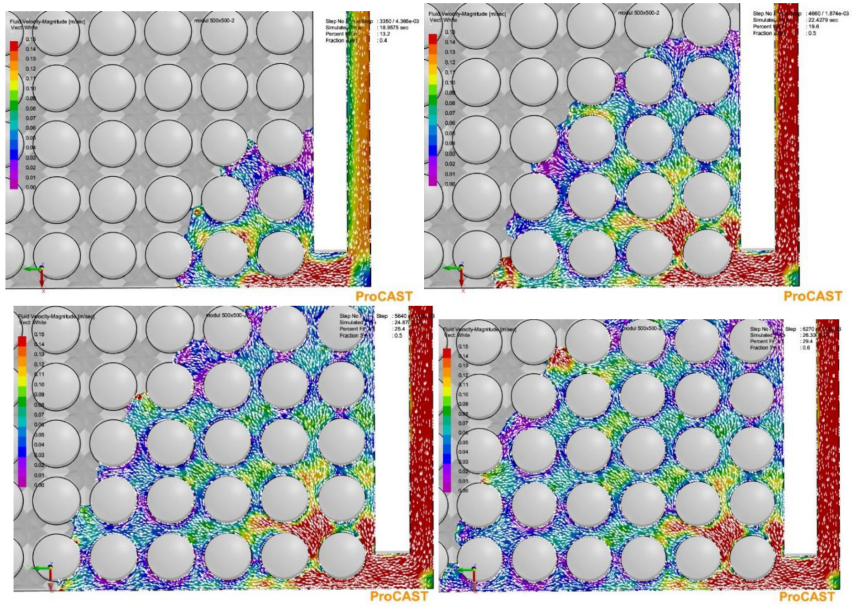

Fig. 4.23 Melt velocity during pouring of the casting

The results of simulation the solidification process of the casting showed that the solidification of the casting body occurs almost uniformly (within 60–90 s) (**Fig. 4.24, *a***). The solidification time of the riser is twice as long, which contributes to the feeding of the walls of the casting with liquid metal from it. The sprue solidifies last, since it contains the hottest metal, and the layers of molding sand around it heat up during pouring, respectively, the temperature gradient between the sprue metal and the mold decreases, slowing down the solidification rate. As a result, shrinkage is concentrated in the riser and the sprue (**Fig. 4.24, *b***).

The porosity in the casting was also studied. The simulation results demonstrated (**Fig. 4.25**) that the porosity of a shrinkage nature is absent in the casting body.

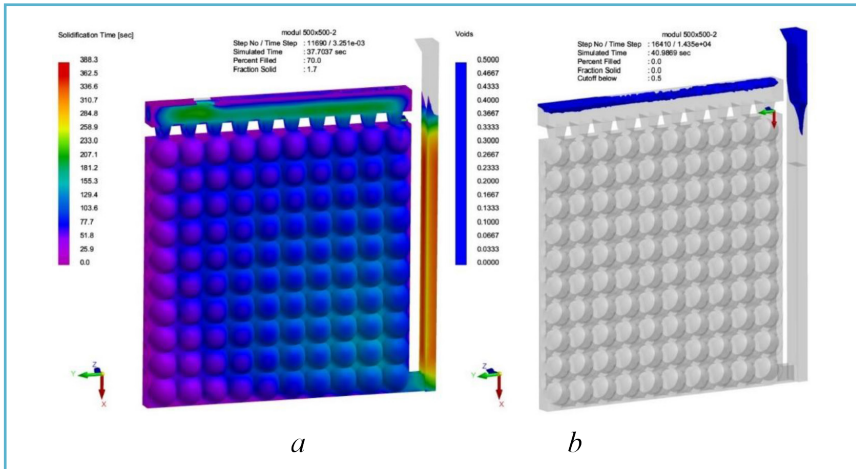

Fig. 4.24 Module casting: *a* — solidification time; *b* — shrinkage

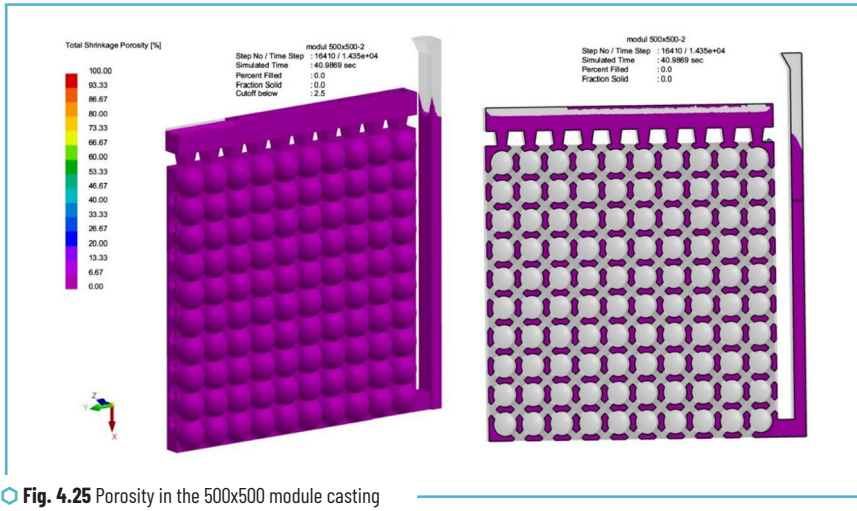

Fig. 4.25 Porosity in the 500x500 module casting

The gating system developed in this way ensures gradual and uniform gasification of the polystyrene foam pattern, contributing to the removal of destruction products from the mold. The melt front velocity of 3–5 cm/s contributes to the rapid replacement of the pattern, but allows to avoid the "coverage" mode of the pattern and the formation of gas defects due to this. During solidification, due to the equilaterality, the casting solidifies almost simultaneously, and shrinkage cavities are concentrated in the riser.

4.3.4 VERIFICATION OF THE TECHNOLOGICAL PROCESS

To verify the technological process of manufacturing hollow cast structures with composite and reinforced non-metallic functional filler from developed steels according to LFC, laboratory and experimental verifications of calculations, simulation and the developed route technological process were carried out.

In this test evaluation, the developed methods for calculating basic parameters and a set of technological divisions, types and characteristics of materials, limits of variation in the parameters of the technological processes of obtaining polystyrene foam patterns, reinforcing composite, preparation and application of refractory coatings on these patterns, as well as pouring the mold and obtaining castings were subject to the developed test evaluation. A casting drawing was previously developed and a pattern was cut out of an EPS 150 (PSB 25—30) polystyrene board on a 3D milling machine, the cavity of which was filled with a reinforcing mixture (**Fig. 4.26**).

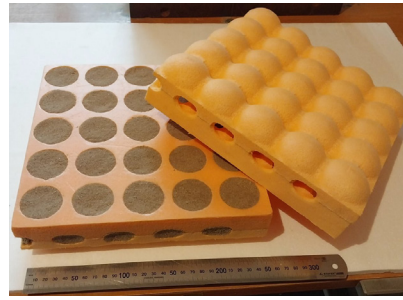

Fig. 4.26 Polystyrene foam pattern of the protective module

In the following, the stages of the technological process were sequentially performed, steel of the required chemical composition was melted and high-quality castings were obtained (**Fig. 4.27**).

Fig. 4.27 Reinforced steel castings of the protective module, which were manufactured using the developed technology

Thus, the created technological processes for obtaining hollow cast structures with composite and reinforced non-metallic functional filler from developed steels using LFC make it possible to obtain reinforced structures that can be used in protective structures.

CONCLUSIONS

Based on the mechanism of interaction of matrix alloy (MA) in the mold in the presence of metal reinforcing elements with polystyrene foam pattern and thermal destruction products in the form of liquid, gaseous and solid phases, a computational model of heat and mass exchange processes was developed with the determination of the heat transfer coefficient in the criterion form (based on the Nusselt, Prandtl, Reynolds criteria) for the flow of liquid MA in the mold.

The task of developing a technological process for obtaining lightweight high-strength steel hollow structures with a non-metallic functional filler, which is a binary part of a single structure and counteracts impact dynamic loads upon contact with high-speed bodies, was solved. Additional reinforcement was carried out in the systems "metal shell — functional filler — solid reinforcing phase or reinforcing phase formed from liquid shell metal", which has not yet been studied in the theory of foundry production, and therefore there are no analogues.

According to the results of research on the features of the hydrodynamic conditions for filling the mold cavity with liquid steel and in the presence of a solid reinforcing phase and thin channels formed in the functional filler, it was established that the time for filling the mold cavity is 7.5...8.0 s for all types of objects under study and the metal flow rate in the thin channels of the filler is 5..7 cm/s, which are optimal for obtaining steel shells when lost foam casting.

The presence of solid metal reinforcement and liquid, solidifying metal of the shell in its thin channels placed in the functional filler affects the heat and mass transfer processes in the mold. Thus, with intensive heating of the functional material due to heat transfer from the reinforcing phase, the functional material heats up during the solidification of the metal shell to a temperature of 1050°C in 130 s (solid state) and during the formation of the reinforcing phase from the shell metal to 1150°C in 100 s. Under such thermophysical conditions, the possibility of sintering (melting) of the non-metallic (metallic) functional layer around the reinforcing phase is created and thereby significantly additionally enhances the operational characteristics of the binary module structure.

It is also determined that the filling of the shell in the thin channels formed in the functional material occurs when pouring metal, which guarantees the specified geometric dimensions of the reinforcing phase and, accordingly, its mechanical properties, which also enhances the operational parameters of the binary module structure.

It was determined that a mixture of quartz sand with liquid glass is the most acceptable functional filler for shell modules. Adding vermiculite to quartz sand may also be promising in order to reduce the mass of the cast module. The use of filler reinforcement with the liquid phase of the shell contributed to an increase in the metal penetration layer and the formation of a metal composite.

According to the results of research on the selection of the optimal chemical composition of steels with specified mechanical properties for hollow structures for the construction of various types of modular protective structures, 35KhGAFL steel with the chemical composition, wt.%: C = 0.30…0.40; Mn = 0.60…0.90; Si = 0.55…0.65; Cr = 0.20…0.70; N = 0.012…0.015; V = 0.08…0.11; S and P ≤ 0.025 of each element; Al = 0.015…0.025. It was established that the best set of mechanical properties for 35KhGAFL steel can be achieved after quenching from a temperature of 930°C in water and tempering at a temperature of 510°C: σ_v = 1150 MPa, σ_τ = 1010 MPa, δ = 16%, ψ = 20%, KCU = 70 J/cm^2, hardness — 31 HRC.

Technological processes for obtaining hollow cast structures with composite and reinforced non-metallic functional filler from developed steels according to LFC have been created and tested, which make it possible to obtain reinforced structures, in particular for protective structures.

FINANCING

The research was carried out within the framework of the project No. state registration 0124U003980 with the support of a grant from the National Research Foundation of Ukraine under the program "Science for Strengthening the Defense Capability of Ukraine".

CONFLICT OF INTEREST

The authors declare that they have no conflict of interest in relation to this research, whether financial, personal, authorship or otherwise, that could affect the research and its results presented in this paper.

USE OF ARTIFICIAL INTELLIGENCE

The authors confirm that they did not use artificial intelligence technologies in creating the submitted work.

REFERENCES

1. Charchi, A., Rezaei, M., Hossainpour, S., Shayegh, J., Falak, S. (2010). Numerical simulation of heat transfer and fluid flow of molten metal in MMA—St copolymer lost foam casting process. Journal of Materials Processing Technology, 210 (14), 2071—2080. https://doi.org/10.1016/j.jmatprotec.2010.07.028
2. Narivskiy, A., Shinsky, O., Shalevska, I., Kvasnitska, Y., Kaliuzhnyi, P., Polyvoda, S. (2023). Modern technological processes of obtaining cast products and structures of responsible purpose from aluminum, ferrous carbon and heat-resistant alloys. Structural materials: manufacture, properties, conditions of use. Kharkiv: TECHNOLOGY CENTER PC, 32—67. https://doi.org/10.15587/978-617-7319-97-8.ch2

3. Shalevska, I. A. (2020) Complex of technological processes of ecologically safe production of lost-foam castings with predicted functional properties. [Doctoral dissertation; Physico-Technological Institute of Metals and Alloys of the National Academy of Science of Ukraine].
4. Kreith, F., Bohn, M. (1997). Principles of Heat Transfer. General Engineering Series. PWS Publishing Company, 793.
5. Shinsky, O. I. (1997). Gazogidrodinamika i tekhnologii litia zhelezouglerodistykh i tcvetnykh splavov po gazifitciruemym modeliam. [Doctoral dissertation; Physico-Technological Institute of Metals and Alloys of the National Academy of Science of Ukraine].
6. Narivskiy, A., Shinsky, O., Shalevska, I., Kvasnitska, Y., Kaliuzhnyi, P., Polyvoda, S. (2023). The influence of external actions and methods of alloying alloys on the operational characteristics of cast products. Structural materials: manufacture, properties, conditions of use. Kharkiv: TECHNOLOGY CENTER PC, 121–157. https://doi.org/10.15587/978-617-7319-97-8.ch4
7. Nagata, S., Sakamoto, M. (1989). Development and applications of metal composites from pressure casting. Materials & Design, 10 (3), 153–158. https://doi.org/10.1016/s0261-3069(89)80031-7
8. Wakai, E., Noto, H., Shibayama, T., Furuya, K., Ando, M., Kamada, T. et al. (2024). Microstructures and hardness of BCC phase iron-based high entropy alloy Fe-Mn-Cr-V-Al-C. Materials Characterization, 211, 113881. https://doi.org/10.1016/j.matchar.2024.113881
9. Shinsky, O., Kvasnytska, I., Shalevska, I., Kaliuzhnyi, P., Neima, O. (2024). Devising a technology for manufacturing hollow cast steel structures with composite and reinforced non-metallic functional filler. Eastern-European Journal of Enterprise Technologies, 6 (12 (132)), 6–14. https://doi.org/10.15587/1729-4061.2024.318553
10. Azeem Ullah, M., Cao, Q. P., Wang, X. D., Ding, S. Q., Abubaker Khan, M., Zhang, D. X., Jiang, J. Z. (2024). Carbon effect on tensile and wear behaviors for a dual-phase Fe61.5Cr17.5Ni13Al8 alloy. Materials Science and Engineering: A, 914, 147128. https://doi.org/10.1016/j.msea.2024.147128
11. Tsyganov, V., Naumik, V., Byalik, H., Ivschenko, L., Mokhnach, R. (2019). Steel-copper nano-composited materials. Contributed Papers from Materials Science and Technology 2019 (MS&T19). Portland, 439–443.
12. Kondratyuk, S. Ye., Veis, V. I., Parkhomchuk, Z. V., Kvasnytska, Y. H., Kvasnytska, K. H. (2024). Thermokinetic Parameters of Solidification and Gradient Structure of Steel Castings. Metallofizika i Noveishie Tekhnologii, 45 (7), 865–872. https://doi.org/10.15407/mfint.45.07.0865
13. Shalevska, I. A., Doroshenko, V. S., Kaliuzhnyi, P. B., Kvasnytska, Yu. G. (2022). Review of the use of cast metal materials in the construction of underground and protective structures. Metal and Casting of Ukraine, 30 (4), 54–61. https://doi.org/10.15407/steelcast2022.04.054
14. ASTM A732/A732M-20. Specification for Castings, Investment, Carbon and Low Alloy Steel for General Application, and Cobalt Alloy for High Strength at Elevated Temperatures. https://doi.org/10.1520/a0732_a0732m-20
15. Shypytsyn, S., Fedorov, H., Kirchu, I., Lykhovey, D., Stepanova, T. (2024). Increasing the physical-mechanical and operational properties of high manganese steels by improving the technological processes of their melting, micro-alloying and modification. Casting Processes, 155 (1), 14–28. https://doi.org/10.15407/plit2024.01.014

16. Yamshinsky, M. M., Fedorov, G. E., Radchenko, K. S. (2015). Termostiikist zharostiikykh stalei dlia roboty v ekstremalnykh umovakh. Visnyk Donbaskoi derzhavnoi mashynobudivnoi akademii, 3, 33—37.
17. DSTU 8781:2018. Steel castings. General specifications (2018). DP «UkrNDNTs». Available at: https://online.budstandart.com/ua/catalog/doc-page.html?id_doc=77524
18. Yamshinsky, M. M., Fedorov, G. E. (2015). Liteinye i mekhanicheskie svoistva zharostoikikh stalei. Lite i metallurgiia, 2, 17—24.
19. ISO 4990:2023. Steel castings — General technical delivery requirements. (2023). ISO. Available at: https://cdn.standards.iteh.ai/samples/84185/33d9639ba3db417ab01fe2a41751f295/ISO-4990-2023.pdf
20. DSTU 9074:2021. Steel. Microstructure Standarts (2021). DP «UkrNDNTs». Available at: https://online.budstandart.com/ua/catalog/doc-page.html?id_doc=94147
21. DSTU 8966:2019. Steel. Metalographic method for the determination of nonmetallic inclusions (2019). DP «UkrNDNTs». Available at: https://online.budstandart.com/ua/catalog/doc-page.html?id_doc=88067
22. ISO 643:1983. Steels — Micrographic determination of the ferritic or austenitic grain size (1983). ISO. Available at: https://cdn.standards.iteh.ai/samples/4773/6ad7e45fca0d4daa86654405f6e2d12e/ISO-643-1983.pdf [in English].
23. DSTU 7809:2015. Carbon Structural Quality Steel Gauged Bars With Special Surface Finish. General specifications (2015). DP «UkrNDNTs». Available at: https://online.budstandart.com/ru/catalog/doc-page?id_doc=64320
24. Shinsky, O., Fedorov, G., Kvasnytska, I., Shalevska, I., Kaliuzhnyi, P., Neima, O., Shalevskyi, A. (2025). Selection of materials for the manufacture of cast hollow metal modules of protective structures. Casting Processes, 159 (1), 11—21. https://doi.org/10.15407/plit2025.01.011
25. Liu, X. J., Bhavnani, S. H., Overfelt, R. A. (2007). Simulation of EPS foam decomposition in the lost foam casting process. Journal of Materials Processing Technology, 182 (1-3), 333—342. https://doi.org/10.1016/j.jmatprotec.2006.08.023
26. Kaliuzhnyi, P., Shalevska, I., Shynskyi, O. (2024). Casting of a Steel Valve Body Using Lost Foam Sand casting: Comparison Between Experimental and Simulation Results. International Journal of Metalcasting, 19 (4), 2409—2418. https://doi.org/10.1007/s40962-024-01487-2

Edited by
Inna Shalevska

MODERN TRENDS IN CONSTRUCTION MATERIALS TECHNOLOGIES

Maksym Kovzel, Oleksandr Babachenko, Daria Togobitska, Oleh Kuzmin, Oktyabrina Chemakina, Anton Kuzmin, Oleksandr Zaporozhets, Igor Dudarev, Larysa Bal-Prylypko, Oleksandr Shcheretskyi, Anatolii Verkhovliuk, Ruslan Sergiienko, Dmytro Kanibolotsky, Volodymyr Shcheretskyi, Ievgenij Dzevin, Oleg Shinsky, Inna Shalevska, Iuliia Kvasnytska, Pavlo Kaliuzhnyi, Oleksandr Neima, Anatolii Shalevskyi

Monograph

Technical editor I. Prudius
Desktop publishing T. Serhiienko

TECHNOLOGY CENTER PC®
Published in December 2025
Enlisting the subject of publishing No. 4452 – 10.12.2012
Address: Shatylova dacha str., 4, Kharkiv, Ukraine, 61165
